Analytical and Experimental Analysis of Tubular Braided Composites

by

Garrett William Melenka

A thesis submitted in partial fulfillment of the requirements for the degree of

Doctor of Philosophy

Department of Mechanical Engineering
University of Alberta

Abstract

Tubular braided composites consist of woven fibers imbedded in a resin matrix. Braided composites are manufactured using a device known as a Maypole braider. Braiding machines can be configured to produce several braiding patterns including: Diamond (1/1), Regular (2/2), Hercules (3/3) and triaxial braids. Presently, most researchers focus on one braiding pattern when evaluating braided composites.

A comprehensive comparison of the different braiding patterns has not been performed. The goal of this thesis is to develop a new analytical model that predicts the mechanical properties of each of the available braiding patterns. To achieve this aim a new Volume Averaging methodology was used. In order to support the proposed analytical model experimental analysis of braided composites samples were performed. Braided composite samples were evaluated using micro-computed tomography in order to characterize the three dimensional structure of braided composites. Braided composite samples were also evaluated under tensile and torsional loads in order to determine the longitudinal and shear moduli for tubular braided composites. Braid samples were examined using a three dimensional digital image correlation (3D DIC) method in order to measure the three dimensional strain fields. The 3D DIC method allow for the mechanical properties of braid samples to be evaluated. The effect of braiding pattern and braid angle on the 3D strain field was also investigated. The 3D DIC results demonstrate the periodic strain field that occurs in tubular braided composite braids due to the nature of the braid manufacturing process.

The Volume Averaging methodology presented in this thesis was also applied to fiber-reinforced 3D printed structures. The results of this work demonstrate the adaptability of the Volume Averaging methodology to different composite structures in order to predict mechanical properties.

The results of this work demonstrate that braids of different geometry can be model using an analytical Volume Averaging method. The presented model results were experimentally validated using a 3D DIC optical measurement technique. The versatility of the Volume Averaging method is also demonstrated since this technique was applied to the modelling of both tubular braided composite braids and fiber-reinforced 3D printed structures.

Preface

The work presented in this thesis has been organized into seven chapters. The first chapter introduces the thesis topic and describes the thesis objectives. Chapter 2 has been accepted as a book chapter in Handbook of Advances in Braided Composites Materials. Chapter 3 and Chapter 6 have been accepted in scientific journals and Chapters 4 and 5 have been submitted for review.

Chapter 2 is a literature review of current modeling techniques for braided composites. The content of Chapter 2 is a portion of a book chapter that appears in Handbook of Advances in Braided Composite Materials:

> Melenka GW, Pastore CM, Ko FK, Carey JP, Advances in 2D and 3D Braided Composite Materials Modeling, Handbook of Advances in Braided Composite Materials: Theory, Production, Testing and Applications, Carey JP (Ed), Woodhead Publishing, 2016

The sections on two dimensional braiding were written by the author of this thesis. These sections can be found in Chapter 2.

Chapter 3 investigates the three dimensional geometry of tubular braided composites using micro-tomographic imaging techniques. The author's contribution to this work includes: design of experimental methodology, data collection, manuscript preparation, and the analysis and interpretation of experimental results.

> Garrett W. Melenka, Eric Lepp, Benjamin K.O. Cheung, Jason P. Carey, Micro-computed tomography analysis of tubular braided composites, Composite Structures, Volume 131, 1 November 2015, Pages 384-396, ISSN 0263-8223

Chapters 4 and 5 have been submitted to the Journal of Composite Materials and are currently under review. These chapters present the experimental methodology for evaluating braided composites and an analytical model for predicting their mechanical properties.

Chapter 6 examined the prediction of the mechanical properties of a fiber reinforced 3D printed structure using a volume averaging methodology. The author's contribution to this work includes: design of experimental methodology, manuscript preparation, analytical model development, data collection, and the analysis and interpretation of the experimental results.

Acknowledgments

First and foremost I would like to thank my supervisor Dr. Jason Carey. Dr. Carey has been an excellent supervisor and I am grateful for his guidance. I greatly appreciate all the opportunities that Dr. Carey has made available to me both related and unrelated to my thesis project. Throughout my degree Dr. Carey has been extremely supportive and has helped me to grow and develop my academic and research skills.

Secondly, I would like to thank Dr. David Nobes. Over the years Dr. Nobes has been an excellent mentor. Through his mentorship and guidance I have been able to greatly improve my technical engineering skills.

Thirdly, I would like to show my appreciation to my two additional committee members Dr. Cagri Ayranci and Dr. Pierre Mertiny. Thank you for your suggestions and guidance.

Finally, I would like to thank my lab mates. There are too many people to thank individually but I would like to express my gratitude to those that I have worked with during my time as a graduate student. The Carey lab group is an extremely supportive group of exceptionally talented students and I am privileged to have been able to worth such a unique group of individuals.

Table of Contents

List of Figures

List of Tables

List of Abbreviations

2D	Two Dimensional
3D	Three Dimensional
DIC	Digital Image Correlation
3D DIC	Three Dimensional Digital Image Correlation
FEA	Finite Element Analysis
UofA	University of Alberta
μCT	Micro-computed tomography
VAS	Volume Average Stiffness

List of Symbols

E_x	Longitudinal Elastic Modulus
E_y	Transverse Elastic Modulus
E_z	Out-of-plane Elastic Modulus
G_{xy}	In-Plane Shear Modulus
G_{yz}	Out-of-plane shear modulus
G_{xz}	Out-of-plane shear modulus
v_{xy}	In-Plane Poisson's Ratio
v_{yz}	Out-of-plane Poisson's Ratio
v_{xz}	Out-of-plane Poisson's Ratio
N	Total Number of Braider Bobbins
θ	Braid angle measured from longitudinal axis
ϕ	Yarn crimp angle
W_y	Yarn Width
L_{und}	Yarn undulation length
V_f	Fiber Volume Fraction
V_m	Matrix Volume Fraction
β	Yarn Shift Angle
a	Yarn Thickness
D_i	Braid Mandrel Diameter
Do	Braid outer diameter
ε_{xx}	Transverse Strain
ε_{yy}	Longitudinal Strain
γ_{xy}	Shear Strain
[S]	Compliance Matrix
[C]	Stiffness Matrix
[A]	Extensional Stiffness Matrix
[B]	Coupling Stiffness Matrix
[D]	Flexural Stiffness Matrix
[T]	Transformation Matrix
[R]	Reuters Matrix

Chapter 1   Introduction

1.1   Motivation

Composite material use is increasing because of their strength and weight characteristics. The aerospace industry accounts for $2 billion in composite research and development in Canada [1], and composites now account for 50% of the Boeing 787 primary structure which results in a 20% weight reduction over conventional aluminum designs [2]. Tubular braided composites are composed of fibers braided onto a mandrel then saturated with resin to increase structural rigidity. Tubular braided composites material properties are altered by varying resin and fiber types or braid geometry to meet design requirements. This adaptability allows use of tubular braided composites in a wide variety of applications such as cardiovascular catheters, bicycle frames and aircraft support structures [3].

Tubular braided composites are manufactured in open and closed mesh configurations and with circular and non-circular cross-sections allowing for use in a wide variety of applications. Braided composites can also be manufactured with a variety of braid patterns: Diamond (1/1), Regular (2/2), Hercules (3/3) and triaxial [4]. Material properties of the tubular braided composites are difficult to characterize due to their non-uniform nature and due to the variety of braid geometries that can be manufactured. Material properties for tubular braided composites are commonly determined experimentally but this limits the implementation of tubular braided composites to specific applications. Several

analytical and finite element models exist [5-11]; however, a generalized model which is capable of determining the mechanical properties of the variety of different braiding patterns does not exist.

Accurate determination of tubular braided composite material properties is vital to increase industrial application. Conventional engineering measurement techniques (i.e. strain gauges and extensometers) are not sufficient to resolve features on the non-uniform tubular braided composite surface and provide true measurements [12]. Current analytical models for tubular braided composites also do not account for changes in braid cross-sectional shape, braid angle or large deformation that is associated with open mesh tubular braided composites or tubular braided composites manufactured with flexible resins.

1.2   Thesis Objectives

A new analytical model for characterizing the elastic properties of tubular braided composites was developed. This new analytical model allows for the elastic properties of different braiding patterns (Diamond, Regular and Hercules) to be predicted. The proposed model is based on a Volume Average Stiffness method in order to account for different braiding patterns and key braiding parameters like braid angle, yarn width, yarn thickness and braid diameter. The presented analytical model can be extended to structures other than tubular braided composites. The volume averaging method can also be applied to fiber reinforced 3D printed structures. The ability to extend the presented modelling approach to both tubular braided composites and fiber reinforced 3D printed structures demonstrates the versatility of the Volume Averaging method.

The model presented was validated experimentally. A comprehensive set of experiments was performed in order to examine the effect of braiding pattern and braiding angle on mechanical properties. Samples were evaluated using tensile and torsional tests in order to experimentally determine longitudinal elastic modulus and in-plane shear modulus for each braid sample.

Due to the complex and non-uniform geometry of braided composites a contact free full field strain measurement technique known as three dimensional digital image correlation (3D DIC) was used.

The outcome of this thesis will result in a generalized model which predicts the mechanical properties of tubular braided composites. The generalized model allows for the mechanical properties of Diamond, Regular, Hercules and triaxial braid patterns to be predicted. The generalized tubular braided composite models, validated with accurate optical measurements, will minimize the need for labor intensive experiments to predict the braid behavior. The different braiding patterns examined in this study may provide improved structural properties depending on the loading conditions subjected to the braid structure. Improved models will allow for the application of tubular braided compsites to structural and medical industries and further research and development.

1.3   Thesis Outline

This thesis is organized into seven chapters. Current modelling techniques used to characterize the behavior of tubular braided composites are summarized in

Chapter 2. To support the analytical model presented in this thesis the geometry of composite braids is examined in Chapter 3. The geometry of a tubular braid was examined using micro-computed tomography in order to fully characterize the three dimensional geometry of a composite braid. Chapter 4 presents the experimental methodology for evaluating tubular braided composites using the 3D DIC strain measurement technique. Diamond and Regular braids are examined under both tensile and torsional loading. The effect of braid pattern and braiding pattern on mechanical properties are examined. Additionally, the effect of braid pattern and braid angle on the three dimensional strain field in each braid sample is examined. The proposed model to characterize the elastic properties of tubular braided composites is presented in Chapter 5. The model presented in Chapter 5 is based on a Volume Average Stiffness method. The proposed model is compared to existing model and experimental results that exist in literature. The proposed model is also validated against tensile and torsional experiment data using the experimental methodology presented in Chapter 4. The methodology used in Chapter 5 to determine the mechanical properties of tubular braided composites is also applied to the predicting of the mechanical properties of fiber-reinforced 3D printed structure. The application of the Volume Average Stiffness method to predict the mechanical properties of fiber-reinforced 3D printed structures is presented in Chapter 6. In Chapter 6 the model results for the fiber-reinforced 3D printed structures are validated against experiments. The model results presented in Chapters 5 and 6 demonstrate the versitilite of the Volume Average Stiffness methodology in order to predict the elastic properties of

different composite structures. A summary of results and a future work for modeling the behaviour of braided composites is presented in Chapter 7.

1.4   References

[1] (2016). *AIAC Guide to Canada's Aerospace Industry*. Available: http://aiac.ca/guide/.

[2] (2016). *Boeing 787 Dreamliner*. Available: http://www.boeing.com/commercial/787/.

[3] J. Carey, G. Melenka, A. Hunt, B. Cheung, M. Ivey and C. Ayranci, "Braided composites in aerospace engineering," *Advanced Composite Materials for Aerospace Engineering: Processing, Properties and Applications,* pp. 175, 2016.

[4] G. W. Melenka, A. J. Hunt, C. M. Pastore, F. K. Ko, M. Munro and J. P. Carey, "Manufacturing processes for braided composite materials," in *Handbook of Advances in Braided Composite Materials: Theory, Production, Testing and Applications*, J. P. Carey, Ed. Woodhead Publishing, 2016, .

[5] C. Ayranci and J. P. Carey, "Predicting the longitudinal elastic modulus of braided tubular composites using a curved unit-cell geometry," *Composites Part B: Engineering,* vol. 41, pp. 229-235, 2010.

[6] J. Carey, A. Fahim and M. Munro, "Predicting elastic constants of 2D-braided fiber rigid and elastomeric-polymeric matrix composites," *J Reinf Plast Compos,* vol. 23, pp. 1845-1857, 2004.

[7] G. W. Melenka, C. M. Pastore, F. K. Ko and J. P. Carey, "Advances in 2D and 3D braided composite materials modeling," in *Handbook of Advances in Braided Composite Materials: Theory, Production, Testing and Applications*, J. P. Carey, Ed. Woodhead Publishing, 2016, .

[8] S. C. Quek, A. M. Waas, K. W. Shahwan and V. Agaram, "Analysis of 2D triaxial flat braided textile composites," *Int. J. Mech. Sci.,* vol. 45, pp. 1077-1096, 2003.

[9] J. Byun, "The analytical characterization of 2-D braided textile composites," *Composites Sci. Technol.,* vol. 60, pp. 705-716, 2000.

[10] L. Xu, S. J. Kim, C. -. Ong and S. K. Ha, "Prediction of material properties of biaxial and triaxial braided textile composites," *J. Composite Mater.,* vol. 46, pp. 2255-2270, 2012.

[11] X. Ji, A. M. Khatri, E. S. Chia, R. K. Cha, B. T. Yeo, S. C. Joshi and Z. Chen, "Multi-scale simulation and finite-element-assisted computation of elastic properties of braided textile reinforced composites," *J. Composite Mater.,* vol. 48, pp. 931-949, 2014.

[12] G. Melenka, D. Nobes and J. Carey, "3D DIC measurement of tubular braided composites," in *ICCM 19,* Montreal, 2013, .

Chapter 2 Background

2.1 Introduction

Industrial and commercial use of composite materials is increasing due to their advantageous strength and weight characteristics [1]. Textile composites comprise of textile structures within a resin matrix. Textile composites are an attractive manufacturing method over conventional unidirectional laminate composites due to their high production rate; yarn interlacing which improves structural stability; and damage tolerance [2]. Because of these factors the use of textile composites is increasing in aerospace, sporting, automotive and marine industries [2-4]. Textile composites encompass a wide variety of textile structures which includes: braids, weaves, and knitting and non-woven fabrics [5]. Textile composite processes are compared in more detail in [6].

Textile composites comprise of a combination of a textile structure within a resin matrix. Textile composites are an attractive manufacturing method over conventional unidirectional laminate composites due to their high production rate. Textile composites are also attractive due to yarn interlacing which improves

structural stability and damage tolerance [2]. Because of these factors the use of textile composites is increasing in aerospace, sporting, automotive and marine industries [2, 3, 7, 8]. Textile composites encompass a wide variety of textile structures which includes: braids, weaves, and knitting and non-woven fabrics [9]. Examples of the wide variety of textile structures that can be implemented in the design of advanced composite structures are shown in Figure 2-1.
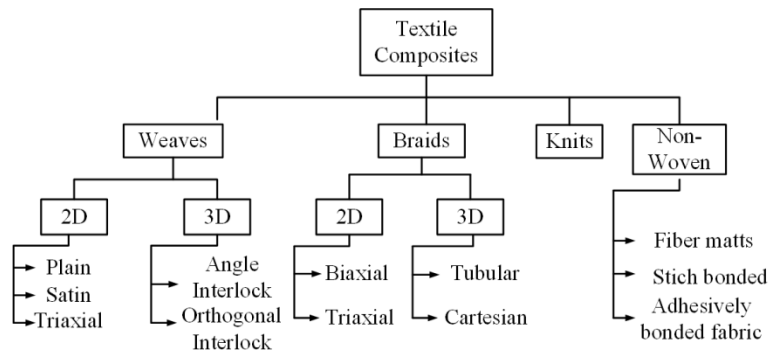
Figure 2-1: Examples of textile structures used in the manufacturing of advanced composite structures [10, 11]

Braids and woven composites are similar since both manufacturing methods consist of interlaced yarns. Woven composites consist of yarns which produce an orthogonally interlaced structure whereas braided composites are formed by non-orthogonally interlaced yarns. A comparison of woven and braided composites is shown in Figure 2-3. Common weave patterns includes: plain (1/1), twill (2/2), twill (3/3). Braid patterns which are analogous to the aforementioned weave

patterns include: Diamond (1/1), regular (2/2) and Hercules (3/3). The geometry of the braid and weave patterns are shown in Figure 2-3.
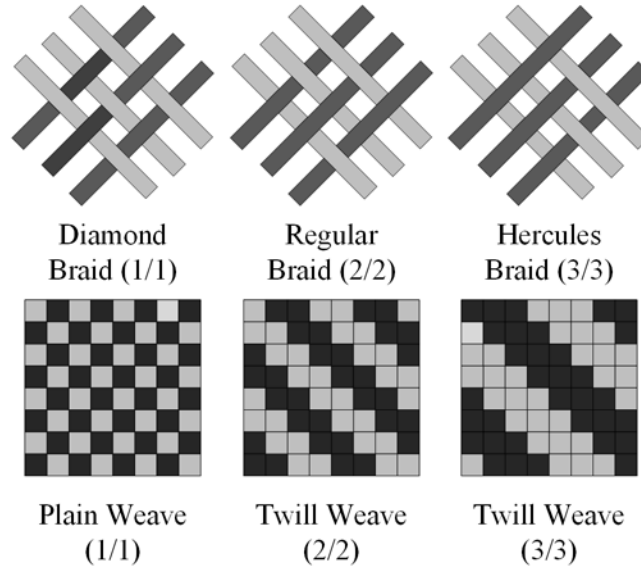
Figure 2-2: Comparison of braid and weave patterns. Top- Braid patterns. Bottom- Weave patterns

The mechanical properties of braided composites must be determined in order for braided composites to be utilized for engineering applications. The analysis of braided composites is more complicated than conventional composite laminates due to the undulating nature of braid yarns. Additionally, the material properties of braided composites are typically anisotropic due to yarn undulations (crimp) and yarn orientation (braid angle). Due to the complicated geometrical nature of braided composites and anisotropic material properties researchers have developed different models to predict their mechanical properties. The most prominent modeling methods for braided composites includes: Classical Laminate Plate Theory based models (CLPT), Fabric Geometry Models (FGM), volume averaging methods, and Finite Element Analysis (FEA) models. Each of these modeling approaches has advantages and disadvantages; understanding the

capability of each modeling method is paramount for predicting the behavior of braided composites. This chapter will describe the various modelling techniques which have been used to determine the elastic properties of braided composites. The literature presented in this chapter is required to support the proposed model in Chapter 5. Thermal properties and failure of braided composites were not explored in this thesis as these properties were not examined with the new proposed model.

2.2 Two-Dimensional Braided Composite Analyitical Models

2.2.1 Braid Unit Cell Geometry

Textile composites are periodic in nature therefore a repeating unit cell is identified and assumed to represent the entire composite behavior that possesses the same architecture. An example of a Diamond braid unit cell geometry is shown in Figure 2-3. In this figure, the braid angle (θ) is defined as the angle between the braid longitudinal axis and the braid yarn. Yarn spacing can be controlled by altering yarn width (W_y), mandrel radius (r_0), braid angle, or the number of braider bobbins (n) as shown in equation 2-1. Matrix only regions occur when the braid yarns are not sufficient to cover the entire braid mandrel surface area. When modeling composite braids authors commonly use a parallelogram [7-9] as seen in Figure 2-3 (a) or a rectangular region [12-17] as depicted in Figure 2-3 (b) to represent the entire braid geometry. Other unit cell geometries are also possible for describing composite braids. Symmetries exist within the unit cell geometries shown in Figure 2-3, therefore the unit cell can be further subdivided into smaller sub-cells [18, 19]. The unit cell geometries shown

in Figure 2-3 are convenient for modeling purposes since geometries can be defined based on physical parameters measured from composite braids.

$$L_{spacing} = \frac{2r_0\pi}{n\sin\theta}$$ 2-1
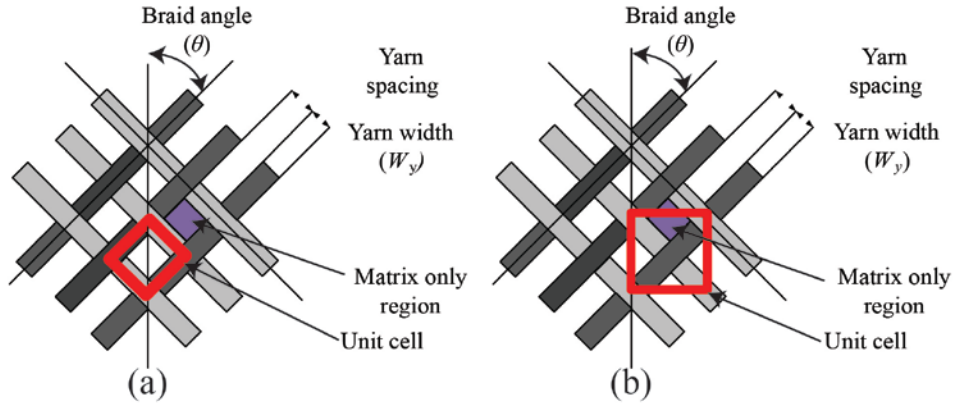
Figure 2-3: Example diamond braid geometry used to determine material properties (a) parallelogram unit cell geometry (b) rectangular unit cell geometry.

2.2.2 Classical Laminate Plate Theory Models

The Classical Laminate Plate Theory (CLPT) is an approach that is commonly used to determine the mechanical properties of composite laminates and is based on the Kirchkoff-Love theory of plates [20]. The CLPT approach provides a method for determining the extensional (**A**), coupling (**B**) and bending (**D**) stiffness matrices which are then used to determine composite effective material properties. The basic equations for the CLPT approach are shown in Equations 2-2, 2-3 and 2-4; these were described in [21]. Several researchers have used a CLPT based method as a basis for determining the mechanical properties of composites braids. CLPT based models were initially used to predict the stiffness

and strength of woven composites but this method was later extended to braided composites.

$$[Q] = \begin{bmatrix} \dfrac{E_{11}}{1 - \upsilon_{12}\upsilon_{21}} & \dfrac{E_{11}\upsilon_{21}}{1 - \upsilon_{12}\upsilon_{21}} & 0 \\ \dfrac{E_{11}\upsilon_{21}}{1 - \upsilon_{12}\upsilon_{21}} & \dfrac{E_{22}}{1 - \upsilon_{12}\upsilon_{21}} & 0 \\ 0 & 0 & G_{12} \end{bmatrix}$$

2-2

$$A_{ij} = \sum_{k=1}^{N} \left(\overline{Q}_{ij} \right)_k \left(z_k - z_{k-1} \right)$$

$$B_{ij} = \frac{1}{2} \sum_{k=1}^{N} \left(\overline{Q}_{ij} \right)_k \left(z_k^2 - z_{k-1}^2 \right)$$

$$D_{ij} = \frac{1}{3} \sum_{k=1}^{N} \left(\overline{Q}_{ij} \right)_k \left(z_k^3 - z_{k-1}^3 \right)$$

2-3

$$\begin{bmatrix} N_x \\ N_y \\ N_{xy} \end{bmatrix} = \begin{bmatrix} A_{11} & A_{12} & A_{16} \\ A_{12} & A_{22} & A_{26} \\ A_{16} & A_{26} & A_{66} \end{bmatrix} \begin{bmatrix} \varepsilon_x^0 \\ \varepsilon_y^0 \\ \gamma_{xy}^0 \end{bmatrix} + \begin{bmatrix} B_{11} & B_{12} & B_{16} \\ B_{12} & B_{22} & B_{26} \\ B_{16} & B_{26} & B_{66} \end{bmatrix} \begin{bmatrix} \kappa_x \\ \kappa_y \\ \kappa_{xy} \end{bmatrix}$$

$$\begin{bmatrix} M_x \\ M_y \\ M_{xy} \end{bmatrix} = \begin{bmatrix} B_{11} & B_{12} & B_{16} \\ B_{12} & B_{22} & B_{26} \\ B_{16} & B_{26} & B_{66} \end{bmatrix} \begin{bmatrix} \varepsilon_x^0 \\ \varepsilon_y^0 \\ \gamma_{xy}^0 \end{bmatrix} + \begin{bmatrix} D_{11} & D_{12} & D_{16} \\ D_{12} & D_{22} & D_{26} \\ D_{16} & D_{26} & D_{66} \end{bmatrix} \begin{bmatrix} \kappa_x \\ \kappa_y \\ \kappa_{xy} \end{bmatrix}$$

2-4

The first model to utilize a CLPT based approach for modeling woven composites was proposed by Ishikawa and Chou [22, 23]. Three methods were outlined: the mosaic model, fiber inclination model and the bridging model. The schematics of three models of Ishikawa and Chou are shown in Figure 2-4. The mosaic model, Figure 2-4 (a), is a simplistic model that treats the fiber undulations as an assembly of asymmetrical cross-ply laminates. The fiber undulation model,

Figure 2-4 (b), expands on the mosaic model by using a sinusoidal equation to model yarn undulations. The bridging model, Figure 2-4 (c), was developed specifically for satin weaves. This model allows for an undulation region and strain yarn regions to be modeled [4]. The mosaic and fiber inclination and bridging models are both one-dimensional models meaning that fiber undulations are only considered in the loading direction of the woven composites. Since the fiber inclination and mosaic models are one-dimensional, they can only be utilized to predict mechanical properties in the direction of the fiber undulations [24-26]. Despite the limitations of the models presented by Ishikawa and Chou, these models are simple to use and implement, and are therefore useful for preliminary design calculations.
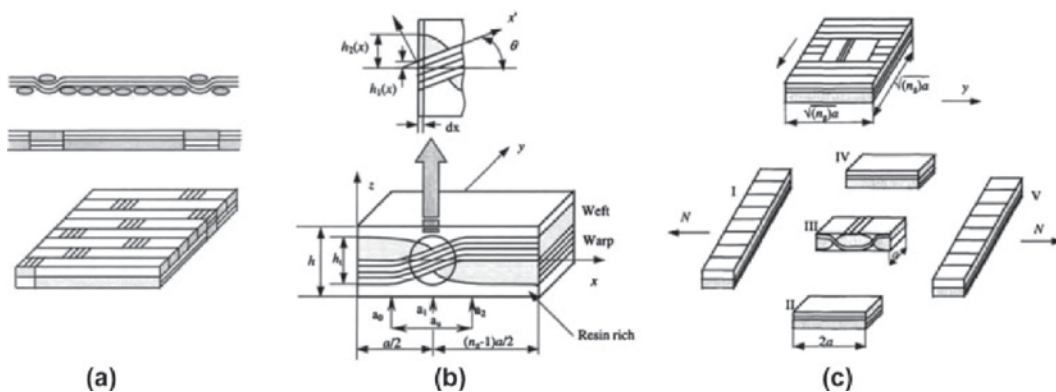
Figure 2-4: Classical laminate plate theory based model of Ishikawa and Chou to represent textile composites

(a) Mosaic Model (b) Fiber Inclination Model (c) Bridging Model [22, 23]

The stiffness matrix for the undulating yarns is calculated using equation 9-5. In this equation, θ represents the off-axis angle (undulation) of the yarns as seen in Figure 2-4 (and not the braid angle).

$$
[Q_{ij}] = \begin{bmatrix} \dfrac{E_x(\theta)}{D_v} & \dfrac{E_y(\theta)\upsilon_{yx}(\theta)}{D_v} & 0 \\ \dfrac{E_y(\theta)\upsilon_{yx}(\theta)}{D_v} & \dfrac{E_y(\theta)}{D_v} & 0 \\ 0 & 0 & G_{xy}(\theta) \end{bmatrix} \qquad \text{2-5}
$$

$$
D_v = 1 - \frac{\upsilon_{yx}(\theta)E_y}{E_x}
$$

The fiber inclination model developed by Ishikawa and Chou was expanded upon by Naik and Shembekar [27-29]. Naik and Shembekar presented a two-dimensional version of Ishikawa and Chou's fiber inclination model where fiber undulations in the warp and weft directions were taken into account. The new model presented by Naik and Shembekar is limited to plain woven composites. A schematic of the woven composite geometry used by Naik and Shembekar is shown in Figure 2-5. This figure shows the undulating fibers in both the warp and weft directions. In addition to extending the CLPT based model to a 2D model for woven fabric lamina, this method was also used for woven fabric laminate analysis and woven fabric laminate design [27-29].
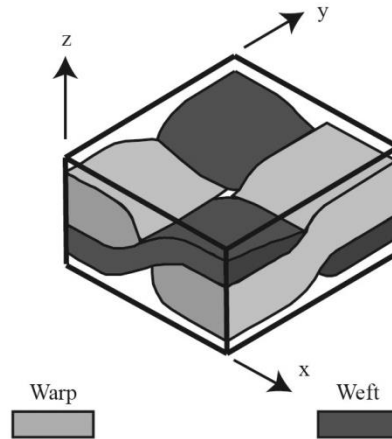
Figure 2-5: Example woven fabric geometry used by Naik and Shembekar [27] to model the 2D elastic

properties of woven composites

Naik and Shembekar compared the results of one dimensional woven composite model with two dimensional model results. In addition, experimental values for woven composites were also compared. Table 2-1 and Table 2-2 compare the results for woven composite with varying combinations of fibers and matrix as well as lamina of varying thicknesses. The analysis of Naik and Shembekar concluded that the 2D parallel-series model best predicted the elastic properties of woven composites in both the warp and weft directions. The analysis performed by Naik and Shembekar confirmed the limitations of the one-dimensional braid models of Ishikawa and Chou.

Table 2-1: Comparison of woven fiber composite models with experimental data E_y (along Warp direction) [27]. Bolded values indicate best agreement with experiment.

Material	Lamina Thickness (h)- mm	Experimental Elastic Modulus (Range)	Elastic Modulus E_y (GPa)			
			1D Parallel Model	1D Series Model	2D Parallel Series	2D Series Parallel
T-300 carbon/ epoxy	0.16	60.3 (56-61)	67.8	54.7	**58.8**	38.1
	0.2	18.1 (15-22)	28.6	24.1	**21.5**	18.4
	0.5	14.8 (14-22)	29.5	24.4	**21.6**	18.4
	0.15	14.5 (10-16)	21.1	23.1	**14.9**	13.9

Table 2-2: Comparison of woven fiber composite models with experimental data E_x (along Weft direction) [27]. Bolded values indicate best agreement with experiment.

Material	Lamina Thickness (h)- mm	Experimental Elastic Modulus (Range)	Elastic Modulus- E_x (GPa)			
			1D Parallel Model	1D Series Model	2D Parallel Series	2D Series Parallel
T-300 carbon/ epoxy	0.16	49.3 (47-50)	54.1	51.5	**45.8**	31.1
	0.2	--	22.1	26.8	**17.1**	16.7
	0.5	13.8 (12-16)	22.1	26.3	**16.1**	15.7
	0.15	14.5 (10-16)	21.1	23.1	**14.9**	13.9

A 2D CLPT based model was also developed by Raju and Wang [25]. This model also built on the work of Ishikawa and Chou [22, 23]. The model presented by Raju and Wang allowed for the mechanical properties of plain weave, 5- harness and 8 harness woven composites to be predicted using a closed form solution. In addition to predicting the mechanical properties of three weave patterns, the CLPT based models was also used to predict the coefficients of thermal expansion for these braid patterns. The CLPT model presented by Raju

and Wang was compared with 3D FEA simulations. The CLPT model results were found to be within 5% of the FEA model results.

In addition to calculating the elastic properties of plain weave, 5-harness and 8-harness woven composites, the model of Raju and Wang also predicted the thermal constants of expansion for each of these three textile composites. Unsatisfactory results were found for predicting the thermal coefficients of expansion for all architectures. Differences between model results and experiments were attributed to assumptions made for the resin mechanical properties and fiber volume fractions used for this analysis.

The model developed by Yang *et al.* [30] known as the fiber inclination model is an extension of Chou and Ishikawa's fiber inclination model and uses a CLPT based formulation. The main advantage of this technique is that it is not limited to a particular braiding or weaving process therefore, this method can be used to model both textile and braided composites. The fiber inclination model of Yang et al. treats braided composites as an assemblage of unit cells where within each unit cell fibers are oriented in four body diagonal directions. A schematic of the unit cell of the fiber inclination model is shown in Figure 2-6. The unit cell in this figure shows four braid yarns oriented across the four corners of the braid unit cell. The mechanical properties of a composite structure are then modeled by assembling a series of unit cells. With this model all fibers are considered to be straight and the crimp, fiber interlocking and bending of yarns is not taken into account. The fiber inclination model of Yang *et al.* was demonstrated to have reasonable results in comparison with experiments; however the accurate

modelling of the Poisson's ratio in the case of 3D braided composites required the addition of axial yarns.
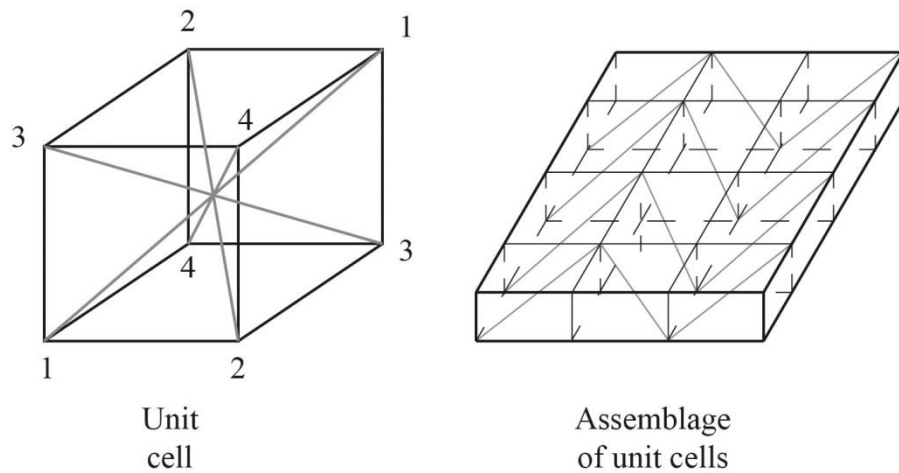
Figure 2-6: Unit cell structure for the fiber inclination model (left). Assembly of unit cells to model a textile or braided structure (right) [28]

One of the first attempts to accurately model braided composites as opposed to woven composites was performed by Aggarwal *et al.* [31]. A generalized CLPT based model was presented that allows for key braiding parameters like yarn undulation, inter-yarn gap, yarn cross-section and braid angle to be accounted for. The model was limited to diamond braid patterns. A parametric study was carried out using the CLPT based model for diamond braided composites to demonstrate the effect of inter-yarn gap, yarn aspect ratio and braid angle on mechanical properties.

The modelling process used by Aggarwal *et al.* [31] is illustrated in Figure 2-7. The representative unit cell is segmented into a series of *M* x *N* sub-cells. This modeling approach is similar to the work of Yang *et al.*, however instead of assuming straight yarns the undulation and curvature of the braid yarns are taken into account. The stiffness matrix for each sub-cell is computed and then the results from the individual sub-cells are combined to calculate the overall stiffness matrix for the braid unit cell.
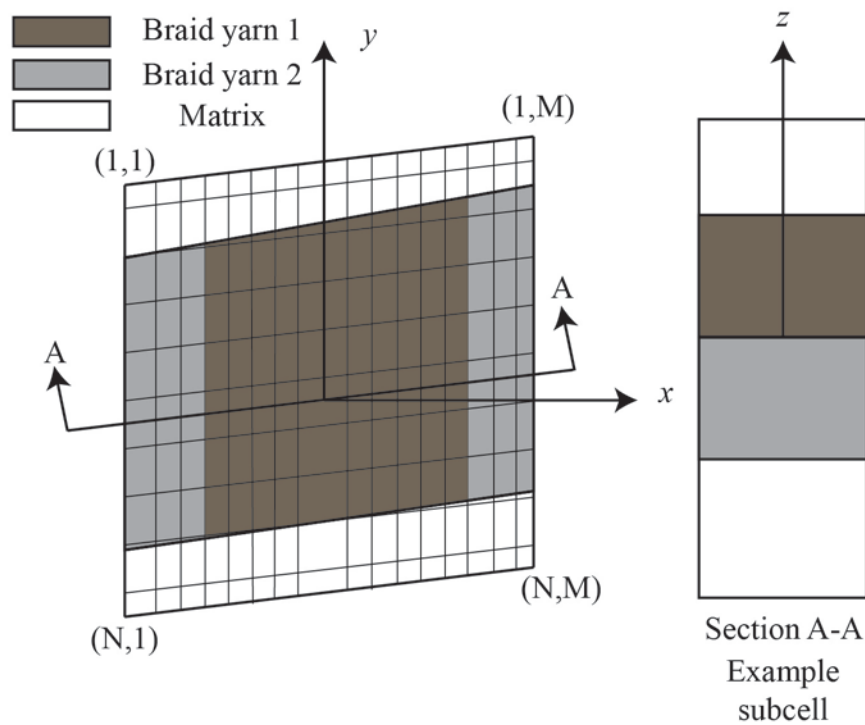
Figure 2-7: Segmented unit cell for modeling the behavior of diamond braided composites [29]. The stiffness matrix for each (*N,M*) sub-cell is computed. The overall stiffness matrix is computed by assembling the results from the individual sub-cells

In order to determine the effective mechanical properties of a diamond braid sub-cells (shown in Figure 2-8) of each slice, each sub-cell is indicated by the index p, are assembled using an iso-stress condition as shown in equation 2-6. All slices, all slices are indicated by the index q, are then combined using an iso-strain condition as shown in Equation 2-7. Finally, the in-plane mechanical properties are determined using Equations 2-8 to 2-11.

$$A_{ij}^{slice} = \sum_{p=1}^{n} \left[A_{ij}^{subcell} \right]_{p}^{-1} \qquad\qquad 2\text{-}6$$

$$A_{ij}^{RUC} = \sum_{q=1}^{n} \left[A_{ij}^{slice} \right]^{-1} \qquad\qquad 2\text{-}7$$

$$E_x = \frac{1}{H} \left(A_{11}^{RUC} - \frac{\left(A_{12}^{RUC} \right)^2}{A_{11}^{RUC}} \right) \qquad\qquad 2\text{-}8$$

$$E_y = \frac{1}{H} \left(A_{22}^{RUC} - \frac{\left(A_{12}^{RUC} \right)^2}{A_{22}^{RUC}} \right) \qquad\qquad 2\text{-}9$$

$$\nu_{xy} = \frac{A_{12}^{RUC}}{A_{22}^{RUC}} = \frac{A_{21}^{RUC}}{A_{22}^{RUC}} \qquad\qquad 2\text{-}10$$

$$G_{xy} = \frac{1}{H} \left(A_{66}^{RUC} \right) \qquad\qquad 2\text{-}11$$

The model of Aggarwal *et al.*, presented here verbatim from their work, was compared with experimental results. Reasonable agreement between the model results and experiments were found for carbon fiber- epoxy braided composites. In addition, the mechanical behavior of cut and uncut braid samples were examined to determine the influence of edge effects on mechanical properties of braided composites [32]. It was demonstrated by Aggarwal *et al.* that the

continuity of braid fibers affects the failure mode of braided composites. The uncut braid samples demonstrated greater failure stresses and strains than the cut braid samples.

The model presented by Raju and Wang for woven composites was adapted to braided composites by Carey *et al.* [33]. This model uses a CLPT based approach in order to model a diamond braid. The model analyzed a composite braid by dividing the unit cell into thirteen regions as shown in Figure 2-9. The unit cell regions were identified as cross-over regions, undulation regions and matrix only regions. The unit cell geometry presented by Carey *et al.* allowed for the analysis of both open and closed mesh diamond braided composites.
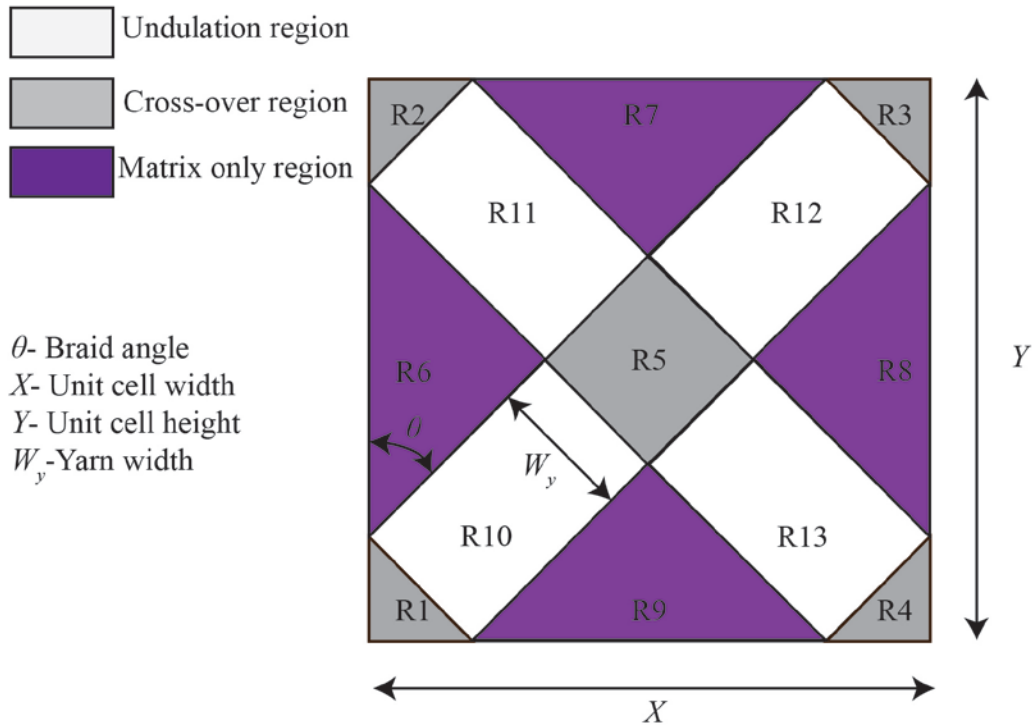
Figure 2-8: Diamond braid geometry for modeling open and closed mesh braids

The model of Carey *et al.* utilizes equations 2-2 to 2-5 as the basis for the CLPT based model. The unit cell geometry is defined by ten lines which are used to determine the limits of integration for the extensional (*A*), coupling (*B*) and bending (*D*) stiffness matrices. The lines that define the braid geometry are shown in equation 2-12. In the equation, *x* and *y* represent the position within the braid unit cell, θ represent the braid angle of the yarns, γ is the complimentary angle to the braid angle, *Y* is the height of the unit cell and L_e is the projected length of the braid yarns as described in Equation 2-13.

$$
\begin{aligned}
y_1 &= x\tan(\gamma) + L_e\cos(\theta) \\
y_2 &= x\tan(\gamma) \\
y_3 &= x\tan(\gamma) - L_e\cos(\theta) \\
y_4 &= -x\tan(\gamma) + L_e\cos(\theta) \\
y_5 &= -x\tan(\gamma) + (Y + L_e\cos(\theta)) \\
y_6 &= -x\tan(\gamma) + Y \\
y_7 &= -x\tan(\gamma) + (Y - L_e\cos(\theta)) \\
y_8 &= x\tan(\gamma) + (Y - L_e\cos(\theta)) \\
y_9 &= -x\tan(\gamma) + (2Y - L_e\cos(\theta)) \\
y_{10} &= x\tan(\gamma) + (L_e\cos(\theta) - Y)
\end{aligned}
\qquad \text{2-12}
$$

$$
L_e = \frac{W_y}{\cos\left(2\theta - \dfrac{\pi}{2}\right)}
\qquad \text{2-13}
$$

The limits of integration to determine the *A*, *B* and *D* stiffness matrices are determined using Equation 2-12. As an example, the *A*, *B* and *D* stiffness matrices are computed for Region 1 shown in Figure 2-9. The area of Region 1 is

22

computed using 2-14. Once the area of Region 1 has been computed, the stiffness matrices can then be determined as shown in Equations 2-15 to 2-17. This procedure is carried out for each of the thirteen regions shown in Figure 2-9 as shown in 2-18. In this equation the thirteen stiffness matrices are summed and averaged over the projected area, P_A, of the braid unit cell.

$$a_{xy} = \int_0^{Le} \int_0^{-x\tan\gamma + Le\cos\theta} dydx = \left[-\frac{(L_e \sin(\theta))^2 \tan(\gamma)}{2} + L_e^2 \sin(\theta)\cos(\theta) \right] \qquad 2\text{-}14$$

$$A = a_{xy} \left[([Q_c(-\theta)] + [Q_c(\theta)])h_c + [Q_m]t_m \right] \qquad 2\text{-}15$$

$$[B] = \frac{1}{2}a_{xy} \left\{ \begin{array}{l} [Q_c(-\theta)]\left(\left(\frac{t_m}{2}\right)^2 - \left(-h_c - \frac{t_m}{2}\right)^2 \right) + \ldots \\[2em] [Q_c(\theta)]\left(-\left(\frac{t_m}{2}\right)^2 - \left(h_c - \frac{t_m}{2}\right)^2 \right) + \ldots \\[2em] [Q_m(\theta)]\left(\left(h_c + \frac{t_m}{2}\right)^2 - \left(h_c - \frac{t_m}{2}\right)^2 \right) \end{array} \right\} \qquad 2\text{-}16$$

$$[D] = \frac{1}{3}a_{xy} \left\{ \begin{array}{l} [Q_c(-\theta)]\left(\left(\frac{t_m}{2}\right)^3 - \left(-h_c - \frac{t_m}{2}\right)^3 \right) + \ldots \\[2em] [Q_c(\theta)]\left(-\left(\frac{t_m}{2}\right)^3 - \left(h_c - \frac{t_m}{2}\right)^3 \right) + \ldots \\[2em] [Q_m(\theta)]\left(\left(h_c + \frac{t_m}{2}\right)^3 - \left(h_c - \frac{t_m}{2}\right)^3 \right) \end{array} \right\} \qquad 2\text{-}17$$

$$[A^*, B^*, D^*] = \frac{1}{P_A} \sum_{n=1}^{13} [A, B, D]_n \qquad 2\text{-}18$$

The model presented by Carey *et al.* assumed a flat unit cell when modeling the braid geometry; however, braids are commonly manufactured in tubular form. In order to expand on Carey *et al.*'s work, Ayranci *et al.* [34] created a curved unit cell as shown in Figure 2-10. The work of Ayranci *et al.* demonstrated the effect of curvature on large diameter braids was negligible while curvature had a more pronounced effect on small diameter composite braids [35].
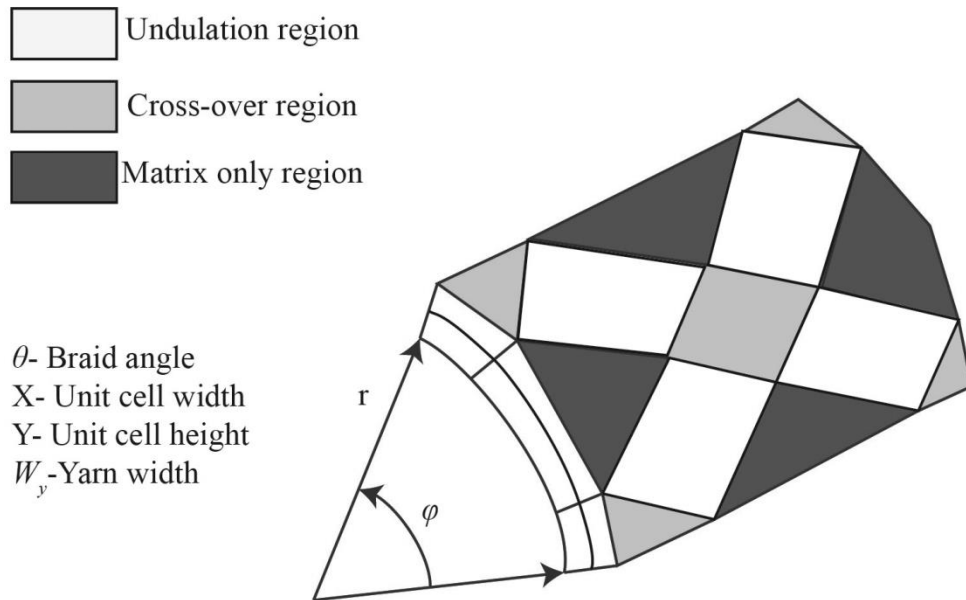
Figure 2-9: Diamond braid geometry that takes into account curvature for modeling open and closed mesh braids [34]

The major difference between Carey *et al.*'s flat braid model and Ayranci *et al.*'s curved model was the analysis of the braid geometry in cylindrical-polar coordinates. The *A*, *B* and *D* stiffness matrices were re-written as:

$$[A] = \int_b^a \left(\int_d^c \left(\left[\int_f^e [Q_c(-\theta)] dr \right] + \left[\int_h^g [Q_c(\theta)] dr \right] + \left[\int_j^i Q_m \right] dr \right) dy \right) d\phi \qquad 2\text{-}19$$

24

$$[B] = \int_b^a \left(\int_d^c \left(\left[\int_f^e [Q_c(-\theta)] r\, dr \right] + \left[\int_h^g [Q_c(\theta)] r\, dr \right] + \left[\int_j^i Q_m \right] r\, dr \right) dy \right) d\phi \qquad \text{2-20}$$

$$[D] = \int_b^a \left(\int_d^c \left(\left[\int_f^e [Q_c(-\theta)] r^2\, dr \right] + \left[\int_h^g [Q_c(\theta)] r^2\, dr \right] + \left[\int_j^i Q_m \right] r^2\, dr \right) dy \right) d\phi \qquad \text{2-21}$$

The limits of integration for Region 1 of the braid unit cell are given in Table 2-3. In this table, the inner radius of the braid is represented by r_{in}, the outer radius of the matrix rich regions is represented by r_m, the top of the $-\theta$ ply is represented by r_- and the top of the $+\theta$ ply is represented by r_+.

Table 2-3: Limits of integration for Region 1 of the Ayranci et al. curved braid unit cell model [34]

a	$L_e \sin(\theta)$
b	0
c	$y_A = -(r_{in}\phi)\tan\gamma + L_e \cos(\theta)$
d	0
e	$-\left(\dfrac{r_m - r_{in}}{2}\right) + (r_- - r_{in})$
f	$-\left(\dfrac{r_m - r_{in}}{2}\right)$
g	$-\left(\dfrac{r_m - r_{in}}{2}\right) + (r_- - r_{in}) + (r_+ - r_-)$
h	$-\left(\dfrac{r_m - r_{in}}{2}\right) + (r_- - r_{in})$
i	$\left(\dfrac{r_m - r_{in}}{2}\right)$
j	$-\left(\dfrac{r_m - r_{in}}{2}\right) + (r_- - r_{in}) + (r_+ + r_-)$

The results for the longitudinal elastic modulus predicted using the models of Carey *et al.* and Ayranci *et al.* are compared in Table 2-4. Also included in this table are the experimental results for tubular braids with a braid angle of 42.5° and 50°. From this table it can be seen that both models agree well with

25

experiments. The results from Carey *et al.* differed from experiments by 8.0 and 4.3% for braid angles of 42.5° and 50° respectively. The curved model of Ayranci *et al.* further improved on the work by Carey *et al.* as would be expected from a model that includes the curvature of the tested samples. The model of Ayranci *et al.* differed from experiments by 2.4 and 2.37% for 42.5° and 50° braids.

Table 2-4: Comparison of longitudinal elastic modulus for flat braid model of Carey et al. and curved braid model of Ayranci *et al.* [34]

Braid Angle (θ)	Carey *et al.* Experimental Elastic Modulus [31]	Carey *et al.* Theoretical Elastic Modulus [31]	% Difference	Ayranci *et al.* Elastic Modulus [30]	% Difference
42.5	6.3±0.11	6.81	8.0	6.45	2.41
50	4.7±0.085	4.90	4.33	4.81	2.37

The models of Carey and Ayranci were both shown to be in good agreement, as can be seen in Table 2-4, with experiments; however, there are several drawbacks to these models. The unit cell geometry has only been defined for Diamond braided composites; the model has not been generalized to allow for the prediction of Regular, Hercules or triaxial braids. Within the braid unit cell, the braid yarns are assumed to have a rectangular cross-section. Micrographs of composite braids readily demonstrate that braid yarns typically exhibit an elongated elliptical or lenticular shape [2]. The models are only capable of predicting the in-plane mechanical properties of as a result of the CLPT assumptions used.

2.2.1 Regression based model for prediction of elastic constants for braided composites

A regression based model has been developed by Carey and Ayranci [36, 37] in order to predict the elastic constants of Diamond braided composites. The aim of the regression based model is to simplify the calculation of elastic constants for open and closed mesh Diamond braided composites. The regression based models of Carey and Ayranci developed a relationship between an angle-ply laminate ($[\pm\theta]$) and open and closed mesh Diamond braided composites.

The regression based model involves three main steps. First, the elastic constants of an angle-ply laminate ($E_x^0, E_y^0, G_{xy}^0, v_{xy}^0$) are calculated using the conventional classical laminate plate theory (CLPT) approach. Second, the geometry of the braided composite is calculated using the unit cell geometry shown in Figure 2-8. Finally, the regression equations, equations 9-22- 9-26, are utilized to calculate the Diamond braided composite elastic constants (E_x, E_y, G_{xy}, v_{xy}).

Using this regression based modeling method Carey et al. demonstrated that the longitudinal elastic modulus (E_x) agreed with experiments with 4% error. Similarly, the regression based model results for shear modulus (G_{xy}) was found to differ from experiment by a range of 10.8-22.1%. Similar differences between experiments and analytical model results of 13-20% were also found.

$$E_x(\theta) = E_x^0(\theta)\left(\frac{V_{f0}}{V_f}\right) \qquad\qquad 2\text{-}22$$

27

$$E_y(\theta) = E_y^0(\theta)\left(\frac{V_{f0}}{V_f}\right)$$

<div align="right">2-23</div>

$$G_{xy}(\theta) = G_{xy}^0(\theta)\left[1.23\cdot\left(\frac{V_{f0}}{V_f}\right) - 0.3\right]$$

<div align="right">2-24</div>

$$\frac{V_{f0}}{V_f} = \frac{4L_e^2\sin(\theta)\cos(\theta) + 2W_y a_u}{X\cdot Y}$$

<div align="right">2-25</div>

$$v_{xy}(\theta) = v_{xy}^0(\theta)\left[\left(0.2476\cdot v_{xy}^0(\theta) + 0.07676\right)\frac{V_{f0}}{V_f} - 0.1964\cdot\left(v_{xy}^0(\theta)\right)^2 + 0.8727\right]$$

<div align="right">2-26</div>

The primary attraction of the regression based modelling method of Carey and Ayranci is the simplicity of the model equations. Since this modeling approach utilizes simplified equations and provides reasonably accurate results this approach lends its self to the preliminary design of braided composites.

2.2.2 Fabric Geometry Models

A fabric geometry model (FGM) was developed to predict the behavior of three dimensional braided composites [38-41]. The FGM model treats the matrix and fibers of a composite braid as composite rods with a defined spatial orientation. The mechanical properties of the composite rods are assembled using a volume average stiffness method in order to predict the global mechanical properties of the composite braid.

Experimental results for biaxial and triaxial braids were compared with the results from the FGM model by Soebroto et al. [40]. In this study, the experimental tensile strength of biaxial and triaxial braids was compared with the tensile strength predicted using the FGM model. An evaluation of the stiffness matrix of the composite was not performed. The FGM model was expanded and improved by Pastore et al. using a self-consistent FGM model [41]. The results of self-consistent FGM model were compared with experiments with triaxial braids with ±63° bias yarns. Good agreement between model results and experiments were found.

As noted by Ayranci et al. [42], FGM based models are primarily utilized for 3D braided composites. Therefore, these models do not include undulations of the braid yarns which may account for differences between model and experimental results for braided composites. One of the benefits of the FGM model however, is that the mechanical properties of textile and braided composites can be easily and quickly calculated. In design applications, the ability to quickly and easily compute the mechanical properties of textile composites may be worth the loss in model accuracy due to neglecting the effect of yarn undulations.

2.2.3   Volume Averaging Models

One of the issues with a CLPT-based model for braided composites is the underlying assumption that is used in this model. CLPT based models assume that a laminate is sufficiently thin and is only subjected to in-plane loading (plane stress state $\sigma_z = \tau_{xz} = \tau_{yz} = 0$) [20, 43]. Due to the braid yarn undulations and the

thickness of the braid yarns, the CLPT based assumption may not be valid for braided composites. As a result, alternative modeling methods are required. A volume averaging (VA) method has been employed by several authors to predict the behavior of triaxial braided composites. This modeling method is similar to the aforementioned FGM model as it utilizes volume averaging to determine the mechanical properties of braided composites. The key difference of the volume averaging stiffness models to the FGM models is that fiber undulations are accounted for in the VA method.

Several authors have utilized a volume averaging method in order to predict the mechanical properties of braided composites. In particular, this method has been most commonly applied to triaxial composite braids [2, 16, 44-46]. This procedure has also been successfully applied to 3D textile composites [41, 47]. The volume averaging method was first applied to determine the viscoelastic properties of spatially reinforced composites [48]. The volume averaging method is advantageous over lamination methods since closed form expressions can be used to describe geometric parameters and elastic properties.

The volume average method involves four main steps. First, geometric expressions are derived to describe the geometry of the individual braid yarns within a unit cell. Second, the mechanical properties of the individual yarns are calculated using micromechanical models such as the Halpin-Tsai micromechanical model, Concentric Cylinder Model (CCM) or other micro-mechanical models [20, 43, 49]. Third, a series of coordinate system transformations are utilized in order to account for yarn undulations and for the

angle of the braid yarns relative to the loading direction. Finally, the stiffness matrices of each yarn and matrix are assembled to determine the effective mechanical properties of the braid structure. The analysis procedure for a braided composite is described in detail below.

The compliance matrix $[S]$ for a transversely isotropic yarn is shown in Equation 2-27. Individual braid yarns are commonly assumed to be transversely isotropic [11, 50, 51]. The coordinate system transformations utilized for braided composites are illustrated in Figure 2-11. The undulation of the individual braid yarns is illustrated in Figure 2-11 (a). Yarn undulations depend on the mandrel diameter of the braid, the number of braid yarns as well as the width and thickness of the individual braid yarns. Figure 2-11 (b) shows the coordinate system transformation used to account for the braid angle of the braid yarns.

$$[S] = \begin{bmatrix} \dfrac{1}{E_1} & -\dfrac{\upsilon_{21}}{E_2} & -\dfrac{\upsilon_{31}}{E_3} & 0 & 0 & 0 \\[2mm] -\dfrac{\upsilon_{12}}{E_1} & \dfrac{1}{E_2} & -\dfrac{\upsilon_{32}}{E_3} & 0 & 0 & 0 \\[2mm] -\dfrac{\upsilon_{13}}{E_1} & -\dfrac{\upsilon_{23}}{E_2} & \dfrac{1}{E_3} & 0 & 0 & 0 \\[2mm] 0 & 0 & 0 & \dfrac{1}{G_{23}} & 0 & 0 \\[2mm] 0 & 0 & 0 & 0 & \dfrac{1}{G_{13}} & 0 \\[2mm] 0 & 0 & 0 & 0 & 0 & \dfrac{1}{G_{12}} \end{bmatrix} \qquad \text{2-27}$$

Once the yarn mechanical properties have been computed a coordinate system transformation is applied to account for the braid yarn undulations using the crimp angle, ϕ, of the braid yarns. The undulation coordinate system transformation is

31

shown in Equation 2-28. This yarn undulation coordinate transformation has been used by several authors for modeling triaxial braided composites [15, 16, 46, 52].

$$\left[S^{1}\right]=\left[T_{1}\right]^{t}\left[S\right]\left[T_{1}\right]$$

where,

$$[T_{1}]=\begin{bmatrix} \hat{m}^{2} & 0 & \hat{n}^{2} & 0 & 2\hat{m}\hat{n} & 0 \\ 0 & 1 & 0 & 0 & 0 & 0 \\ \hat{n}^{2} & 0 & \hat{m}^{2} & 0 & -2\hat{m}\hat{n} & 0 \\ 0 & 0 & 0 & \hat{m} & 0 & -\hat{n} \\ -\hat{m}\hat{n} & 0 & \hat{m}\hat{n} & 0 & \hat{m}^{2}-\hat{n}^{2} & 0 \\ 0 & 0 & 0 & \hat{n} & 0 & \hat{m} \end{bmatrix}$$

2-28

where

$$\hat{m} = \cos(\phi) = \frac{1}{\sqrt{1+\tan^{2}(\phi)}}$$

$$\hat{n} = \sin(\phi) = \frac{\tan(\phi)}{\sqrt{1+\tan^{2}(\phi)}}$$

A second coordinate system transformation is then used to transform each yarn to the unit cell global coordinate system. This coordinate system accounts for the braid angle, θ, of the bias braid yarns. The global coordinate system transformation is shown in Equation 2-29.

$$S_{XYZ} = [T]^{T}\left[S'_{xyz}\right][T]$$

2-29

where

$$[T]=\begin{bmatrix} c^{2} & s^{2} & 0 & 0 & 0 & 2cs \\ s^{2} & c^{2} & 0 & 0 & 0 & -2cs \\ 0 & 0 & 1 & 0 & 0 & 0 \\ 0 & 0 & 0 & c & s & 0 \\ 0 & 0 & 0 & -s & c & 0 \\ -cs & cs & 0 & 0 & 0 & c^{2}-s^{2} \end{bmatrix}$$

$$c = \cos(\theta)$$
$$s = \sin(\theta)$$
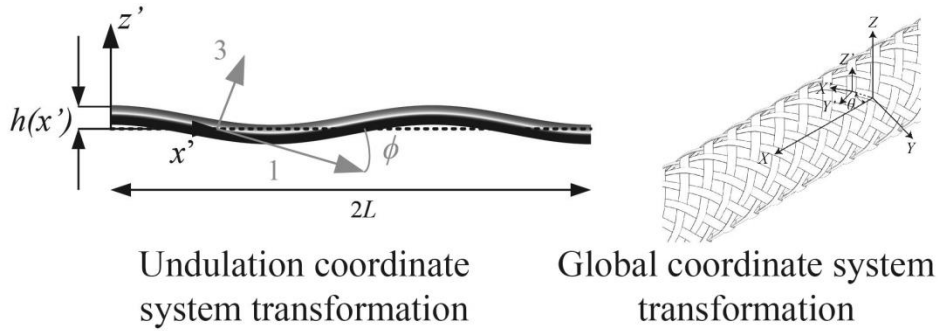
Figure 2-10: Coordinate system transformations (Left) Conversion of stiffness matrix [S] from yarn coordinate (*1-2-3*) system to undulation coordinate system (*x'-y'-z'*) (Right) Conversion of undulation stiffness matrix $[S_{XYZ}{}']$ to global coordinate system (*X-Y-Z*). The variables [*T*] represent coordinate system transformation matrices.

Finally, volume averaging is performed to account for the contribution of each yarn within the braid unit cell. The volume averaging equations for both a biaxial and triaxial braided composites are shown in Equation 2-30. In this equation C_{global} represents the global stiffness matrix for the braided composite. The volume averaging method takes into account the contribution of bias, axial and matrix by computing the volume fraction of each of these constituents within a unit cell. The volume fraction of the clockwise yarn is given by $V_{f\theta+}$, counter-clockwise yarn by, $V_{f\theta-}$ and matrix by V_m within the braid unit cell. Axial yarns can also be taken account using V_{fa} for triaxial braid structures. The elastic properties of the braided composite can be determined by inverting the final global stiffness matrix as shown in Equation 2-31.

$$C_{globalBiaxial} = V_{f\theta+}C_{XYZ}^{+} + V_{f\theta-}C_{XYZ}^{-} + V_m C_{XYZ}^{m}$$

<div align="right">2-30</div>

$$C_{globalTriaxial} = V_{f\theta+}C_{XYZ}^{+} + V_{f\theta-}C_{XYZ}^{-} + V_{fa}C_{XYZ}^{a} + V_m C_{XYZ}^{m}$$

$$S_{global} = C_{global}^{-1}$$

<div align="right">2-31</div>

In order to perform the volume averaging method, a series of coordinate system transformation are required. The coordinate system transformations are based on the braided composite's geometry; therefore the geometry of the braid structure must be known. Commonly, the geometry of braided composites is determined by examining micrographs of the braid structure in order to determine the yarn undulation period, L, and amplitude, A [16, 46]. This method has been utilized by several authors in order to model the undulating nature of triaxial braid yarns [15, 16, 53] an example of the sinusoidal function used to model yarn undulations is shown in Equation 9.11.

$$z' = A\cos\left(\frac{\pi x'}{L}\right)$$

$$\tan(\phi) = \frac{\pi A}{L}\cos\left(\frac{\pi x'}{L}\right)$$

<div align="right">2-32</div>

The crimp angle, ϕ, of the braid yarns can be determined by computing the derivative of the braid undulation equation. The crimp angle is then used to compute the coordinate system transformation of the braid yarns

Alternatively, to model the undulations of braid yarns, Byun et al. [52] assumed a lenticular shape for braid yarns and derived equations to calculate the crimp angle

and fiber yarn volume. Using the lenticular yarn assumption the yarn crimp angle, ϕ, can be found using Equation 2-33.

$$\phi = \sin^{-1}\left(\frac{L_s}{2r_u}\right)$$ 2-33

where L_s is the undulation length of the braid yarns and r_u is the radius of the braid yarn undulations. A third approach to determining the amplitude and undulation length of the braid yarns is to acquire micrographs of the braid yarns. An example micrograph of a braid yarn showing the yarn undulation length and amplitude is shown in Figure 2-12.
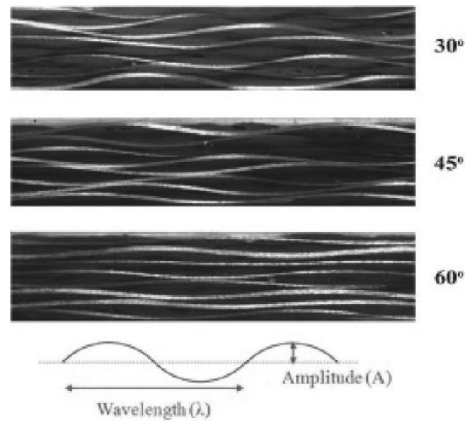
Figure 2-11: Example micrograph of a composite braid showing the wavelength and amplitude of the braid yarns [46]

The results of a volume average analytical model were compared with experiments by Kier *et al.* [46]. In this work, results for a triaxial braided composite with bias yarn angles of 30, 45 and 60° were compared with experiments. Table 2-5 compares the results from the analytical model and

experiments. This table shows that the longitudinal elastic modulus (E_x) differed from experiments between 8.9 and 18.3%, while the transverse elastic modulus (E_y) differed from experiments by 1.4 to 9.4%. The difference between experiments and the shear modulus (G_{xy}) ranged from 0.45 to 9.25%.

Table 2-5: Comparison of volume average stiffness analytical model results with experimental results for a triaxial braided composite Kier *et al.* [46]

	Analytical Model Results			Experimental Results		
	30°	45°	60°	30°	45°	60°
E_x *(GPa)*	58.3	29.4	28.4	53.1 ± 0.8	27.9 ± 1.1	23.2 ± 0.8
E_y *(GPa)*	8.06	13.9	22.6	7.3 ± 0.5	13.7 ± 1.2	22.1 ± 0.1
G_{xy} *(GPa)*	10.8	9.35	8.85	9.80 ± 0.13	9.89 ± 0.35	8.81 ± 0.54
v_{xy}	0.995	0.535	0.328	0.93	0.59	0.3

2.2.4 Finite Element Techniques for 2D Braided Composites

Finite element analysis (FEA) modeling is another common approach that is used to examine textile and braided composites. FEA models can be used to study the stiffness properties, 3D stress-strain fields, damage development and failure of composite braids. FEA models are advantageous over traditional analytical models due to the ability to model braid geometry using computer aided design (CAD) tools. The use of CAD software to create braid geometries allows for braids to be parametrically designed. Another advantage that FEA models offer over conventional analytical models is the ability to depict the stress and strain distribution throughout the braid geometry [7]. The use of CAD software

packages has limitations when modeling braided composite geometry. These programs utilize an idealized geometry when evaluating braid mechanical properties. In reality, imperfections occur during the braiding and curing process which can have detrimental effects on mechanical properties. As a result, braid geometries can be recreated using micro-computed tomography (μCT) imaging techniques. Micro-computed tomography is an x-ray based imaging technique that recreates 3D geometry from radiographic images. The use of μCT data allows for a precise reconstruction of the physical geometry of a braided composite [54-57]. Since this technique recreates braid geometries from physical geometries this method can be used to examine the effect of defects or imperfections that may occur during braid fabrication.

Finite element model results can be compared with experiments using techniques such as the 'Virtual Field Method' can be used to compare full field solutions from FEA models and digital image correlation (DIC) experimental results [58].

FEA models typically utilize a multi-scale modeling procedure. Micro-scale modeling predicts the mechanical properties of the resin infused yarns. Commonly, micro-scale modeling is performed using analytical equations such as the Halpin-Tsai semi-empirical model or the Concentric Cylinder Model (CCM). Yarn porosity and matrix and fiber volume fractions are accounted for during the micro-scale modeling step. Meso-scale modeling of braided composites takes advantage of periodic boundary conditions that exist due to the repeating nature of braided composites. All FEA models focus on representing the braid as a representative volume element (RVE), which is the smallest sub-volume which

represents the entire braid geometry. The meso-scale models allow for the predicting of braided composites mechanical properties and allow for visualization of the stress and strain distribution within the RVE. Finally, a macro-scale model allows for the prediction of the elastic response of an entire braided composite structure. The homogenized elastic properties calculated using the meso-scale model is used as inputs to predict the overall behavior of a braided composite structure. The modeling hierarchy used for analyzing braided composites is illustrated in Figure 2-13. The road map for examining braided composites using a FEA approach has been described by Lomov et al. [59].
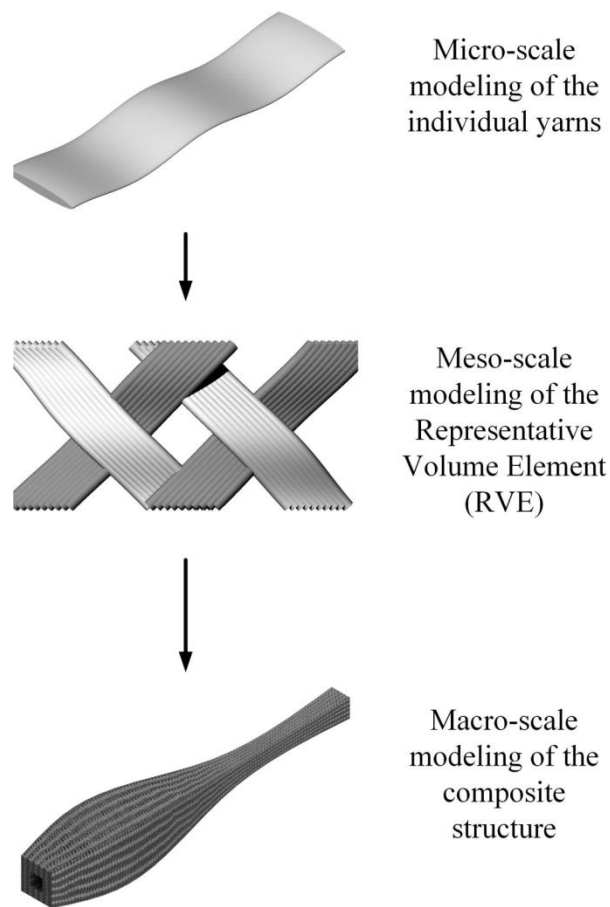
Figure 2-12: Finite element analysis of braided composites modeling hierarchy. Micro-scale modeling to determine matrix/fiber mechanical properties. Meso-scale modeling to determine braided composite elastic properties. Macro-scale modeling to determine the elastic response of a composite structure.

One of the first concerted efforts to model the mechanical behavior of braided composites using a FEA approach was performed by Goyal *et al.* [60]. In this study, a Regular (2/2) braid geometry was analyzed. Additionally, the effect of yarn shape was explored, in particular lenticular and flattened shapes for the braid yarns. This work also led to an examination of the stress fields in Regular braided composites [61]. The results of the FEA model of Goyal *et al.* were compared with experiments for a carbon fiber/epoxy Regular braid. Model results were

39

compared for both flattened and lenticular yarn geometries. Comparison between model results and experiments can be seen in Table 2-6. The author notes that better FEA results can be obtained by accurately modeling the braided composite geometry.

Table 2-6: Comparison of FEA model results for flattened and lenticular yarn geometry with experimental results for a carbon/ fiber epoxy braid [60].

Elastic Modulus	Flattened (GPa)	Lenticular (GPa)	Experimental Elastic Modulus (GPa)
Longitudinal Elastic Modulus	64.67	77.6	67.8 ± 3.85

The FEA method has also been used in order to predict the behavior of other common braid configurations including: Diamond (1/1), Regular (2/2), Hercules (3/3) and triaxial braid patterns [7, 17, 62]. The study by Xu *et al.* compared the results of different braid geometries using the FEA modeling approach [17]. An example comparison of the elastic properties of carbon fiber/ epoxy Diamond, Regular, Hercules and Regular Triaxial braided composites is shown in Figure 2-14. This figure demonstrates that the elastic properties of braided composites are lower than a $\pm\theta$ angle ply laminate. The study by Xu *et al.* also demonstrates the effect of braid pattern on braided composite elastic properties.
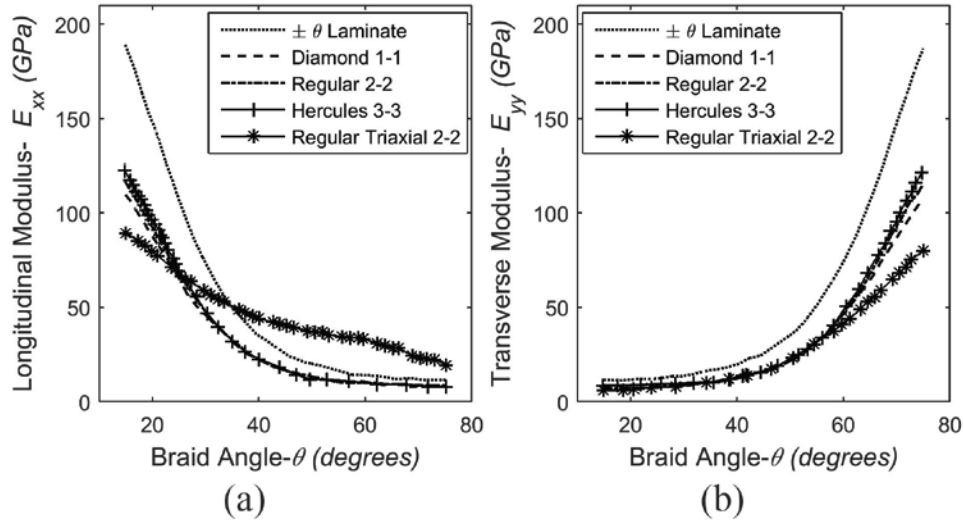
Figure 2-13: Comparison of elastic properties of carbon fiber/epoxy Laminate, Diamond, Regular, Hercules

and Regular Triaxial braided composites (a) Longitudinal elastic modulus (b) Transverse elastic modulus.

Plots reproduced from Xu *et al.* [17]

One of the most advanced simulations of braided composites was performed in

Picket *et al.* [63]. In this work a braiding simulation program was utilized in

order to simulate and generate the braid perform structure. In addition, a mesh

free Smooth Particle Hydrodynamics model was implemented in order to

accurately model the resin rich regions within the braid structure. An example of

the braid geometry and resin is shown in Figure 2-15. This figure clearly shows

three braid layers as well as matrix rich regions. This modeling method produces

a highly accurate representation of a braided composite structure; however this

approach is computationally intensive.
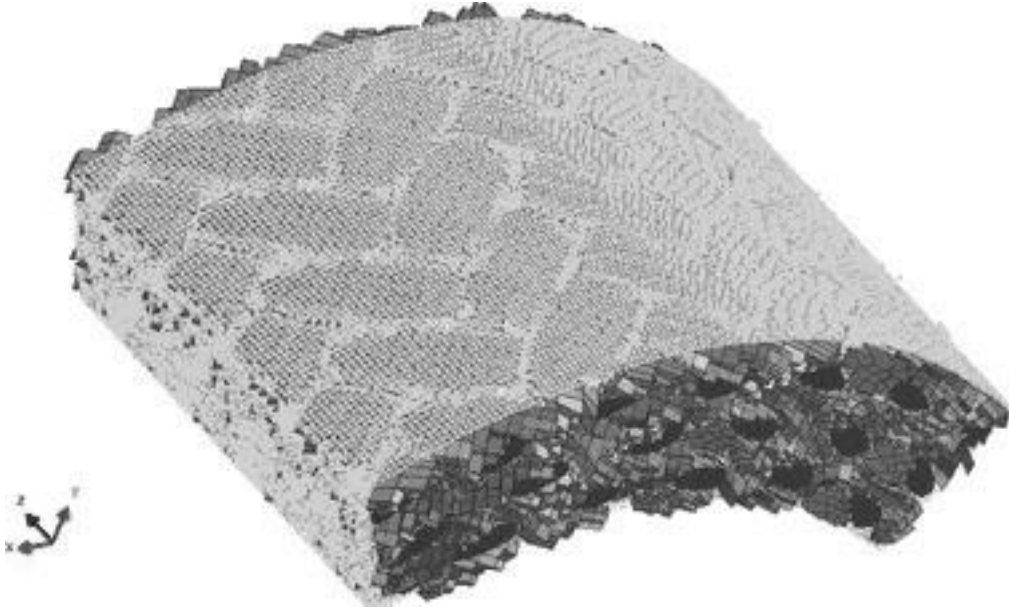
Figure 2-14: Representative volume element that uses a finite element approach and a Smooth Particle Hydrodynamic model to simulate load transfer between the braid yarns and matrix [63].

2.3   Proposed Braid Model

In order to develop a generalized model to describe the mechanical properties of braided composites a modelling frame-work must be selected.   The goal of this thesis is to develop a generalized model which can predict the mechanical properties of tubular braided composites.   In order to achive this objective the Volume Averaging methodology has been selected.   Since the Volume Averaging method allows for yarn undulations and braid yarn orientation to be taken into account this method can be generalized to predict the mechanical properties of different braiding patterns.   Tubular braid geometries can be described mathematically using equations similar to the ones presented by Alpyildiz *et al.* [64].   The combination of the Volume Averaging method and generalized braiding equations will allow for the variety of different braiding patterns to be analytically predicted.   The Volume Averaging methodology is relatively simple

to implement and does not require specialized software. As shown in Section 2.2.3 current Volume Averaging methods have shown good agreement with experimental results.

2.4 Conclusions

In this chapter a variety of models are presented. Braided composites have been modeled using both analytical models as well as finitel element analysis models. Analytical models for braided composites have used a number of approaches including: CLPT-based models, Volume Averaging Models, and Fabric Geometry Models. The analytical models presented allow for the mechanical properties of braided composites to be rapidly computed. By contrast finite element analysis models allow for accurate description of braided composite geometry. FEA models can be created based on computer aided design software packages or based on three-dimensional geometries measured using computed tomography. FEA modesl are generally more accurate than analytical models but this technique is computationally intensive and requires specialize software knowledge. Conversely, analytical models require less computation time and can be implemented using scripted programming languages like Python or MATLAB.

2.5 References

[1] C. Ayranci and J. Carey, "2D braided composites: A review for stiffness critical applications," *Composite Structures,* vol. 85, pp. 43-58, 2008.

[2] J. H. Byun, "The analytical characterization of 2-D braided textile composites," *Composites Sci. Technol.,* vol. 60, pp. 705-716, 2000.

[3] P. Qu, X. Guan, Y. Jia, S. Lou and J. Nie, "Effective elastic properties and stress distribution of 2D biaxial nonorthogonally braided composites," *J. Composite Mater.,* vol. 46, pp. 997-1008, 2012.

[4] P. Tan, L. Tong and G. P. Steven, "Modelling for predicting the mechanical properties of textile composites - A review," *Composites Part A: Applied Science and Manufacturing,* vol. 28, pp. 903-922, 1997.

[5] G. Fang and J. Liang, "A review of numerical modeling of three-dimensional braided textile composites," *J. Composite Mater.,* vol. 45, pp. 2415-2436, 2011.

[6] J. P. Carey, G. W. Melenka, A. J. Hunt and C. Ayranci, "Introduction to braided composite material behavior," in *Handbook of Advances in Braided Composite Materials: Theory, Production, Testing and Applications*, J. P. Carey, Ed. Woodhead Publishing, 2016, .

[7] X. Ji, A. M. Khatri, E. S. Chia, R. K. Cha, B. T. Yeo, S. C. Joshi and Z. Chen, "Multi-scale simulation and finite-element-assisted computation of elastic properties of braided textile reinforced composites," *J. Composite Mater.,* vol. 48, pp. 931-949, 2014.

[8] P. Tan, L. Tong and G. P. Steven, "A three-dimensional modelling technique for predicting the linear elastic property of opened-packing woven fabric unit cells," *Composite Structures,* vol. 38, pp. 261-271, 1997.

[9] G. Fang and J. Liang, "A review of numerical modeling of three-dimensional braided textile composites," *J. Composite Mater.,* vol. 45, pp. 2415-2436, 2011.

[10] B. N. Cox and G. Flanagan, *Handbook of Analytical Methods for Textile Composites [Microform] : Under Contract NAS1-19243 / Brian N. Cox, Gerry Flanagan.* Hampton, Va. : National Aeronautics and Space Administration, Langley Research Center ; Springfield, Va. : National Technical Information Service, distributor, 1997], 1997.

[11] T. Chou and F. K. Ko, *Textile Structural Composites.* Amsterdam ; New York : Elsevier ; New York, NY, U.S.A. : Distributors for the U.S. and Canada, Elsevier Science Pub. Co., 1989, 1989.

[12] J. Carey, M. Munro and A. Fahim, "Longitudinal elastic modulus prediction of a 2-D braided fiber composite," *J Reinf Plast Compos,* vol. 22, pp. 813-831, 2003.

[13] C. Ayranci, "Predicting the elastic properties of two dimensionally braided tubular composite structures towards the design of braid-reinforced polymer medical catheters," *ProQuest Dissertations and Theses,* 2010.

[14] J. H. Byun, "The analytical characterization of 2-D braided textile composites," *Composites Sci. Technol.,* vol. 60, pp. 705-716, 2000.

[15] S. C. Quek, A. M. Waas, K. W. Shahwan and V. Agaram, "Analysis of 2D triaxial flat braided textile composites," *Int. J. Mech. Sci.,* vol. 45, pp. 1077-1096, 2003.

[16] R. F. El-Hajjar, S. S. Shams and D. J. Kehrl, "Closed form solutions for predicting the elastic behavior of quasi-isotropic triaxially braided composites," *Composite Structures,* vol. 101, pp. 1-8, 2013.

[17] L. Xu, S. J. Kim, C. -. Ong and S. K. Ha, "Prediction of material properties of biaxial and triaxial braided textile composites," *J. Composite Mater.,* vol. 46, pp. 2255-2270, 2012.

[18] Z. Tang and R. Postle, "Deformation analysis of 3D braided structural composites," *Text. Res. J.,* vol. 73, pp. 563-569, 2003.

[19] L. Carvalho, R. A. S. Moreira and J. A. Simões, "Application of a vibration measuring technique to evaluate the dynamic stiffness of porcine periodontal ligament," *Technology and Health Care,* vol. 14, pp. 457-465, 2006.

[20] R. M. Jones, *Mechanics of Composite Materials.* Washington, Scripta Book Co. 1975], 1975.

[21] B. K. O. Cheung and J. P. Carey, "Macromechanics of composite materials," in *Handbook of Advances in Braided Composite Materials: Theory, Production, Testing and Applications*, J. P. Carey, Ed. Woodhead, 2016, .

[22] T. Ishikawa and T. -. Chou, "Stiffness and strength behaviour of woven fabric composites," *J. Mater. Sci.,* vol. 17, pp. 3211-3220, 1982.

[23] T. Ishikawa and T. W. Chou, "Stiffness and strength properties of woven composites," in 1982, pp. 489-449.

[24] C. Ayranci and J. Carey, "2D braided composites: A review for stiffness critical applications," *Composite Structures,* vol. 85, pp. 43-58, 2008.

[25] I. S. Raju and J. T. Wang, "Classical Laminate Theory Models for Woven Fabric Composites," *J. Compos. Technol. Res.,* vol. 16, pp. 289-303, 1994.

[26] N. K. Naik and V. K. Ganesh, "An analytical method for plain weave fabric composites," *Composites,* vol. 26, pp. 281-289, 1995.

[27] N. K. Naik and P. S. Shembekar, "Elastic behavior of woven fabric composites: I-lamina analysis," *J. Composite Mater.,* vol. 26, pp. 2196-2225, 1992.

[28] P. S. Shembekar and N. K. Naik, "Elastic behavior of woven fabric composites: II-laminate analysis," *J. Composite Mater.,* vol. 26, pp. 2226-2246, 1992.

[29] N. K. Naik and P. S. Shembekar, "Elastic behavior of woven fabric composites: III-Laminate design," *J. Composite Mater.,* vol. 26, pp. 2522-2541, 1992.

[30] J. Yang, C. Ma and T. Chou, "Fiber Inclination Model of Three-Dimensional Textile Structural Composites," *J. Composite Mater.,* vol. 20, pp. 472-484, 1986.

[31] A. Aggarwal, S. Ramakrishna and V. K. Ganesh, "Predicting the in-plane elastic constants of diamond braided composites," *J. Composite Mater.,* vol. 35, pp. 665-688, 2001.

[32] A. Aggarwal, S. Ramakrishna and V. Ganesh, "Predicting the strength of diamond braided composites," *J. Composite Mater.,* vol. 36, pp. 625-643, 2002.

[33] J. Carey, M. Munro and A. Fahim, "Longitudinal elastic modulus prediction of a 2-D braided fiber composite," *J Reinf Plast Compos,* vol. 22, pp. 813-831, 2003.

[34] C. Ayranci and J. P. Carey, "Predicting the longitudinal elastic modulus of braided tubular composites using a curved unit-cell geometry," *Composites Part B: Engineering,* vol. 41, pp. 229-235, 2010.

[35] C. Ayranci, D. Romanyk and J. P. Carey, "Elastic properties of large-open-mesh 2D braided composites: Model predictions and initial experimental findings," *Polymer Composites,* vol. 31, pp. 2017-2024, 2010.

[36] C. Ayranci and J. P. Carey, "Experimental validation of a regression-based predictive model for elastic constants of open mesh tubular diamond-braid composites," *Polymer Composites,* vol. 32, pp. 243-251, 2011.

[37] J. Carey, M. Munro and A. Fahim, "Regression-based model for elastic constants of 2D braided/woven open mesh angle-ply composites," *Polym Compos,* vol. 26, pp. 152-164, 2005.

[38] C. Pastore and F. K. KO, "A processing science model for three dimensional braiding," *How to Apply Advanced Composites Technology,* pp. 371-376, 1988.

[39] D. W. Whyte, *Structure and Properties of 3-D Braid Reinforced Composites,* 1986.

[40] H. B. Soebroto, T. Hager, C. M. Pastore and F. K. Ko, "Engineering design of braided structural fiberglas composites," in *National SAMPE Symposium and Exhibition (Proceedings),* 1990, pp. 687-696.

[41] C. M. Pastore and Y. A. Gowayed, "Self-consistent fabric geometry model: modification and application of a fabric geometry model to predict the elastic properties of textile composites," *J. Composites Technol. Res.,* vol. 16, pp. 32-36, 1994.

[42] C. Ayranci and J. Carey, "2D braided composites: a review for stiffness critical applications," *Composite Structures,* vol. 85, pp. 43-58, 2008.

[43] I. M. Daniel and O. Ishai, *Engineering Mechanics of Composite Materials.* New York: Oxford University Press, 2006.

[44] M. M. Shokrieh and M. S. Mazloomi, "An analytical method for calculating stiffness of two-dimensional tri-axial braided composites," *Composite Structures,* vol. 92, pp. 2901-2905, 2010.

[45] S. C. Quek, A. M. Waas, K. W. Shahwan and V. Agaram, "Analysis of 2D triaxial flat braided textile composites," *Int. J. Mech. Sci.,* vol. 45, pp. 1077-1096, 2003.

[46] Z. T. Kier, A. Salvi, G. Theis, A. M. Waas and K. Shahwan, "Estimating mechanical properties of 2D triaxially braided textile composites based on microstructure properties," *Composites Part B: Engineering,* vol. 68, pp. 288-299, 2014.

[47] M. Pankow, A. M. Waas, C. -. Yen and S. Ghiorse, "A new lamination theory for layered textile composites that account for manufacturing induced effects," *Composites Part A: Applied Science and Manufacturing,* vol. 40, pp. 1991-2003, 2009.

[48] A. F. Kreger and G. A. Teters, "Use of averaging methods to determine the viscoelastic properties of spatially reinforced composites," *Mechanics of Composite Materials,* vol. 15, pp. 377-383, 1980.

[49] A. K. Kaw, *Mechanics of Composite Materials.* CRC press, 2005.

[50] J. Carey, A. Fahim and M. Munro, "Predicting elastic constants of 2D-braided fiber rigid and elastomeric–polymeric matrix composites," *J Reinf Plast Compos,* vol. 23, pp. 1845-1857, 2004.

[51] J. H. Byun, "The analytical characterization of 2-D braided textile composites," *Composites Sci. Technol.,* vol. 60, pp. 705-716, 2000.

[52] J. H. Byun, "The analytical characterization of 2-D braided textile composites," *Composites Sci. Technol.,* vol. 60, pp. 705-716, 2000.

[53] M. Pankow, A. M. Waas, C. -. Yen and S. Ghiorse, "A new lamination theory for layered textile composites that account for manufacturing induced effects," *Composites Part A: Applied Science and Manufacturing,* vol. 40, pp. 1991-2003, 2009.

[54] H. Bale, M. Blacklock, M. R. Begley, D. B. Marshall, B. N. Cox and R. O. Ritchie, "Characterizing three-dimensional textile ceramic composites using synchrotron x-ray micro-computed-tomography," *J Am Ceram Soc,* vol. 95, pp. 392-402, 2012.

[55] P. Badel, E. V. Sallé, E. Maire and P. Boisse, "Simulation and tomography analysis of textile composite reinforcement deformation at the mesoscopic scale," *International Journal of Material Forming,* vol. 2, pp. 189-192, 2009.

[56] L. P. Djukic, I. Herszberg, W. R. Walsh, G. A. Schoeppner and B. Gangadhara Prusty, "Contrast enhancement in visualisation of woven composite architecture using a MicroCT Scanner. Part 2: Tow and preform coatings," *Composites Part A: Applied Science and Manufacturing,* vol. 40, pp. 1870-1879, 2009.

[57] L. P. Djukic, I. Herszberg, W. R. Walsh, G. A. Schoeppner, B. Gangadhara Prusty and D. W. Kelly, "Contrast enhancement in visualisation of woven composite tow architecture using a MicroCT Scanner. Part 1: Fabric coating and resin additives," *Composites Part A: Applied Science and Manufacturing,* vol. 40, pp. 553-565, 2009.

[58] F. Pierron and M. Grédiac, *The Virtual Fields Method. [Electronic Resource] : Extracting Constitutive Mechanical Parameters from Full-Field Deformation Measurements.* New York : Springer, c2012, 2012.

[59] S. V. Lomov, D. S. Ivanov, I. Verpoest, M. Zako, T. Kurashiki, H. Nakai and S. Hirosawa, "Meso-FE modelling of textile composites: Road map, data flow and algorithms," *Composites Sci. Technol.,* vol. 67, pp. 1870-1891, 2007.

[60] D. Goyal, X. Tang, J. D. Whitcomb and A. D. Kelkar, "Effect of various parameters on effective engineering properties of 2×2 braided composites," *Mechanics of Advanced Materials and Structures,* vol. 12, pp. 113-128, 2005.

[61] D. Goyal and J. D. Whitcomb, "Analysis of stress concentrations in 2×2 braided composites," *J. Composite Mater.,* vol. 40, pp. 533-546, 2006.

[62] P. Qu, X. Guan, Y. Jia, S. Lou and J. Nie, "Effective elastic properties and stress distribution of 2D biaxial nonorthogonally braided composites," *J. Composite Mater.,* vol. 46, pp. 997-1008, 2012.

[63] A. K. Pickett, J. Sirtautas and A. Erber, "Braiding simulation and prediction of mechanical properties," *Appl Compos Mater,* vol. 16, pp. 345-364, 2009.

[64] T. Alpyildiz, "3D geometrical modelling of tubular braids," *Text. Res. J.,* vol. 82, pp. 443-453, 2012.

Chapter 3 Micro-computed tomography analysis of tubular braided composites

A version of this chapter has been published as:

Melenka G.W., Lepp, E; Cheung, B.K.O.; Carey, J.P., Micro-computed tomography analysis of tubular braided composites, Composite Structures, (2015).

3.1 Introduction

Two dimensional (2D) tubular braided composites comprise of woven fibers impregnated within a resin matrix [1, 2]. Tubular braided composites (TBC's) are manufactured by weaving fibers onto a mandrel; the fibers are then saturated with resin to produce a final product [1]. Braiding allows for the angle between fibers to be varied whereas the angle of woven fibers is fixed [3]. The material properties of braided composites can be altered by varying the resin, fiber or braid geometry (yarn volume fraction or braid angle). This versatile manufacturing method could be applied to a range of engineering fields that include biomedical devices, sports equipment, automotive, or structural applications [4].

Similar to composite laminates, the mechanical properties of tubular braided composites can be predicted using the braid geometry and with the mechanical properties of the composite constituents [5, 6]. Accurate knowledge of the matrix and fiber volume fractions is required for these mechanical models. Currently, mechanical models for tubular braided composites assume an idealized geometry for predicting material properties. Accurate knowledge of tubular composite tow

50

architecture is also required to model the mechanical properties of tubular braided composites. Several methods have been used to model the geometry of composite braids. Composite braid geometries were initially modeled using the mosaic model of Ishikawa and Chou [7] and the fiber undulation model of Naik *et al.* [8]. Recently, braid strand path has been modeled by assuming fibers follow a sinusoidal path [6, 9, 10]; however, these models do not account for variations that may occur during composite braid manufacturing. To assess the accuracy of these models, it is necessary to develop a technique is necessary to evaluate the accuracy and consistency of tubular braids manufactured using a Maypole braider.

Void volume fraction in tubular composite braids impact matrix volume fraction and strand macro-mechanics. Voids can adversely affect mechanical properties [11, 12]. The void content is conventionally determined using methods such as matrix digestion or matrix burn off [13]; these provide the total void content of the composite sample but do not provide information on the distribution or size of voids within the sample geometry. Void content can also be determined using optical microscopy analysis methods in order to quantify void content [14, 15]. Optical methods are time intensive as successive 2D cross-sections of the composite sample are required. Finally, optical microscopy, matrix burn off and matrix digestion are destructive methods [16, 17].

A method that allows for both the determination of fiber tow architecture and void content is x-ray micro-computed tomography (μCT) [18]. X-ray μCT creates a cross-sectional image of an object. Contrast seen in the scan images is the result

of differences in x-ray attenuation. Material density and elemental composition both affect the attenuation of a sample, allowing for differentiation of different materials within a single μCT sample.

The complex fiber-tow-architecture of flat composite braids has been examined with μCT [19-21]. Void content for textile composites [22, 23] as well as void content measurement and fiber tow geometry has focused on flat textiles or 3D woven textiles [19, 20, 22, 23] have been investigated using standard methods. Little and Schilling [24, 25] performed void content measurement of composite laminates using μCT images, but these structures lack the complexity of the braided interwoven structure. To the best of the author's knowledge no works in the literature exist that investigate void content or fiber tow architecture for tubular braided composites using a μCT measurement method. Void content measurement is assesses using the same techniques for braided composites as for composite materials in general; however, manufacturing, impregnation and curing processes can influence void content. Few papers were found that investigated the void content of tubular braids specifically. There is no literature that specifically examines the size and distribution of voids in tubular composite braids. As well, there is little literature which investigates or reports the void content of tubular braided composites. Void content has been assessed for tubular braided composites using acid digestion and ultrasonic methods [26, 27] however neither of this methods provide information on the statistical distribution of voids throughout a composite sample [28].

The aim of this study is to investigate surface pores and voids of tubular braided composites using a μCT measurement method. The size and distribution of voids and surface pores throughout the tubular braid structure will be measured to assess the statistical distribution of defects in the braid structure. In addition, the tubular braid geometry will be investigated to quantify the individual yarn cross-sectional area, aspect ratio, braid angle and braid strand period. Accurate measurement is necessary to improve current braid geometrical models and to assess the quality and consistency of the braid manufacturing process. To simplify and automate the braid strand identification and measurement process, a cylinder unwrapping algorithm has been developed to convert the original tubular braid μCT images into a flattened braid structure. This study will provide a new method for accurately assessing braid strand path geometry and voids content measurements that are necessary for accurate prediction of tubular composite braid material properties and modeling [5, 6].

3.2 Methods

The tubular braided preform was prepared using a Maypole braider (Steeger USA, K80-72, Steeger USA, Inman, SC). The braid preform was manufactured using Kevlar (Kevlar49, 5680 denier, Dupont, Mississauga On) fibers. The braid was manufactured in a diamond braid configuration using 18 carriers. Once the braid perform was manufactured, it was placed over an 11.1mm (7/16") Teflon (polytetrafluoroethylene (PTFE)) mandrel and impregnated using a hand lay-up process with a thermoset resin (Epon825, Momentive Specialty Chemicals Inc., Columbus OH) and hardener (Ancamine1482, Air Products, Allentown PA)

combination with a resin to hardener ratio of 100:19. The braid was then oven cured at 110°C for 2 hours. An example of a braid preform and cured braid sample are shown in Figure 3-1.
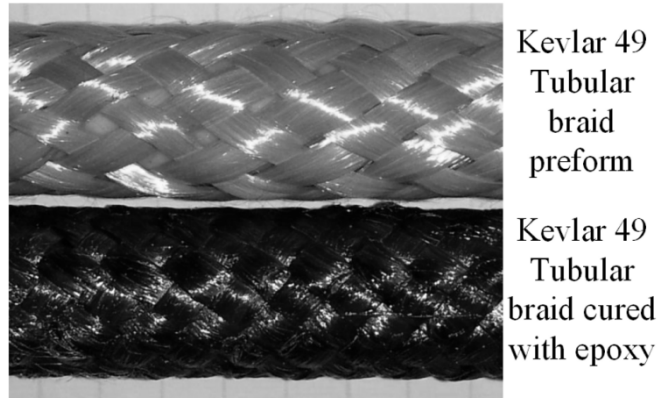
Figure 3-1: Tubular braided composites Top: Kevlar49 braid preform bottom: Cured Kevlar49 braid with an epoxy resin

A non-destructive μCT measurement technique was used to quantify voids within tubular braided composite structures and to assess the braid fiber strand geometry. Most μCT studies of composites have focused on glass and carbon fiber composites as opposed to Kevlar fibers [12, 19, 20, 22, 23]. The braid sample was imaged using a Skyscan 1076 μCT scanner (Bruker-MicroCT, Kontich, Belgium). The X-Ray beam energy used in this study was 51 kV at 110 μA. The μCT images collected in TIFF image format were 2000 x 1048 pixels with a voxel size of 18.2 μm^3 and a bit depth of 16. The μCT images were imported into NRecon v1.6.9 (SKYSCAN, Kontich, Belgium), to produce bitmap images containing cross-sectional slices of the scanned sample. The final bitmap images have an

image size of 2000 x 2000 pixels. An example of the two-dimensional cross-sectional slice of the tubular braid sample is shown in Figure 3-2.
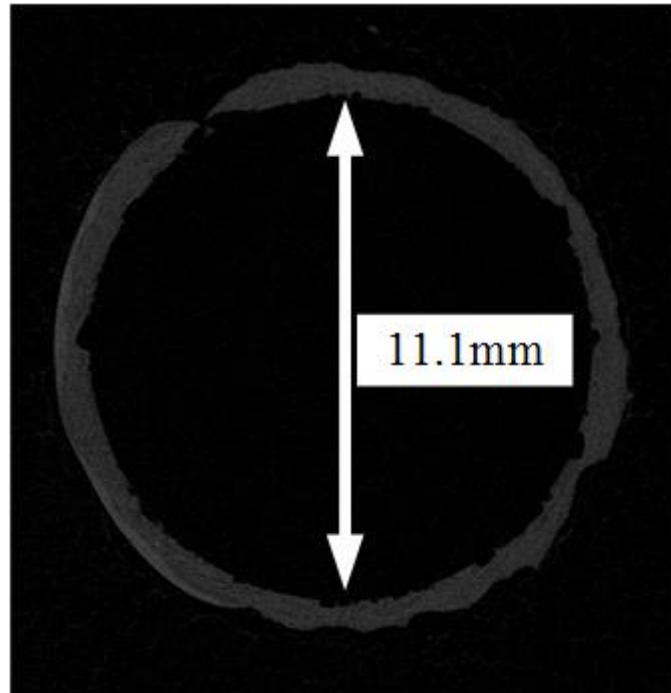
Figure 3-2: Two dimensional cross-sectional image slice of a tubular composite braid sample

3.2.1   Braid Geometry Reconstruction

Reconstruction of the tubular braided composite sample into a 3-dimensional (3D) model was carried out using a 3D image processing software package (ScanIP, SimpleWare, Bradninch Hall, United Kingdom). Bitmap images were resampled by a factor of 50% reduce memory used during the modeling process. Resampling the images reduces memory usage from 636 megabytes to 79 megabytes. A recursive Gaussian smoothing filter of 1 voxel was used to remove grayscale noise and small ring artifacts. The braid images were thresholded to capture the braid sample features.   Morphological opening and closing operations were applied to the thresholded images. This process was used to remove noise from

the braid images. The final recreated 3D geometry was exported as a stereo lithography (STL) file and then imported into a scientific visualization package (ParaView, Kitware, Clifton Park, NY). The recreated 3D geometry is shown in Figure 3-3. The recreated braid geometry shows the undulation of the individual fiber strands as well fiber stand texture.

Figure 3-3: Three dimensional braid geometry recreated from μCT images

3.2.2   Void Content and Surface Pore Determination

3.2.2.1   Void and Surface Pore Identification

The void content and surface pore of the tubular braid sample was examined by determining the volume and distribution of the voids and surface pores within the sample. Voids can be seen in the individual 2D image slices of the braid sample (Figure 3-4). The braid sample in this study exhibited fully enclosed voids which occurred between the inner and outer diameter of the sample (Figure 3-4). Surface pores caused by the complex undulating architecture of the braid fibers can also be seen in the cross-sectional braid images (Figure 3-3 and Figure 3-4). Enclosed voids and surface pores will be examined individually. The ideal braid geometry should have no enclosed voids and the inside diameter should be a smooth surface that matches the cylindrical mandrel that was used to fabricate the

braid sample. The ideal braid state was determined using the image analysis process described below.
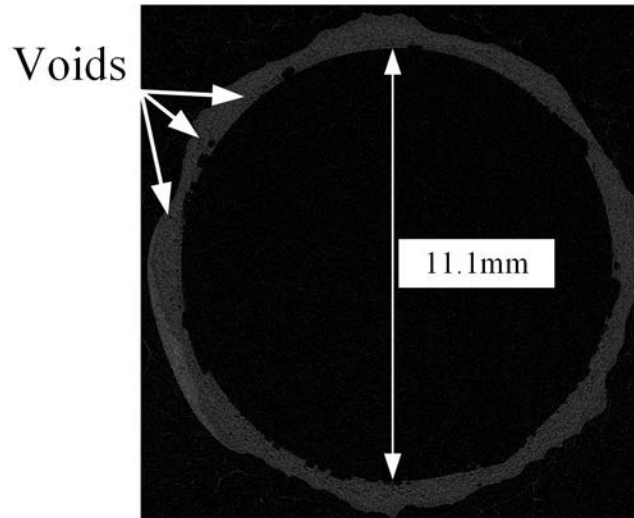
Figure 3-4: Enclosed voids within the braid sample demonstrated in a two dimensional cross-sectional image slice of a tubular braided composite sample

Both the enclosed voids and surface pores were examined using the same process. To analyze voids and surface pores the braid sample mask created using ScanIP was duplicated to form a second mask identical to the first. A morphological close of 10 voxels was used to close regions where voids were present. A Boolean subtraction of the original braid mask with the morphologically closed mask was used to determine the sample void content. The masking process for examining braid surface pores is illustrated in Figure 3-5. The volumes of the braid sample mask and the void content mask were determined by calculating the voxel volume of the braid and surface pores masks using the "Volume" command in SimpleWare ScanIP such that void volume fraction could be quantified using equation 3-1. The braid sample mask was used to compute the braid sample

volume (V_{sample}) and the braid void mask was used to determine the sample void volume (V_{voids}).

$$\%V_{voids} = \frac{V_{voids}}{V_{sample} + V_{voids}} \qquad\qquad 3\text{-}1$$
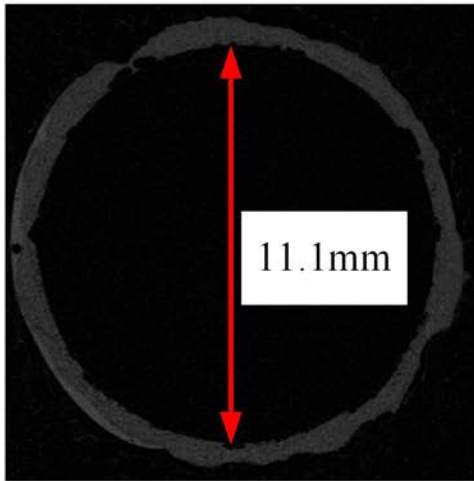
(a)
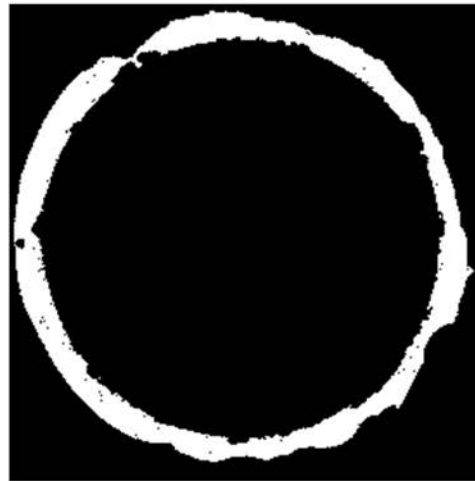
(b)

(c)
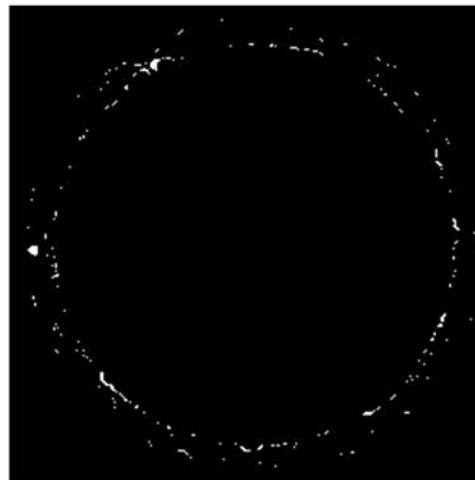
(d)

Figure 3-5: Determination of tubular braid void content (a) Initial bitmap image
(b) binarized image (c) image and mask overlay to determine braid void content
(d) final image of braid surface pores

3.2.2.2   *Void Size and Distrubution Analysis*

Analysis of void size and distribution was performed using a custom image
analysis program (MATLAB R2014a, The MathWorks Inc, Natick, MA, USA).
The void mask created in Section 3.2.2.1 was exported as a RAW image stack and
then imported using the custom image analysis program.   Void size and
distribution was examined by identifying individual voids.   Individual voids were
identified by identifying connected regions using the MATLAB function
'bwconncomp'.   After identifying each individual void the voxel volume and
centroid of each individual void was computed using the command 'regionprops'.
Once each void was identified the 3D void geometry was exported to Paraview
(ParaView 3.98.0, Kitware, Inc. Clifton Park, New York) to visualize the 3D void
distribution.

3.2.3   Tubular Braid Unwrapping Algorithm

To simplify the analysis of the braid geometry an unwrapping algorithm was
applied to the tubular braid μCT images. Unwrapping the braid images simplifies
the braid strand identification process and allows for automation of the braid
strand analysis. In order to view the braids as a flat weave, a transformation of
the original circular braid images was performed. Two pieces of information were
necessary to perform this transformation, termed "unwrapping": (1) the apparent
center of the tubular braid cross section and (2) the radius at which the
unwrapping was to occur. If the origin of the braid center was offset, the braid

59

would not appear as flat. If the unwrapping was performed at a radius other than that of the braid yarns, then the pixels in the annular region of interest (ROI) containing the braid would be distorted and pixel data must either be lost or added to map into the rectangular space.

3.2.3.1 Location of Braid Origin

As in Figure 3-2, one plane view of the original μCT scans captured slices of the circular cross-section of the tubular braids. During the scanning process there was potential error in the longitudinal alignment of the tubular braid that resulted in a progressive spatial shift in the image data. For a single image, this could be corrected manually by overlaying a circle approximating the geometry of the braid onto the image. This was accomplished through the user input of a number of points along the outer radius of the circle, from which a best fit approximation of circle is performed [29]. From this, an estimate for the braid origin is determined at either end of the set of images. A linear interpolation is performed between the top and bottom slices to determine the approximate origin along the sample at each slice location.

3.2.3.2 Image Coordinate Transform

Mapping an image from polar to Cartesian coordinates will always result in a loss of data [30]. An image in the polar coordinate system has fewer pixels at lower radial distance than at large radial distances. When these polar images are converted to a Cartesian coordinate system, pixels close to the origin and below the unwrapping radius are sparse and must be interpolated between where those beyond the unwrapping radius are truncated or averaged. The MATLAB function

'triScatteredInterp' was used to interpolate and remove data as required by the coordinate conversion. The "length" dimension of the unwrapped image θ was made equal to the circumference at this unwrapping radius ($\theta = 2\pi R_u$), so that the pixel mapping at this radius was 1:1, as can be seen in Figure 6. The resolution in the "width" dimension r was selected at a 1:1 ratio between the polar and Cartesian spaces. The unwrapping radius, R_u, originates from the center of the braiding axis and ends at the half width of the braid (Figure 3-6 (a)). Distortion in the braid unwrapping occur in the angular direction θ at radii greater or less than the unwrapping radius, R_u. Selection of these resolutions is critical for an accurate image, and as such this conversion was done so that the dimensions of the digitally unwrapped braid image would replicate that of a physically unwrapped braid; that is the thickness of the braid (radial distance) and the width of the braid (angular distance or braid circumference) would be preserved.

(a)   (b)
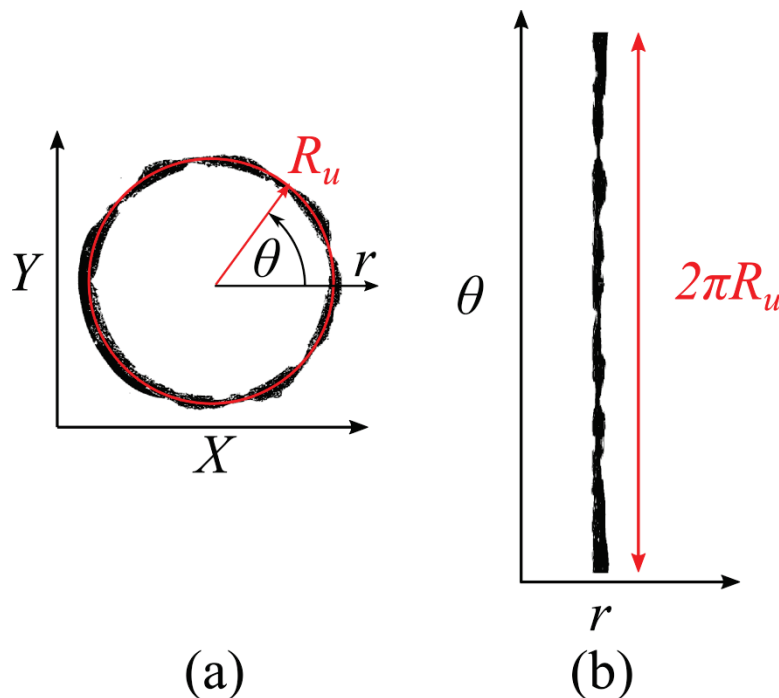
Figure 3-6: Coordinate system transformation from Polar coordinates to Cartesian coordinates (a) original braid geometry in Polar Coordinates (b) unwrapped braid geometry in Cartesian coordinates

3.2.3.3 Sensitivity of Image Coordinate Transform

Once the braid origin was identified for the image sequence the image unwrapping algorithm was applied. The sensitivity of the unwrapping algorithm to the selection of the origin is demonstrated in Figure 3-7. Figure 3-7 (a) shows an example two dimensional image of a circular object which is to be unwrapped. Figure 3-7 (b) demonstrates the final image after the unwrapping algorithm has been correctly applied. Correct selection of the origin is critical. Figure 3-7 (c) and (d) demonstrate the effect the distortion that can occur when the origin is selected incorrectly, with even a single pixel offset (Figure 3-7 (c)) having a significant effect on the unwrapped image.
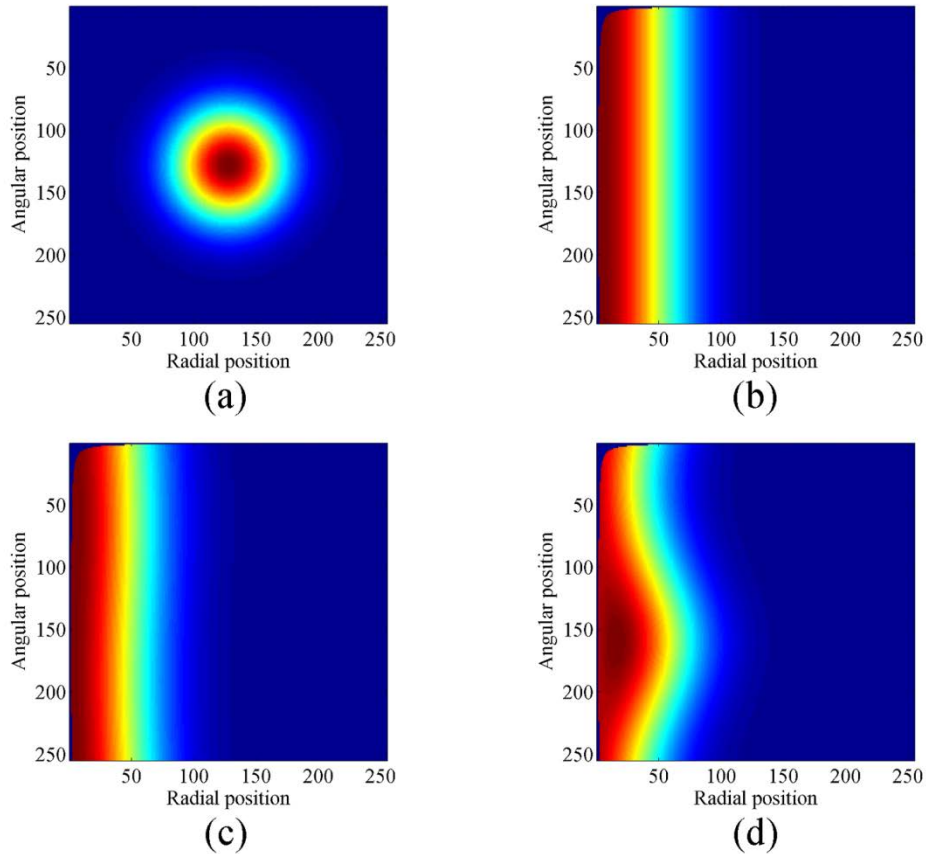
Figure 3-7: Example circular image that a unwrapping algorithm is applied to (a) the original image in polar coordinates; (b) image unwrapped correctly with origin located at [128,128]; (c) image unwrapped with slight distortion, origin selected at [128, 129]; and (d) image unwrapped with heavy distortion, origin selected at [120,120]

3.2.4 Braid Strand Analysis

Once the cylinder unwrapping algorithm was applied to the μCT images of a braid sample, the new set of bitmap images were imported into ScanIP. An example of the original and unwrapped bitmap images created using the algorithm described in section 2.3 are shown in Figure 3-8. The unwrapping algorithm was applied to the braid samples to simplify the segmentation and analysis of the individual yarns within the braid geometry. Similar segmentation techniques as those described above in Section 2.1 were used to form a 3D mask of the

63

unwrapped braid sample. The unwrapped 3D braid geometry is shown in Figure
3-9.
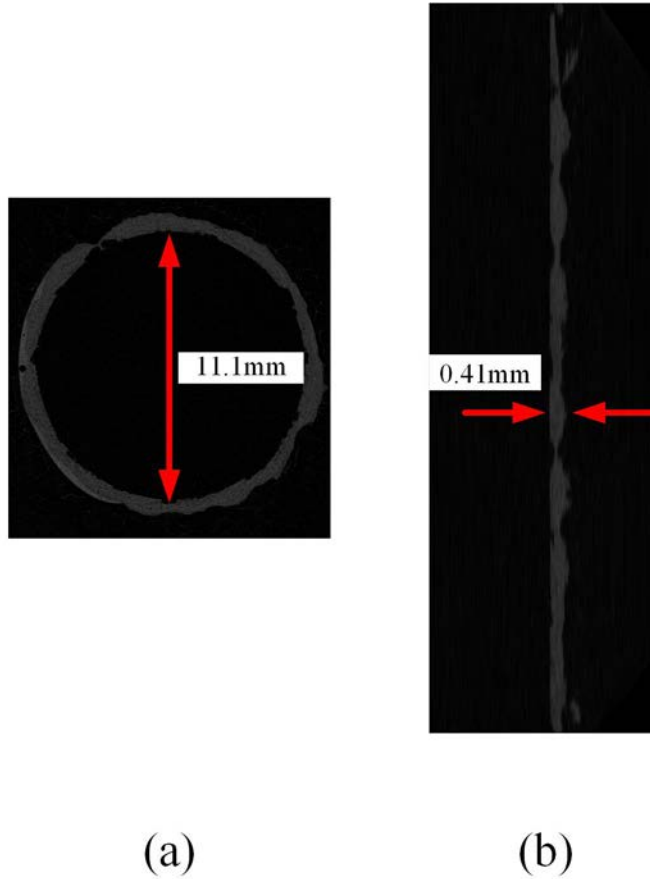
Figure 3-8: Braid sample bitmap images (a) original cylindrical braid sample (b)
unwrapped braid sample

Figure 3-9: Unwrapped 3D braid geometry created using the unwrapped two dimensional braid images

Once the 3D braid geometry, shown in Figure 9, was created the individual braid strands were segmented. The strands were segmented by using ScanIP's "point to point" line tool in order to identify the individual braid yarns. An example flat braid geometry and strand segmentation lines are shown in Figure 3-10.

Figure 3-10: Segmentation of braid yarns using the 3D braid geometry created using SimpleWare

Following braid yarns segmentation, the "3D planar editing tool" in ScanIP was used to bisect the top and bottom halves of the braid sample model, and then capture each half within its own individual mask. As a result of these steps, all strands of the braid sample were separated into several isolated segments. Using a "floodfill" tool the segments of a single strand were captured in a new mask. An example of the final segmented yarn strands is shown in Figure 3-11.
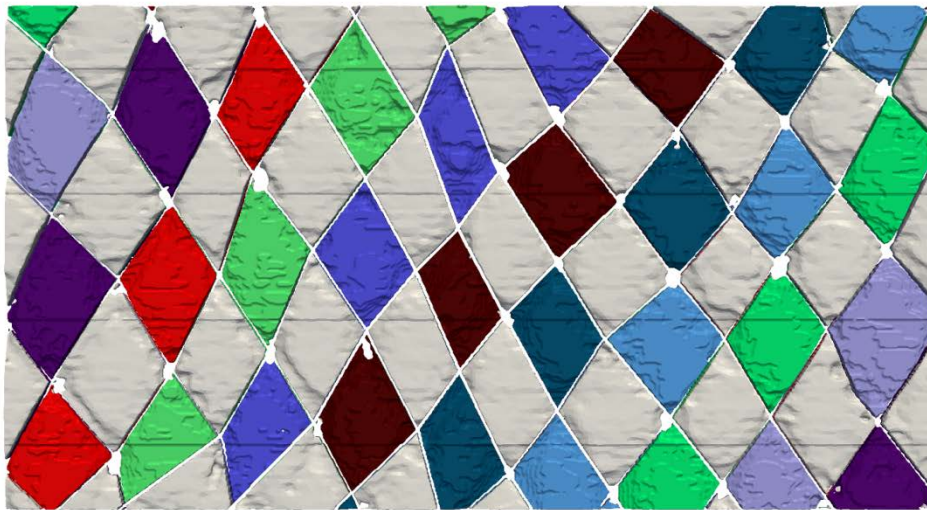
Figure 3-11: Segmentation of individual braid yarns. Each braid yarn has been segmented and an individual color has been assigned to each yarn

Finally, a comparison of the original cylindrical braid geometry and unwrapped braid geometry with segmented yarns is shown in Figure 3-12. Each of the segmented yarns was assigned an individual grayscale value so that each of the yarns could be analyzed individually.

Figure 3-12: Unwrapping of original cylindrical μCT scans. Left: original tubular braid geometry. Right: unwrapped braid geometry with individual yarns identified.

A new stack of bitmap images with each yarn identified was created in SimpleWare and then exported. The images were converted to a PNG image stack using and image processing program (ImageJ, National Institutes of Health, Bethesda, Maryland, USA) for further processing. A comparison of an original flat bitmap image and final image with each yarn identified with a different grayscale value is shown in Figure 3-13. Figure 3-13 (b) shows that each braid yarn has been identified with varying grayscale values.
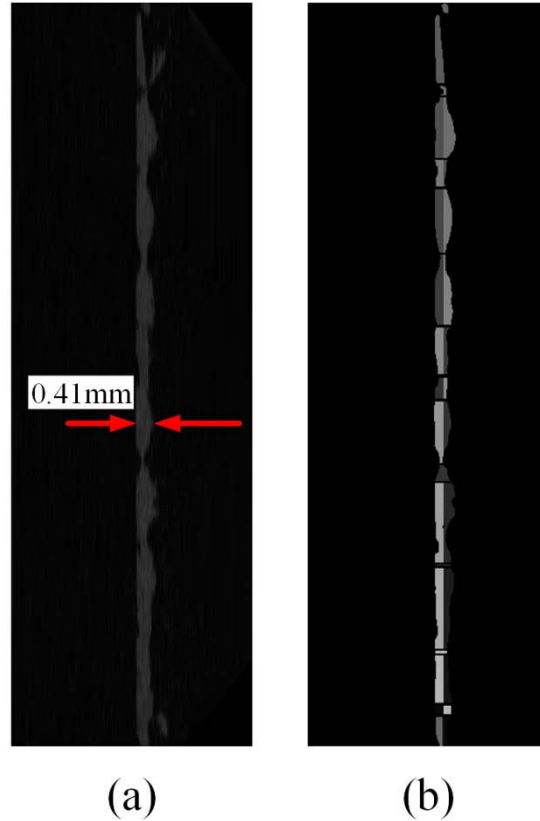
Figure 3-13: Identification of individual braid yarns (a) original unwrapped braid image (b) unwrapped braid with a different grayscale value assigned to each yarn

3.2.4.1 Exportation of Braid Strand Data for Individual Strand Analysis

To quantify the individual braid strand geometries the unwrapped and segmented braid images created in section 2.4 were imported and processed using a custom image analysis program (MATLAB R2014a, The MathWorks Inc, Natick, MA, USA). Here, the centroid, cross-sectional area, aspect ratio, braid angle and fiber undulation period of each strand on each image slice was determined, with the differing grayscale values of each strand being used to distinguish between each strand.

The position vector, $r_{xyz}(i)$, describes the instantaneous strand direction for each of the individual braid yarns ($i = 1 \ldots 18$). The position vector (r_{xyz}) and the global

coordinate system for the flattened braid geometry are shown in Figure 3-14. The

incremental change of a strand's weaving path (crimp angle defined in Figure

3-15) was used to track its angular orientation (ϕ) as it moved along the braid

sample by using a rearranged dot product formula:

$$\phi = \cos^{-1}\left(\frac{r_{xz}(i) \cdot z}{|r||z|}\right)$$

3-2
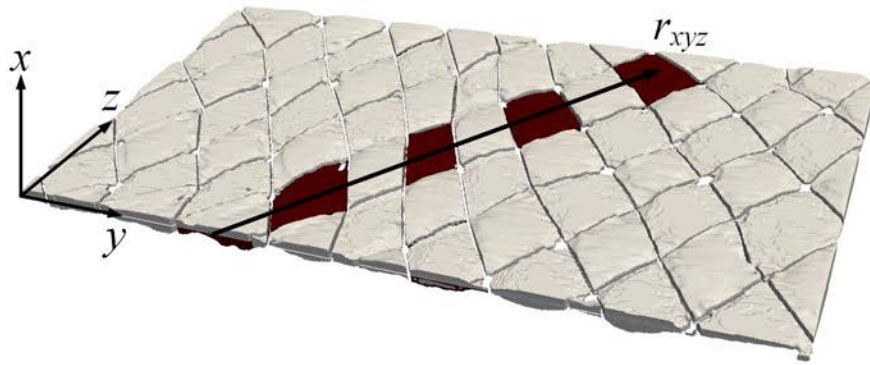
(a)
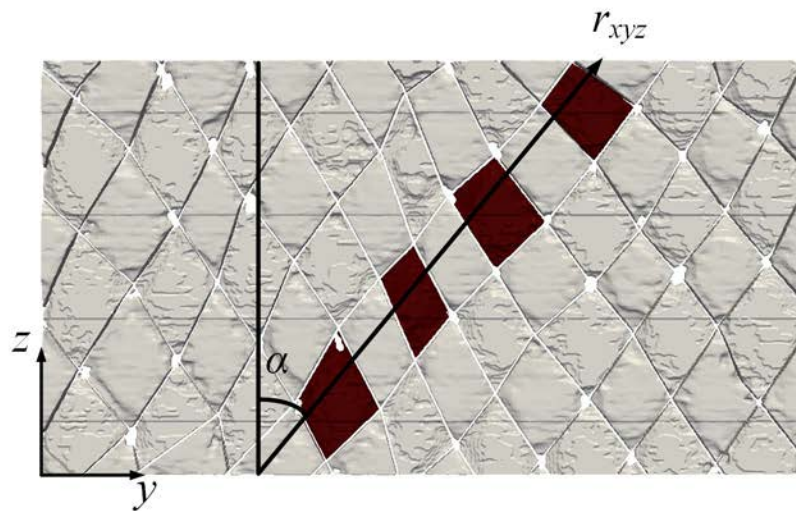
(b)

Figure 3-14: Summary of angle-finding process: (a) The position vector between centroid coordinates on neighboring image slices, r_{xyz}, describes the instantaneous direction in which a strand moves. Projecting r_{xyz} onto the x-z plane gives a vector describing the strand's instantaneous weaving path, r_{xz}, with the orientation angle being the crimp angle (φ) it makes with the global z axis. (b) Projecting this vector onto the y-z plane gives a vector describing the strand's instantaneous angular path, r_{yz}, with the braid angle (α) being the angle it makes with the global z axis.
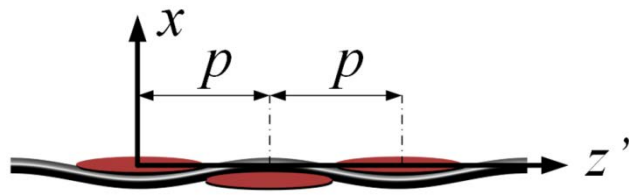
Figure 3-15: The half period length (*p*) of the strand's weaving pattern, *p*, is defined as the length of one half of the strand's (approximately sinusoidal) weaving cycle.

Where $r_{xz}(i)$ is the position vector describing the change of the strand's crimp angle from one image slice to the next in the *x-z* plane and *z* is the unit vector in the *z* direction. By similar means, $r_{xy}(i)$, the incremental change of a strand's braid angle (*α*) in the *x-y* plane, was taken in place of $r_{xz}(i)$ to track the braid angle. Polynomial fits were applied to both the crimp and braid path data to ensure the crimp angle and braid angle data was smooth.

Knowledge of the braid angle (*α(i)*) at all locations along a strand as well as the change in *z* value between each image slice (*dz*) allowed for the global *z* coordinates of the sample to be transformed into local *z'* coordinates for each strand, using the braid angle shown in Figure 3-14 (b). This figure illustrates that a coordinate system transformation was applied to the cross-sectional images of each braid strand using the braid angle, *α(i)*, of each yarn. This coordinate system transformation was required to determine the actual cross-sectional area and yarn height and width rather that the projected dimensions in the global *x,y,z* coordinate system.

71

At all locations along the braid sample, the cross-sectional area (A) of a single strand was found by taking the area recorded from the corresponding image slice, then applying trigonometric correction factors based upon the values of orientation and braid angle found for that strand at the same location along the sample. The orientation angle was used again to correct the maximum height of the strand found for the same image slice. Assuming the cross-section of each strand was elliptical in shape, this allowed the aspect ratio (a_r) of the strand's cross-section to be found at all locations, according to:

$$a_r = \frac{a}{b} = \frac{\pi ab}{\pi b^2} = \frac{A}{\pi b^2}$$

3-3

where a and b are the cross-section's major and minor radii, respectively. Next, the Cartesian coordinates of the CT images were converted to polar coordinates. As the weaving path (x-coordinate of the centroid) of the strands was already equivalent to the strand's radial distance from the center of the braid sample, the same value could be used as the polar r-coordinate. The θ-coordinate was found using the arc length formula:

$$s = r\theta$$

3-4

By treating the full top-to-bottom length of the CT images as the arc length (s) when θ was equal to 2π radians, r was able to be determined. Then, the θ-coordinate could be found for each strand on each image using:

72

$$\theta = \frac{y}{r}$$

<div align="right">3-5</div>

where y is the y-coordinate of the strand's centroid on a particular image. With the new coordinate system in place, strands could be plotted to reconstruct their tubular structure. The difference in θ coordinates between neighboring parallel strands could be taken to determine the angular spacing between them as they moved along the sample. Using the same tubular datasets, the approximate intersection points between one particular strand and all other strands weaving in the orthogonal direction could be determined by taking the distance along the x axis at which they were closest together. The intersection points were arranged in order of increasing distance in the global z direction, and then were converted to their equivalent distance along the strand's local coordinate system. Taking the difference in distance between these intersection points, the half-period length (p) of the strand's oscillating weaving path (Figure 3-15) could be determined at several points along the braid sample.

The x-coordinates of all strands at all positions along the braid sample were previously averaged together to quantify the actual radius of the tubular structure. The same was applied to the braid angle, aspect ratio, and cross-sectional area to find their nominal values. Finally, the nominal half period length of the braid sample's strands was determined using:

$$p = \frac{r_0 \beta}{2 \sin \alpha}$$

<div align="right">3-6</div>

where β is the shift angle between strands and α is the average braid angle. In all cases, β is simply $2\pi/n$, where n is the number of strands moving in one direction.

All data collected from the strands was plotted as a function of the distance in the z-direction at which it was taken. The oscillating datasets (weaving path, cross-sectional area, aspect ratio, and angular orientation) were plotted with respect to their own local strand coordinates so data for multiple strands could be visualized with minimal phase shift between them. This same data could then be averaged together to view the mean weave path, area, aspect ratio, and angular orientation over the length of a strand.

3.3   Results

3.3.1   Void Content and Surface Pore Determination

The recreated braid geometry in Figure 3-3 shows the presence of surface pores along the inside diameter of the braid sample. The distribution of surface pores within the braid samples is shown in Figure 3-16. This figure shows the three dimensional distribution of surface pores throughout the braid sample.   The surface pores shown in this figure were visualized by creating a 3D representation using the segmented images shown in Figure 3-5. Figure 3-16 (b) and (c) show that many surface pores occur along the crossover regions between braid yarns. The section view of the braid sample in Figure 3-16 (d) illustrates that many surface pores occur along the inside diameter of the sample.
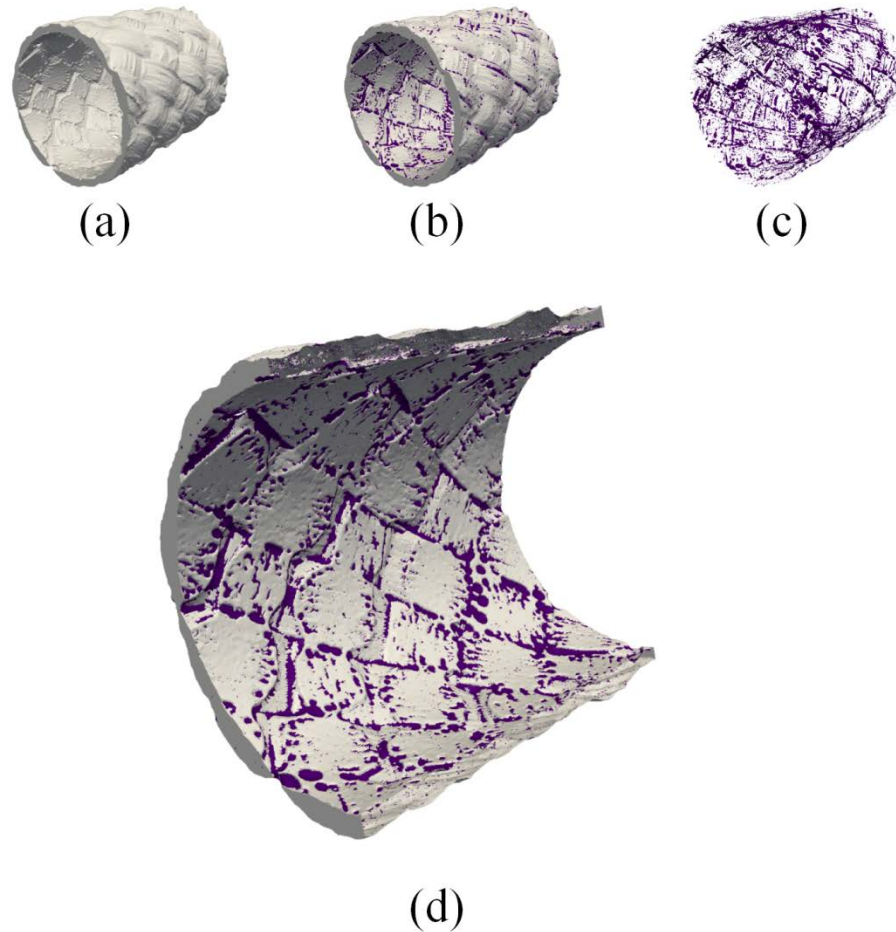
Figure 3-16: Three dimensional visualization of braided composite surface pore distribution (a) 3D braid geometry (b) 3D braid geometry with surface pores (c) 3D dimensional distribution of surface pores throughout the braid sample (d) Cross-sectional view of braid geometry with surface pores

Similarly, the internal enclosed voids were examined and visualized to show the distribution of voids throughout the braid sample. Visualization of the 3D distribution of enclosed voids is shown in Figure 3-17. Figure 3-17 (a) shows the entire braid geometry with voids while Figure 3-16 (b) shows the void distribution. Figure 3-17 (c) shows a cross-sectional view of the braid sample with enclosed voids.
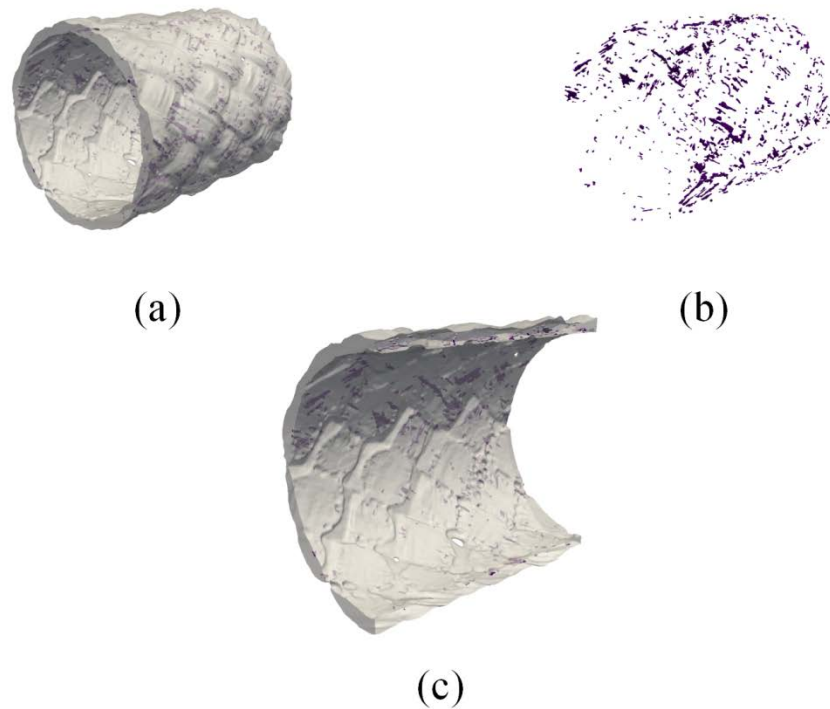
Figure 3-17: Enclosed voids within the braid geometry (a) braid geometry and enclosed voids (b) enclosed voids only (c) section view of braid and enclosed voids

The volume fraction of the surface pores shown in Figure 16 and the voids shown in Figure 3-17 were determined and are shown in Table 1. The volume of the braid sample as well as the void volume was calculated by determining the voxel volume of the braid geometry, void geometry and surface pore geometry. Table 3-1 shows that the volume fraction of the braid surface pores is 2.44% while the volume fraction of the enclosed voids was less than half, at 1.04%.

Table 3-1: Void volume fraction of braid sample comparing volume fraction of surface pores and voids

Sample	Sample Volume (mm^3)	Voids Volume (mm^3)	Volume Fraction (%)
Volume fraction of surface pores	424.19	10.61	2.44
Volume fraction of enclosed voids	466	4.91	1.04

3.3.1.1   *Void Size and Distribution*

Analysis of void size and distribution was performed using a custom image analysis program (MATLAB R2014a, The MathWorks Inc, Natick, MA, USA). Identification of each individual void is shown in Figure 3-18. In this image, a total of 644 voids were identified. The color map in this image represents the number assigned to each void ranging from 1 to 644.
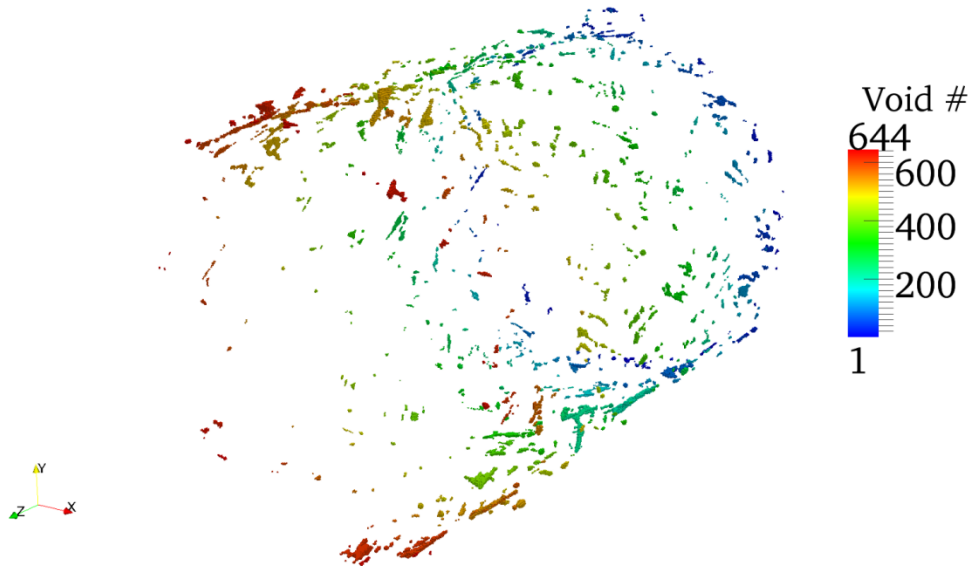
Figure 3-18: Identification of individual braid voids. The three dimensional

distribution of the individual voids is displayed. The color map displayed in this figure identifies the individual voids throughout the sample.

The volume of each void identified in Figure 3-18 was computed and compared in Figure 3-19. Figure 3-19 (a) compares the identified voids and shows that several large voids are present within the braid geometry having a volume greater than $0.05mm^3$ while the majority of the voids have a volume of less than $0.05mm^3$.The distribution of voids within the braid sample is shown in Figure 3-19 (b). From this image it can be seen that the majority of the voids are less than $0.05mm^3$. The median void volume was found to be $0.0033 \ mm^3$ and the 25th and 75th percentiles were found to be 0.0022 and $0.0065 \ mm^3$ respectively. The skewness of the void volume dataset was computed and determined to be 7.8. This shows that the void volume data is skewed since the skewness is greater than 3.0. The high skewness is caused by the large voids found in the braid sample used in this study. Figure 3-19 (c) shows a Weibull distribution fitted to the void volume probability density function. A Chi-Square (χ^2) goodness of fit test was also performed to determine if this distribution was appropriate. In this case the null hypothesis was accepted with 95% confidence meaning that the Weibull distribution is an acceptable method for describing the void volume distribution. Using the Weibull distribution the mean void size was determined to be 0.0074 mm^3 with a variance of $7.3 \ 10^{-3} \ mm$. The largest void within the braid geometry, void # 215 with an area of $0.2248mm^3$, can be seen in Figure 3-19. Figure 3-20 shows the position of the largest void within the braid geometry. This figure

shows the relative size of the largest void to other voids within the braid geometry.
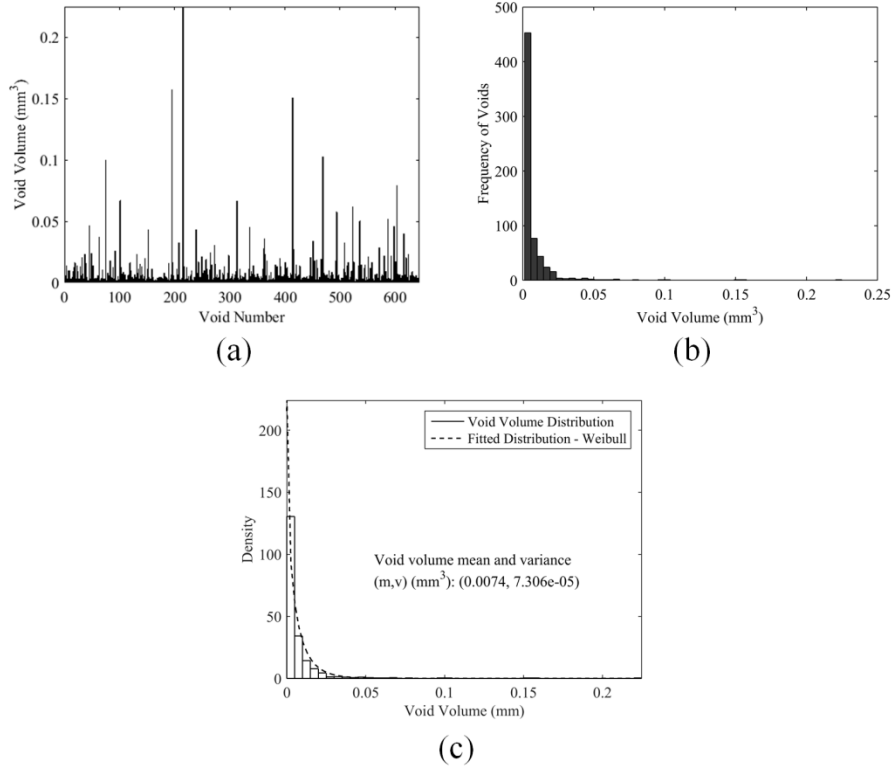
Figure 3-19: Distribution of voids throughout braid sample. (a) Comparison of void size and void number (b) Histogram of void distribution in the braid sample (c) Weibull distribution fitted to the void volume distribution
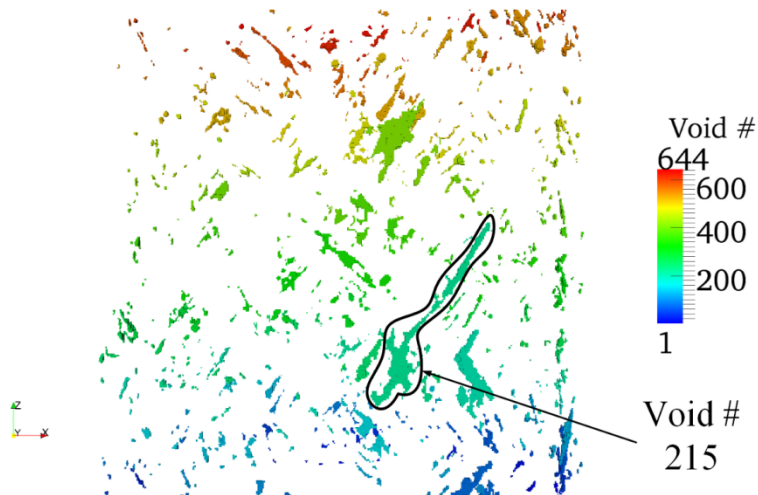
Figure 3-20: Three dimensional void distribution with the largest void identified

3.3.1.2   Braid Strand Analysis

The unwrapped and segmented braid images were examined using a custom MATLAB image processing program. The centroid, cross-sectional area, aspect ratio, braid angle and fiber undulation period of each strand was determined, with the differing grayscale values of each strand being used to distinguish between each strand.

The undulating strand path for each of the braid yarns is displayed in Figure 3-21. This figure shows the weaving path of the individual yarns in the weft and warp directions (Figure 3-21 (a)). The average weaving path for the braid in both the weft and warp direction is also show in this figure (Figure 3-21 (b)).
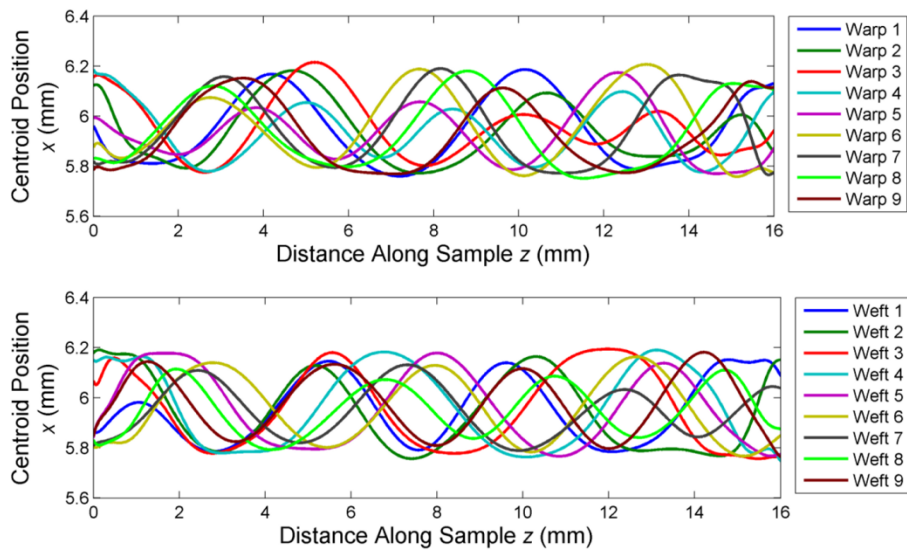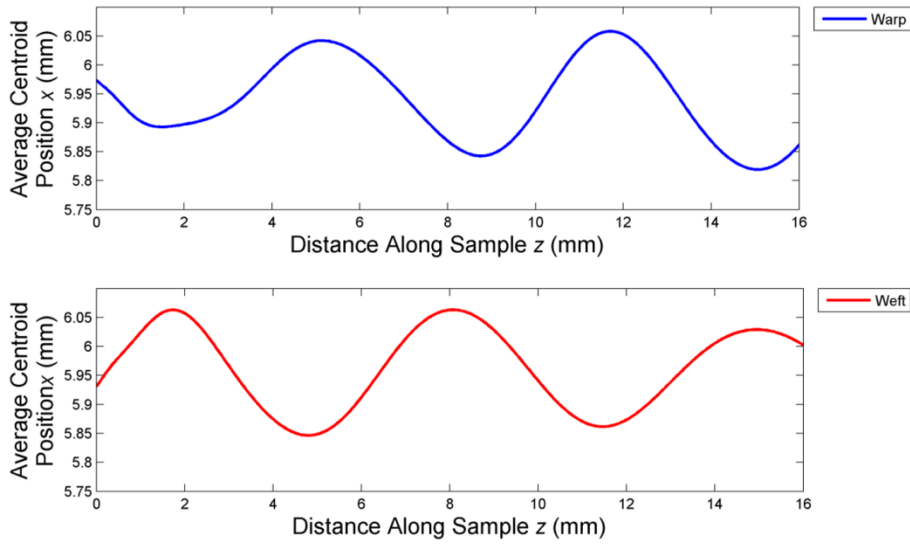
Figure 3-21: Weaving path of the braid yarns in the *x-z* plane (a) weaving path of the individual yarns in the weft (clockwise) and warp (counterclockwise) direction (b) average weaving path of the weft and warp yarns

The angular path of each braid strand in the *y-z* plane was also determined. The braid angular path is defined in Figure 3-14. The angular path of each yarn in both the warp and weft directions is shown in Figure 3-22.

81
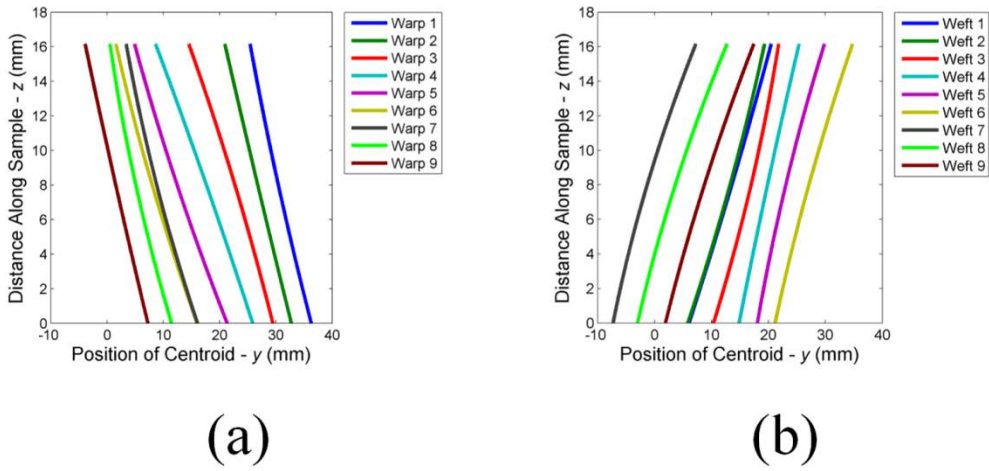
Figure 3-22: Angular path of individual braid yarns (a) warp strand angular path (b) weft strand angular path

The results from the braid strand analysis also allowed for the visualization of the 3D path of the yarn centroids. The 3D position of each yarn centroid is visualized in Figure 3-23. This figure shows the undulating nature of each braid yarn and displays their angular position around the braid circumference.
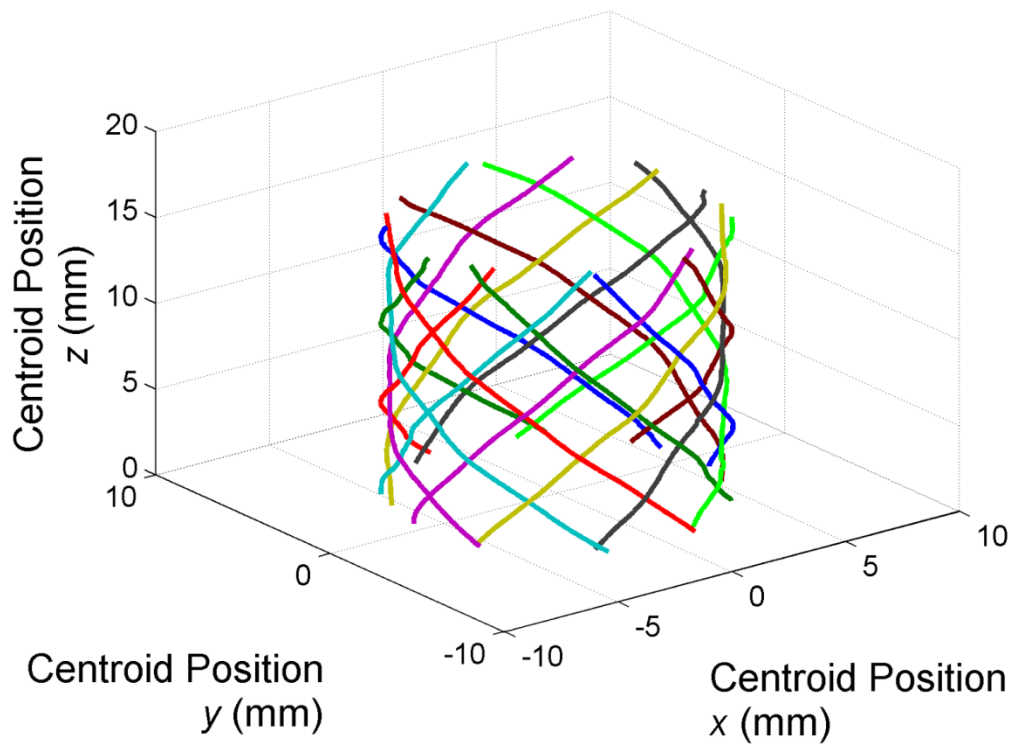
Figure 3-23: Three dimensional plot of braid centroids determined using the results from the braid strand analysis

The results from the braid strand analysis are shown in Table 3-2. This table compares the braid strand results for all braid yarns. As well, results are also displayed for yarns in the clockwise (weft) and counterclockwise (warp) directions.

Table 3-2: Braid strand analysis results comparing all strands, warp strands and weft strands of the braid sample with mandrel diameter 11.1 mm

Braid Strand		Radial Distance (mm)	Cross-Sectional Area- A (mm^2)	Aspect Ratio- a_r	Braid Angle $-\alpha$ (deg)	Fiber Undulation Half Period- p (mm)
All Strands	Average	5.95	0.86	7.13	39.26	3.31
	Standard Deviation	0.13	0.14	1.6	5.77	0.49
Warp Strands (CCW)	Average	5.94	0.85	7.25	39.17	3.32
	Standard Deviation	0.13	0.14	1.62	5.76	0.53
Weft Strands (CW)	Average	5.96	0.87	7	39.35	3.29
	Standard Deviation	0.13	0.15	1.59	5.56	0.44

The weaving paths shown in Figure 3-21 were used to determine the fiber undulation half period shown in Table 3-2. The undulation half period of the braid yarns is defined in Figure 3-15 and equation 3-6. Figure 3-21 shows the sinusoidal path of the centroids of the individual braid yarns.

The cross-sectional area and aspect ratio of each yarn shown in Table 3-2 were determined by assuming the yarns have an elliptical shape [9, 31]. The aspect ratio of each yarn was determined by the cross-sectional area of each yarn from the grayscale images and using equation 3-4. The angular strand paths in Figure 3-22 were used to calculate the braid angle (α) of each yarn.

3.4   Discussion

There are several studies that have utilized the μCT imaging technique in order to investigate composite materials [11, 12, 19-22, 25, 32, 33]. Currently, no studies

exist that examine tubular braided composites using the μCT imaging technique. The method outlined in this manuscript will allow for both the investigation of voids within tubular composite braids and evaluation of braid strand geometry. Demonstrating this capability in the complex tubular braid architecture allows this method to be applied to a broad range of composite materials and structures.

3.4.1 Void Content Determination

Void content has previously been assessed for tubular braided composites using acid digestion and ultrasonic methods however neither of these methods provide information on the statistical distribution of voids throughout a composite sample [26, 27]. Kruesi *et al.* found void volume fractions that ranged from 1.74-3.71% for composite braids measured using conventional void volume fraction measurement techniques [26]. The void content in this study was found to be 1.04% for enclosed voids and 2.44% for surface pores. Previously, a successive polishing and imaging method has been used to characterize the void distribution of a plain weave textile composite [14]. In this study common void locations and common void shapes for textile composites were identified. However, void volume fraction and void statistics were not reported.

A study by Zhu *et al.* examined the effect of void content on the tensile strength of fabric laminates [34]. This study demonstrated that an increase in void content from 0.4% to 8% results in a decrease in longitudinal tensile strength of 2%. It was also demonstrated that crack initiation and growth is caused by the presence of voids within the composite structure. This study demonstrates the importance of minimizing void content since voids result in a reduction in composite material

tensile strength. As well, voids within the epoxy matrix initiate crack growth which leads to premature failure of the composite material.

Surface pores and voids can be seen throughout the tubular braid sample examined in this study (Figure 3-3, Figure 3-16, Figure 3-17). The enclosed voids and surface pores were examined separately since these defects are caused by differing mechanisms. The surface pores along the inside diameter of the braid sample shown in Figure 3-16 are due to the undulations of the braid yarns. The surface pores occur along the cross-over regions between the braid yarns. By contrast, the enclosed voids only occur within the braid geometry as shown in Figure 3-17. The enclosed voids are caused by entrapped air within the resin and braid yarn. The enclosed voids are randomly distributed throughout the braid sample whereas the braid surface pores follow the braid strand path.

The comparison of the volume fractions of the enclosed voids and surface pores is shown in Table 3-1. This table shows that the surface pore volume fraction is greater than the enclosed void volume fraction. The difference in void and surface pore volumes is also demonstrated in Figure 3-16 and Figure 3-17.

The tubular braided composite sample used in this study was manufactured using a manual impregnation process. The above void and surface pore analysis show that defects occurred in the braid sample due to the current resin impregnation process. In order to improve the consistency of resin impregnation and to minimize the number of voids and surface pores in the braid sample a resin transfer molding (RTM) or vacuum assisted resin transfer molding process

(VARTM) should be employed [35]. The µCT measurement technique and image processing method outlined in this manuscript can then be used to assess the improved consistency of resin impregnation of various resin impregnation methods.

3.4.2 Braid Strand Analysis

The µCT measurement technique has allowed for a variety of braid geometrical parameters to be investigated. Similar analysis for flat three-dimensional textile composites has been performed by Bale *et al.* [32]. The results from the µCT measurement technique provide a wealth of information for braid geometries. Information obtained using this method includes the braid angle of the individual yarns and the radial distance of braid yarns from the braid center. Other parameters that can be determined include: yarn cross-sectional area and aspect ratio and the individual yarn crimp angle. All of the information collected using the µCT measurement technique can be used to assess the quality and consistency for manufactured braids without damaging the braid sample. The geometrical parameters measured using the µCT measurement technique can be used to compare physical braid geometrics with idealized braid geometry models [9].

Current analytical and finite element models for tubular braided composites utilize idealized geometries in order to predict braid mechanical properties [6, 9, 10, 36, 37]. All of these models make assumptions regarding the braid geometry such as the yarn cross-sectional shape; yarn major and minor diameters; fiber undulation period; as well as, matrix and fiber volume fractions. Key parameters like braid angle have been measured by wrapping transparent paper on the

specimens and manually measuring the angle using a protractor [5]. Similarly, assumptions regarding yarn shape and size have been made based on two dimensional micrographs of yarns [31]; however this method does not capture variations in yarn shape and size throughout the braid sample. Therefore, the ability to quantify tubular braid geometry in three dimensions will result in improved tubular braid models since measurements of all braid yarns can be performed.

In addition to improving current models, the three dimensional braid geometry generated in this study could be used for finite element analysis (FEA) [38]. A FEA model generated using the geometry created in this study would allow for examination of the effect of surface pores and voids on mechanical properties. The voids and surface pores shown in Figure 3-15 and Figure 3-16 will result in stress concentrations that will have a significant effect on braid mechanical properties [34]. This FEA model could also be compared with FEA models created using idealized braid geometries [36] to demonstrate the effect for fiber strand variations and surface pores on mechanical properties.

3.5 Conclusions

A μCT measurement method was utilized in order to investigate tubular braided composites. This measurement method was used to quantify the presence of voids and surface pores in the braid structure. In addition, this method allows for assessment of the three dimensional geometry of composite braids. The method outlined in this manuscript can be used to assess the quality and consistency of the tubular braided composite manufacturing process. Understanding the three

dimensional geometry of tubular braided composites will lead to improved analytical models since these models are sensitive to braid geometric effects. In addition, the three dimensional braid geometry generated in the study could also be for further finite element studies.

The results presented in this chapter are important for understanding the structure of tubular braided composites. The presence of voids and surface pores within the braid structure will affect the mechanical properties of braided composites. An understanding of the presence of voids and surface pores within the braid geometry is required for the experimental analysis of braided composites as can be seen in Chapter 4. Additionally void content can have an effect on elastic properties. Understanding the presence of voids and surface pores in the structure of braided composites is important for the analytical modelling of tubular braided composites as can be seen in Chapter 5.

3.6   References

[1] F. K. Ko, C. M. Pastore and A. A. Head, *Handbook of Industrial Braiding.* Covington, Kentucky: Atkins and Pearce, 1989.

[2] D. Branscomb, D. Beale and R. Broughton, "New directions in braiding," *Journal of Engineered Fibers and Fabrics,* vol. 8, pp. 11-24, 2013.

[3] F. K. Ko, "Braiding," in *ASM International, Engineered Materials Handbook* Anonymous American Society of Metals, 1987, pp. 519-528.

[4] C. Ayranci and J. Carey, "2D braided composites: A review for stiffness critical applications," *Composite Structures,* vol. 85, pp. 43-58, 2008.

[5] C. Ayranci and J. P. Carey, "Predicting the longitudinal elastic modulus of braided tubular composites using a curved unit-cell geometry," *Composites Part B: Engineering,* vol. 41, pp. 229-235, 2010.

[6] J. Carey, M. Munro and A. Fahim, "Longitudinal elastic modulus prediction of a 2-D braided fiber composite," *J Reinf Plast Compos,* vol. 22, pp. 813-831, 2003.

[7] T. Ishikawa and T. -. Chou, "Stiffness and strength behaviour of woven fabric composites," *J. Mater. Sci.,* vol. 17, pp. 3211-3220, 1982.

[8] N. K. Naik and P. S. Shembekar, "Elastic behavior of woven fabric composites: I-lamina analysis," *J. Composite Mater.,* vol. 26, pp. 2196-2225, 1992.

[9] T. Alpyildiz, "3D geometrical modelling of tubular braids," *Text. Res. J.,* vol. 82, pp. 443-453, 2012.

[10] P. Potluri, A. Rawal, M. Rivaldi and I. Porat, "Geometrical modelling and control of a triaxial braiding machine for producing 3D preforms," *Composites Part A: Applied Science and Manufacturing,* vol. 34, pp. 481-492, 2003.

[11] Y. Nishikawa, S. Baba and M. Takahashi, "Optimization of x-ray computerized tomography for polymer materials," *International Journal of Polymeric Materials and Polymeric Biomaterials,* vol. 62, pp. 295-300, 2013.

[12] A. E. Scott, I. Sinclair, S. M. Spearing, M. N. Mavrogordato and W. Hepples, "Influence of voids on damage mechanisms in carbon/epoxy composites determined via high resolution computed tomography," *Composites Sci. Technol.,* vol. 90, pp. 147-153, 2014.

[13] Anonymous "ASTM D2734-09 standard test methods for void content of reinforced plastics," ASTM International, West Conshohocken, PA, 2009.

[14] Y. A. Gowayed, "The Effect of Voids on the Elastic Properties of Textile Reinforced Composites," *J. Composites Technol. Res.,* vol. 19, pp. 168-173, 1997.

[15] I. M. Daniel and O. Ishai, *Engineering Mechanics of Composite Materials.* New York: Oxford University Press, 2006.

[16] F. J. Guild and J. Summerscales, "Microstructural image analysis applied to fibre composite materials: a review," *Composites,* vol. 24, pp. 383-393, 1993.

[17] M. H. Hassan, A. R. Othman and S. Kamaruddin, "Void content determination of fiber reinforced polymers by acid digestion method," *Advanced Materials Research,* vol. 795, pp. 64-68, 2013.

[18] Anonymous "ASTM E1441-11 standard guide for computed tomography (CT) imaging," ASTM International, West Conshohocken, PA, 2011.

[19] L. P. Djukic, I. Herszberg, W. R. Walsh, G. A. Schoeppner, B. Gangadhara Prusty and D. W. Kelly, "Contrast enhancement in visualisation of woven composite tow architecture using a MicroCT Scanner. Part 1: Fabric coating and resin additives," *Composites Part A: Applied Science and Manufacturing,* vol. 40, pp. 553-565, 2009.

[20] L. P. Djukic, I. Herszberg, W. R. Walsh, G. A. Schoeppner and B. Gangadhara Prusty, "Contrast enhancement in visualisation of woven composite architecture using a MicroCT Scanner. Part 2: Tow and preform coatings," *Composites Part A: Applied Science and Manufacturing,* vol. 40, pp. 1870-1879, 2009.

[21] F. Desplentere, S. V. Lomov, D. L. Woerdeman, I. Verpoest, M. Wevers and A. Bogdanovich, "Micro-CT characterization of variability in 3D textile architecture," *Composites Sci. Technol.,* vol. 65, pp. 1920-1930, 2005.

[22] M. Kosek and P. Sejak, "Visualization of voids in actual C/C woven composite structure," in *Special Issue on the 12th European Conference on Composite Materials, ECCM 2006,* 2008, pp. 1465-1469.

[23] J. S. U. Schell, M. Renggli, G. H. van Lenthe, R. Müller and P. Ermanni, "Micro-computed tomography determination of glass fibre reinforced polymer meso-structure," *Composites Sci. Technol.,* vol. 66, pp. 2016-2022, 2006.

[24] J. E. Little, X. Yuan and M. I. Jones, "Characterisation of voids in fibre reinforced composite materials," *NDT and E International,* vol. 46, pp. 122-127, 2012.

[25] P. J. Schilling, B. P. R. Karedla, A. K. Tatiparthi, M. A. Verges and P. D. Herrington, "X-ray computed microtomography of internal damage in fiber reinforced polymer matrix composites," *Composites Sci. Technol.,* vol. 65, pp. 2071-2078, 2005.

[26] A. H. Kruesi and G. H. Hasko, "Computer controlled resin impregnation for fiber composite braiding," in *Int SAMPE Symp Exhib,* 1987, pp. 309-317.

[27] S. D. Senibi, "Application of thermal experimental study to the development of expandable mandrel RTM technique for fabrication of seamless composite tubes," in *International SAMPE Symposium and Exhibition (Proceedings),* 1998, pp. 1310-1321.

[28] Y. Nikishkov, L. Airoldi and A. Makeev, "Measurement of voids in composites by X-ray Computed Tomography," *Composites Sci. Technol.,* vol. 89, pp. 89-97, 2013.

[29] I. Kasa, "A circle fitting procedure and its error analysis," *Instrumentation and Measurement, IEEE Transactions On,* vol. 1001, pp. 8-14, 1976.

[30] W. Park and G. S. Chirikjian, "Interconversion between truncated Cartesian and polar expansions of images," *IEEE Trans. Image Process.,* vol. 16, pp. 1946-1955, Aug, 2007.

[31] J. H. Byun, "The analytical characterization of 2-D braided textile composites," *Composites Sci. Technol.,* vol. 60, pp. 705-716, 2000.

[32] H. Bale, M. Blacklock, M. R. Begley, D. B. Marshall, B. N. Cox and R. O. Ritchie, "Characterizing three-dimensional textile ceramic composites using synchrotron x-ray micro-computed-tomography," *J Am Ceram Soc,* vol. 95, pp. 392-402, 2012.

[33] P. Badel, E. V. Sallé, E. Maire and P. Boisse, "Simulation and tomography analysis of textile composite reinforcement deformation at the mesoscopic scale," *International Journal of Material Forming,* vol. 2, pp. 189-192, 2009.

[34] H. Zhu, B. Wu, D. Li, D. Zhang and Y. Chen, "Influence of Voids on the Tensile Performance of Carbon/epoxy Fabric Laminates," *Journal of Materials Science and Technology,* vol. 27, pp. 69-73, 2011.

[35] P. Potluri, A. Manan, M. Francke and R. J. Day, "Flexural and torsional behaviour of biaxial and triaxial braided composite structures," *Composite Structures,* vol. 75, pp. 377-386, 2006.

[36] L. Xu, S. J. Kim, C. -. Ong and S. K. Ha, "Prediction of material properties of biaxial and triaxial braided textile composites," *J. Composite Mater.,* vol. 46, pp. 2255-2270, 2012.

[37] D. Goyal, X. Tang, J. D. Whitcomb and A. D. Kelkar, "Effect of various parameters on effective engineering properties of 2 × 2 braided composites," *Mechanics of Advanced Materials and Structures,* vol. 12, pp. 113-128, 2005.

[38] P. G. Young, T. B. H. Beresford-West, S. R. L. Coward, B. Notarberardino, B. Walker and A. Abdul-Aziz, "An efficient approach to converting three-dimensional image data into highly accurate computational models," *Philosophical Transactions of the Royal Society A: Mathematical, Physical and Engineering Sciences,* vol. 366, pp. 3155-3173, 2008.

Chapter 4 Experimental Analysis of Diamond and Regular Tubular Braided Composites using Three Dimensional Digital Image Correlation

A version of this chapter has been submitted as:

Melenka G.W., Carey, J.P., Experimental Analysis of Diamond and Regular Tubular Braided Composites using Three Dimensional Digital Image Correlation, Journal of Composite Materials (2016).

4.1 Introduction

Tubular braided composites are composed of impregnated and cured interwoven yarns. Tubular braided composites are a beneficial manufacturing process over conventional composite manufacturing methods due to the high production rate, customizable stiffness and strength, and high damage tolerance due to the nature of the interwoven structure. Braids can be produced as either two dimensional (2D) or three dimensional (3D) structures. Tubular braided composites are a two dimensional braided composites produced using a Maypole or Radial braiding machine. Tubular braids can be produced in a number of braiding patterns which includes Diamond (1/1), Regular (3/3) or Hercules (3/3) patterns [1, 2]. In addition, axial fibers can be introduced during the manufacturing process to produce triaxial braided structures [1, 2].

There are several studies that have investigated the mechanical properties of flat braided composites using analytical models [3-7]. These studies have examined both flat biaxial and triaxial braided composites. As well, there have been several studies that have examined the mechanical properties of tubular braided composites; however, these studies have been exclusively on Diamond (1/1) braid patterns [8-12].

Many studies have experimentally evaluated braided composites. Conventional mechanical testing methods have been used to evaluate the elastic properties of braided composites [3, 4, 10, 11]. Several recent studies have used an optical two dimensional digital image correlation (2D DIC) measurement method to evaluate flat braided composites [6, 7]. The 2D DIC technique allows for full field strain measurement for flat braided composites. Due to the inhomogeneous nature of braided composites and the three dimensional structure of tubular braided composites a three dimensional digital image correlation (3D DIC) measurement method is advantageous over conventional discrete measurement devices like strain gauges since strain over multiple unit cells can be measured [12-14]. Small diameter braided composites also have a high radius of curvature and therefore 2D DIC measurements cannot be used to accurately measure surface strains. The study by Leung *et al.* examined the 3D strain field for Diamond (1/1) braided composites [12]. This study examined the unit cell strain field of a Diamond braided composite using the 3D DIC measurement method.

The aim of this work is to present a methodology for assessing the strain field and evaluating the mechanical properties of braided composites, using tubular

structures as the case study. Braids will be subjected to both tension and torsion loads. The braid samples will be evaluated using a contact-free 3D DIC technique. Braids of varying braid angles (35, 45 and 55°) and varying braid type (Diamond (1/1) and Regular (2/2)) will be evaluated. Digital image correlation measurements have been performed for braided composites but a comprehensive study which examines the effect of braiding pattern and braiding angle on braid strain does not currently exist in literature. Presently, several analytical, geometrical and finite element models exist for braided composites; however, a comprehensive analysis of the effect of braiding pattern and braiding angle on braided composites local and bulk stress strain behavior has not been performed. This is the first in a two part series aimed at the investigation of the effect of braid angle and braid pattern on tubular braided composites. The methodology presented in this manuscript will be used to examine and validate a new analytical model for predicting the elastic properties of tubular braided composites.

4.2   Experimental Methods

4.2.1   Sample Preparation

Braid preforms were manufacturing using a Maypole braiding machine (Steeger HS140/36-91, Steeger GmbH and Co., Wuppertal, West Germany). Braid preforms were manufacturing with Kevlar fibers (Kevlar49, 1420 denier, Dupont, Mississauga, On). Braid preforms were manufactured in two braid patterns: Diamond (1/1) and Regular (2/2). A schematic of the two braid patterns used in this study is shown in Figure 4-1. Both braid patterns were manufactured using the maximum number of carriers of the braiding machine (36) to ensure

comparable fiber volume fractions for both braiding patterns while using the same fiber denier. The image shown in Figure 4-2 demonstrates the Diamond braid pattern produced when operating a braiding machine using the full-load configuration. Using 36 braid carriers results in 18 individual yarn bundles being produced. An equivalent braid pattern could be produced using 18 yarn carriers and doubling the denier of the yarns. A discussion on the braiding patterns produced using a 36 carrier is presented by Melenka *et al. [2]*. Braid samples were manufactured with a range of braid angles: 35, 45 and 55 degrees to demonstrate the effect of braid angle on strain field and mechanical properties. Four samples of each braid type and braid angle were manufactured for this study resulting in a total of 24 samples tested. This study is a subset of a larger study where a total of 144 braid samples were produced. A small subset of the braid samples were selected to fully detail the methods used in order to experimentally evaluate tubular braided composites.

Diamond (1/1)   Regular (2/2)
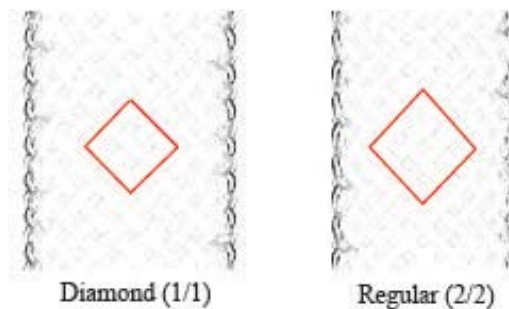
Figure 4-1: Example braid patterns: Diamond (1/1), Regular (2/2). Open mesh braids (low cover factor) are displayed to emphasize the difference in braiding patterns**.**
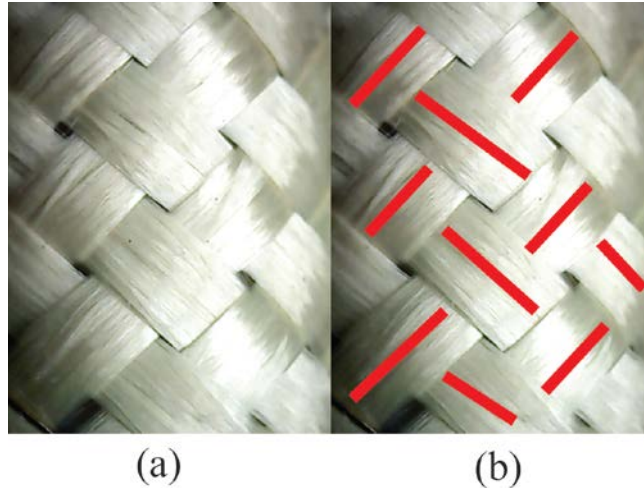
Figure 4-2: Full load Diamond braid pattern with individual yarns identified. Yarns used for this braid were 1420 denier. (a) Resulting diamond braid geometry. (b) Braid geometry identifying the individual braid yarns. Using a braiding machine with a full load of 36 carriers to produce a Diamond pattern results in a braid with 18 cross-over points around the braid circumference.

The braid preforms were impregnated with a resin (EPON 825, Momentive Specialty Chemicals Inc., Columbus, OH) and hardener (Ancamine 1482, Air Products and Chemicals, Allentown, PA). The resin and hardener was mixed at a ratio of 100:19. The braid performs were placed over an 11.1mm (7/16") polytetrafluoroethylene (PTFE) mandrel and then impregnated using a hand lay-up process with the mixed resin and hardener. The braid samples were cured in an oven at 110°C for 2 hours. The sample curing procedure has been used in several previous studies [9, 12-14] producing high quality composites. After curing, all braid samples were cut to a final length of 177.8mm (7"). Images of the manufactured braid samples are shown in Figure 4-3. In this figure the effect of braid pattern and braid angle on the braid geometry can be seen.

97
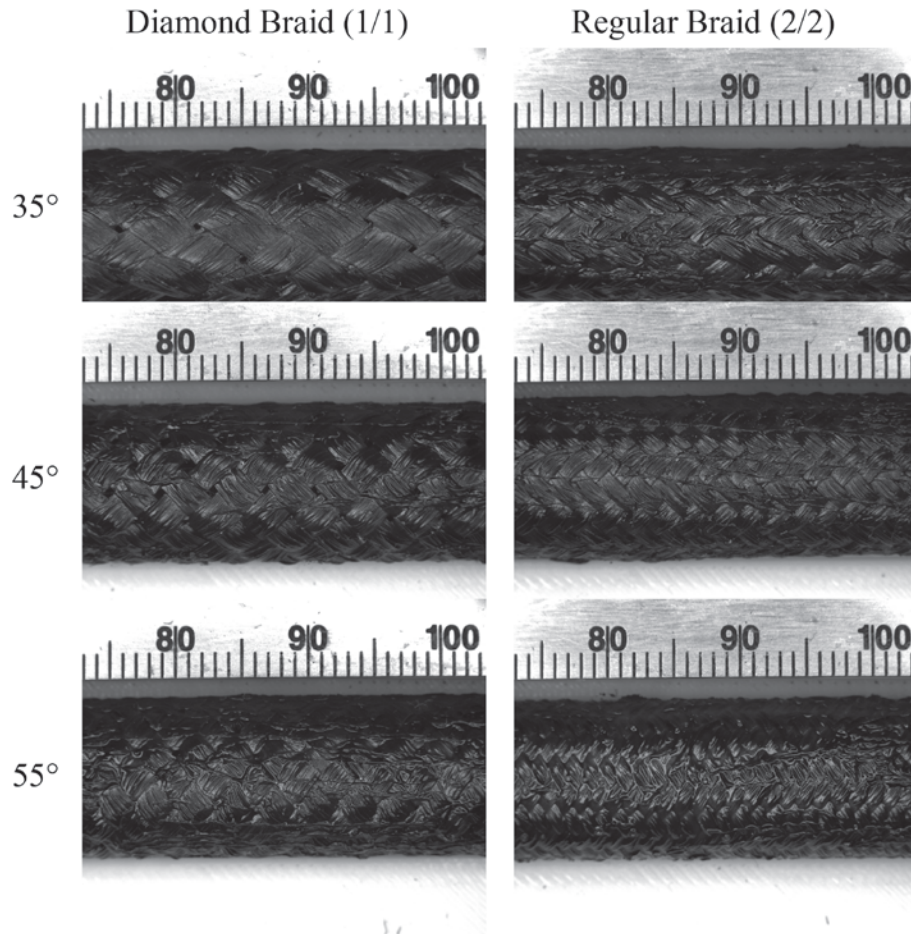
Figure 4-3: Example braid samples demonstrating the effect of braid angle and braid pattern on geometry.

4.2.1.1 Braid Geometry Measurement

The external diameter of the cured braid samples was measured using a micrometer (0-25 ±0.01mm Mitutoyo 102-0701, Kawasaki, Japan). The internal diameter of the braid samples was measured using a telescoping gauge (8-12.7mm Telescoping Gauge, TESA USA, North Kingstown, RI) and the aforementioned micrometer. Ten measurements along the sample length were taken for both the internal and external diameter measurements. The overall length of each braid sample was measured using calipers (D4105- 8" digital calipers, Woodstock Inc., Bellingham, WA).

The braid angle and yarn width of each braid sample was measured optically by acquiring images of the braid samples using a machine vision camera (Basler Pilot piA2400-17gm, Basler AG, Ahrensburg, Germany) equipped with a 35mm lens (NVM-35, Navitar, Rochester, NY) and 10mm extension tube (CML10, Thor Labs, Newton, NJ). The braid angle and yarn width was then measured using image processing software (ImageJ, National Institutes of Health, Bethesda, Maryland). A representative image of a braid sample used to measure braid angle and yarn width is shown in Figure 4-4. Ten measurements for braid angle and yarn width were recorded for each braid sample.
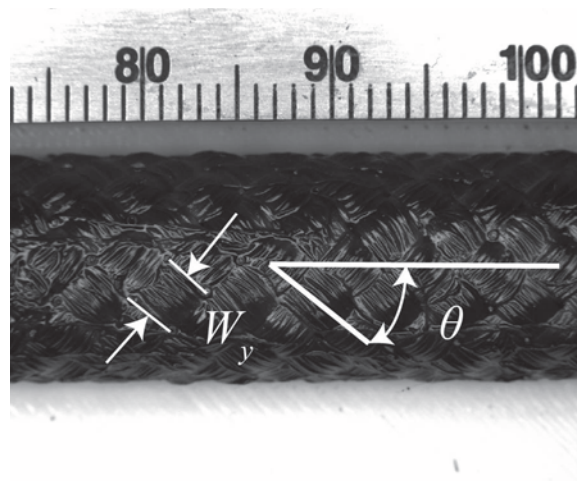
Figure 4-4: Representative image of a braid sample used to measure yarn width and braid angle.

4.2.2 Sample Mechanical Testing

Mechanical tests were performed in order to evaluate the effect of braid angle and braid pattern on the longitudinal elastic modulus and shear modulus of the tubular braided composite samples. For both experimental setups sample strain was measured using a 3D DIC measurement technique. Images of the braid samples

were collected with a pair of high resolution cameras (AVT GT3400, Allied Vision Technologies, Stadtroda, Germany). The cameras were each equipped with 35mm camera lenses (LM35SC, Kowa Optical Projects Co., Tokyo, Japan) and extension tubes (CML5, Thor Labs, Newton, NJ). The imaging equipment used in this study was selected to provide a field of view of approximately 39.3 x 29.4mm. This field of view was selected to allow for the visualization of multiple braid unit cells along the length of the braid samples. Image acquisition and data collection was performed using a custom data acquisition program (MATLAB 2016a, The MathWorks Inc., Natick, MA). Images of the braid samples were recorded at a rate of 0.5 hZ. Load cell and image acquisition data was synchronized using custom data acquisition program.

4.2.2.1 Sample Preparation

End tabs were bonded to the braid samples to allow for tensile and torsional loads to be applied to the braid sample. The end tabs were bonded to the braid samples using a high strength two part epoxy (Loctite E-20HP; Hysol, Henkel, Rocky Hill, Co.). Prior to testing, the surface of the braid samples was prepared to improve the contrast in the samples images for displacement measurement using the 3D DIC measurement method [12-14]. The braid samples are first painted black (Painter's Touch Flat Black, Rust-Oleum Corp, Concord, On). After painting the braid surface black a white speckle pattern, using a mixture of white paint (5212 Opaque White, Createx Airbrush Colors, Createx Colors, East Granby CT) and reducer (4012 High Performance Reducer, Createx), was applied to the braids using an airbrush (Custom Micron B, Iwata Medea Inc., Portland, OR). An

example of a braid sample with applied speckle pattern is shown in Figure 4-5. The high contrast speckle pattern shown in Figure 4-5 is required for the 3D DIC strain measurement algorithm [15].
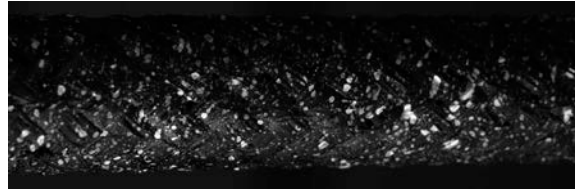
Figure 4-5: Example image of a braid sample with speckle pattern applied to the braid surface.

4.2.2.2   Tension Testing Apparatus

Tensile loads were applied to the braid samples using a universal testing machine (MTS, Eden Prairie, MN, USA). Data from the test frame was recorded using a data acquisition system (NI-USB 6211 DAQ, National Instruments, Austin, TX). Tensile loads applied to the tubular braids were measured using a load cell (44 KN load cell, 661.12B, MTS, Eden Prairie, MN, USA). The load cell has four sensitivity ranges: 4.4KN, 11KN, 22KN and 44KN. The load cell was operated using the 4.4KN range. The test samples were loaded at a rate of 0.5mm/min. This load rate was chosen to ensure failure of the samples occurs within 1-10 minutes of testing as per ASTM D3039 [16]. The tensile testing apparatus is shown in Figure 4-6.
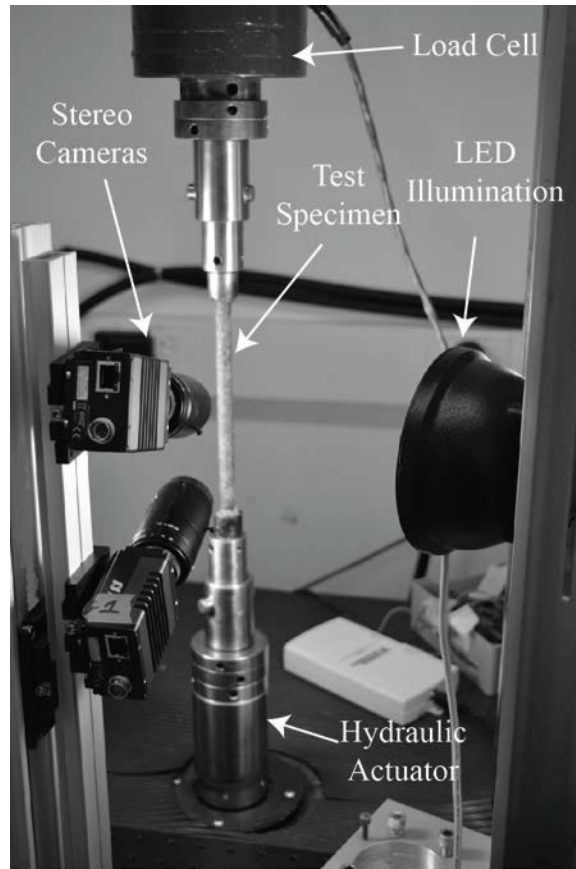
Figure 4-6: Tension testing apparatus for evaluating the tensile properties of tubular braided.

4.2.2.3 Torsion Testing Apparatus

Torsional loads was applied using a torsion testing apparatus (Torsion Master, MTS, Eden Prairie, MN, USA) equipped with a 20 Nm load cell. The 20 Nm load cell was used in this study as in a previous study it was found that sample failure occurred beyond the range of a 2 Nm torsional load cell [14].The test samples were loaded at a rate of 0.05 rad/min [9, 13]. The torsion testing apparatus is shown in Figure 4-7. Data from the torsion test frame was recorded using a data acquisition system (NI-USB 6211 DAQ, National Instruments, Austin, TX).
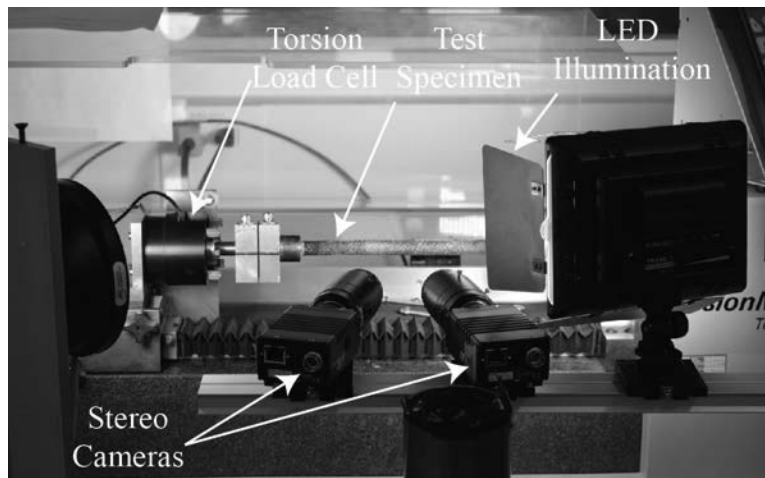
Figure 4-7: Torsion testing apparatus for evaluating the tensile properties of tubular braided

4.2.3 3D DIC Processing

Acquired images of the braid samples were processed using a commercial software package (DaVis version 8.2.0 StrainMaster 3D, LaVision GmbH, Gottingen, Germany) to measure displacement and strain of the braid samples. The stereo images collected in this study were calibrated and scaled using a custom calibration target. A schematic of the custom image calibration target is shown in Figure 4-8. Calibration of the stereo images is required to scale the images into physical units. The calibration also determines the intrinsic and extrinsic parameters for each camera [17].
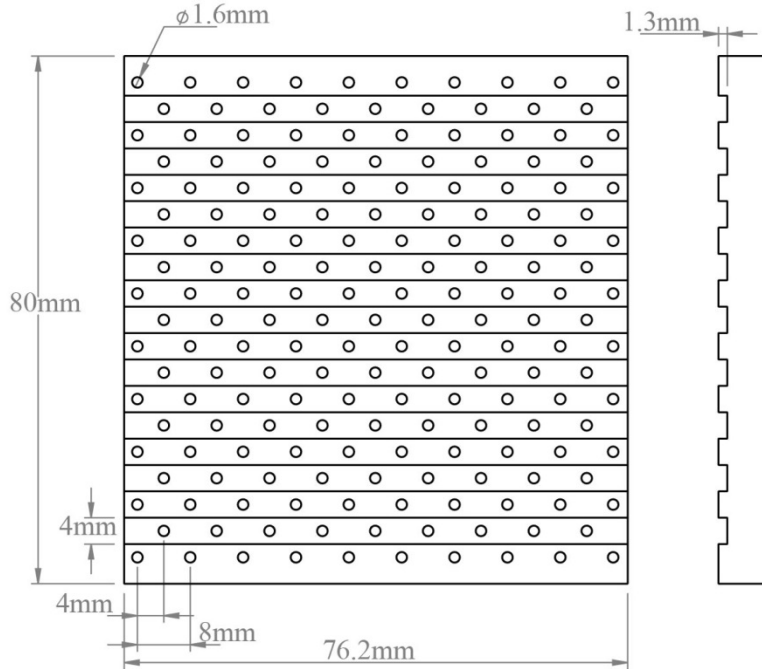
Figure 4-8: Custom 3D calibration target to calibration stereo images.

The braid images were processed by first applying a sliding average filter to each image. The sliding average filter was used to increase the contrast in the recorded sample images. The three dimensional displacement vector fields were determined using a Least Squares optical flow displacement measurement algorithm [17, 18]. The sample images were processed using a subset size of 31 pixels and a set size of 8 pixels.

4.2.4   3D DIC Post-Processing

Once the displacement vector field has been created using the DaVis software package, sample strain can be computed. The displacement vector fields were analyzed using a custom DIC post-processing script which made use of the PIVMat toolbox (PIVMat Toolbox 3.03) using MATLAB (MATLAB 2016a, MathWorks, Natick, Mass.) [19]. This toolbox was used to compute longitudinal

104

(ε_y), transverse (ε_x) and torsional strain (γ_{xy}) from the 3D displacement vector fields. In addition, the surface geometry (*x*,*y*,*z*) of the braid samples can also be examined using this toolbox. The toolbox was also used to plot and visualize the strain field results for the tested braid samples.

4.3   Results and Discussion

4.3.1   Braid Geometry Analysis

The 3D DIC measurement technique allows for measurement of three dimensional displacement and strain. In addition, this method can be used to examine the 3D geometry of a test sample. The surface height of a test specimen can be extracted from the 3D DIC dataset. Example 3D braid surfaces are shown in Figure 4-9. The undulations of the braid yarn can be seen throughout the surface of the braid sample. The braid surface shown in Figure 4-9 was visualized by exporting the braid surface height data into a VTK (Visualization Tool Kit) file format to allow the braid surface to be visualized using a scientific visualization package (ParaView 3.98.0, Kitware, Inc. Clifton Park, New York).
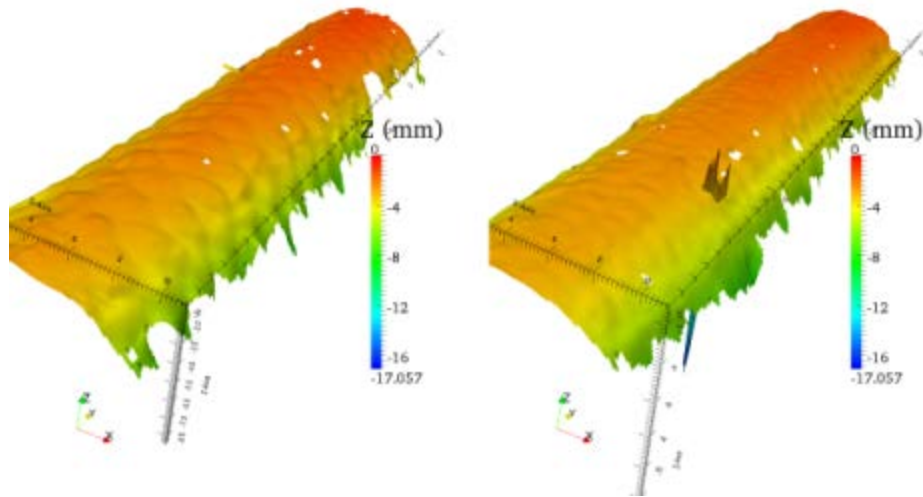
Figure 4-9: Example 3D braid surface of a Left: Diamond (1/1) and Right: Regular (2/2) with θ=55° braid extracted using a 3D DIC dataset. Discontinuities in the braid surface represent regions where poor image correlation occurred.

The surface height data, like the surfaces shown in Figure 4-9, was used to determine the diameter of each braid sample. The braid surface height was examined at five locations along the longitudinal axis of each braid sample. Example braid surface height data points are shown in Figure 4-10. The surface height points in Figure 4-10 shows the undulation of the braid surface. These plots also show that there is a taper to the braid surface height due to the position of the stereo cameras relative to the braid sample. The braid diameter was determined for each braid sample using the surface height data shown in Figure 4-10 and using a circle fitting routine [20]. The fitted braid diameter values were compared with the physical braid diameter measurements. Comparison of the physically measured braid diameters with the braid diameters determined from the 3D DIC surface height data helps to ensure that the stereo cameras used in this

study have been properly oriented and calibrated in order to accurately measure the displacement and strain of the braid samples.
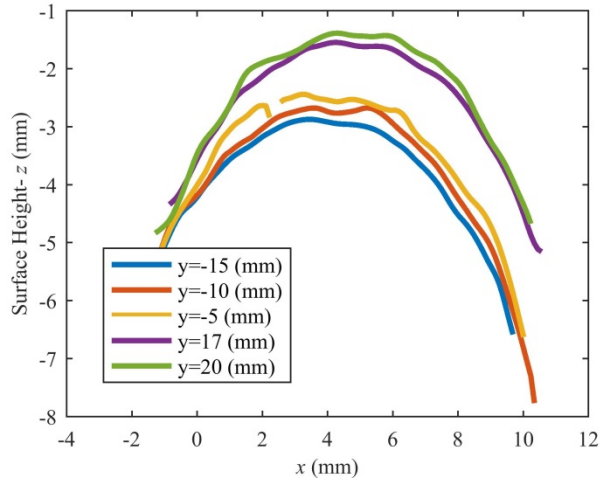
Figure 4-10: Example braid surface height at five locations along the y-axis of a braid sample. The braid surface heights will be used to estimate the diameter of the braid sample.

Comparison of the physical braid sample diameter measurements with the surface height fitted diameter is shown in Table 4-1. This table shows good agreement between the physical micrometer measurements and the fitted surface height data. The maximum difference between the measured and fitted diameters was 2.2%. This shows that the 3D DIC measurement data provides good agreement with physical measurements. The results shown in Table 4-1 demonstrate the accuracy of the 3D DIC measurement technique. The fitted diameter results have greater variation than the physical measurements. Variation in the fitted diameter measurements could be due to regions of the braid sample with poor contrast which resulted in poor image correlation. The braid surface shown in Figure 4-9

shows regions where poor image correlation occurred. Poor image correlations results in discontinuities in the braid surface.

Table 4-1: Comparison of braid sample diameters measured using physical measurements and using fitted surface height data

Sample	Measured Diameter (mm)	Measured Diameter St Dev (mm)	Fitted Diameter (mm)	Fitted Diameter St Dev (mm)	% Difference
D35_21	12.590	0.043	12.544	0.248	0.368
D35_22	12.464	0.081	12.409	0.252	0.440
D35_23	12.476	0.071	12.270	0.448	1.655
D35_24	12.494	0.061	12.502	0.217	0.065
D45_21	12.539	0.055	12.261	0.446	2.217
D45_22	12.561	0.046	12.460	0.231	0.807
D45_23	12.616	0.082	12.533	0.304	0.655
D45_24	12.515	0.048	12.426	0.102	0.712
D55_21	12.691	0.059	12.738	0.280	0.368
D55_22	12.648	0.052	12.439	0.134	1.656
D55_23	12.688	0.041	12.716	0.421	0.217
D55_24	12.623	0.081	12.635	0.512	0.093
R35_21	12.392	0.038	12.593	0.130	1.625
R35_22	12.411	0.059	12.611	0.213	1.612
R35_23	12.403	0.043	12.321	0.414	0.659
R35_24	12.250	0.070	12.431	0.217	1.474
R45_21	12.455	0.079	12.604	0.563	1.194
R45_22	12.497	0.042	12.432	0.157	0.519
R45_23	12.546	0.032	12.427	0.188	0.949
R45_24	12.360	0.076	12.601	0.333	1.953
R55_21	12.580	0.035	12.657	0.234	0.613
R55_22	12.631	0.076	12.610	0.173	0.163
R55_23	12.528	0.036	12.580	0.193	0.417
R55_24	12.703	0.047	12.683	0.229	0.155

4.3.2 Tensile Test Results

4.3.2.1 Representative Strain Images

Representative strain fields for the six braid permutations used in this study are shown in Figure 4-11. This image demonstrates the effect of braiding pattern and braid angle on the longitudinal strain field. Figure 4-11 also shows the non-uniform strain patterns that occur due to the undulations of the braid yarns. The strain fields in Figure 4-11 demonstrate that high regions of strain occur at the cross-over points between braid yarns. During testing, matrix failure occurs at the cross-over points. After matrix failure occurs, the braid sample experience necking.
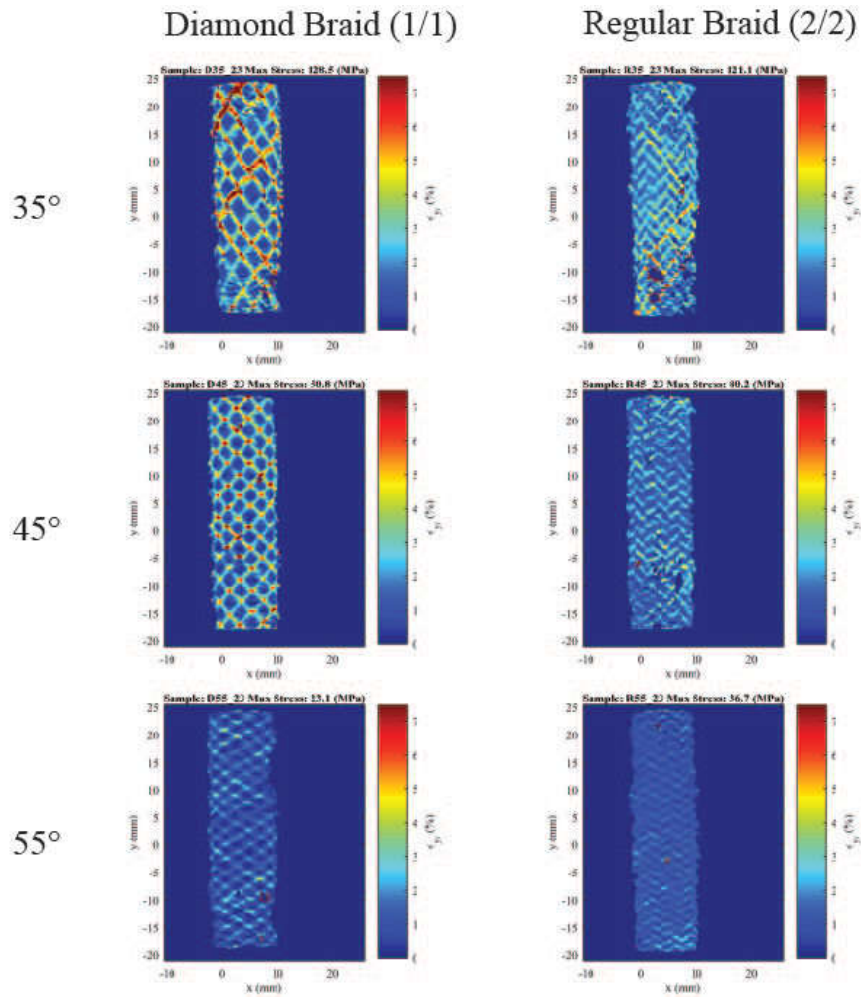
Figure 4-11: Comparison of tensile strain (ε_{yy}) for braided composites of different braiding patterns and braiding angles. Two braid patterns are shown: Diamond (1/1) and Regular (2/2). Three braid angles were investigated: 35, 45 and 55°. The strain field at the maximum stress is reported for each braid sample.

Similarly, the measured transverse strain, ε_{xx}, for the six braid patterns examined in this study is shown in Figure 4-12. This figure shows the contraction of the braid sample diameter due to the applied tensile load.
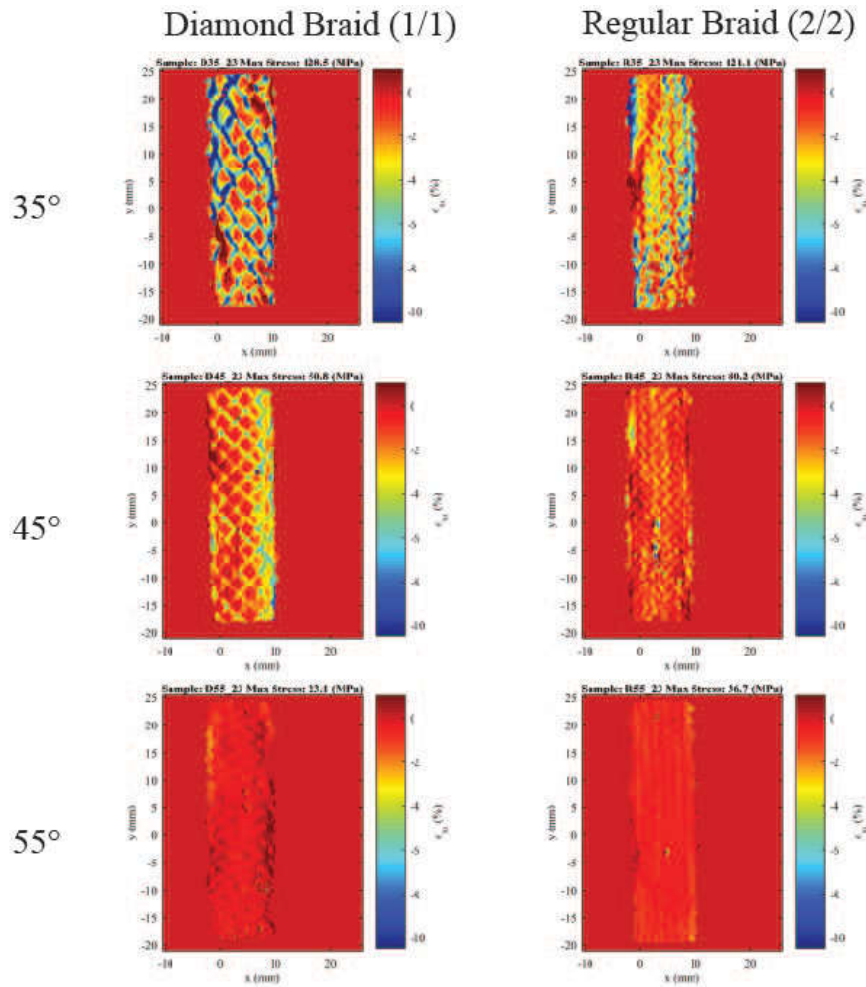
Figure 4-12: Comparison of transverse strain (ε_{xx}) for braided composites of different braiding patterns and braiding angles. Two braid patterns are shown: Diamond (1/1) and Regular (2/2). Three braid angles were investigated: 35, 45 and 55°. The strain field at maximum stress for each sample is reported.

To illustrate the non-uniform strain behavior of the braid samples the strain along the longitudinal axis of the braid samples was plotted. The strain pattern along the longitudinal axis of the Diamond braid samples is shown in Figure 4-13. The vertical line in each of the strain fields in Figure 4-13 (a) indicates the location where the braid strain field was plotted in Figure 4-13 (b). Similarly the variation in strain along the longitudinal axis of the Regular braid samples is shown in Figure 4-14. Figure 4-13 and Figure 4-14 demonstrate the variation in strain

111

along the longitudinal axis of the braid samples. As well, the period of the strain

pattern corresponds to the period of the braid yarns.
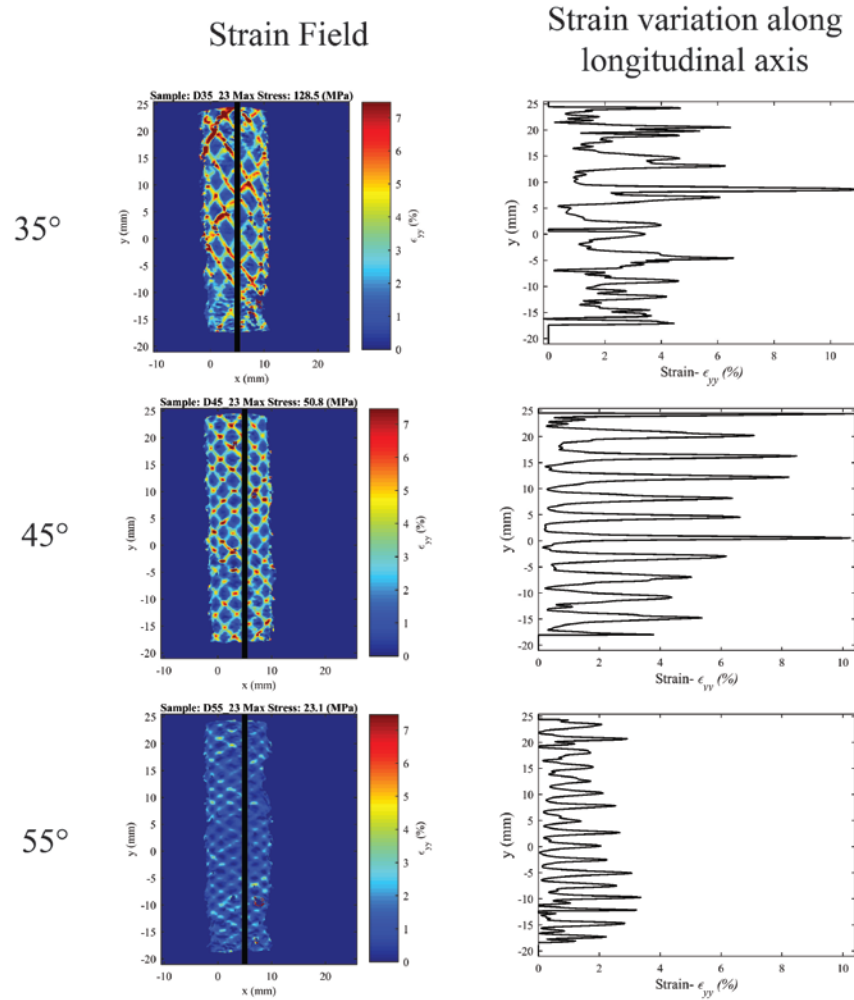
Figure 4-13: Strain pattern variation for Diamond Braids (1/1) along sample length (Left) Braid strain field (Right). Varying strain pattern along the sample longitudinal axis.
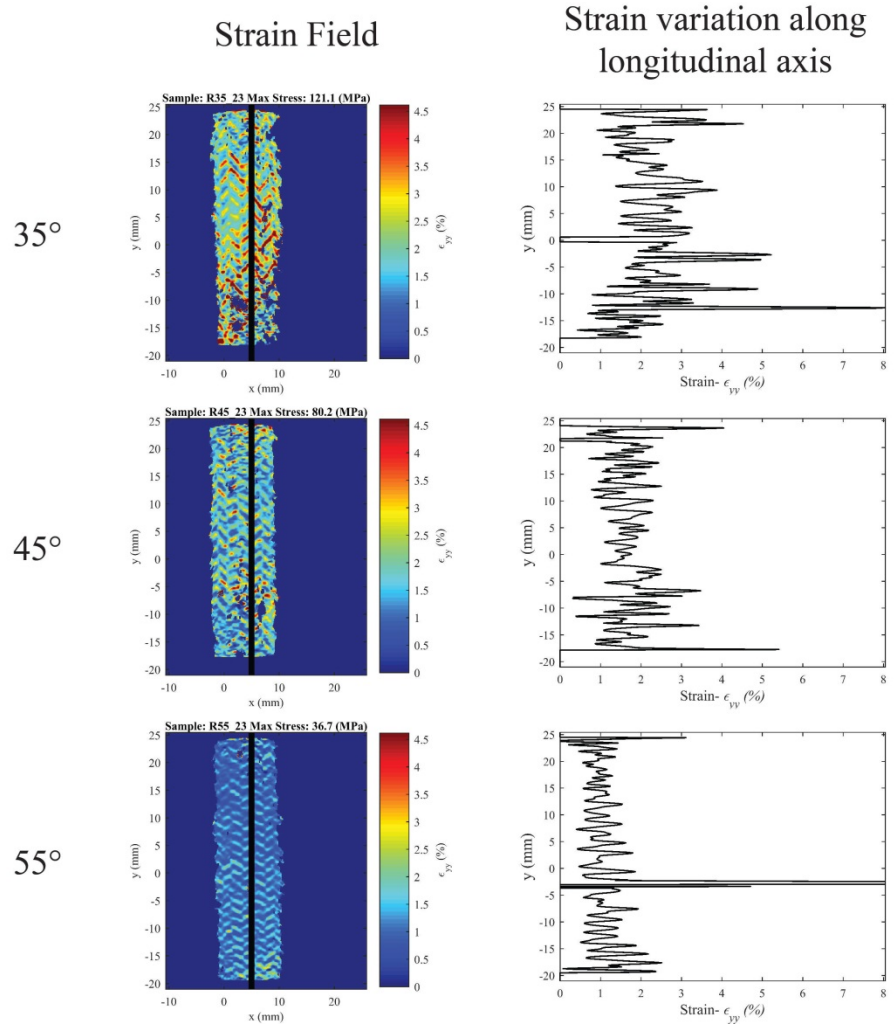
Figure 4-14: Strain pattern variation for Regular Braids (2/2) along sample length (a) Braid strain field (b). Varying strain pattern along the sample length.

The strain fields shown in Figure 4-13 and Figure 4-14 show the variation of strain throughout each braid sample. These figures demonstrate the effect of braiding pattern and braiding angle on the strain fields of tubular braided composites.

4.3.3   Stress-Strain Plots

To determine the effective stress-strain behavior of the braid samples an average

strain was computed in order to determine the bulk strain behavior of the tubular

braided composite samples. The bulk strain of the braid samples will be used to

determine the elastic modulus of the test samples. A rectangular region, 10mm

wide by 20mm long, was utilized to determine the average strain for each of the

braid samples. An example of the average strain region used in this study is

shown in Figure 4-15. This region was selected to ensure that the braid tensile

strain field was averaged over multiple braid unit cells. The strain fields in Figure

4-11 demonstrate that there is significant variation in the strain field due to the

periodic nature of the braid sample architecture. The study by Naik *et al* [21]

indicated that strain gauges smaller than the braid unit cells will cause scatter in

strain measurements results. Therefore, the average strain region shown in Figure

4-15 was used in order to measure the effective strain for each braid sample. A

similar averaging technique was performed by Kier *et al* [7] for evaluating the

effective tensile strain behavior of 2D triaxial braided composites.
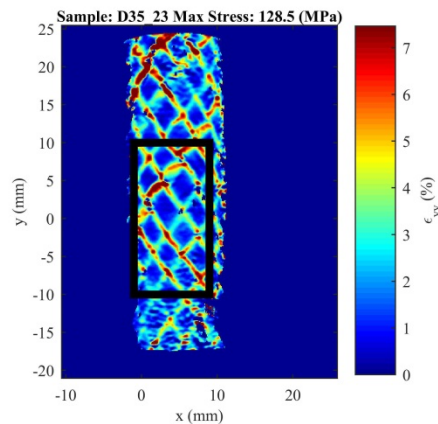
Figure 4-15: Rectangular region used to determine the average tensile strain for

each braid sample. The average tensile strain region is 10mm x 20mm.

The resulting stress-strain curves for the braid samples can be seen in Figure 4-16. This figure demonstrates the effect of braiding pattern on stress-strain behavior. For both the Diamond and Regular braids the 35° braid samples exhibit the greatest toughness and fail at higher stresses than the 45 and 55° braid samples. The 55° braid samples exhibit the lowest failure stress and lowest toughness of the braid samples. In this study, the end tab adhesive failed for the samples D35_24, R35_23 and R35_24. The failure of the end tab adhesive can be seen in Figure 4-16 as there is a sharp drop in the stress-strain curve for these samples. The linear region of the stress-strain curve for these samples was still captured therefore; the longitudinal elastic modulus can still be determined.
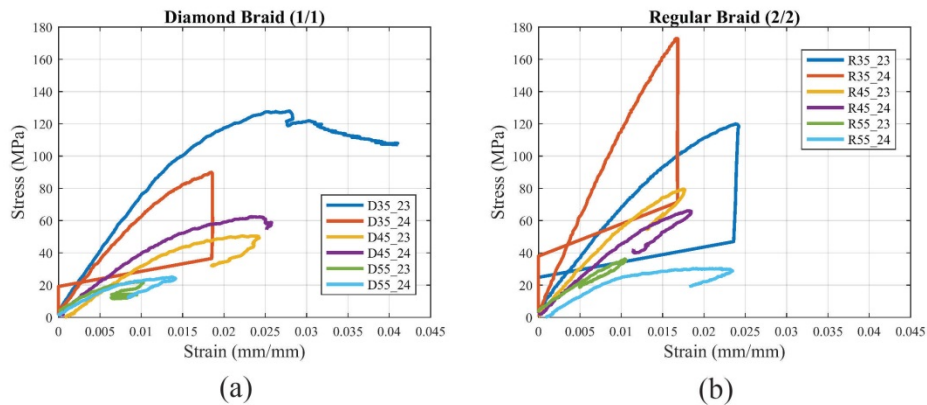
Figure 4-16: Stress-strain curves for braid samples (a) Diamond braid stress-strain curves (b) Regular braid stress strain curves.

The stress-strain curves for the tested braid samples up to maximum stress are shown in Figure 4-17. The linear region of the stress-strain curves shown in

Figure 4-17 will be used to determine the longitudinal elastic moduli of each of the braid samples.
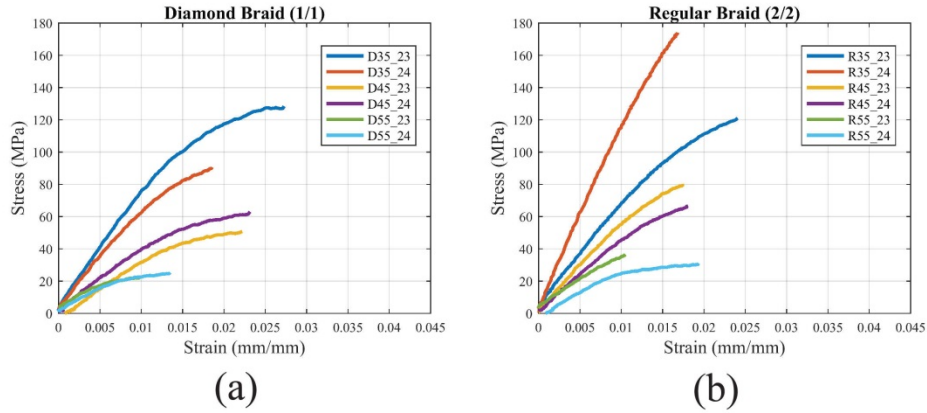
Figure 4-17: Stress-strain curves for braid samples showing the stress-strain behavior up to the maximum stress: (a) Diamond braid stress-strain curves (b) Regular braid stress strain curves.

The longitudinal elastic modulus was determined for each of the braid samples using the stress-strain curves shown in Figure 4-17. The resulting elastic moduli for both the Diamond and Regular braids are shown in Figure 4-18. This figure demonstrates the correlation between braid angle (θ) and longitudinal elastic modulus. As braid angle increases, the longitudinal elastic modulus of the braid samples decreases. This trend has been observed by many other authors of when analyzing tubular braided composites [3, 4, 7, 10, 11, 22].
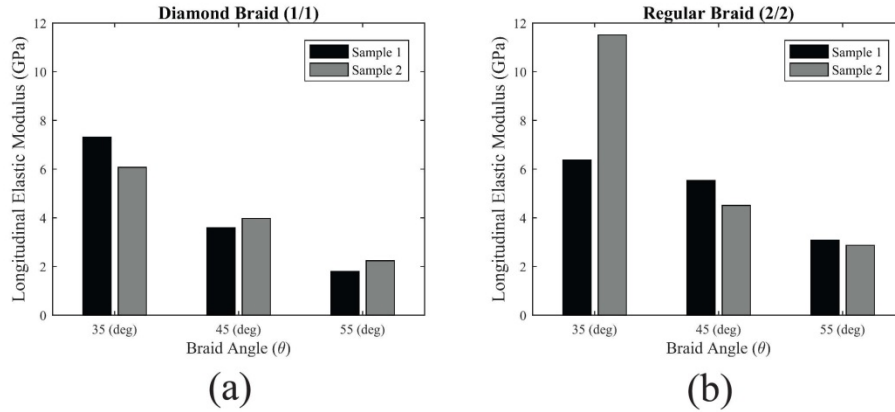
Figure 4-18: Comparison of Longitudinal Elastic Moduli for braids manufactured with 35, 45 and 55 degree braid angles (a) Diamond braid (1/1) (b) Regular braid (2/2).

Similarly, the maximum stress of each braid sample was compared. The comparison of the maximum stress for each braid sample at each braid angle can be seen in Figure 4-19. Findings show that maximum stress decreases as braid angle increases.
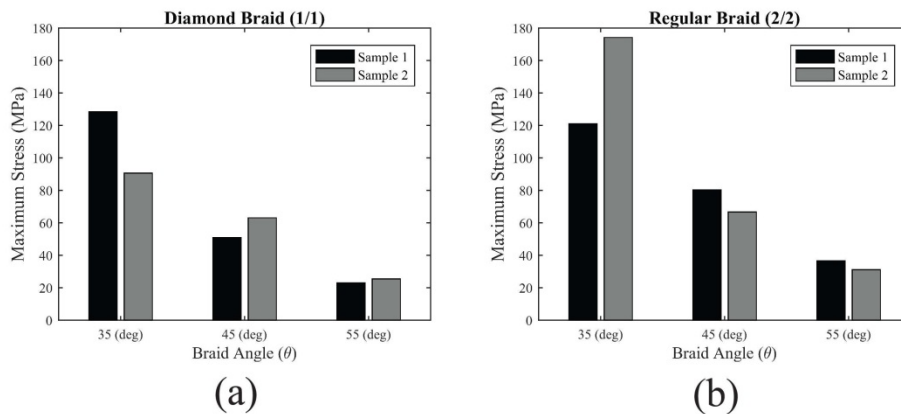
Figure 4-19: Comparison of Yield Strength for braids manufactured with 35, 45 and 55 degree braid angles (a) Diamond braid (1/1) (b) Regular braid (2/2).

There results in Figure 4-18 and Figure 4-19 demonstrate the relationship between braid angle and the effect on longitudinal elastic modulus and maximum stress.

These figures demonstrate that lower braid angles have greater longitudinal moduli and maximum stress due to the orientation of the braid fibers relative to the longitudinal axis of the braid samples. The trend shown in Figure 4-18 and Figure 4-19 is consistent with the work of several authors that have examined tubular braided composites [3, 4, 7, 10, 11, 22]. The method for determining the longitudinal elastic modulus presented in this manuscript will be utilized to validate a new model which predicts the elastic properties of both Diamond and Regular braid patterns.

4.3.4 Torsion Testing Results

4.3.4.1 Representative Shear Strain Images

Tubular braided composite samples were also subjected to torsional loads. Shear strain, γ_{xy}, was computed from the displacement vector field using the equation:

$$\gamma_{xy} = \frac{\partial u_y}{\partial x} + \frac{\partial u_x}{\partial y} \tag{4-1}$$

Where u represents the displacement vector field measured using the 3D DIC measurement technique. The braid strain figures for the six sample configurations shown in Figure 4-20 demonstrate the effect of braiding pattern and braid angle (θ) on the shear strain field. Figure 4-20 also shows the non-uniform strain patterns that occur due to the undulations of the braid yarns.
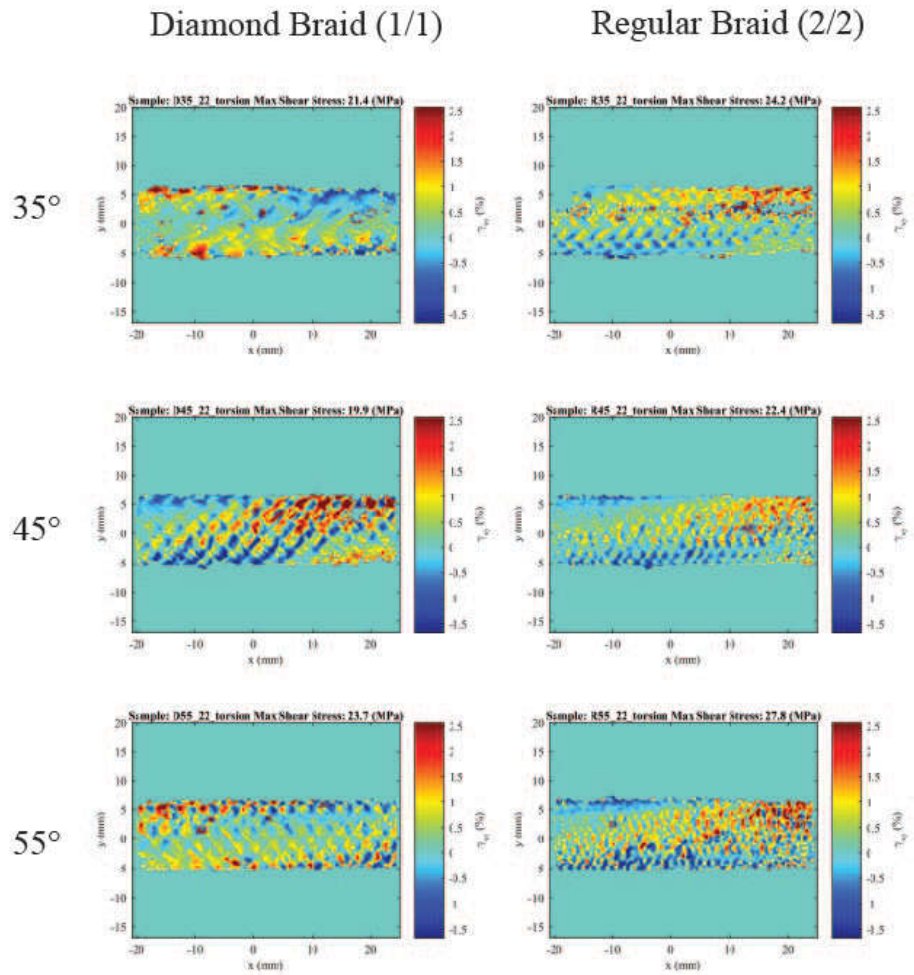
Figure 4-20: Comparison of shear strain for braided composites of different braiding patterns and braiding angles. Two braid patterns are shown: Diamond (1/1) and Regular (2/2). Three braid angles were investigated: 35, 45 and 55°.

The non-uniform shear strain behavior of the braid samples along the rotational axis of the tubular braid samples was plotted in Figure 4-21 and Figure 4-22 for Diamond and Regular braided samples, respectively. The figures demonstrate the variation in strain along the rotational axis of the braid samples. As well, the period of the strain pattern corresponds to the period of the braid yarns. The shear strain patterns shown in both figures also demonstrate the variation in shear strain along the length of the braid samples. Higher shear strain occurs on the right

119

hand size of the braid samples (x>0mm) as the torsional load was applied to this side of the braid samples.
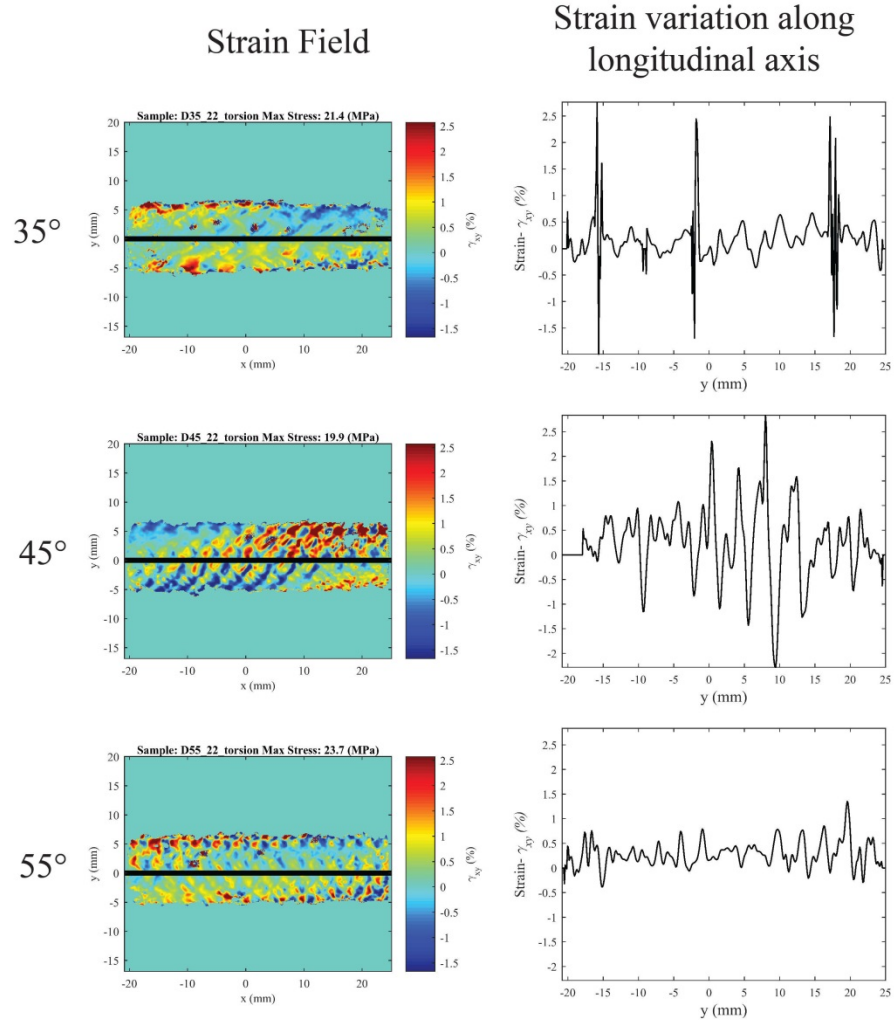
Figure 4-21: Shear strain pattern variation for Diamond Braids (1/1) along sample length (a) Braid strain field (b) Varying strain pattern along the sample length.
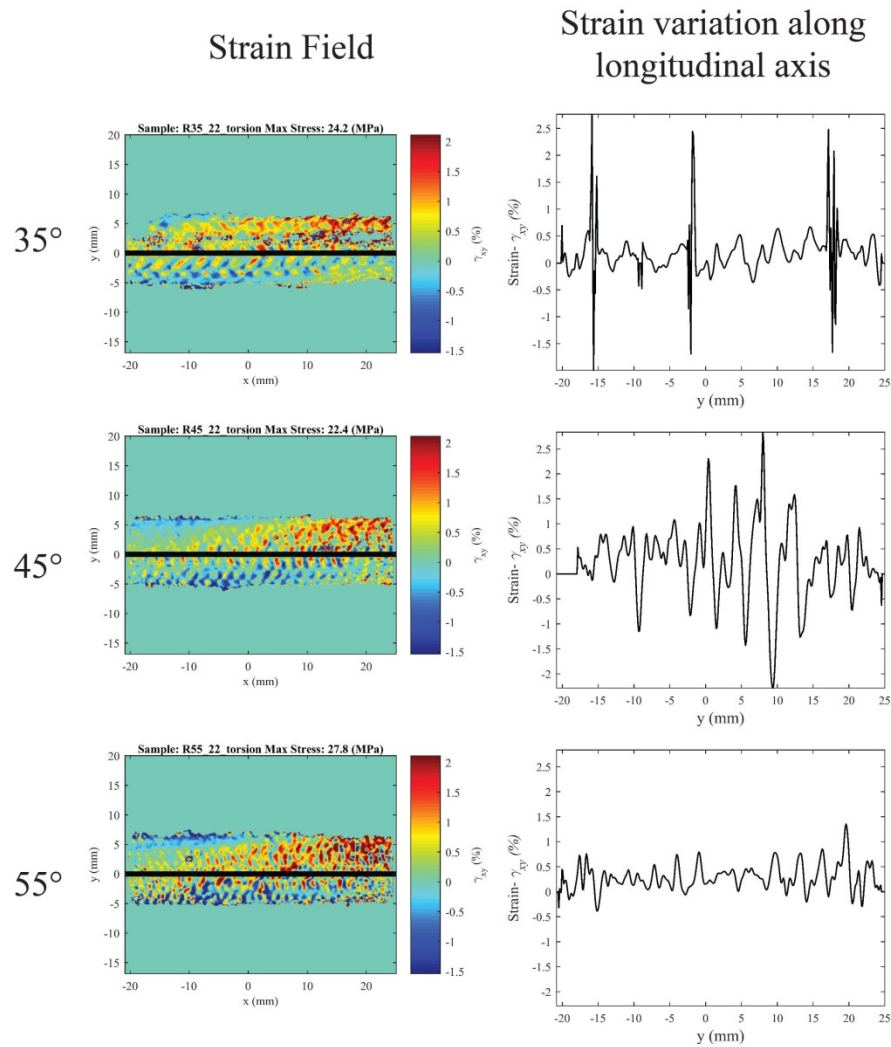
Figure 4-22: Shear strain pattern variation for Regular Braids (2/2) along sample length (Left) Braid strain field (Right) Varying strain pattern along the sample length.

4.3.4.2 Shear Stress-Shear Strain Plots

To examine the effective mechanical properties of the tubular braided composite samples due to an applied torsional load a rectangular region was selected to measure the average shear strain for each sample. A rectangular region that measured 20mm by 10mm was selected to determine the average shear strain for each braid sample. The average strain region is shown in Figure 4-23. A similar

averaging technique was performed by Kier *et al.* for evaluating the effective

shear strain behavior of 2D triaxial braided composites [7].
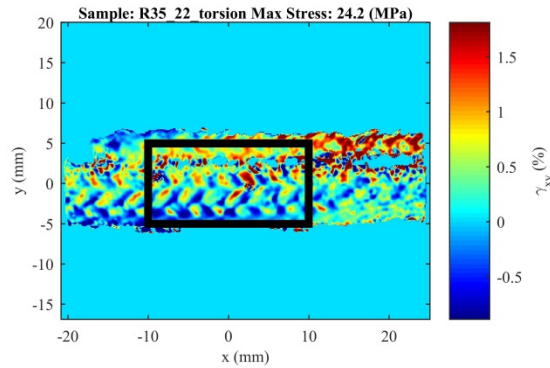
Figure 4-23: Rectangular region used to determine the average shear strain for each braid sample. The average shear strain region is 20mm x 10mm.

The shear stress-strain curves for the tubular braided composite samples are shown in Figure 4-24. This figure shows that for each sample a linear region exists up to maximum shear stress. After the maximum shear stress is reached there is a progressive decrease in the shear stress-shear strain behavior. After maximum shear stress is reached, torsional buckling of the braid samples occurs. Example images of the braid samples where torsional buckling has occurred are shown in Figure 4-25.
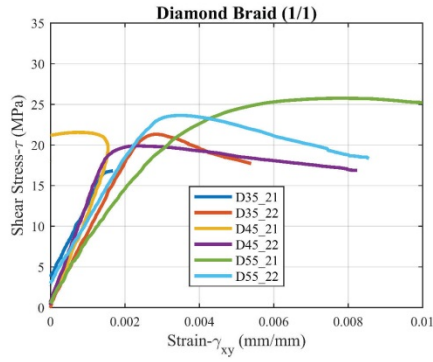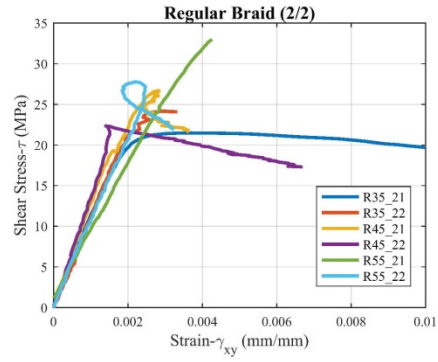
Figure 4-24: Shear stress versus shear strain curves for braid samples (a) Diamond braid stress-strain curves (b) Regular braid stress strain curves.
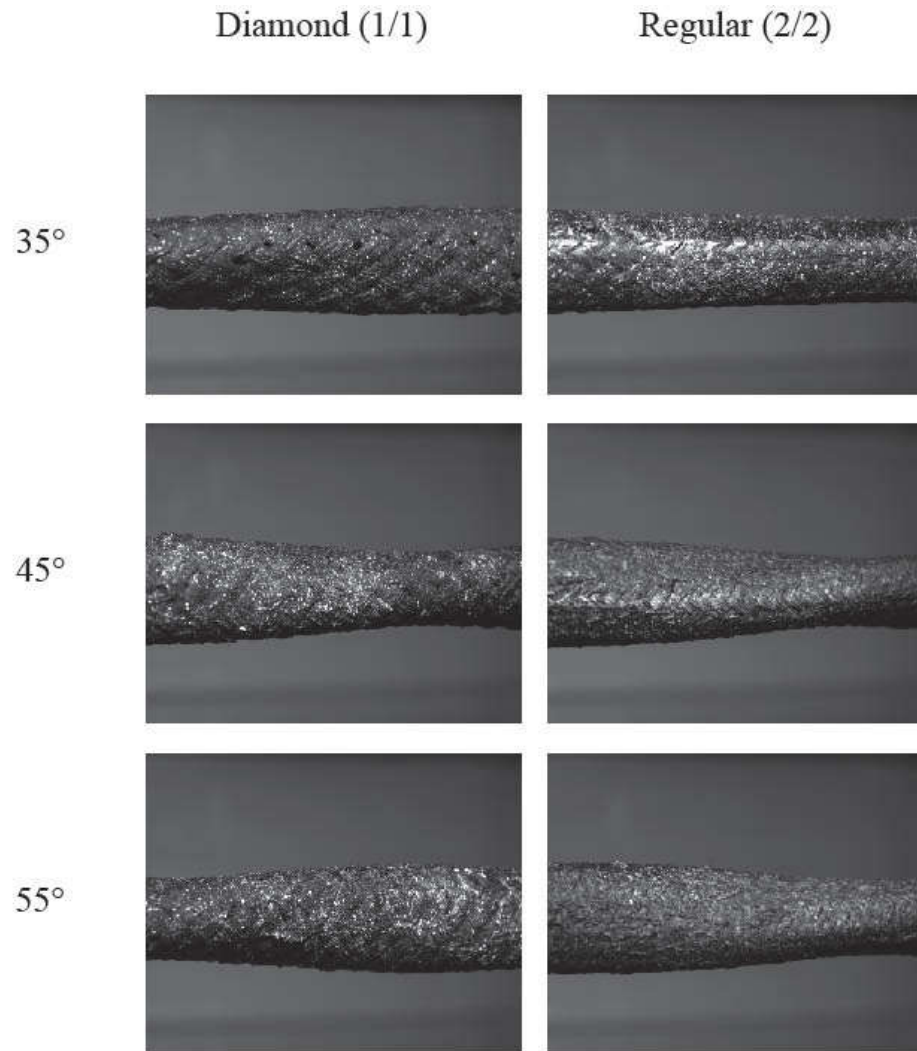
Figure 4-25: Torsional Buckling of Braid Samples (a) Diamond 35 (b) Regular 35 (c) Diamond 45 (d) Regular 45 (e) Diamond 55 (f) Regular 55).

The shear stress versus shear strain curves for the tubular braided composite samples up to maximum shear stress are shown in Figure 4-26. The linear portion of the shear stress versus shear strain curves shown in this figure will be used to determine the shear modulus (G_{xy}) for each of the braid samples. Shear modulus for each of the braid samples was determined using the relation [23]:

$$\tau = G_{xy}\gamma_{xy} \qquad\qquad 4\text{-}2$$
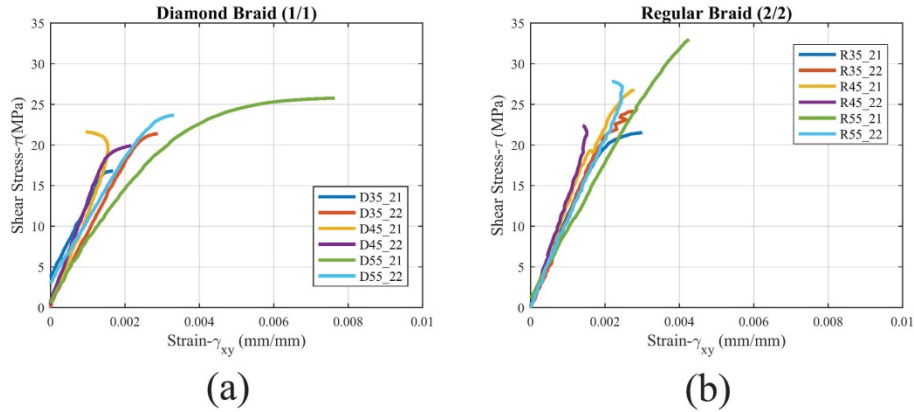
Figure 4-26: Shear stress versus shear strain curves for braid samples (a) Diamond braid stress-strain curves (b) Regular braid stress strain curves.

The resulting shear moduli for each braid sample are shown in Figure 4-27. The resulting shear moduli shown in Figure 4-27 do not show a distinct relationship between braid angles and shear modulus like the trend seen for longitudinal elastic moduli as shown in Figure 4-18.
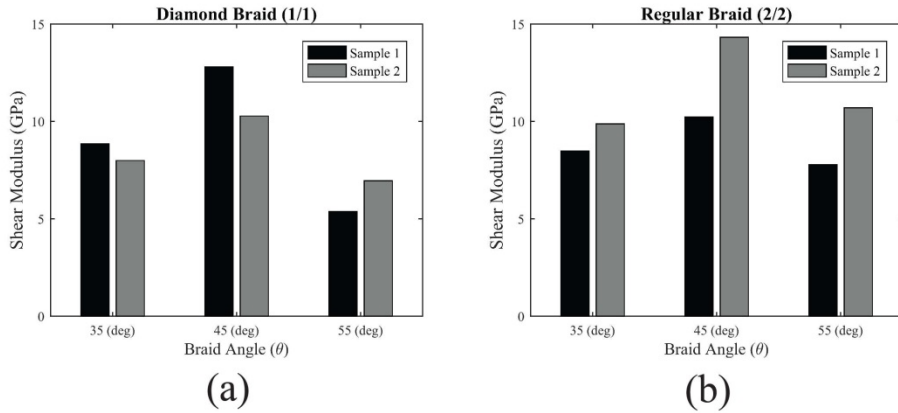
Figure 4-27: Comparison of Shear Moduli for braids manufactured with 35, 45 and 55 degree braid angles (a) Diamond braid (1/1) (b) Regular braid (2/2).

Similarly, the maximum shear stress for each braid sample is compared in Figure 4-28.
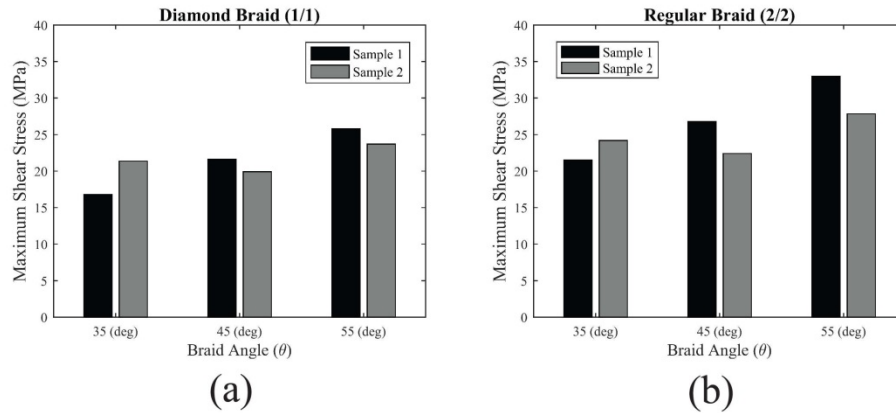
Figure 4-28: Comparison of Maximum Shear Stress for braids manufactured with 35, 45 and 55 degree braid angles (a) Diamond braid (1/1) (b) Regular braid (2/2).

4.3.4.3 *Analysis of Braided Composite Shear Behavior*

The shear modulus of the braid samples was also calculated using Equation (4-3). The shear modulus of each braid sample was determined using the torsion (T) versus angular rotation (θ) datasets recorded using the MTS TorsionMaster test frame. The resulting shear moduli for the braid samples determined using Equation (4-3) are shown in Figure 4-29. Figure 4-27 and Figure 4-29 demonstrate that significant differences exist between the experimentally determined shear moduli of the tubular braid samples when using Equations (4-2) and (4-3). The studies by Ayranci *et al.* [8, 9] found significant differences between experiments and model predictions for the shear modulus of tubular braided composite samples. When examining closed mesh braided composites experiments different from model predictions by 10.6, 2.67 and 1.46% for braids manufactured with 10.6, 8.5 and 7.0mm braid diameters [9]. For open mesh braids the model results of Ayranci *et al* differed from experiments by 27% [8].

For the difference between experimentally determined and theoretical shear modulus found by Ayranci *et al.* could be due to the fact that Equation (4-3) was used to determine the shear modulus of the braid samples. Shear modulus, *G*, is determined by measuring the angular deflection, *θ*, and torsion, *T*, applied to a cylindrical structure. As well, the polar moment of inertia, *J*, and length, *L*, of sample is required in order to determine shear modulus. This study is focused on using a 3D DIC method in order to experimentally determine the shear modulus of tubular braided composites; therefore the Shear Stress-Shear Strain (Equation (4-2)) was used to determine shear modulus. Equation (4-3) may under predict shear modulus as the braid samples tested in this study are not homogeneous or isotropic as well the geometry of the braid samples varies due to the undulation of the braid yarns [24].

$$\theta = \frac{TL}{JG} \qquad\qquad 4\text{-}3$$
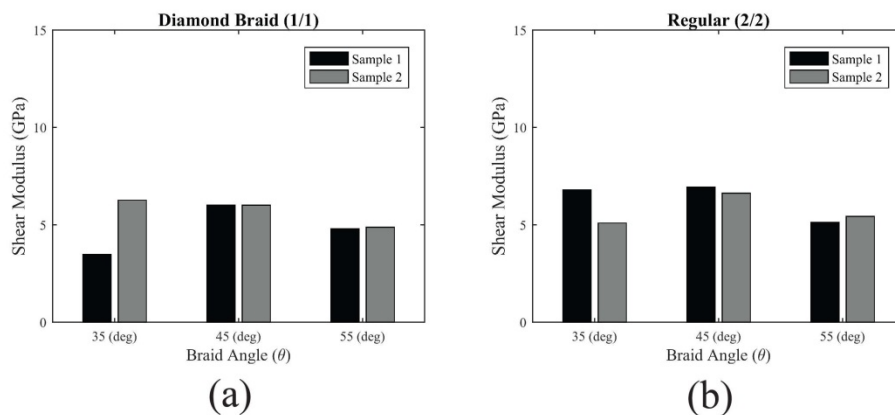
Figure 4-29: Comparison of Shear Moduli for braids manufactured with 35, 45 and 55 degree braid angles (a) Diamond braid (1/1) (b) Regular braid (2/2). Shear modulus was computed using the mechanics of materials equation for angular deflection due to a torsional load.

4.4　Conclusions

Tubular braided composites were manufactured in both a Diamond and Regular braid configuration. Braid samples were also manufactured using three different braiding angles (35, 45 and 55°). The different braiding patterns and braid angles were evaluated using an optical 3D DIC measurement technique. Braid samples were evaluated using both tensile and torsional loads. The results of this study demonstrate the effect of braiding pattern and braid angle on the strain pattern for both applied tensile and torsional applied loads. Several studies have utilized DIC measurements in order to evaluated braided composites. This study examines the effects of braiding pattern and braid angle on the strain field that develops for each of the different braiding configurations. Each of the braid configurations were evaluated for different loading conditions i.e. tension and torsion. The methodology presented in this manuscript will be applied to the experimental validation of a model which predicts the elastic properties of both Diamond and Regular braided composites. An analytical model for predicting the mechanical properites of Diamond and Regular braided composites is presented in Chapter 5. Braided composite samples in Chapter 5 were evaluated using the 3D DIC methodology. Experimental results obtained using the 3D DIC measurements will be used to compare with the proposed analytical model presented in Chapter 5.

4.5   References

[1] T. Alpyildiz, "3D geometrical modelling of tubular braids," *Text. Res. J.,* vol. 82, pp. 443-453, 2012.

[2] G. W. Melenka, A. J. Hunt, C. M. Pastore, F. K. Ko, M. Munro and J. P. Carey, "Manufacturing processes for braided composite materials," in *Handbook of Advances in Braided Composite Materials: Theory, Production, Testing and Applications*, J. P. Carey, Ed. Woodhead Publishing, 2016, .

[3] J. Byun, "The analytical characterization of 2-D braided textile composites," *Composites Sci. Technol.,* vol. 60, pp. 705-716, 2000.

[4] S. C. Quek, A. M. Waas, K. W. Shahwan and V. Agaram, "Analysis of 2D triaxial flat braided textile composites," *Int. J. Mech. Sci.,* vol. 45, pp. 1077-1096, 2003.

[5] M. M. Shokrieh and M. S. Mazloomi, "An analytical method for calculating stiffness of two-dimensional tri-axial braided composites," *Composite Structures,* vol. 92, pp. 2901-2905, 2010.

[6] R. F. El-Hajjar, S. S. Shams and D. J. Kehrl, "Closed form solutions for predicting the elastic behavior of quasi-isotropic triaxially braided composites," *Composite Structures,* vol. 101, pp. 1-8, 2013.

[7] Z. T. Kier, A. Salvi, G. Theis, A. M. Waas and K. Shahwan, "Estimating mechanical properties of 2D triaxially braided textile composites based on microstructure properties," *Composites Part B: Engineering,* vol. 68, pp. 288-299, 2014.

[8] C. Ayranci, D. Romanyk and J. P. Carey, "Elastic properties of large-open-mesh 2D braided composites: Model predictions and initial experimental findings," *Polymer Composites,* vol. 31, pp. 2017-2024, 2010.

[9] C. Ayranci and J. P. Carey, "Effect of diameter in predicting the elastic properties of 2D braided tubular composites," *J. Composite Mater.,* vol. 44, pp. 2031-2044, 2010.

[10] C. Ayranci and J. P. Carey, "Predicting the longitudinal elastic modulus of braided tubular composites using a curved unit-cell geometry," *Composites Part B: Engineering,* vol. 41, pp. 229-235, 2010.

[11] J. Carey, A. Fahim and M. Munro, "Predicting elastic constants of 2D-braided fiber rigid and elastomeric–polymeric matrix composites," *J Reinf Plast Compos,* vol. 23, pp. 1845-1857, 2004.

[12] C. K. Leung, G. W. Melenka, D. S. Nobes and J. P. Carey, "The effect on elastic modulus of rigid-matrix tubular composite braid radius and braid angle change under tensile loading," *Composite Structures,* vol. 100, pp. 135-143, 2013.

[13] G. Melenka, D. Nobes and J. Carey, "3D DIC measurement of tubular braided composites," in *ICCM 19,* Montreal, 2013, .

[14] G. W. Melenka, S. Hoxha, D. S. Nobes and J. P. Carey, "Analytical and experimental analysis of tubular braided composites," in *CANCOM 2015- Canadian International Conference on Composite Materials,* Edmonton, Alberta, Canada, 2015, .

[15] M. A. Sutton, J. J. Orteu and H. W. Schreier, *Image Correlation for Shape, Motion and Deformation Measurements : Basic Concepts, Theory and Applications.* New York, N.Y: Springer, 2009.

[16] ASTM D3039 / D3039M-14, "Standard Test Method for Tensile Properties of Polymer Matrix Composite Materials," 2014.

[17] LaVision GmbH, "Product-Manual for DaVis 8.2.0 StrainMaster Item-Number(s): 1003017," 2014.

[18] D. Fleet and Y. Weiss, "Optical flow estimation," in *Handbook of Mathematical Models in Computer Vision*Anonymous Springer, 2006, pp. 237-257.

[19] F. Moisy. PIVMat A PIV post-processing and data analysis toolbox for matlab. 2015. Available: http://www.fast.u-psud.fr/pivmat/.

[20] S. M. Thomas and Y. T. Chan, "A simple approach for the estimation of circular arc center and its radius," *Computer Vision, Graphics, and Image Processing,* vol. 45, pp. 362-370, 1989.

[21] R. A. Naik, P. G. Ifju and J. E. Masters, "Effect of fiber architecture parameters on deformation fields and elastic moduli of 2-D braided composites," *J. Composite Mater.,* vol. 28, pp. 656-681, 1994.

[22] G. W. Melenka and J. P. Carey, "Development of an Analytical Model for Tubular Braided Composites," *ICCM20,* 2015.

[23] R. C. Hibbler, "Mechanical properties of materials," in *Mechanics of Materials*, 6th ed., R. C. Hibbler, Ed. New York: Prentice Hall, 2004, pp. 83.

[24] R. C. Hibbler, "Torsion," in *Mechanics of Materials*, 6th ed., R. C. Hibbler, Ed. New York: Prentice Hall, 2004, .

Chapter 5   Development of Generalized Analytical Model for

Tubular Braided-Architecture Composites

A version of this chapter was submitted as:

Melenka G.W., Carey, J.P. Development of an Analytical Model for Diamond and

Regular Tubular Braided Composites

5.1   Introduction

Tubular braided composites consist of braided yarns infused by a matrix material.

Tubular braided composites are fabricated using a Maypole braider or Radial

braider and can be manufactured with different braiding patterns.   Braiding

patterns include: Diamond (1/1), Regular (2/2), Hercules (3/3) and triaxial

(Diamond or Regular with axial yarns) [1-5].   Tubular braided composites can

also be manufactured in open and closed mesh configurations [6-10].   The

different braid patterns and braid configurations allows for tubular braided

composites to be applied to a wide range of applications.

Braided composites are an attractive manufacturing method over conventional

composite laminates due to a high production rate, yarn interlacement and damage

tolerance [11].   Due to these factors the use of braided composites is increasing in

aerospace, sporting, automotive and marine industries [11-13].   Characterization

of tubular braided composites is complicated by their non-uniform nature,

variable constituents, and variable geometries.   The material properties of tubular

braided composites are commonly determined experimentally however this limits the implementation of tubular braided composite to specific applications [11].

Several models have been developed in order to predict the mechanical properties of tubular braided composites. The modeling approaches that are currently used for braided composites include: classical laminate plate theory (CLPT) based models [7, 9], finite element models (FEA) [13, 14] and volume averaging models [11, 15-17]. Many of the braid models that exist are limited to single braid configurations. For example, the CLPT based models of Carey and Ayranci are limited to only diamond braided composites and the volume averaging method of Quek *et al.* is limited to 2D triaxial braids. Several FEA studies have been performed on braided composites where varying braid configurations have been considered [13, 14], however these models are computationally intensive and require specialized training and software to implement [11]. Despite the fact that many analytical, geometrical and finite element models exist for braided composites [7, 9, 11, 13-17], a comprehensive analysis and comparison of the different possible braiding patterns has not been performed. Currently, a generalized analytical model does not exist specifically for tubular composite braids which cover the range of braiding patterns that can be produced using this method.

The model presented in this chapter was validated using data collected from tensile and torsional tests for braid samples produced with Diamond (1/1) and Regular (2/2) braid geometries. The braid samples were produced over a range of braiding angles, 35-55°, in order to investigate the effect of braiding angle on

elastic properties. A three-dimensional digital image correlation (3D DIC) measurement technique will be used in order measure braid sample strain.

The aim of this work is to develop a generalized analytical model of tubular braided composites based on the geometrical and mechanical properties of tubular composite braids. A generalized analytical model will provide a powerful tool for the design and implementation of tubular braided composites. In addition, the model will also account for the micromechanical material properties of fiber and resin used to create the braid structure. The proposed model will utilize key braid parameters to provide a powerful design tool for tubular braided composites manufacturers since braids of varying geometry, fiber and matrix can be modeled. Since the material properties of composite braids can be easily predicted using this method this will allow for more widespread implementation of tubular braided composites.

5.2   Proposed Model Development

A new generalized model is presented in this paper for describing the mechanical properties of tubular braided composites. The model will be implemented by using micromechanical models to account for matrix and fiber contributions. Geometries of the tubular braid structures will be described using braid equations similar to Alpyildiz *et al.* [18]. The braid equations allow for tubular braided composite to be represented using simple mathematical expressions which can implemented into solid modeling programs to allow for the visualization and analysis of braid geometries. Finally, a volume averaging method will be used to

133

account for the contribution of the clockwise and counter-clockwise yarns within the braid unit cell.

5.2.1   Micromechanics

In order to model the mechanical properties of tubular braided composites the mechanical properties of the braid fibers and matrix must be taken into account. The individual braid yarns are assumed to behave as a transversely isotropic material [5, 7, 9, 11, 15-17]. The compliance matrix, $[S]$, for the braid yarns in the local coordinate system (1-2-3) is shown in equation (5-1). The stiffness matrix, [C], for the braid yarns in the local coordinate system (1-2-3) can be determined by computing the inverse of the compliance matrix [S] as shown in (**5-2**). The elastic constants shown in equation (5-1) were determined using micromechanical models [19, 20]. The rule of mixtures equations were used to determine the longitudinal elastic modulus E_1 and major Poisson's ratio, v_{12}. The Halpin-Tsai equations were used to determine the transverse elastic modulus E_2 and in-plane shear modulus G_{12}. Finally, semi-empirical models were used to determine the out-of-plane shear modulus G_{23} and out-of-plane shear modulus v_{23} [9]. Since the yarns are assumed to be transversely isotropic $E_2 = E_3$ and $G_{12} = G_{13}$.

$$[S] = \begin{bmatrix} \dfrac{1}{E_1} & -\dfrac{\upsilon_{21}}{E_2} & -\dfrac{\upsilon_{31}}{E_3} & 0 & 0 & 0 \\[2mm] -\dfrac{\upsilon_{12}}{E_1} & \dfrac{1}{E_2} & -\dfrac{\upsilon_{32}}{E_3} & 0 & 0 & 0 \\[2mm] -\dfrac{\upsilon_{13}}{E_1} & -\dfrac{\upsilon_{23}}{E_2} & \dfrac{1}{E_3} & 0 & 0 & 0 \\[2mm] 0 & 0 & 0 & \dfrac{1}{G_{23}} & 0 & 0 \\[2mm] 0 & 0 & 0 & 0 & \dfrac{1}{G_{13}} & 0 \\[2mm] 0 & 0 & 0 & 0 & 0 & \dfrac{1}{G_{12}} \end{bmatrix}$$

$$(5\text{-}1)$$

$$[C] = [S]^{-1}$$

$$(5\text{-}2)$$

5.2.2 Braided Composite Geometry

The tubular braided composite geometry will be described using equations that take into account key braiding parameters such as braid angle (θ), yarn width (W_y), yarn thickness (a), mandrel diameter (D_0), and the number of braider bobbins (N). The five braiding parameters (θ, W_y, a, D_0, N) can be used to describe the geometry of tubular braids. Example braid geometries for Diamond (1/1) and Regular (2/2) braided composites are shown in Figure 5-1. The fully parametric braid geometries shown in this figure were generated using a custom Python script and a computer aided design software package (Rhinoceros 3D 5.0, Robert McNeel & Associates, Seattle, WA, USA) to visualize the three dimensional braid geometries.
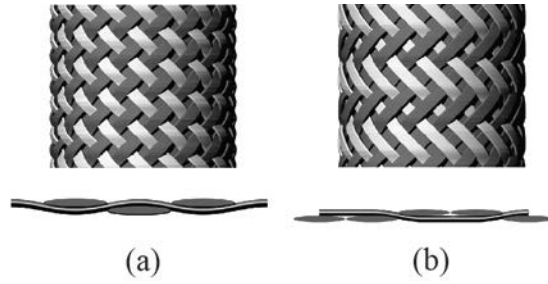
Figure 5-1: Example braided composite geometries (a) Diamond braid (1/1) (b) Regular braid (2/2)

The undulation length of braid yarns within a unit cell was determined based on the number of braider yarns (N), braid nominal radius ($r_0=D_0/2$) and braid angle (θ). The relationship between braid yarn shift angle (β) and undulation length is illustrated in Figure 5-3. The braid shift angle, β, shown in Figure 5-3 is related to half the total number of yarn carriers ($n = N/2$) used to fabricate the braid geometry. The equation shift angle equation is shown in equation (5-4).
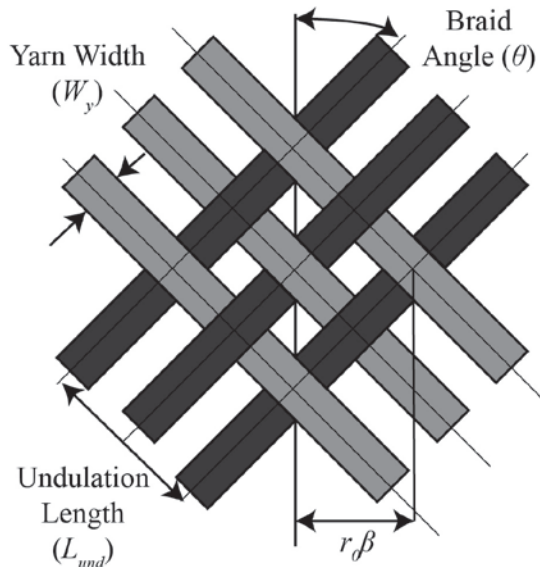
Figure 5-2: Braid unit cell geometry

$$\beta = \frac{2\pi}{n} \qquad\qquad\qquad\qquad 5\text{-}3$$

The volume fraction of fibers within a unit cell can be calculated using equation (5-4). The unit cell fiber volume fraction was derived from the unit cell fiber volume defined by Potluri *et al.* [21]. The volume fraction of fibers within the unit cell will be used to account for the contribution of yarns and matrix within the braid unit cell.

$$V_{fuc} = \frac{W_y n}{8 \cdot r_0 \cos\theta} \qquad\qquad\qquad 5\text{-}4$$

In order to model the mechanical behavior of braided composites two coordinate system transformations are required. These coordinate system transformations are computed using geometric parameters of the composite braids. The coordinate system transformation in Figure 5-4 (a) is required in order to account for the undulation of the braid yarns and depends on the crimp angle (ϕ) of the braid yarns. The coordinate system transformation in Figure 5-4 (b) accounts for the braid angle (θ) of the clock-wise and counter-clockwise yarns.
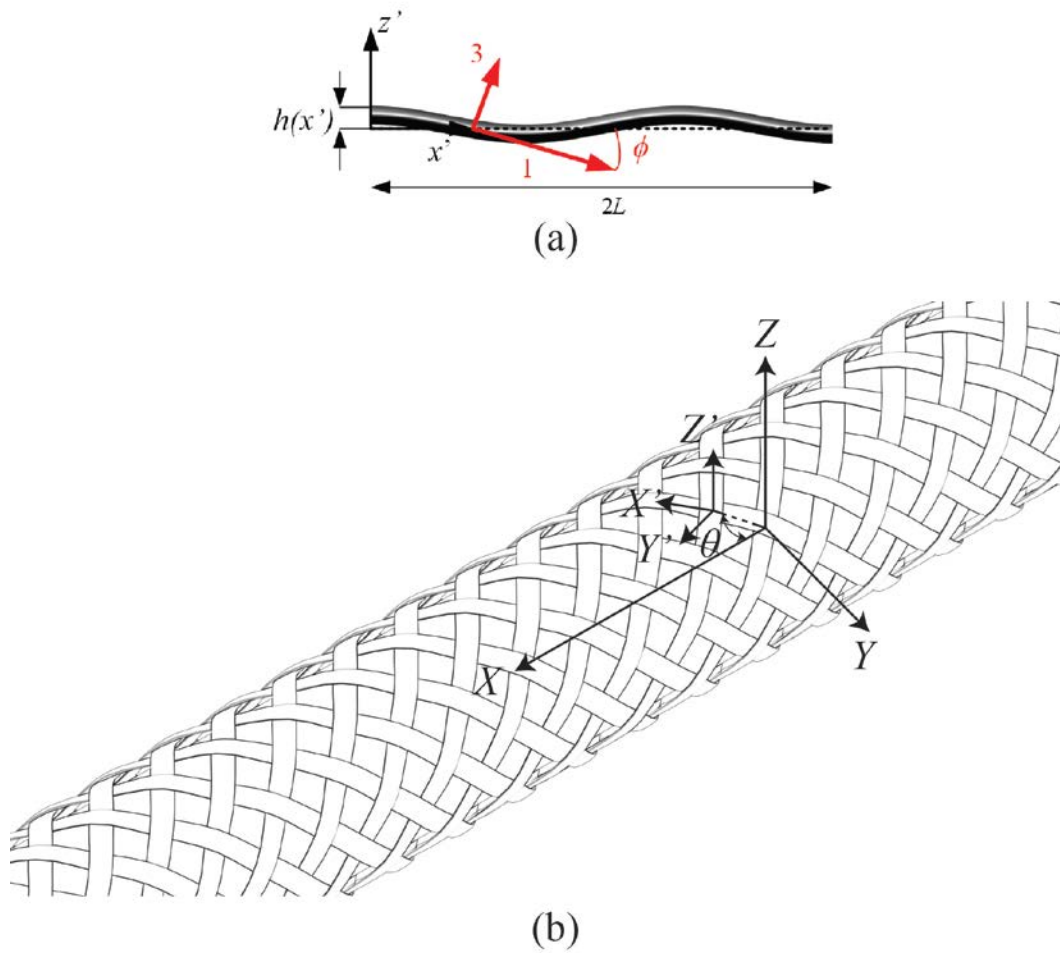
Figure 5-3: Coordinate system transformations (a) Conversion from yarn coordinate system (*1-2-3*) to undulation coordinate system (*x'-y'-z'*) (b) Conversion of undulation coordinate system (*x'-y'-z'*) to global coordinate system (*X-Y-Z*).

The braid yarns were assumed to follow a sinusoidal path due to the repeating nature of the braiding process [5, 18, 21, 22]. The equations for the braid yarns will be described in their local coordinate system (*x'-y'-z'*). This coordinate system is required since a coordinate system transformation will be required for the volume averaging method described in section 2.3.

The equation for a diamond braided composite is shown in equation (5-5). In this equation, L_{und} represents the length of one undulation of a braid yarn. The variable k represents the braid yarn period and the variable a represents the thickness of the braid yarn. The undulation height of the braid yarn is represented by the variable $h(x')$ and the position along the undulation length is represented using the variable x'.

$$L_{und} = \frac{r_0 \beta}{\sin \theta}, \quad k = \frac{2\pi}{L_{und}}$$

5-5

$$h(x') = \frac{a}{2} \sin(k \cdot x')$$

In addition the crimp angle of the braid yarns (ϕ) was determined along the braid yarn length. The braid yarn crimp angle was determined by computing the derivative of the braid yarn undulation height equation ($h(x')$). Determination of the braid yarn crimp angle is shown in (5-6). The braid yarn crimp angle is necessary for accounting for the effect of yarn undulations of braid mechanical properties.

$$\tan(\phi) = \frac{dh(x')}{dx'} = \frac{a}{2} \cdot k \cdot \cos(k \cdot x')$$

$$m = \cos(\phi) = \frac{1}{\sqrt{1 + \tan^2(\phi)}}$$

5-6

$$n = \sin(\phi) = \frac{\tan(\phi)}{\sqrt{1 + \tan^2(\phi)}}$$

Equations for Regular braids were determined using similar equation to the sinusoidal Diamond braid equation shown in equation (5-5). Equations for the undulation height of Regular braids are shown in (5-7). The difference between diamond and regular is demonstrated in equations (5-7). This equation shows that Regular braids are described by a piece-wise function. Equation (5-7) divides the Regular braid yarn path into undulating and non-undulating regions. The yarn crimp angle for Regular braid was computed in a similar manner to the diamond braid shown in equation (5-6). The undulation of the Diamond and Regular braid patterns are compared in Figure 5-4.

$$
h(x^{'}) = \begin{cases}
\dfrac{a}{2}, & if\ 0 \le x^{'} \le \dfrac{\beta}{2}\dfrac{r_0}{\cos(\alpha)} \\[2ex]
\dfrac{-a}{2}\sin\left(\dfrac{2\pi\cos(\alpha)x^{'}}{r_0\beta}+\dfrac{\pi}{2}\right), & if\ \dfrac{\beta}{2}\dfrac{r_0}{\cos(\alpha)} \le x^{'} \le 2\cdot\dfrac{\beta}{2}\dfrac{r_0}{\cos(\alpha)} \\[2ex]
\dfrac{-a}{2}, & 2\cdot\dfrac{\beta}{2}\dfrac{r_0}{\cos(\alpha)} \le x^{'} \le 3\cdot\dfrac{\beta}{2}\dfrac{r_0}{\cos(\alpha)} \\[2ex]
\dfrac{a}{2}\sin\left(\dfrac{2\pi\cos(\alpha)x^{'}}{r_0\beta}+\dfrac{\pi}{2}\right), & if\ 3\cdot\dfrac{\beta}{2}\dfrac{r_0}{\cos(\alpha)} \le x^{'} \le 4\cdot\dfrac{\beta}{2}\dfrac{r_0}{\cos(\alpha)}
\end{cases}
\qquad 5\text{-}7
$$
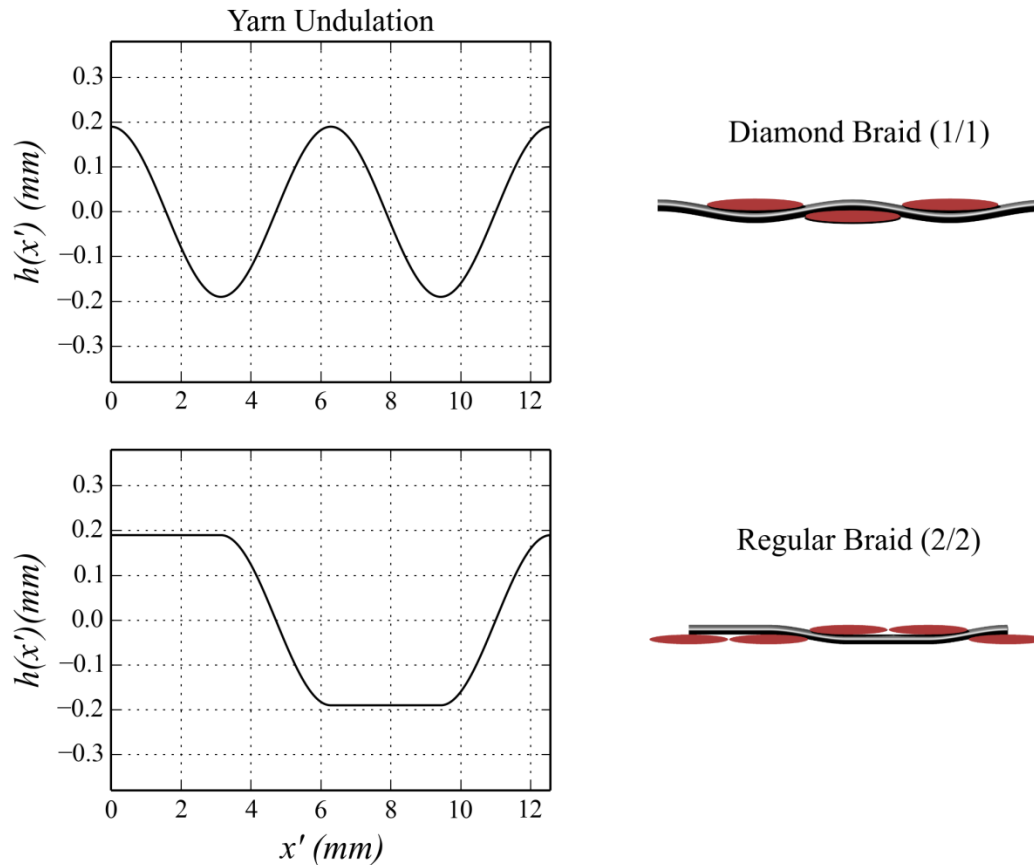
Figure 5-4: Comparison of Diamond (1/1) and Regular (2/2) braid yarn undulations in the undulation coordinate system (x'-y'-z')

5.2.3 Volume Averaging

A volume averaging stiffness method has been utilized in order to determine the material properties of tubular braided composites [23-25]. This method was selected since it allows for the mechanical properties of the wide variety of braid geometries shown in section 5.2.2 to be determined. The volume averaging stiffness method has been previously used to model the behavior of 2D triaxial braided composites [11, 15-17] however; this method has not been generalized to account for the braid geometries shown in section 5.2.2.

The volume averaging method involves three main steps. First, a coordinate system transformation is performed to convert from the local yarn coordinate system (*1-2-3*) to the undulation coordinate system (*x'-y'-z'*). The local to undulation coordinate system transformation is illustrated in Figure 5-3 (a). This figure shows that the braid crimp angle, ϕ, is used to transform from the local coordinate system to the undulation coordinate system.

Two approaches have been used to account for braid yarn undulations. The first approach by Byun *et al.* determined the effective compliance matrix $[S'_{xyz}]$ for the undulating braid yarns [11]. The transformation matrix used to convert from the local (*1-2-3*) coordinate system to the undulation (*x'-y'-z'*) coordinate system is shown in equation ((5-8)). The yarn crimp angle (ϕ) is determined by calculating the derivative of the braid yarn equations ((5-5), (5-7) and (5-18)) shown in section 5.2.2. The compliance matrix $[S'_{xyz}]$, shown in equation (5-9), in the undulation coordinate system is calculated by integrating over the yarn undulation length. The second approach by Quek *et al.* determines the effective stiffness matrix $[C'_{xyz}]$ of the undulating yarns [16]. The calculation of the effective yarn stiffness is shown in (5-10). The two methods used to determine the effective mechanical properties of the undulating yarns will be utilized in this chapter. The study by Quek *et al.* found significant differences between predicted and measured shear moduli when using the effective stiffness calculation shown in (5-10). The discrepancy between measured and predicted shear moduli has been highlighted by Shokreih *et al.* [17].

142

The second step in the volume averaging method is illustrated in Figure 5-3 (b) where a second coordinate system transformation is performed to convert from the undulation coordinate system (x'-y'-z') to the global coordinate system (X-Y-Z). The transformation matrix [T] to convert from the undulation to global coordinate system is shown in equation (5-12). In this equation the braid angle (θ) is used determine the stiffness matrix, [C_{XYZ}], of each braid yarn in the global coordinate system. The calculation of the stiffness matrix [C_{XYZ}] is shown in equation (5-13).

$$
[T'_{xyz}] =
\begin{bmatrix}
m^2 & 0 & n^2 & 0 & 2mn & 0 \\
0 & 1 & 0 & 0 & 0 & 0 \\
n^2 & 0 & m^2 & 0 & -2mn & 0 \\
0 & 0 & 0 & m & 0 & -n \\
-mn & 0 & mn & 0 & m^2-n^2 & 0 \\
0 & 0 & 0 & n & 0 & m
\end{bmatrix}
\qquad \text{5-8}
$$

$$
m = \cos(\phi)
$$
$$
n = \sin(\phi)
$$

$$
[S'_{xyz}] = \frac{1}{L_{und}} \int_0^{L_{und}} [T'_{xyz}]^T [S][T'_{xyz}] dx
\qquad \text{5-9}
$$

$$
[C'_{xyz}] = \frac{1}{L_{und}} \int_0^{L_{und}} [T'_{xyz}]^{-1} [C][R][T'_{xyz}][R]^{-1} dx
\qquad \text{5-10}
$$

143

$$[R] = \begin{bmatrix} 1 & 0 & 0 & 0 & 0 & 0 \\ 0 & 1 & 0 & 0 & 0 & 0 \\ 0 & 0 & 1 & 0 & 0 & 0 \\ 0 & 0 & 0 & 2 & 0 & 0 \\ 0 & 0 & 0 & 0 & 2 & 0 \\ 0 & 0 & 0 & 0 & 0 & 2 \end{bmatrix}$$

5-11

$$[T] = \begin{bmatrix} c^2 & s^2 & 0 & 0 & 0 & 2cs \\ s^2 & c^2 & 0 & 0 & 0 & -2cs \\ 0 & 0 & 1 & 0 & 0 & 0 \\ 0 & 0 & 0 & c & s & 0 \\ 0 & 0 & 0 & -s & c & 0 \\ -cs & cs & 0 & 0 & 0 & c^2 - s^2 \end{bmatrix}$$

$$c = \cos(\theta)$$
$$n = \sin(\theta)$$

5-12

$$C_{XYZ} = [T]^{-1}[C'_{xyz}][R][T][R]^{-1}$$

5-13

The final step in the volume averaging procedure accounts for the contributions of the clockwise and counter-clockwise braid yarns and, if present, axial yarns. The volume averaging equations for Diamond and Regular braid yarns are illustrated in section 5.2.2. The volume averaging method accounts for the contribution of the clockwise (θ^+) and counter-clockwise (θ^-) braid yarns. In addition, matrix only regions and axial yarns can also be accounted for. The final overall stiffness matrix $[C^G]$ for the braided composite is determined by computing the volume fraction of the clockwise ($V_{f\theta+}$), counter-clockwise ($V_{f\theta-}$) and excess matrix (V_m) within the braid unit cell. The equation for the overall stiffness matrix $[C^G]$ is

144

shown in equation (5-14). Finally, the elastic constants for the tubular braided composites are determined from the global compliance matrix $[S^G]$ shown in equation (5-15). The determination of the elastic constants is shown in equation (5-16).

$$\left[C^G\right] = V_{f\theta+}\left[C^+_{XYZ}\right] + V_{f\theta-}\left[C^-_{XYZ}\right] + V_m\left[C^m_{XYZ}\right]$$

5-14

$$S^G = \left[C^G\right]^{-1}$$

5-15

$$E_x = \frac{1}{S^g_{11}}, \ E_y = \frac{1}{S^g_{22}}, \ E_z = \frac{1}{S^g_{33}}$$

$$G_{xy} = \frac{1}{S^g_{66}}, G_{yz} = \frac{1}{S^g_{44}} \ G_{xz} = \frac{1}{S^g_{55}}$$

5-16

$$\upsilon_{xy} = \frac{-S^g_{12}}{S^g_{11}}, \ \upsilon_{zx} = \frac{-S^g_{13}}{S^g_{33}}, \ \upsilon_{yz} = \frac{-S^g_{23}}{S^g_{22}}$$

The prediction of the elastic constants of tubular braided composites was automated by creating a custom program (MATLAB, 2016b, The Math Works, Natick, MA) that automates the above volume averaging and geometrical analysis procedure. Using this method the effect of braid geometry or matrix and fiber material properties can be rapidly explored and can therefore be used as a design tool for manufacture tubular braided composites.

5.3   Model Predictions and Discussion

The proposed model described in Section 5.2 will first be compared with existing models. The proposed model will also be compared with experimental results. Extensive geometric measurements of each braid sample were recorded. Critical braid dimensions of braid angle (θ), inner diameter (D_i), outer diameter (D_o), and yarn width (W_y) were recorded for each sample. The resulting average braid dimensions are summarized in Table 5-1. The braid dimensions shown in Table 5-1 will be used as inputs in order to compare the predicted model results with the experimentally determined elastic properties of the tubular braided composite samples. Table 5-1 also illustrates the relationship between braid angle (θ) with yarn width (W_y) and braid outer diameter (D_o). For both the Diamond and Regular braids in this study as the braid angle increases the measured width of the braid yarns decreases. As well, the outer diameter of the braid increases with increasing braid angle.

Table 5-1: Geometric measurements of test specimen

Braid Pattern	Number of Yarns-n	Number of Bobbins	Yarn Width-W_y (mm)	Expected Braid Angle-θ (deg)	Measured Braid Angle-θ (deg)	Outer Diameter-D_0 (mm)	Inner Diameter D_i (mm)	Yarn Thickness-a (mm)	Number of Samples
1/1	18	36	3.044	35	34.228	12.412	11.503	0.455	20
1/1	18	36	2.593	45	43.905	12.438	11.501	0.468	20
1/1	18	36	2.343	55	53.219	12.557	11.530	0.514	20
2/2	36	36	1.890	35	35.595	12.336	11.512	0.412	20
2/2	36	36	1.610	45	45.372	12.467	11.559	0.454	20
2/2	36	36	1.345	55	55.288	12.561	11.550	0.505	20

5.3.1   Example Model Predictions

To demonstrate results predicted using the model presented in Section 5.2 elastic moduli for a Diamond and Regular braid will be presented. The assumed yarn mechanical properties and braid dimensions are shown in Table 5-2. For this comparison the Diamond and Regular braids will be compared by utilizing the same number of bobbins to manufacture the braid structure. The two braids will have equivalent fiber volume fractions since the same number of braider bobbins were used to produce these braids.

Table 5-2: Yarn mechanical properties and geometry for a Diamond (1/1) and Regular (2/2) braided composite

Material Properties	
Longitudinal Elastic Modulus E_{11} (GPa)	79.7
Transverse Modulus $E_{22} = E_{33}$ (GPa)	5.9
In Plane Shear Modulus $G_{12} = G_{13}$ (GPa)	1.5
Out of Plane Shear Modulus G_{23} (GPa)	4.71
In-Plane Poisson's Ratio $v_{12} = v_{13}$	0.33
Out of Plane Poisson's Ratio v_{23}	0.25
Yarn Fiber Volume Fraction V_{fy}	0.6
Total Braid Fiber Volume Fraction V_f	0.55
Yarn Width W_y (mm)	3.1
Braid Thickness a (mm)	0.38
Braid Diameter	11.1mm
Number of Braiding Machine Bobbins	36

Representative results comparing the elastic modulus of a Diamond and Regular braid are shown in Figure 5-5. This figure shows the effect of braiding pattern on elastic constants for braids produced with equivalent fiber volume fractions. Figure 5-6 demonstrates that the proposed model predicts that Diamond braids will have similar Longitudinal (E_{xx}) and Transverse (E_{yy}) modulus while differences in the Shear moduli (G_{xy}) can be seen in Figure 5-5 (c). Similar Longitudinal (E_{xx}) and Transverse (E_{yy}) moduli are observed in Figure 5-6 is due to equivalent fiber volume fractions for both braiding geometries. The small differences in elastic properties between the Diamond and Regular braids are due to the undulation of the braid yarns. The undulations of braid yarns are demonstrated in Figure 5-1 and Figure 5-4. The difference in mechanical properties can be attributed to the effect of the crimp angle (ϕ) of the braid yarns. The effect of crimp angle is demonstrated in Figure 5-4. In this figure, it can be seen that fiber undulations are limited to specific regions for the Regular braids

whereas undulation occur throughout the diamond braid strand path. Since the fiber undulations are more limited for Regular braids than Diamond braids; this results in a greater contribution of the braid yarns to the in-plane elastic properties (E_{xx} and E_{yy}) than the Diamond braid pattern. Similarly, the shear moduli of the Diamond and Regular braids are compared in Figure 5-6 (c). The shear modulus for the two braid geometries is not symmetric about 45° as is commonly predicted for braided composites [8]. The asymmetry shown in Figure 5-6 is due to several factors: the effect of braid angle (θ) on cover factor and the crimp (ϕ) of the braid yarns. Both the braid cover factor and yarn crimp are a function of braid angle. This figure demonstrates that the Diamond braids exhibit a higher shear modulus (G_{xy}) than the Regular braid pattern. The model results shown in Figure 5-6 demonstrate the ability of the proposed model to allow for direct comparison between different braiding patterns.
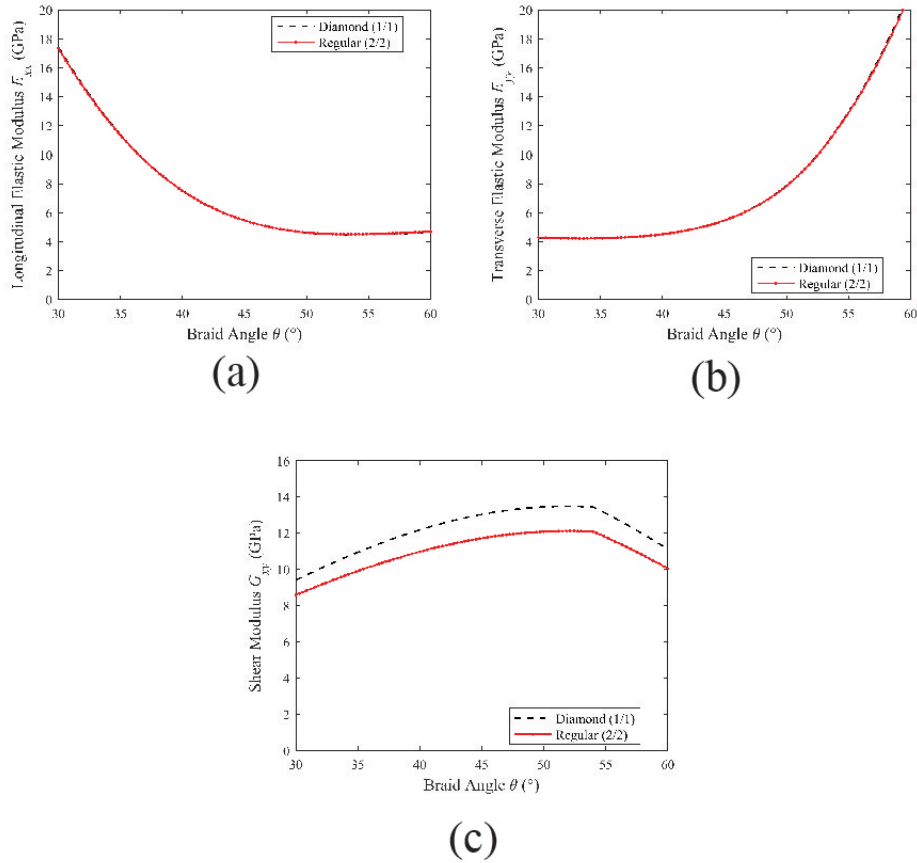
Figure 5-5: Comparison of Diamond (1/1) and Regular (2/2) elastic moduli for braid manufactured using 36 bobbins, a mandrel diameter of 11.1mm and a yarn width of 3.1mm (a) Longitudinal Elastic Modulus (E_{xx}) (b) Transverse elastic moduli (E_{yy}) (c) Shear modulus (G_{xy})

5.3.2   Comparison with Existing Models

The braid model developed in section 2 was also compared with the results of existing models which exist in literature. Several analytical and finite element analysis (FEA) models exist for braided composites however; many of these models are limited to only one braid configuration i.e. Regular braids, Diamond Braids or Triaxial braids [7, 9, 13-17, 26, 27]. One limitation of the existing studies is that some or all of the critical parameters for manufacturing braided

150

structures including: braid diameter (D_0), number of bobbins used to produce the braid structure (N), yarn width (W_y) and yarn thickness (a) are neglected. These parameters are necessary in order to produce comparable braid structures. The motivation behind the model presented in Section 5.2 is to allow for various braid configurations to be modeled and for designers to be able produce braids with known material properties using input parameters from the braid manufacturing process.

The study by Ayranci *et al.* developed a curved unit cell model based on CLPT theory in order to predict the mechanical properties of tubular braided composites [7]. The model of Ayranci *et al.* is exclusively able to predict the mechanical properties of Diamond (1/1) braided composites. The model of Ayranci *et al.* stated braid yarn dimensions (W_y and a) but the number of yarns (N) used to produce the braid structure were not stated.

Comparison between the proposed model and the CLPT based model of Ayranci *et al.* in Figure 5-7. The yarn mechanical properties used for this comparison are summarized in Table 5-4. This figure shows both models predict a decrease in longitudinal elastic modulus as braid angle increases. The model of Ayranci and Carey assumes that yarn undulation only occurs within defined regions within the braid unit cell [7, 9]. Braid yarns are assumed to be flat in the cross-over regions (where clockwise and counter-clockwise yarns overlap). This assumption will result in an over prediction of the longitudinal elastic modulus of a diamond braid since the braid yarn crimp angle is neglected in the cross-over regions. The crimp or undulation of Diamond braids is illustrated in Figure 5-4. This assumption

results in a greater contribution of the braid yarns in the longitudinal direction in the cross-over regions. The braid models of Ayranci and Carey also assumes that the braid unit cell geometry will exhibit symmetrical behavior as a function of braid angle (θ). This means that the braid unit cell height and width will vary proportionally as a braid angle changes. This assumption is not physically possible since the braid unit cell width ($W_{unitCell}$) is a constant value that will depend on the braid mandrel radius (r_0) and the number of braid yarns (n) used to fabricate the braid geometry. The relationship between mandrel diameter, number of braider yarns and braid angle are described by equations (5-4) and (5-6).

Table 5-3: Yarn mechanical properties and geometry for a Diamond (1/1) braided composite examined by Ayranci *et al.* [7]

Material Properties	
Longitudinal Elastic Modulus E_{11} (GPa)	79.7
Transverse Modulus $E_{22} = E_{33}$ (GPa)	5.9
In Plane Shear Modulus $G_{12} = G_{13}$ (GPa)	1.5
Out of Plane Shear Modulus G_{23} (GPa)	4.71
In-Plane Poisson's Ratio $v_{12} = v_{13}$	0.33
Out of Plane Poisson's Ratio v_{23}	0.25
Yarn Fiber Volume Fraction V_{fy}	0.6
Total Braid Fiber Volume Fraction V_f	0.55
Yarn Width W_y (mm)	3.1
Braid Thickness a (mm)	0.38
Braid Diameter D_i (mm)	11.1
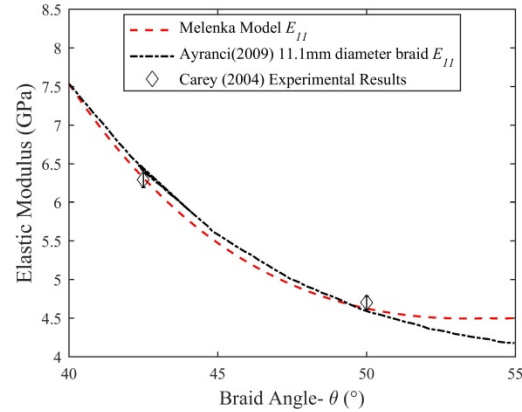
Figure 5-6: Comparison of proposed model results with the CLPT base model results of
Ayranci *et al.* [7]

The works by Ayranci *et al.* also examined the Shear modulus of Diamond braided composites [8]. The experimentally determined Shear moduli for braids with different differing braid diameter and braid diameters were evaluated by Ayranci et al. The dimensions and resulting elastic moduli are summarized in Table 5-5. The braid samples examined in Table 5-5 are labeled Kevlar- Large-Torsion (KLTO), Kevlar-Medium-Torsion (KMTO) and Kevlar-Small-Torsion (KSTO) to indicate braids of varying diameter. The experimentally determined Shear Moduli examined by Ayranci *et al.* were compared with the results of the proposed model. Comparison of the proposed model results and Ayranci *et al.*'s experimental results can be seen in Figure 5-8. Figure 5-8 shows that there is agreement between the proposed model results and the experimental results for braids with varying braid diameter and braid angles.

Table 5-4: Experimentally determined Shear moduli by Ayranci *et al*. [8]

Braid Name	Braid Angle- θ (°)	Yarn Width (mm)	Thickness (mm)	Outer Diameter (mm)	Shear Modulus G_{xy} (GPa)
KLTO	53.46 ±0.378	1.984	0.285	10.194	11.19±0.57
KMTO	51.56±0.513	1.833	0.302	8.591	11.59±0.46
KSTO	47.64±0.532	1.773	0.303	7.068	12.32±0.4
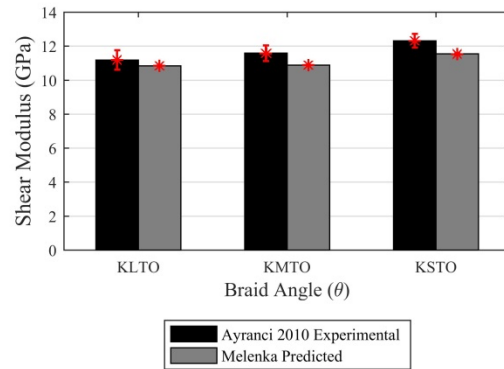
Figure 5-7: Comparison of experimentally determined and proposed model shear moduli

The FEA model by Ji *et al.* predicted the mechanical properties of Regular (2/2) biaxial and triaxial braided composites [13]. This study demonstrates the effect of braid angle (θ) on mechanical properties. This study also demonstrated the asymmetric relationship between the longitudinal and transverse elastic moduli. The proposed model was compared to the model results of Ji *et al*. The yarn mechanical properties used for the model comparison are shown in Table 5-6. The model of Ji *et al*. stated braid yarn dimensions (W_y and a) but the number of yarns used to produce the braid structure or mandrel diameter used to form the braid was not stated.

Comparison between the proposed model and FEA model of Ji *et al.* results can be seen in Figure 5-9. This figure shows good agreement between the two model results. The both models exhibit a decreasing longitudinal elastic modulus with braid angle and increasing transverse elastic modulus with braid angle. Both models also exhibit an asymmetric relationship between the longitudinal and transverse elastic moduli.

Table 5-5: Yarn mechanical properties and geometry for a Regular (2/2) braided composite examined by Ji *et al.* [13]

Material Properties	
Longitudinal Elastic Modulus E_{11} (GPa)	182.71
Transverse Modulus $E_{22} = E_{33}$ (GPa)	11.81
In Plane Shear Modulus $G_{12} = G_{12}$ (GPa)	8.43
Out of Plane Shear Modulus G_{23} (GPa)	4.71
In-Plane Poisson's Ratio $v_{12} = v_{13}$	0.23
Out of Plane Poisson's Ratio v_{23}	0.25
Yarn Fiber Volume Fraction V_{fy}	0.8
Total Braid Fiber Volume Fraction V_f	0.55
Yarn Width W_y (mm)	3.0
Braid Thickness a (mm)	0.2875
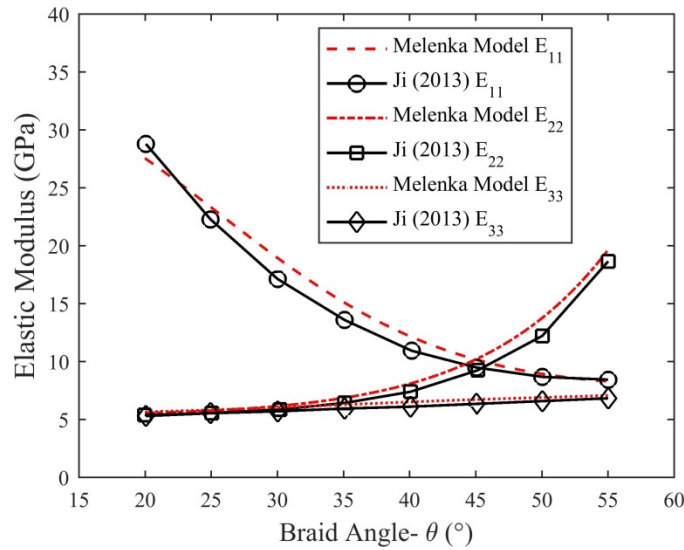
Figure 5-8: Comparison between the proposed model results and model results of Ji *et al.*
[13]. The longitudinal (E_{11}), transverse (E_{22}) and out-of-plane (E_{33}) elastic moduli are
compared.

The FEA model of Xu *et al.* analyzed the mechanical properties of Diamond
(1/1), Regular (2/2) and Hercules (3/3) braids [14]. The model presented by Xu
et al. is consistent with other braided composite models in that this model predicts
decreasing longitudinal elastic modulus with braid angle and an increasing
transverse elastic modulus with braid angle. The model by Xu *et al.* does not
demonstrate asymmetrical behavior between longitudinal and transverse elastic
modulus as seen by Ji *et al.*. The symmetry demonstrated in the model by Xu
et al. is due to the unit cell geometry used to describe the different braid
geometries. The unit cell geometry described by Xu *et al.* varies proportionally
with braid angle similar to the model of Ayranci *et al*.

The proposed model and the FEA model of Xu *et al.* are compared in Figure 5-10.
The yarn mechanical properties used for this comparison are summarized in Table
5-7. The study by Xu *et al.* used glass fiber/epoxy for Diamond braids and carbon

156

fiber/ epoxy for Regular braids. Subtle differences exist between the proposed

model and FEA model of Xu *et al*. In particular, the model of Xu *et al*. does not

exhibit an asymmetric relationship for the longitudinal and transverse elastic

moduli about 45°. The lack of asymmetry in the Xu *et al*. model results in

deviation between the proposed model and the model results of Xu *et al*., in

particular for elastic modulus results above 45°.

Table 5-6: Yarn mechanical properties and geometry for a Diamond (1/1) and Regular (2/2) braided composite examined by Xu *et al*. [14]

Material Properties	Glass fiber/ epoxy	Carbon fiber/ epoxy
Longitudinal Elastic Modulus E_{11} (GPa)	58.39	236.76
Transverse Modulus $E_{22} = E_{33}$ (GPa)	21.52	10.26
In Plane Shear Modulus $G_{12} = G_{13}$ (GPa)	7.87	7.17
Out of Plane Shear Modulus G_{23} (GPa)	8.11	4.17
In-Plane Poisson's Ratio $v_{12} = v_{13}$	0.23	0.23
Out of Plane Poisson's Ratio v_{23}	0.33	0.43
Yarn Width W_y (mm)	3.1	
Braid Thickness a (mm)	0.38	
Braid Diameter D (mm)	30	
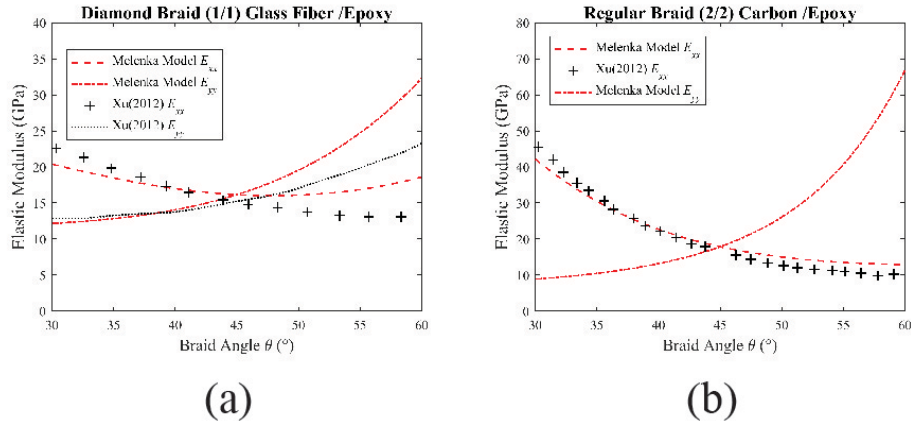
Figure 5-9: Comparison of the proposed model results and model results of Xu *et al.* [14]. (a) Comparison of Diamond (1/1) braid results for a glass fiber/epoxy braid (b) Comparison of Regular (2/2) braid results for a carbon fiber/ epoxy braid.

5.4   Experimental Model Validation

In order to validate the model presented in this chapter a series of mechanical tests were performed to compare model predictions with experimental results.   To experimentally analyze tubular braided composites three braid angles were evaluated (35, 45 and 55°) and two braid patterns were used (Diamond and Regular).   All braids were manufactured using the same number of braider bobbins and manufactured with the same braid mandrel diameter.   The braid samples were tested in both tension and torsion which allows for the longitudinal elastic modulus and shear modulus to be determined.   The complete experimental methodology is described in Chapter 4   All braid samples were evaluated using a three dimensional digital image correlation technique in order to measure full-field strain of each braid sample.

5.4.1 Longitudinal Elastic Modulus

Representative strain fields for a Diamond (1/1) and Regular (2/2) braid are shown in Figure 5-11. A total of 10 samples were evaluated for each braid angle which resulted in a total of 60 tests. Strain fields like the ones shown in Figure 5-11 were used to evaluate the stress-strain behavior of each braid sample. The resulting average elastic moduli and standard deviation for each braid angle and braid type are summarized in Figure 5-12. Figure 5-12 shows a decrease in longitudinal elastic modulus with an increase in braid angle.
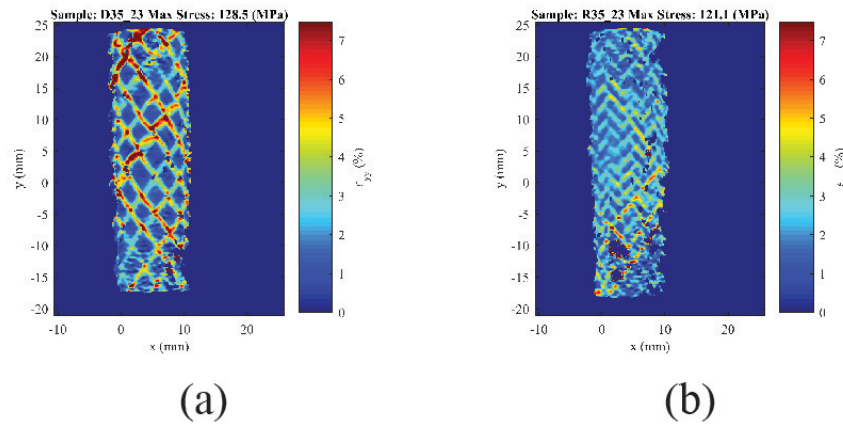
Figure 5-10: Representative strain fields generated from images collected during tensile tests (a) Diamond braid (1/1) 35° braid angle (b) Regular Braid (2/2) 35° braid angle.
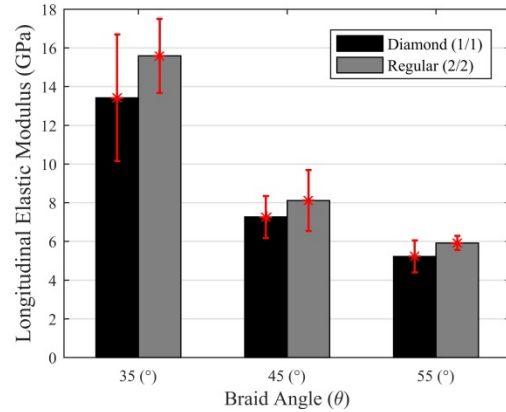
Figure 5-11: Comparison of experimentally determined longitudinal elastic modulus of Diamond (1/1) and Regular (2/2) braids

The experimental and model results for both the Diamond and Regular braid geometries are compared in Figure 5-13. This figure shows that the proposed braid model and experimental results both predict that increasing braid angle result in a decrease in longitudinal elastic modulus for both Diamond and Regular braids. Figure 5-12 and Figure 5-13 also show that Regular braids manufactured with the same number of braider bobbins and braid yarn denier results in greater longitudinal elastic moduli than Diamond braids for braids of the same braid angle.
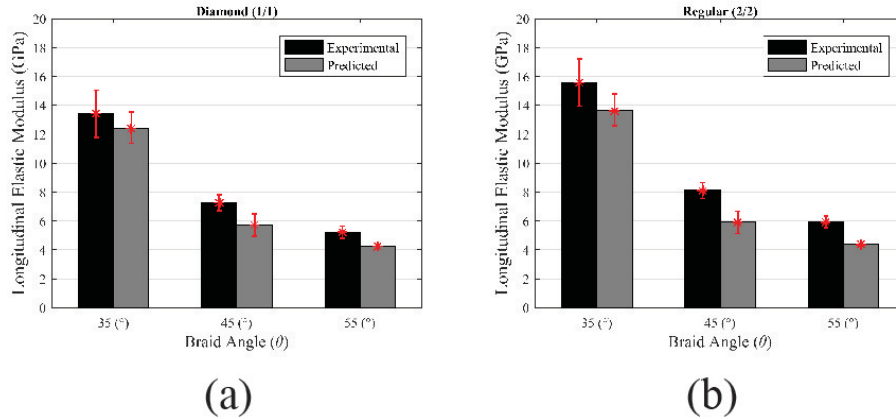
Figure 5-12: Comparison of longitudinal elastic modulus experimental results
with proposed model results (a) Diamond braid (1/1) (b) Regular braid (2/2)

5.4.2 Shear Modulus

The shear moduli of Diamond and Regular braids were examined in a similar to the longitudinal elastic moduli as shown in Section 4.1. Representative shear strain fields for both Diamond and Regular braids are shown in Figure 5-14. As well, the resulting shear moduli for the experimentally measured braid samples are compared in Figure 5-15.
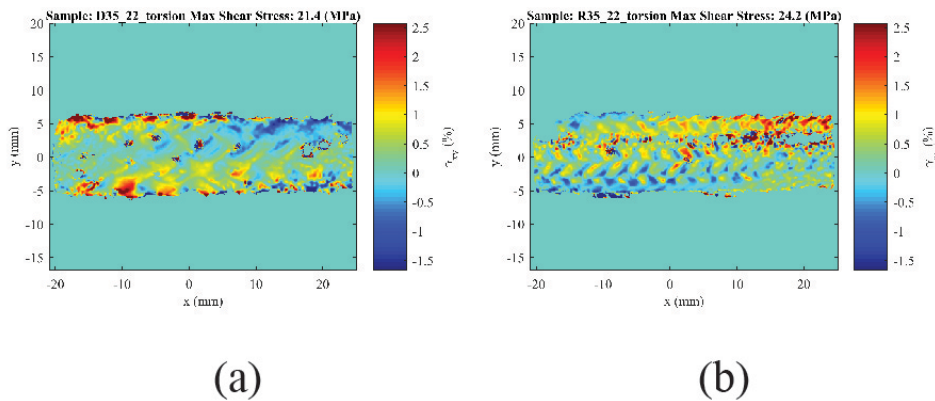
Figure 5-13: Representative shear strain fields generated from images collected during torsion tests (a) Diamond braid (1/1) 35° braid angle (b) Regular Braid (2/2) 35° braid angle.
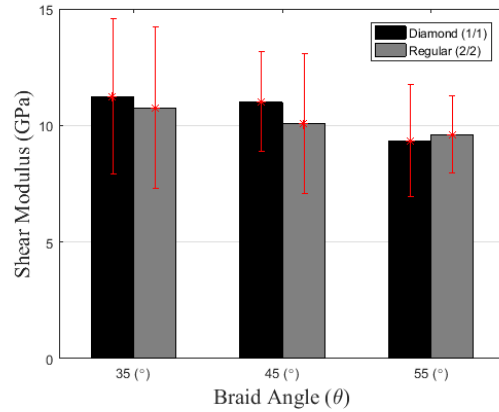
Figure 5-14: Comparison of experimentally determined shear modulus of Diamond (1/1) and Regular (2/2) braids

Experimental and model results for the Diamond and Regular braids are compared in Figure 5-16. Figure 5-16 shows that there is a decrease in shear modulus with an increase in braid angle. The Diamond braid shear moduli were determined to be 11.22±3.34, 11.00±2.156 and 9.32±2.41 GPa for braids manufactured with braid angles of 35, 45 and 55° respectively. Similarly, the Regular braid shear moduli were determined to be 10.73±3.47, 10.73±3.00 and 9.61±1.65 GPa for braid angles of 35, 45 and 55° respectively. The results in Figure 5-15 demonstrate that there is significant variation in shear modulus results for both Diamond and Regular braids.

The experimental results for the Diamond and Regular braids were compared with the proposed model results. Comparison of the predicted and experimental results can be seen in Figure 5-16. This figure shows that there is agreement between the predicted and experimentally determined shear moduli for both the Diamond and Regular braid configurations. The shear modulus for the Diamond and Regular braids was determined by computing the average of resulting shear moduli using

162

equations (5-10) and (5-11). Using (5-10) to compute the effective mechanical properties of the composite braids provides a lower bound for the shear modulus while using equation (5-11) provides an upper bound for the shear modulus. Using the average shear modulus by using a combination of equations (5-10) and (5-11) provided agreement between the shear moduli for both the Diamond and Regular braids as can be seen in Figure 5-16. Similar bounding techniques are used for estimating shear moduli as demonstrated by Jones [20].

Previous studies that have examined the in-plane shear modulus of braided composites have demonstrated that experimental and model results can result in significant differences. For example the study by Quek *et al.* found that model predictions and experimental results for the in-plane shear modulus varied by 27% [16, 17]. Better agreement between model and experimental results was achieved by Shokreih *et al.* where model and experimental results differed by 6.92%. It has been suggested that using a combination of iso-stress and iso-strain assumptions may result in better agreement with experiments [26]. The model presented in this chapter uses a combination of iso-stress and iso-strain conditions in order to predict in-plane shear modulus for braided composites. The results in Figure 5-16 demonstrate agreement between experimental and model results for in-plane shear modulus.
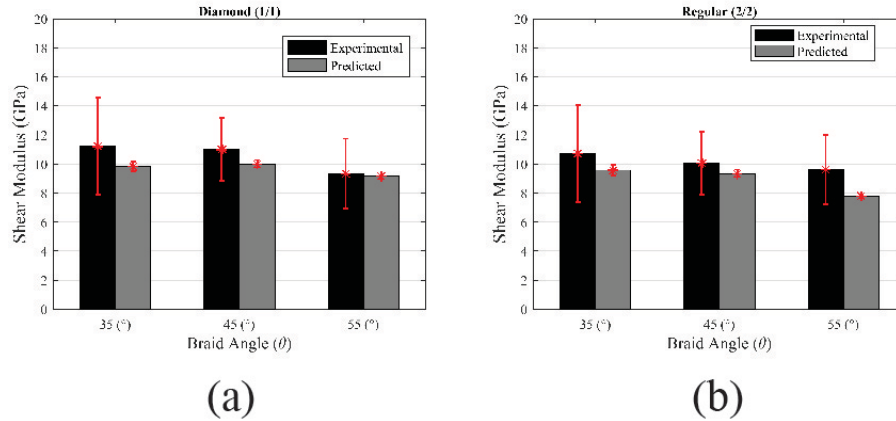
Figure 5-15: The effect of braid angle variation on shear modulus (a) Diamond braid (1/1) (b) Regular braid (2/2)

5.4.3   Additional Model Applications

The braid model presented in section 2 can also be applied to Hercules (3/3) braids. The undulations of Hercules braids can be described using an equation in a similar manner to Regular braids as shown in (5-18). The equation to describe the geometry of the Hercules braid is based on the geometric equations of Alpildyiz *et al.* [18]. The stand path of a Hercules braid is demonstrated in Figure 5-17. Similar to Regular braids, Hercules braids exhibit regions where no yarn undulations occur.   Since Hercules braids exhibit less yarn undulation than Diamond and Regular braids this leads to in an increase in in-plane elastic properties compared to Diamond and Regular braids. The effect of braid pattern on elastic properties is demonstrated in Figure 5-18.   The Hercules braid is included in this chapter to demonstrate the capability of the proposed braid model. Experimental validation of the Hercules braid results was not performed as it is not possible to manufacture Hercules braids using a 36 carrier braiding machine; therefore a comparison with other braid patterns (Diamond and Regular) was not

164

possible. Comparison of the different braiding machine configurations to produce

different braiding patterns is described by Melenka *et al.* [28].

$$
h(x') = \begin{cases}
\dfrac{a}{2}, & if\ 0 \le x' \le \dfrac{\beta}{2}\dfrac{r_0}{\cos(\alpha)} \\[2mm]
\dfrac{a}{2}, & if\ \dfrac{\beta}{2}\dfrac{r_0}{\cos(\alpha)} \le x' \le 2\cdot\dfrac{\beta}{2}\dfrac{r_0}{\cos(\alpha)} \\[2mm]
\dfrac{a}{2}\sin\left(\dfrac{2\pi\cos(\alpha)x'}{r_0\beta}+\dfrac{\pi}{2}\right), & if\ 2\cdot\dfrac{\beta}{2}\dfrac{r_0}{\cos(\alpha)} \le x' \le 3\cdot\dfrac{\beta}{2}\dfrac{r_0}{\cos(\alpha)} \\[2mm]
-\dfrac{a}{2}, & if\ 3\cdot\dfrac{\beta}{2}\dfrac{r_0}{\cos(\alpha)} \le x' \le 4\cdot\dfrac{\beta}{2}\dfrac{r_0}{\cos(\alpha)} \\[2mm]
-\dfrac{a}{2}, & if\ 4\cdot\dfrac{\beta}{2}\dfrac{r_0}{\cos(\alpha)} \le x' \le 5\cdot\dfrac{\beta}{2}\dfrac{r_0}{\cos(\alpha)} \\[2mm]
\dfrac{-a}{2}\sin\left(\dfrac{2\pi\cos(\alpha)x'}{r_0\beta}+\dfrac{\pi}{2}\right), & if\ 5\cdot\dfrac{\beta}{2}\dfrac{r_0}{\cos(\alpha)} \le x' \le 6\cdot\dfrac{\beta}{2}\dfrac{r_0}{\cos(\alpha)}
\end{cases}
\tag{5-17}
$$
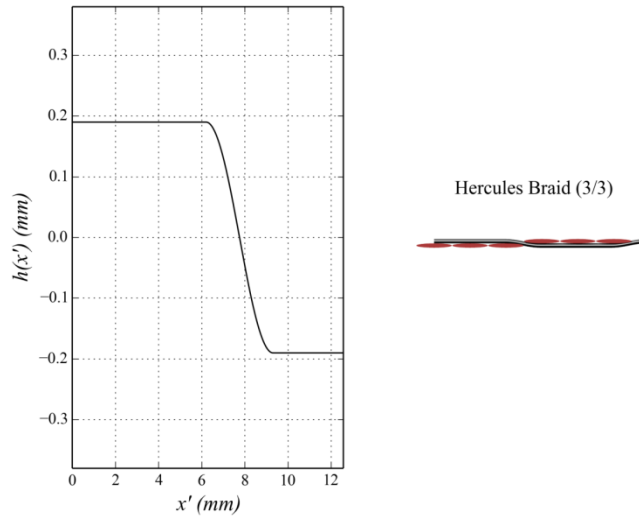
Figure 5-16: Example yarn undulations of a Hercules (3/3) braid

165
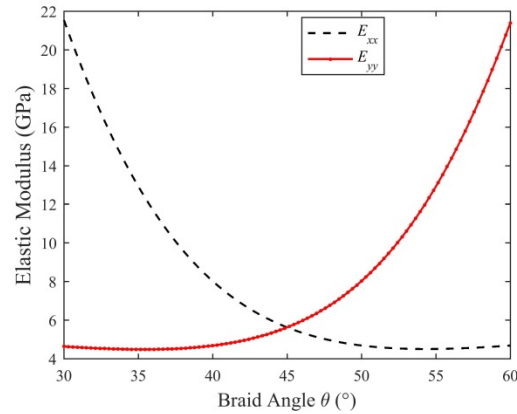
Figure 5-17: Comparison of longitudinal and transverse elastic moduli for a Hercules (3/3) braid

5.5 Conclusions

The braid model presented in this chapter is a useful method for predicting the elastic constants for tubular braided composites. The presented model is adaptable to the variety of braiding configuration that exist since the model allows for Diamond (1/1), Regular (2/2) and Hercules (3/3) braids to be modeled. The model presented in this chapter has been validated against experimental results for Diamond (1/1) and Regular (2/2) braids as these braid configurations can be manufactured using a 36 carrier braiding machine. The model presented in this chapter utilizes physical parameters utilized during the manufacturing of braids. The ability to use physical braiding parameters allows this model to be utilized during the design of braided composites.

One of the main advantages of the model presented in this chapter is this model can be easily implemented using a scripting programming language like MATLAB or Python. Designers can quickly and easily manipulate braid parameters in order to produce a structure with required elastic properties. The analytical model presented in this chapter is intended to be used as a design tool

for designing and manufacturing tubular braided composites and to complement existing FEA models which exist for evaluating tubular braided composites [13, 14]. Once a suitable braid has been designed using the proposed analytical model a FEA model can then be used to refine the mechanical properties prediction for the particular braid structure. This provides a more computationally efficient process as FEA models will not be required for initial design iterations.

5.6   References

[1] D. Brunnschweiler, "Braids and Braiding," *Journal of the Textile Institute Proceedings,* vol. 44, pp. P666-P686, 09/01; 2015/02, 1953.

[2] D. Brunnschweiler, "The Structure and Tensile Properties of Braids," *Journal of the Textile Institute Transactions,* vol. 45, pp. T55-T77, 01/01; 2015/02, 1954.

[3] F. K. Ko, "Braiding," in *ASM International, Engineered Materials Handbook*Anonymous American Society of Metals, 1987, pp. 519-528.

[4] F. K. Ko, C. M. Pastore and A. A. Head, *Handbook of Industrial Braiding.* Covington, Kentucky: Atkins and Pearce, 1989.

[5] T. Chou and F. K. Ko, *Textile Structural Composites.* Amsterdam ; New York : Elsevier ; New York, NY, U.S.A. : Distributors for the U.S. and Canada, Elsevier Science Pub. Co., 1989, 1989.

[6] C. Ayranci, D. Romanyk and J. P. Carey, "Elastic properties of large -open- mesh 2D braided composites: Model predictions and initial experimental findings," *Polymer Composites,* vol. 31, pp. 2017-2024, 2010.

[7] C. Ayranci and J. P. Carey, "Predicting the longitudinal elastic modulus of braided tubular composites using a curved unit-cell geometry," *Composites Part B: Engineering,* vol. 41, pp. 229-235, 2010.

[8] C. Ayranci and J. P. Carey, "Effect of diameter in predicting the elastic properties of 2D braided tubular composites," *J. Composite Mater.,* vol. 44, pp. 2031-2044, 2010.

[9] J. Carey, M. Munro and A. Fahim, "Longitudinal elastic modulus prediction of a 2-D braided fiber composite," *J Reinf Plast Compos,* vol. 22, pp. 813-831, 2003.

[10] J. Carey, A. Fahim and M. Munro, "Predicting elastic constants of 2D-braided fiber rigid and elastomeric–polymeric matrix composites," *J Reinf Plast Compos,* vol. 23, pp. 1845-1857, 2004.

[11] J. H. Byun, "The analytical characterization of 2-D braided textile composites," *Composites Sci. Technol.,* vol. 60, pp. 705-716, 2000.

[12] P. Tan, L. Tong and G. P. Steven, "Modelling for predicting the mechanical properties of textile composites - A review," *Composites Part A: Applied Science and Manufacturing,* vol. 28, pp. 903-922, 1997.

[13] X. Ji, A. M. Khatri, E. S. Chia, R. K. Cha, B. T. Yeo, S. C. Joshi and Z. Chen, "Multi-scale simulation and finite-element-assisted computation of elastic properties of braided textile reinforced composites," *J. Composite Mater.,* vol. 48, pp. 931-949, 2014.

[14] L. Xu, S. J. Kim, C. -. Ong and S. K. Ha, "Prediction of material properties of biaxial and triaxial braided textile composites," *J. Composite Mater.,* vol. 46, pp. 2255-2270, 2012.

[15] R. F. El-Hajjar, S. S. Shams and D. J. Kehrl, "Closed form solutions for predicting the elastic behavior of quasi-isotropic triaxially braided composites," *Composite Structures,* vol. 101, pp. 1-8, 2013.

[16] S. C. Quek, A. M. Waas, K. W. Shahwan and V. Agaram, "Analysis of 2D triaxial flat braided textile composites," *Int. J. Mech. Sci.,* vol. 45, pp. 1077-1096, 2003.

[17] M. M. Shokrieh and M. S. Mazloomi, "An analytical method for calculating stiffness of two-dimensional tri-axial braided composites," *Composite Structures,* vol. 92, pp. 2901-2905, 2010.

[18] T. Alpyildiz, "3D geometrical modelling of tubular braids," *Text. Res. J.,* vol. 82, pp. 443-453, 2012.

[19] I. M. Daniel and O. Ishai, *Engineering Mechanics of Composite Materials.* New York: Oxford University Press, 2006.

[20] R. M. Jones, *Mechanics of Composite Materials.* Washington, Scripta Book Co. 1975], 1975.

[21] P. Potluri, A. Rawal, M. Rivaldi and I. Porat, "Geometrical modelling and control of a triaxial braiding machine for producing 3D preforms," *Composites Part A: Applied Science and Manufacturing,* vol. 34, pp. 481-492, 2003.

[22] G. W. Melenka, E. Lepp, B. K. O. Cheung and J. P. Carey, "Micro-computed tomography analysis of tubular braided composites," *Composite Structures,* vol. 131, pp. 384-396, 11/1, 2015.

[23] A. Kregers and Y. G. Melbardis, "Determination of the deformability of three-dimensionally reinforced composites by the stiffness averaging method," *Mechanics of Composite Materials,* vol. 14, pp. 1-5, 1978.

[24] A. Kregers and G. Teters, "Determination of the elastoplastic properties of spatially reinforced composites by the averaging method," *Mechanics of Composite Materials,* vol. 17, pp. 25-31, 1981.

[25] A. Kregers and A. Zilauts, "Limiting values of reinforcement factors for fibrous composites with a three-dimensional structure," *Mechanics of Composite Materials,* vol. 20, pp. 530-536, 1985.

[26] A. Hallal, R. Younes and F. Fardoun, "Review and comparative study of analytical modeling for the elastic properties of textile composites," *Composites Part B: Engineering,* vol. 50, pp. 22-31, 2013.

[27] Z. T. Kier, A. Salvi, G. Theis, A. M. Waas and K. Shahwan, "Estimating mechanical properties of 2D triaxially braided textile composites based on microstructure properties," *Composites Part B: Engineering,* vol. 68, pp. 288-299, 2014.

[28] G. W. Melenka, A. J. Hunt, C. M. Pastore, F. K. Ko, M. Munro and J. P. Carey, "Manufacturing processes for braided composite materials," in *Handbook of Advances in Braided Composite Materials: Theory, Production, Testing and Applications*, J. P. Carey, Ed. Woodhead Publishing, 2016, .

Chapter 6   Evaluation and Prediction of the Mechanical Properties of Continuous Fiber-Reinforced 3D Printed Structures

A version of this chapter has been published as:

Melenka, G.W., Cheung B.O., Schofield, J, Dawson M.R., Carey J.P., Evaluation and Prediction of the Tensile Properties of Continuous Fiber-Reinforced 3D Printed Structures, Composite Structures, 153: 866-875, 2016

6.1   Introduction

Three dimensional (3D) printing or Rapid Prototyping (RP) is a manufacturing process that produces components from computer-aided design (CAD) software. Three dimensional printing is not an entirely new technology but the advent of open source, low cost 3D printers has led to drastic proliferation of this technology. This process has become highly popular with researchers and hobbyists for the design and manufacture of 3D parts as it allows for the rapid design and manufacture of complex component.

3D printing can be divided into several categories including: Fused Deposition Modeling (FDM), Selective Laser Melting (SLM), Stereolithography (STL) or Laminated Object Manufacturing (LOM) [1]. Most low-cost desktop 3D printers utilize FDM as the manufacturing process. FDM forms a 3D geometry by assembling individual layers of extruded thermoplastic filament. The FDM manufacturing process is useful for rapidly producing prototypes and in some

170

cases can be used to produce functional components. However, there are disadvantages to utilizing FDM printed parts for functional components. FDM components are formed by an additive manufacturing process combining successive layers of molten thermoplastic. Due to this process delamination of the component layers can occur resulting in premature failure. Additionally, FDM printed parts typically have lower elastic properties than injection molded components of the same thermoplastics [2].

Several authors have evaluated the mechanical properties of FDM 3D printed parts [3, 4]. The primary focus of these studies has been on conventional FDM printed components [3-5]. These studies have evaluated both commercial FDM 3D printers [3-5] as well as low-cost desktop 3D printers [2]. Currently, new thermoplastic materials are becoming available; these include thermoplastic filaments with embedded metallic particles or reinforced with short carbon fibers [6, 7]. Additionally, a new 3D printer has become commercially available that reinforces 3D printed parts with continuous Glass Fiber, Kevlar Fiber or Carbon Fiber filaments (the MarkOne by MarkForged). This new 3D printer, MarkOne by MarkForged, is designed to produce functional 3D printed parts which are stronger than conventional FDM printed components. The MarkOne 3D printer reinforces FDM printed parts by embedding concentric rings of fibers that follow the components geometry. Specifically, the objective of these new FDM printing methods is to increase the strength of 3D printed parts so that these components can be used for functional products rather than producing non-functional scale models. Currently, continuous fiber reinforced 3D printed parts have not been

extensively investigated in literature. The use of continuous carbon fiber reinforcement was performed by Mori *et al* using a RepRap based 3D printer; however, this study did not evaluate or determine the elastic properties of the carbon fiber reinforced 3D printed components [8]. Understanding the tensile properties of fiber reinforced 3D printed components is necessary to ensure these components meet their required design specifications.

To determine if continuous fiber reinforced FDM printed components can be used for functional components, the mechanical properties need to be determined. The first objective of this study is to evaluate the tensile properties of continuous fiber reinforced 3D printed components produced using the MarkOne 3D printer by performing conventional tensile tests. The second objective of this study is to develop a methodology that allows designers to predict the material properties of continuous fiber FDM printed components. Conventional composite material modeling techniques, such as classical laminate plate theory (CLPT) or volume averaging methods [3, 5, 9-12], can be applied to these materials in order to predict its mechanical properties.

Based on the aforementioned composite material modeling framework a mathematical model for predicting the tensile properties of fiber reinforced 3D printed components will be presented. The results of this study aims to provide designers with a methodology for determining the mechanical properties of fiber reinforced 3D printed components. The presented mathematical model will reduce the need for multiple design iterations in order to produce functional 3D printed components. The Volume Averaging framework has been used in

Chapter 5 in order to determine the mechanical properties of tubular braided composites. The analytical models presented in Chapter 5 and in this chapter demonstrate the versatility of the Volume Averaging methodology.

6.2 Methods

6.2.1 Mechanical Testing

Samples for mechanical testing were fabricated using a MarkOne desktop 3D printer (MarkOne, MarkForged, Somerville, MA). The sample geometry was created according to ASTM D638-14 (ASTM D638-14 Standard Test Method for Tensile Properties of Plastics) using a Type I geometry [13]. The geometry used in this study and critical dimensions are shown in Figure 6-1. The test specimen geometry was created using a computer aided design (CAD) software package (SolidWorks 2015 SP4.0, Dassault Systems, Waltham, MA). The specimen geometry was exported as a stereolithography file (STL) and loaded into a 3D printer slicing software package (Eiger 1.2, MarkForged, Somerville, MA). The Eiger software package is required to control the placement of the fiber reinforcement; therefore other open-source 3D printing software was not used. All samples were printed with a nylon filament (nylon, MarkForged, Somerville, MA) with Kevlar fiber reinforcement (Kevlar Reinforcement, MarkForged, Somerville, MA).
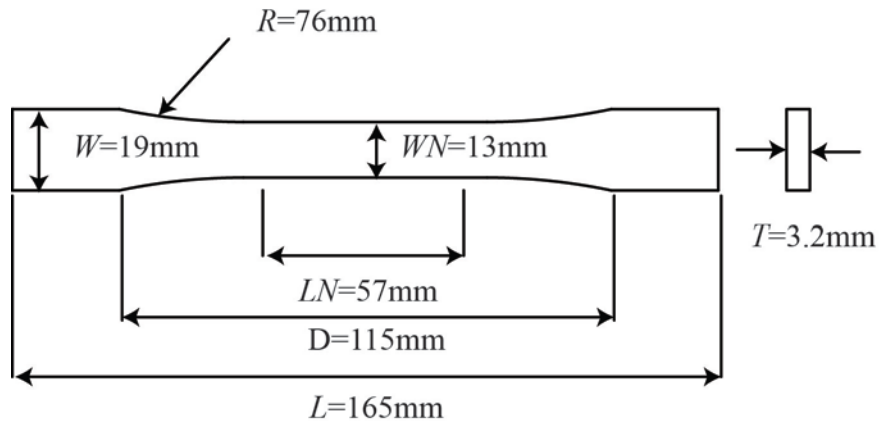
Figure 6-1: Test specimen geometry for tensile testing of 3D printed parts.
Geometry specified according to ASTM D638-14.

The printing parameters used to manufacture the test specimen are summarized in Table 6-1. The MarkOne 3D printer reinforces printed structures using continuous Kevlar, Carbon or Glass fibers. For this study, Kevlar fibers were utilized to reinforce the test specimens. Kevlar was chosen due to the research group's prior experience with this material [14-17]. Three dimensional printed samples are reinforced with concentric fiber rings. The number of possible rings ranges from none (pure polymer) to 5 rings for this geometry; with the limiting factor being the thin 13mm (WN) neck region. The number of concentric fiber rings was varied to quantify the effect of concentric rings on the mechanical properties of the 3D printed test specimen. Samples were printed with 5, 4, 2 and no concentric fiber rings. The number of concentric rings used in this study was selected to characterize the effect of fiber reinforcement on 3D printed samples over the spectrum of possible fiber reinforcement values. The reinforcement of the test specimens with Kevlar yarns is shown in Figure 6-2.

Table 6-1: Test specimen print parameters

Print Parameters	
Layer Height (mm)	0.1
Infill Percentage (%)	10
Infill Orientation (degrees)	45
Number of infill layers	8
Shell Thickness (mm)	0.4
Number of Shells	2
Number of floor layers	4
Number of ceiling layers	4
Number of solid layers	8
Total number of layers	32
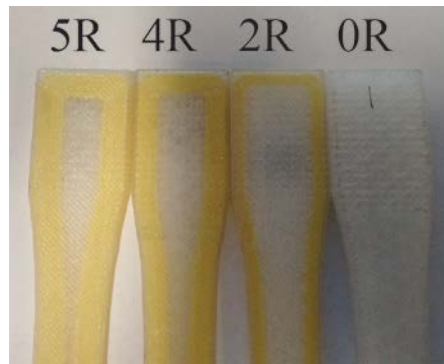
Figure 6-2: Concentric ring reinforcement of test specimens. 5R-five concentric Kevlar fiber rings. 4R- four concentric Kevlar rings. 2R- two concentric Kevlar rings. 0R- no Kevlar reinforcement

6.2.2 Dimensional Measurement of Samples

Prior to performing mechanical tests, Kevlar reinforced 3D printed samples were measured to evaluate the dimensional accuracy of the MarkOne 3D printer. The width at end tabs (W), gauge section width (WN) and thickness (T), shown in Figure 6-1, were measured; the latter three using a micrometer (0-25 ±0.01mm Mitutoyo 102-0701, Kawasaki, Japan). For each test sample dimension (W, WN and T), five measurements were recorded.

6.2.3 Testing Parameters

The fiber reinforced 3D printed specimens were evaluated by performing tensile tests. The test setup used to evaluate the 3D printed samples is shown in Figure 6-3. An MTS tensile testing frame (MTS 810 Material Test System, MTS, Eden Prairie, USA) with a 100 KN (22 Kip) load cell was used to apply loads to the test specimen. Strain of the test samples was measured using a 25.4 mm (1") gauge length extensometer (MTS 634.12E-24, MTS, Eden Prairie, USA). Samples were loaded at a rate of 0.5mm/min and data from the load cell and extensometer was collected at a rate of 20Hz.
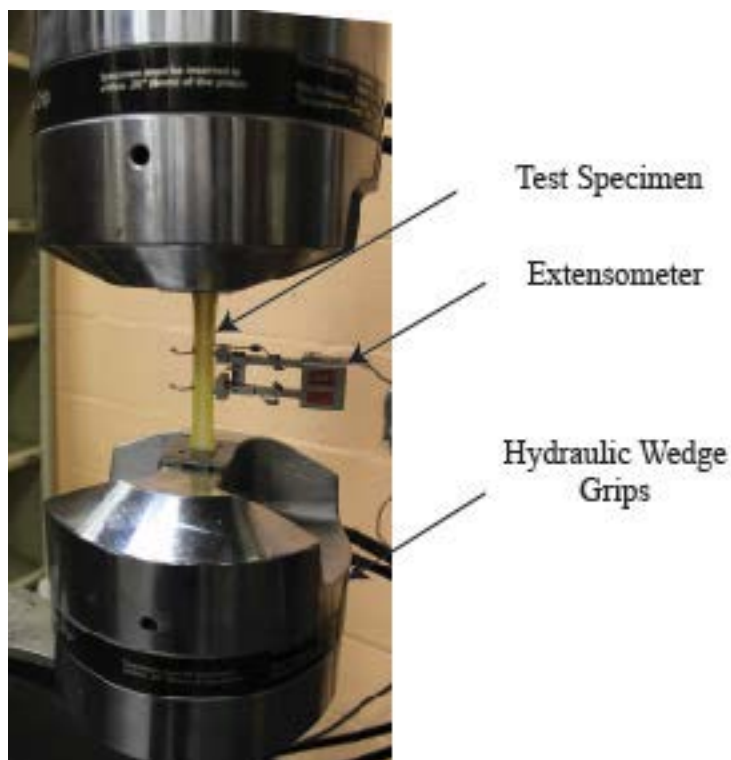
Figure 6-3: Mechanical testing setup to evaluate the tensile properties of Kevlar reinforced 3D printed specimen.

6.2.4 Optical Microscopy

Test samples used in this study were examined using an optical microscope. Optical microscopy was performed in order to gain insights into the internal structure of the 3D printed samples and to examine the failure mechanism for these samples. Samples were mounted using cold cure epoxy resin (Cold Cure, System Three Resins, Inc., Auburn, WA, USA) in 1" diameter sample cups (Buehler Canada, Whitby, ON, Canada). Resin and hardener were mixed, according to manufacturer specifications, at a ratio of 2:1 and poured over sample sections of the fiber reinforced 3D printed parts. The resin was allowed to cure at room temperature for a minimum of 12 hours.

Following curing, the samples were then prepared using a 4-step method to ready the samples for imaging. First, samples were ground until plane using a 320 grit SiC paper, and large scratches were removed using a 600 grit SiC paper. The sample was then polished using diamond suspensions on polishing cloths, beginning at 9-micron monocrystalline diamond suspensions followed by a 3 micron monocrystalline diamond suspension. Final polishing was performed with a 0.05-micron alumina suspension on polishing cloth. All consumables were supplied from Buehler Canada. The sample polishing procedure is outlined in Table 6-2.

Table 6-2: Outline of sample preparation for imaging

Task	Surface
Grinding	320 grit SiC paper
Grinding	600 grit SiC paper
Polishing	9 micron diamond suspension, polishing cloth
Polishing	3 micron diamond suspension, polishing cloth
Final polishing	0.05 micron alumina suspension, polishing cloth

Samples were then imaged using a high resolution camera (Basler piA2400-17gm, Basler AG, Ahrensburg, DE) mounted with a variable magnification lens (Infiniprobe MS, Infinity USA, Boulder, CO, USA). The magnification of this particular set of images was between 2x and 3x, thus in the final images the pixel width is approximately 1 to 2 μm.

6.2.5 Prediction of Elastic Constants

A new volume averaging method has been implemented in order to predict the elastic constants of fiber reinforced 3D printed parts. The volume averaging method utilized is an analytical model based on a volume average stiffness method to predict the effective elastic constants of a fiber reinforced 3D printed part [10]. The fiber reinforced 3D printed parts consist of several different regions, each with their own elastic constants. The analytical model allows for the contribution of each of these regions to be accounted for in order to predict the effective elastic modulus of the fiber reinforced 3D printed specimen. The analytical model has been developed as a custom MATLAB script (MATLAB

2015a, The MathWorks, Natick, MA) to allow for rapid computation of the mechanical properties of a 3D printed structure.

In order to predict the mechanical properties of the Kevlar-reinforced 3D printed samples the mechanical properties of the nylon filament and Kevlar reinforcement were assumed as the specific mechanical properties were not specified by the manufacturer. The assumed mechanical properties for the nylon filament and Kevlar fibers are summarized in Table 6-3 and Table 6-4 respectively [18, 19].

Table 6-3: Assumed elastic constants of nylon filament [19]

Material Property	Value
Elastic Modulus –E (GPa)	0.35- 3.5
Shear Modulus G (GPa)	0.13- 1.30
Poisson's ratio - v	0.35

Table 6-4: Assumed elastic constants of Kevlar 29 yarns [18]

Material Property	Value
Longitudinal Elastic Modulus –E_{f1} (GPa)	79.8
Transverse Elastic Modulus E_{f2} (GPa)	2.59
In-plane Shear Modulus G_{f12} (GPa)	2.1
Poisson's ratio – v_{12}	0.33
Poisson's ratio - v_{23}	0.1

6.2.6   Internal Microstructure

A schematic of the internal structure of the fiber reinforced 3D printed specimen is shown in Figure 6-4. It can be seen that four distinct regions exist within the test samples: shell layers form the external structure of the test specimen where the extruded nylon is oriented along the longitudinal axis of the test specimen; solid layers which consist of closed layers of nylon and alternate orientation between ±45° from the longitudinal axis; infill layers which consist of sparse

layers of nylon. Similar to the solid layers, infill layers alternate orientation between ±45° from the longitudinal axis; and, Kevlar layers which consist of concentric rings of Kevlar fibers. The Kevlar fibers are oriented along the longitudinal axis of the test sample. The Kevlar layers also consist of infill regions as the Kevlar yarns do not fill the entire cross-section of the test samples.
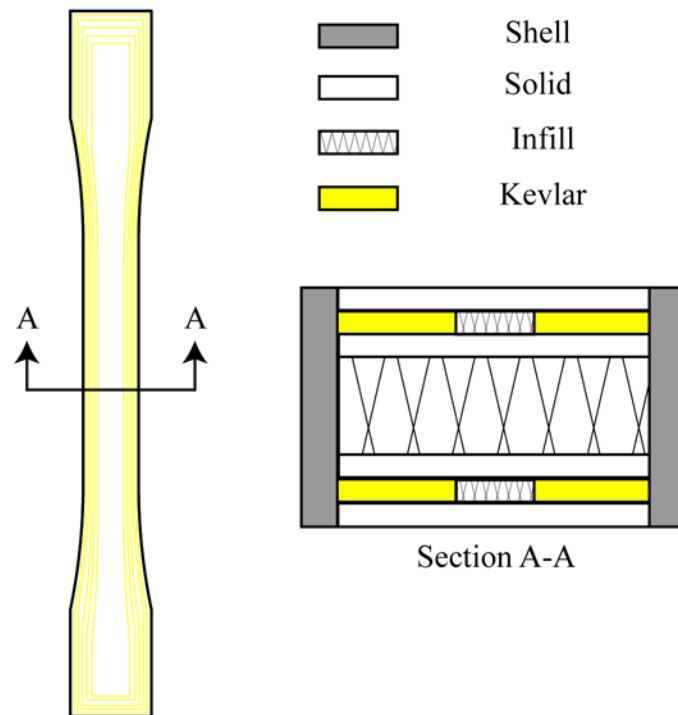
Figure 6-4: Schematic of the structure of the fiber reinforced 3D printed test specimen. Left: top view of the 3D printed test specimen. Right: Cross-sectional view (Section A-A) of the test specimen. Solid regions are represented as solid white rectangles, infill regions have a hatch pattern and Kevlar reinforced regions are represented as yellow.

A cross-sectional image that shows the internal structure of a single test specimen is shown in Figure 6-5, in which infill and shell regions can be seen. A top view of a test specimen is also shown in Figure 6-6. Here, the orientation of the solid layers is 45° from the longitudinal axis of the test specimen. The schematic in

Figure 6-4 and the images in Figure 6-5 and Figure 6-6 will be used to determine

the geometry and structure of the test sample.
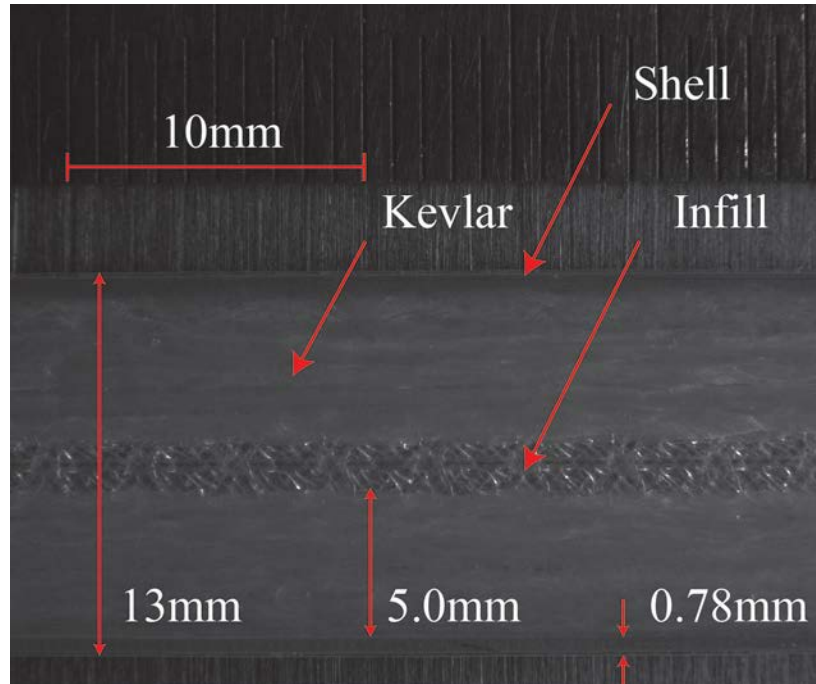
Figure 6-5: Cross-sectional image of a test specimen. The shell, infill and Kevlar regions of the test specimen are shown.
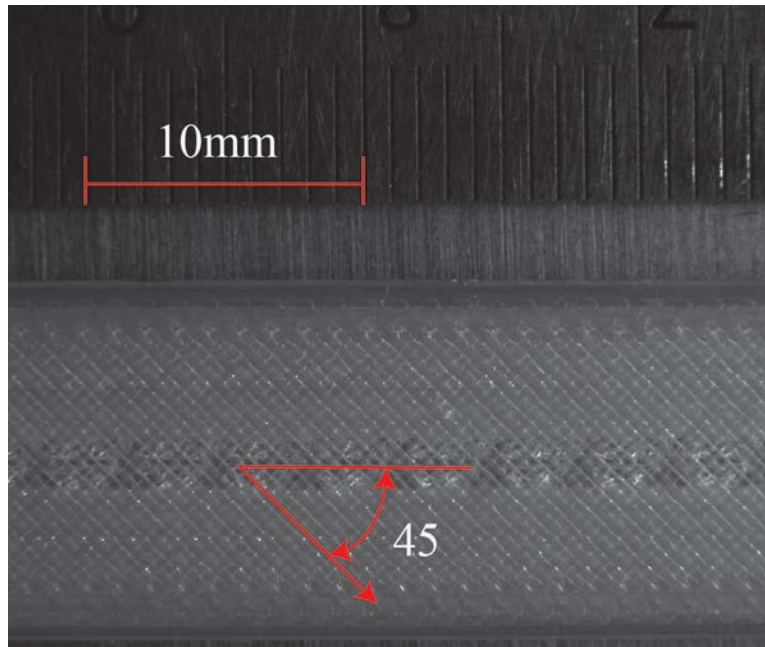
Figure 6-6: Top view of a test sample showing the orientation of the solid layers. Solid layers are oriented 45° from the longitudinal axis.

The volume fraction of each component of the test specimen was determined from the geometry of the sample. The dimensions of the individual components within the test specimen are summarized in Table 5. The variables summarized in Table 6-5 were used to calculate the volume (in mm^3) of each component using equations 6-1- 6-7.

Table 6-5: Sample geometry internal dimensions

Sample Geometry Variable	Value
Height (*H*)-mm	57
Width (*W*)-mm	13
Thickness (*T*)- mm	3.2
Width of Fiber (W$_{fiber}$) - mm	0.7
Number of fiber layers (*N$_{fiber}$*)	6
Number of fiber concentric rings (*N$_{concentric}$*)	5,4,2,0
Layer Thickness (*T$_{layer}$*) - mm	0.1
Number of Floor Layers (N$_{floor}$)	4
Number of Ceiling Layers (*N$_{ceiling}$*)	4
Number of Solid Layers (N$_{solid}$)	8

The total sample volume ($V_{tensile}$) is:

$$V_{tensile} = H \cdot W \cdot T \qquad \text{6-1}$$

The floor volume (V_{floor}) is given by:

$$V_{floor} = [W - (W_{shell} \cdot 2)] \cdot H \cdot T_{layer} \cdot N_{floor} \qquad \text{6-2}$$

The ceiling volume ($V_{ceiling}$) is given by:

$$V_{ceiling} = [W - (W_{shell} \cdot 2)] \cdot H \cdot T_{layer} \cdot N_{ceiling} \qquad \text{6-3}$$

The solid volume (V_{solid}) is found as:

$$V_{ceiling} = [W - (W_{shell} \cdot 2)] \cdot H \cdot T_{layer} \cdot N_{solid} \qquad \text{6-4}$$

The infill volume (V_{infill}) is given by:

$$V_{infill} = [W - (W_{shell} \cdot 2)] \cdot H \cdot T_{layer} \cdot N_{infill} \qquad \text{6-5}$$

The fiber volume (V_{kevlar}) is found as:

$$V_{kevlar} = W_{fiber} \cdot T_{layer} \cdot N_{concentric} \cdot 2 \cdot N_{fiber} \qquad \text{6-6}$$

The infill Volume in Fiber Region ($V_{infillFiber}$) mm^3 is given by:

183

$$V_{\text{inf illfiber}} = \left[W - (2 \cdot W_{shell}) - (W_{fiber} \cdot N_{concentric} \cdot 2) \right] \cdot T_{layer} \cdot H \cdot N_{fiber} \qquad \text{6-7}$$

The volume fraction of each section of the test specimen is computed using Equations (6-8) – (6-12). Where the volume fraction of the floor (V_{ffloor}) and ceiling $(V_{fceiling})$ layers are found using:

$$V_{ffloor} = \frac{V_{floor}}{V_{tensile}} \qquad \text{6-8}$$

$$V_{fceiling} = \frac{V_{ceiling}}{V_{tensile}} \qquad \text{6-9}$$

The volume fractions of the solid (V_{fsolid}) and infill layers $(V_{finfill})$ are found using:

$$V_{fsolid} = \frac{V_{solid}}{V_{tensile}} \qquad \text{6-10}$$

$$V_{f \inf ill} = \frac{V_{\inf ill}}{V_{tensile}} \qquad \text{6-11}$$

And finally, the volume fraction of the Kevlar Fibers $(V_{fkevlar})$ is found using:

$$V_{fkevlar} = \frac{V_{kevlar}}{V_{tensile}} \qquad \text{6-12}$$

6.2.7 Volume Average Stiffness Method

The effective elastic constants of the fiber reinforced 3D printed samples will be determined using a volume average stiffness method [9-12]. The volume

184

averaging method involves three main steps. First, micromechanical models are used to determine the effective properties of the FDM printed components. Second, a coordinate system transformation is applied to the solid and infill layers. Third, volume averaging of the stiffness matrices of each of the cross-sectional regions is performed.

To determine the micromechanical properties of the solid, infill and shell regions the model developed by Rodriguez *et al.* is used to determine the unidirectional constants for a FDM component [5]. The model of Rodriguez *et al.* treats FDM-printed parts as a plastic/void composite. The elastic properties for nylon shown in Table 3 were used to determine the micromechanical properties of the shell, infill and solid layers. Equations (6-13) – (6-17) are used to determine the mechanical properties of the FDM printed sections. In equations (6-13) – (6-17) ρ_1 represents the void density in each component. Void density for the solid layers was assumed to be 10% while the infill sections were assumed to have a void density of 90%. Equations (6-13) – (6-17) demonstrate that the FDM printed portions of the test specimen will behave in a transversely isotropic manner.

$$E_{11} = (1 - p_1)E \qquad \qquad \text{6-13}$$

$$E_{22} = (1 - p_1^{1/2})E \qquad \qquad \text{6-14}$$

$$G_{12} = G \frac{(1 - p_1)(1 - p_1^{1/2})}{(1 - p_1) + (1 - p_1^{1/2})} \qquad \qquad \text{6-15}$$

$$\upsilon_{12} = (1 - p_1)\upsilon \qquad \qquad \text{6-16}$$

$$\upsilon_{21} = (1 - p_1^{1/2})\upsilon \qquad \qquad \text{6-17}$$

Once the micromechanical properties of the solid, infill and shell regions are determined the compliance matrix of each region can be populated. The compliance matrix for a transversely isotropic material is shown in (6-18).

$$[S] = \begin{bmatrix} \dfrac{1}{E_1} & -\dfrac{\upsilon_{21}}{E_2} & -\dfrac{\upsilon_{31}}{E_3} & 0 & 0 & 0 \\[2mm] -\dfrac{\upsilon_{12}}{E_1} & \dfrac{1}{E_2} & -\dfrac{\upsilon_{32}}{E_3} & 0 & 0 & 0 \\[2mm] -\dfrac{\upsilon_{13}}{E_1} & -\dfrac{\upsilon_{23}}{E_2} & \dfrac{1}{E_3} & 0 & 0 & 0 \\[2mm] 0 & 0 & 0 & \dfrac{1}{G_{23}} & 0 & 0 \\[2mm] 0 & 0 & 0 & 0 & \dfrac{1}{G_{13}} & 0 \\[2mm] 0 & 0 & 0 & 0 & 0 & \dfrac{1}{G_{12}} \end{bmatrix} \qquad \text{6-18}$$

The solid and infill regions of the test specimen are transformed using the rotation matrix, [T], shown in equation (6-19). In this equation c represents cosine and s represents sine and θ is the angle of the solid and infill layers. The new stiffness matrix [Sxyz] relative to the global specimen coordinate system is determined for all solid and infill layers.

$$S_{XYZ} = [T]^T [S'_{xyz}][T] \qquad \text{6-19}$$

where

$$[T] = \begin{bmatrix} c^2 & s^2 & 0 & 0 & 0 & 2cs \\ s^2 & c^2 & 0 & 0 & 0 & -2cs \\ 0 & 0 & 1 & 0 & 0 & 0 \\ 0 & 0 & 0 & c & s & 0 \\ 0 & 0 & 0 & -s & c & 0 \\ -cs & cs & 0 & 0 & 0 & c^2 - s^2 \end{bmatrix}$$

and

$$c = \cos(\theta)$$
$$s = \sin(\theta)$$

The stiffness averaging is performed by determining the volume fraction of each section within the test specimen in order to determine the contribution of each section to the overall mechanical properties. The stiffness averaging equation used to predict the mechanical properties of the test specimen is shown in (6-20). This equation shows that the contribution of the infill, shell, solid and Kevlar fiber regions are taken into account in order to determine the effective properties of the fiber reinforced 3D printed test specimen.

$$[C^G] = V_{fshell}[C_{shell}] + V_{f\,\text{inf}\,ill-\theta}[C_{\text{inf}\,ill-\theta}] + V_{f\,\text{inf}\,ill+\theta}[C_{\text{inf}\,ill+\theta}] + V_{fsolid-\theta}[C_{solid-\theta}] + V_{fsolid+\theta}[C_{solid+\theta}] + V_{fkevlar}[C_{kevlar}]$$

6-20

To determine the effective mechanical properties of the fiber reinforced 3D printed parts the global stiffness matrix is inverted as shown in (6-21). Finally, the effective elastic constants can be determined as shown in equation (6-22).

$$S^G = \left[C^G\right]^{-1}$$

<div align="right">6-21</div>

$$E_x = \frac{1}{S^g_{11}}, \quad E_y = \frac{1}{S^g_{22}}, \quad E_z = \frac{1}{S^g_{33}}$$

$$G_{xy} = \frac{1}{S^g_{66}}, \quad G_{yz} = \frac{1}{S^g_{44}} \quad G_{xz} = \frac{1}{S^g_{55}}$$

<div align="right">6-22</div>

$$\upsilon_{xy} = \frac{-S^g_{12}}{S^g_{11}}, \quad \upsilon_{zx} = \frac{-S^g_{13}}{S^g_{33}},$$

$$\upsilon_{yz} = \frac{-S^g_{23}}{S^g_{22}}$$

6.3   Results

6.3.1   Dimensional Measurement

Geometric measurements of the test samples were performed to evaluate the consistency of the MarkOne 3D printer. Measurements were also required in order to determine the cross-sectional area of the test samples. The geometric measurements of the test samples were compared with the nominal dimensions for the ASTM D638 Type I dogbone sample shown in Figure 6-1. The width of the narrow section (WN), width at both end tabs (W1 and W2) and sample thickness (T) was compared for all samples. A t-test was used to compare the nominal sample dimensions with the measured sample dimensions. A p-value of <0.05 was used as the criteria to indicate that a statistically significant difference

exists between the nominal sample and measured sample dimensions. The resulting sample measurements and comparison with the nominal sample dimensions are summarized in Table 6-6- Table 6-9. From these tables it can be seen that the sample dimensions deviated from the nominal dimensions. A similar measurement method was used by Melenka *et al.* to compare nominal and printed sample dimensions [2].

Table 6-6: Comparison of MarkForged MarkOne sample width with nominal dimensions

Sample Measurement	Width Narrow (WN)		
Nominal Dimension (mm)	13.00	% Difference	*p*-value
Sample 2R - Average (Standard Deviation)	13.09 (0.10)	0.72	<0.001
Sample 4R - Average (Standard Deviation)	13.11 (0.11)	0.86	<0.001
Sample 5R - Average (Standard Deviation)	13.09 (0.08)	0.72	<0.001
Sample Ny - Average (Standard Deviation)	13.05 (0.06)	0.39	<0.001

Table 6-7: Comparison of MarkForged MarkOne sample end tab width with nominal dimension

Sample Measurement	Width End Tab 1 (W1)		
Nominal Dimension (mm)	19.00	% Difference	*p*-value
Sample 2R - Average (Standard Deviation)	19.06 (0.06)	0.46	<0.001
Sample 4R - Average (Standard Deviation)	19.14 (0.08)	1.15	<0.001
Sample 5R - Average (Standard Deviation)	19.10 (0.08)	0.81	<0.001
Sample Ny - Average (Standard Deviation)	19.06 (0.17)	0.46	0.015

Table 6-8: Comparison of MarkForged MarkOne sample end tab width with nominal dimension

Sample Measurement	Width End Tab 2 (W2)		
Nominal Dimension (mm)	19.00	% Difference	*p*-value
Sample 2R - average (standard deviation)	19.08 (0.071)	0.66	<0.001
Sample 4R - average (standard deviation)	19.13 (0.09)	1.02	<0.001
Sample 5R - average (standard deviation)	19.09 (0.09)	0.71	<0.001
Sample Ny - average (Standard Deviation)	19.037 (0.06)	0.29	<0.001

Table 6-9: Comparison of MarkForged MarkOne sample thickness with nominal dimension

Sample Measurement	Thickness (T)		
Nominal Dimension (mm)	3.20	% Difference	p-value
Sample 2R - Average (Standard Deviation)	3.30 (0.03)	3.15	<0.001
Sample 4R - Average (Standard Deviation)	3.28 (0.03)	2.76	<0.001
Sample 5R - Average (Standard Deviation)	3.32 (0.07)	3.81	<0.001
Sample Ny - Average (Standard Deviation)	3.28 (0.02)	2.71	<0.001

6.3.2 Microstructure Analysis

The microstructure of the 3D printed samples was examined using a camera equipped with an optical microscope. Figure 6-7 shows a sampling of the images obtained via optical microscopy. The first image, Figure 6-7 (a), reveals the cross section of the fiber reinforced part. Here the shell, infill, and Kevlar regions can be clearly identified. In the Kevlar regions, nylon gaps can be observed between each of the concentric rings of reinforcing fiber. Figure 6-7 (b) highlights the waviness of the reinforcing fibers. The mechanical significance and potential impact of this misalignment will be further discussed in Section 6.4.3. Figure 6-7 (c) shows the fiber path at the corner of the printed part. Note that this particular sample was not ground parallel to the sample, and thus some of the fiber reinforcement appears to have been removed. Figure 6-7 (d) was not mounted in epoxy resin and is an image of the failure location. This image supports the

proposition that fiber pull-out may have been a primary failure mechanism for the failure of the part, as will be discussed in Section 4.4. Note a large portion of the matrix has been displaced independent of the fibers, indicating insufficient adhesion between the fibers and matrix.
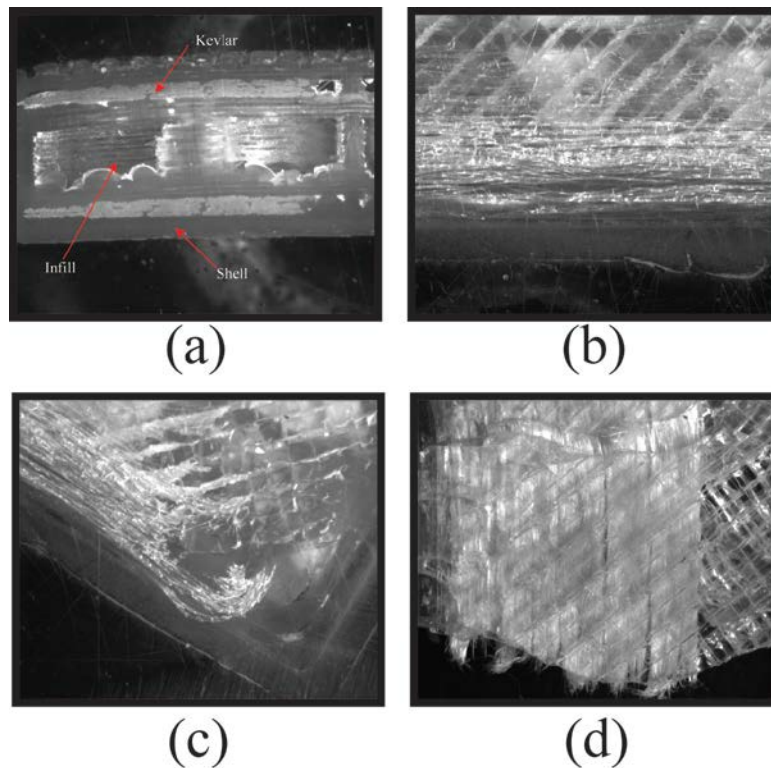
Figure 6-7: Microscope images of fiber reinforced 3D printed parts, showing (a) cross section with shell, Kevlar, and infill regions; (b) waviness of reinforcing fibers; (c) close-up of fiber orientation at corner; and (d) fiber pull-out consistent with failure locations.

6.3.3 Mechanical Testing Results

Mechanical testing was performed on four sample configurations (Ny, 2R, 4R and 5R) to examine the effect of fiber reinforcement on the mechanical properties. The resulting stress-strain diagrams for the four sample configurations are shown in Figure 6-8. The stress-strain curves shown in Figure 8 demonstrate the effect

of variations to the Kevlar reinforcement of the 3D printed samples on stress-strain behavior.
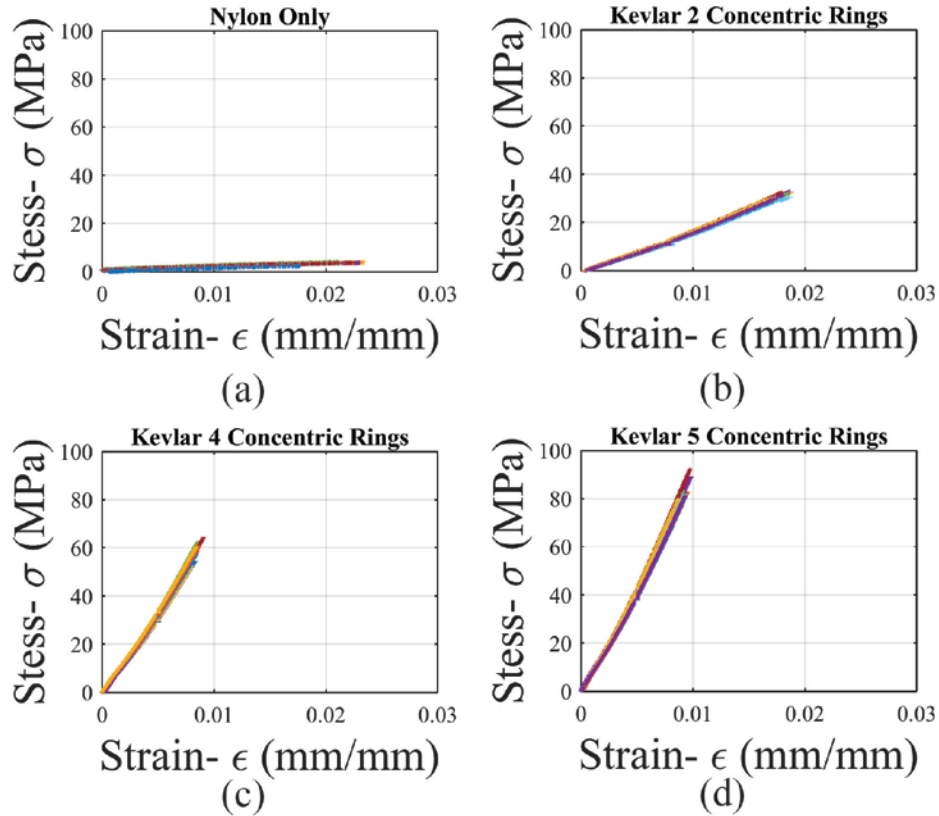
Figure 6-8: Stress-strain curves for the four Kevlar fiber reinforcement configurations (a) nylon only sample configuration (b) two-concentric Kevlar rings configuration (c) four concentric Kevlar rings configuration (d) five concentric Kevlar rings configuration. Stress-strain curves only show up to maximum stress for each sample.

The elastic modulus of each sample configuration was determined from the stress-strain curves shown in Figure 6-8. The average elastic moduli for the four sample configurations are shown in Figure 6-9. This figure shows the resulting elastic moduli and standard deviation for each sample configuration. Figure 6-9 demonstrates that an increase in fiber reinforcement results in an increase in

elastic modulus. This figure also shows that fiber reinforcement results in a dramatic increase in elastic modulus compared to nylon only 3D printed samples.
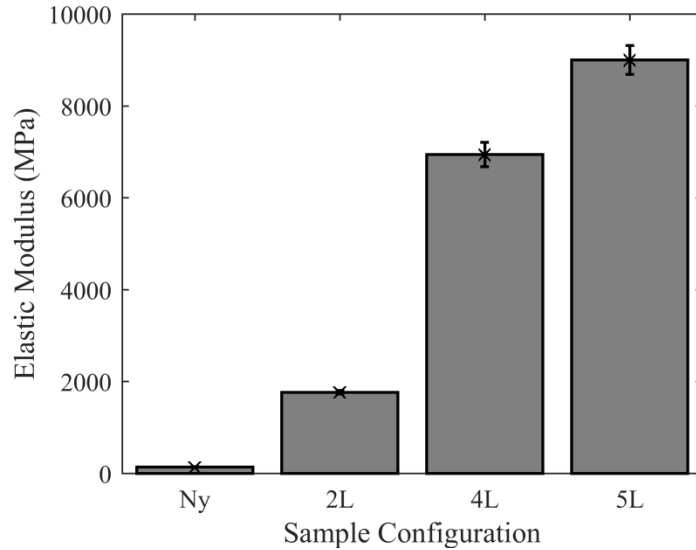
Figure 6-9: Comparison of the experimentally determined elastic moduli of the four fiber reinforced 3D printed sample configurations.

The ultimate tensile strength of the fiber reinforced test samples was also examined. Figure 6-10 shows the resulting average ultimate tensile strength and standard deviation for the three fiber-reinforced sample configurations. This figure demonstrates that as fiber reinforcement increases, the ultimate tensile strength of the fiber reinforced 3D printed components also increases. The nylon only samples were excluded from this comparison as failure was not achieved during testing due to their high toughness.
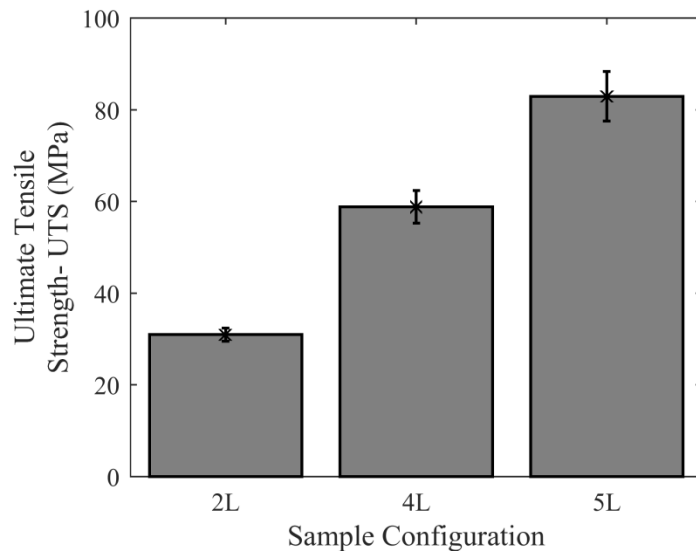
Figure 6-10: Comparison of experimentally measured fiber reinforced 3D printed test samples ultimate strength.

6.3.4 Elastic Constant Prediction for Fiber Reinforced 3D Printed Parts

The effective elastic constants of the fiber reinforced 3D printed samples were predicted using a rule of mixtures and volume average stiffness mathematical model described in Section 2.3. The geometric values shown in Table 6-5 were used to estimate the contribution of the Solid, infill, and fiber sections of the test specimen. The mechanical properties of the nylon filament and Kevlar fibers were assumed based on the values in Table 6-3 and Table 6-4.

The resulting predicted elastic moduli for the four sample configurations investigated are shown in Figure 6-11. Figure 6-11 demonstrates that the VAS model predicts and increase in elastic modulus as fiber reinforcement increases.

195
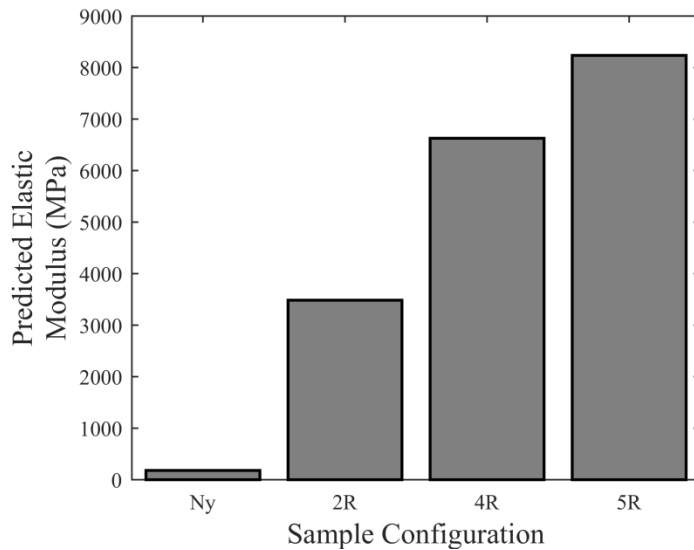
Figure 6-11: Predicted elastic moduli for fiber reinforced 3D printed samples using a volume averaging stiffness method.

6.4 Discussion

6.4.1 Dimensional Measurement

The dimensional accuracy of the MarkOne 3D printer was evaluated. The dimensions of the 3D printed test specimen were compared with nominal CAD dimensions for the 3D printed geometry. Table 6-6 to Table 6-9 demonstrate that the printed sample geometries differed from the nominal CAD part dimensions. The results in Table 6-6 through Table 6-9 are consistent with other studies that have evaluated the dimensional accuracy of desktop 3D printed parts [2]. Table 6-6 to Table 6-9 show that the measure sample dimensions typically vary ±0.1mm from the nominal dimensions of the original CAD model. Understanding the dimensional accuracy of desktop 3D printers is necessary as this allows designers to select appropriate fits and tolerances for functional components produced using this manufacturing method. A comprehensive understanding of geometric

accuracy can aid the designer in predicting error and compensating for the inherent limitations of the 3D printer.

6.4.2 Microstructure Analysis

The images produced from the optical microscopy analysis are of sufficient quality for qualitative analysis. Some error was noted in the alignment of specimen plane to the ground sample plane, as can be easily seen in Figure 6-7 (c). This is a result of the manual polishing approach that was used. As well, it was noted that debris collected in the larger voids of the sample (most notably in the infill regions), contributing to the scratches that can be seen in the images. Additionally, a lack of wetting of Kevlar fibers in the printed sample led to some fraying of fibers during the grinding and polishing, degrading the quality of the polished surface as this would lead to fiber debris during the final polishing steps.

6.4.3 Mechanical Testing

The stress-strain plots in Figure 6-8 demonstrate the effect of fiber reinforcement on the behavior of fiber reinforced 3D printed components. The stiffness, ultimate strength and ultimate strain all increase as the quantity of fiber reinforcement increases. Figure 6-8 also demonstrates the increase in stiffness of fiber reinforced 3D printed components relative to nylon only samples. This is expected because of the Kevlar fibers have a much greater elastic modulus and ultimate tensile strength than nylon. Therefore, the addition of Kevlar fibers results in an increase in the effective properties of the 3D printed samples.

The stress-strain curves in Figure 6-8 (b)-(d) demonstrate non-linear behavior. The non-linear behavior of the fiber-reinforced 3D printed specimen is due to the MarkOne 3D printer manufacturing process. Kevlar fibers are embedded into the test specimen in specific regions of the 3D printed part. During the fiber embedding process however tension is not applied to the Kevlar strands, as a result fiber waviness occurs in the Kevlar strands (shown in Figure 6-12). This figure shows that the Kevlar fibers are not completely aligned with the longitudinal axis of the test sample. Fiber waviness effects the mechanical properties of the 3D printed parts as the embedded fibers are not entirely aligned with the loading axis of the test samples. The effect of fiber waviness on the mechanical properties of composite laminates was demonstrated by Hsiao *et al* [22]. As the samples are loaded the embedded fibers begin to straighten due to the applied tensile load. This straightening of the embedded yarns explains the non-linear behavior of the samples shown in Figure 6-8 (b)-(d).
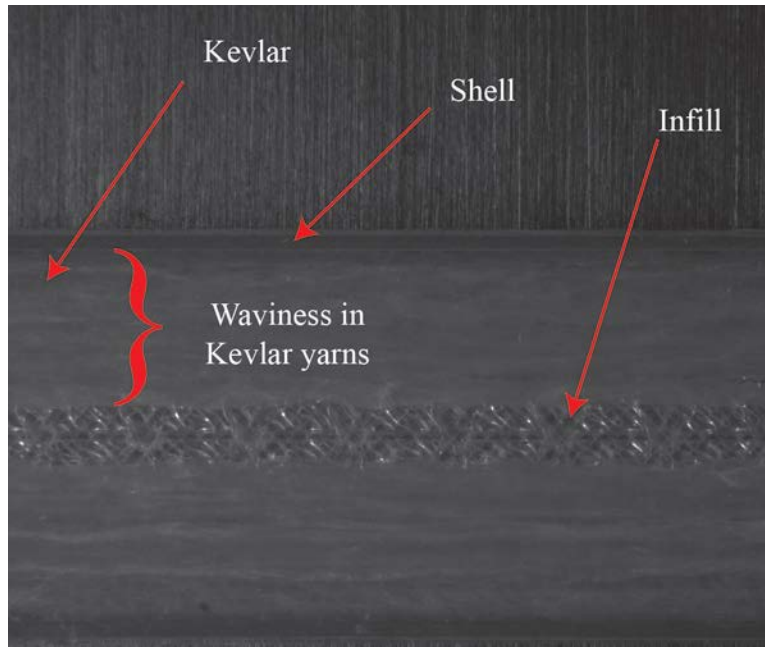
Figure 6-12: Cross-sectional view of a Kevlar reinforced 3D printed test sample. The waviness of Kevlar fibers demonstrated in this image.

The effect of fiber reinforcement on 3D printed parts is shown in Figure 6-9 and Figure 6-10. These figures demonstrate that both the elastic modulus and ultimate tensile strength increase as fiber reinforcement increases.

The failure location for the fiber reinforced 3D printed samples was consistent for all samples tested. The failure location can be seen in Figure 6-13. In this figure, the fiber placement path generated using the Eiger 3D printing software and a failed sample is shown. It can be seen that sample failure occurs at the location where the fiber path begins for the sample. All geometries manufactured using the MarkOne 3D printer will have a start location for the continuous fiber reinforcement. Figure 6-13 demonstrates that understanding the start location of the fiber reinforcement is critical for manufacturing functional components. When designing components to be manufactured using this 3D printing method

the start location of the fiber reinforcement should be placed in a position of low loading in order to prevent premature failure due to the stress concentration caused by the fiber start location.
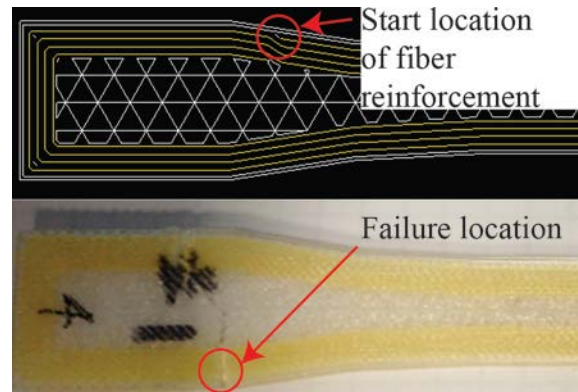
Figure 6-13: Sample failure location. Sample failure occurs at the starting location of the Kevlar fiber reinforcement.

6.4.4 Comparison of mechanical model results with experiments

The mechanical properties of the fiber reinforced 3D printed specimen were predicted using a volume averaging stiffness method. This approach allows for the mechanical properties of the fiber reinforcement and thermoplastic filament to be taken into account. In addition, the volume averaging method allows for the contribution of the different internal structures of the fiber reinforced 3D printed components to be analyzed.

The results from experimental analysis of the fiber reinforced 3D printed specimen and the predicted elastic modulus for the test specimen are compared in Table 6-10. This table shows good agreement between the predicted elastic modulus for the fiber reinforced 3D printed test samples with the experimental test data. In particular, the 4 and 5 concentric Kevlar ring samples differed from

experiment by 6.2 and 0.1% respectively. A larger discrepancy was determined for the 2 concentric ring fiber reinforced samples. In this case the predicted and experimental results differed by 57.5%. This difference could again be due to the waviness of the Kevlar fibers. The lower experimental modulus could be due to the misalignment of the Kevlar yarns with respect to the longitudinal axis. The misalignment of the fiber yarns will result in a reduction in the elastic modulus of the test samples. The volume averaging method assumes that the Kevlar yarns are straight and no waviness in the yarns exists. The large discrepancy between the volume averaging results and test results for the 2 concentric ring sample could also be due to the fiber volume fraction. The 2 concentric rings samples have a fiber volume fraction of 4.0%. The low fiber volume fraction could be below the lower limit which is valid for the volume average stiffness method. Another reason for the difference between the model results for the 2 concentric ring samples could also be due to poor bonding between the fibers and the nylon matrix. Composite material models assume that fibers and matrix are perfectly bonded [21]. Imperfect fiber-matrix bonds could results in fiber pull-out or slipping which would results in a lower elastic modulus than the predicted modulus. The results shown in Table 6-10 show that higher fiber volume fractions are better predicted using the volume averaging method, therefore the methodology presented in this manuscript should be used for modeling structures that have fiber volume fractions of 8% and above. As shown in this study greater fiber reinforcement results in an increase in stiffness and ultimate strength, therefore high volume fractions of fibers should be used for stiffness and strength

critical applications. Additionally, different fiber reinforcement patterns may be useful to improve the mechanical properties of fiber reinforced 3D printed parts. This study examined concentric fiber reinforcement but the Eiger 3D printing software also allows for full layers of fiber reinforcement.

Table 6-10: Comparison of measured and predicted elastic modulus for fiber reinforced 3D printed test samples

	2 Concentric Rings Average (StDev)	4 Concentric Rings Average (StDev)	5 Concentric Rings Average (StDev)
Elastic Modulus Experimental (MPa)	1767.2 (39.3)	6920.0 (272.3)	9001.2 (314.2)
Elastic Modulus Predicted (Mpa)	4155.7	7380.0	8992.1
% Difference	57.5	6.2	0.1
Fiber Volume Fraction (Vf) %	4.04	8.08	10.1

The comparison in Figure 6-10 demonstrates that the volume averaging method can be used to effectively predict the mechanical properties of fiber reinforced 3D printed parts with higher number of fiber rings. The volume averaging method described in Section 6.2.7 has been implemented so that designers can quickly predict the mechanical properties of fiber reinforced 3D printed components. The approach described in this section can be used to predict the mechanical properties of other fiber reinforcing materials including glass fiber and carbon fiber. Both of these fiber reinforcements are available for the MarkOne 3D printer.

6.5 Conclusions

The tensile properties of fiber reinforced 3D printed components were evaluated in this study. Tensile tests were performed on four combinations of samples that were produced using the MarkOne 3D printer. The testing results demonstrated that an increase in the volume of fiber reinforcement results in an increase in stiffness and ultimate strength of the test samples.

In addition, a Volume Averaging stiffness method has been developed in order to predict the tensile properties of the fiber reinforced 3D printed samples. The experimental and predictive model results demonstrated good agreement in particular for sample configurations with higher fiber volume fractions. The predictive model allows for the tensile properties of fiber reinforced 3D printed parts, in particular for sample configurations with higher fiber volume fractions, to be easily predicted. This model will allow for designers to predict the tensile properties of fiber reinforced 3D printed parts so that they can be used for functional applications which require specific tensile properties. This study provides a basis for predicting the tensile properties of fiber reinforced 3D printed structure. Further research is required to fully characterize the mechanical behavior of these structures. Compression, bending and torsion tests are required in order to fully characterize the mechanical behavior of these fiber reinforced 3D printed structures.

This chapter demonstrates the versatility of the Volume Averaging method. In Chapter 5 it was demonstrated that the Volume Averaging method can be used to predict the mechanical properties of tubular braided composites. This chapter

shows that the Volume Averaging method can be applied to fiber-reinforced 3D printed structures.

6.6   References

[1] I. Gibson, D. Rosen and B. Stucker, *Additive Manufacturing Technologies : 3D Printing, Rapid Prototyping, and Direct Digital Manufacturing.* New York, NY : Springer, 2015; Second edition, 2015.

[2] G. W. Melenka, J. S. Schofield, M. R. Dawson and J. P. Carey, "Evaluation of dimensional accuracy and material properties of the MakerBot 3D desktop printer," *Rapid Prototyping Journal,* vol. 21, pp. 618-627, 2015.

[3] J. F. Rodriguez, J. P. Thomas and J. E. Renaud, "Characterization of the mesostructure of fused-deposition acrylonitrile-butadiene-styrene materials," *Rapid Prototyping Journal,* vol. 6, pp. 175-186, 2000.

[4] S. Ahn, M. Montero, D. Odell, S. Roundy and P. K. Wright, "Anisotropic material properties of fused deposition modeling ABS," *Rapid Prototyping Journal,* vol. 8, pp. 248-257, 2002.

[5] J. F. Rodríguez, J. P. Thomas and J. E. Renaud, "Mechanical behavior of acrylonitrile butadiene styrene fused deposition materials modeling," *Rapid Prototyping Journal,* vol. 9, pp. 219-230, 2003.

[6] ColorFab. *ColorFab BrassFill 3D Printing Filament.* Available: http://colorfabb.com/brassfill. 2016

[7] 3DXTech, "Carbon Fiber Reinforced PLA Filament," 2014.

[8] K. Mori, T. Maeno and Y. Nakagawa, "Dieless Forming of Carbon Fibre Reinforced Plastic Parts Using 3D Printer," *Procedia Engineering,* vol. 81, pp. 1595-1600, 2014.

[9] A. Kreger and G. Teters, "Use of averaging methods to determine the viscoelastic properties of spatially reinforced composites," *Mechanics of Composite Materials,* vol. 15, pp. 377-383, 1980.

[10] A. Kregers and Y. G. Melbardis, "Determination of the deformability of three-dimensionally reinforced composites by the stiffness averaging method," *Mechanics of Composite Materials,* vol. 14, pp. 1-5, 1978.

[11] A. Kregers and G. Teters, "Determination of the elastoplastic properties of spatially reinforced composites by the averaging method," *Mechanics of Composite Materials,* vol. 17, pp. 25-31, 1981.

[12] A. Kregers and A. Zilauts, "Limiting values of reinforcement factors for fibrous composites with a three-dimensional structure," *Mechanics of Composite Materials,* vol. 20, pp. 530-536, 1985.

[13] ASTM D638-14, "Standard Test Method for Tensile Properties of Plastics," 2014.

[14] J. Carey, M. Munro and A. Fahim, "Longitudinal elastic modulus prediction of a 2-D braided fiber composite," *J Reinf Plast Compos,* vol. 22, pp. 813-831, 2003.

[15] C. Ayranci and J. P. Carey, "Predicting the longitudinal elastic modulus of braided tubular composites using a curved unit-cell geometry," *Composites Part B: Engineering,* vol. 41, pp. 229-235, 2010.

[16] C. K. Leung, G. W. Melenka, D. S. Nobes and J. P. Carey, "The effect on elastic modulus of rigid-matrix tubular composite braid radius and braid angle change under tensile loading," *Composite Structures,* vol. 100, pp. 135-143, 2013.

[17] G. W. Melenka, S. Hoxha, D. S. Nobes and J. P. Carey, "Analytical and experimental analysis of tubular braided composites," in *CANCOM 2015-Canadian International Conference on Composite Materials,* Edmonton, Alberta, Canada, 2015, .

[18] S. Kawabata, "Measurement of the transverse mechanical properties of high-performance fibres," *Journal of the Textile Institute,* vol. 81, pp. 432-447, 1990.

[19] MATWEB *Overview of materials for nylon 6, Extruded*. Available: http://www.matweb.com, 2015

[20] I. M. Daniel and O. Ishai, *Engineering Mechanics of Composite Materials*. New York: Oxford University Press, 2006.

[21] R. M. Jones, *Mechanics of Composite Materials*. Washington, Scripta Book Co. 1975], 1975.

[22] H. Hsiao and I. Daniel, "Effect of fiber waviness on stiffness and strength reduction of unidirectional composites under compressive loading," *Composites Sci. Technol.,* vol. 56, pp. 581-593, 1996.

Chapter 7   Conclusions, Recommendations and Future Work

7.1   Conclusions

The goal of this thesis was to evaluate and characterize the elastic properties of tubular braided composites. In Chapter 3 the three dimensional structure of a tubular braided composite was evaluated using a micro-computed tomography technique. The results of this study demonstrated the three dimensional geometric structure of tubular braided composites. The results obtained in Chapter 3 served as the motivation for the analytical model presented in Chapter 5. In Chapter 3 it was demonstrated that braid yarns within the tubular braid structure follow a sinusoidal path. The sinusoidal nature of braid yarns within the tubular braided composite geometry was used in Chapter 5 to allow for the effect of braid yarns to be accounted for. In addition, the void content and surface porosity of tubular braided composites was examined in Chapter 3. This is the first study to examine the geometry and void content of tubular braided composites using a μCT imaging technique.

Braid samples in this thesis were evaluated using a three dimensional digital image correlation method (3D DIC). The methodology for evaluating tubular braided composites experimentally is presented in Chapter 4. The 3D DIC technique was advantageous as it allows for full field strain measurement along the length of a tubular braid sample. Additionally, this method can be easily adapted for different loading conditions. Due to the adaptability of this optical strain measurement method tubular braided composites were evaluated under both

tensile and torsional loading conditions. The ability to evaluate braided composites under both tensile and torsional loads allowed for longitudinal elastic modulus and shear modulus of the composite braids to be determined. The versatility of the 3D DIC measurement technique is advantageous over conventional strain measurement techniques like strain gauges or extensometers. Additionally, the ability to measure the full-field strain behavior of braided composites rather than discrete data points is vital for understanding the behavior of braided composites due to their non-uniform structure.

The newly developed model for predicting the mechanical properties of tubular braided composites is presented in Chapter 5. The model presenting in this thesis utilizes a Volume Averaging method in order to predict the mechanical properties of tubular braided composites. To support the newly presented analytical model experimental validation has been performed using the methodology presented in Chapter 4. The model presented in this thesis has been validated experimentally for Diamond and Regular braids over a range of braid angles (35-55°). The model presented in this thesis was implemented as MATLAB scripts allowing for rapid computation of braid mechanical properties. In order to predict the mechanical properties of braided composites inputs to the proposed braid model include: braid angle (θ), yarn width (W_y), yarn thickness (a), mandrel diameter (D_0), and the number of braider bobbins (N). In addition to braid geometry parameters model inputs include the type of braid and yarn micromechanical properties. Since the model presented in this manuscript can be automated and allows for rapid calculation of braid mechanical properties; the presented model is

a beneficial tool for design iterations of tubular braided composites. Braiding parameters can quickly be modified and the effect of braiding parameters on mechanical properties can be readily obtained. Few studies in literature have experimentally of analytically examined braided composites over a range of braiding angles and braiding patterns. The results in Chapters 4 and 5 provide a wealth of new information for the modelling and analysis of tubular braided composites.

In addition to presenting a new analytical model for tubular braided composites, this thesis also demonstrated the application of the Volume Averaging methodology to 3D printed fiber reinforced composite materials. The Volume Averaging model for predicting the mechanical properties of fiber-reinforced 3D printed structures is presented in Chapter 6. The ability to model both the mechanical properties and tubular braided composites and fiber reinforced 3D printed composites demonstrates the versatility of the Volume Averaging technique. The results from the Volume Averaging model for fiber-reinforced 3D printed structures were validate against experiments and good agreement was found between the theoretical and experimental results. The analytical models presented in Chapters 5 and 6 demonstrate the versatility of the Volume Averaging technique as this methodology has been applied to braided composites as well as fiber-reinforced 3D printed structures.

7.2 Recommendations

The mechanical properties of tubular braided composites are strongly influenced by the geometry of the braided structure and the mechanical properties of the

matrix and fibers within the braid structure. Key braiding geometric variables include: braid angle (θ), yarn width (W_y), yarn thickness (a), mandrel diameter (D_0) and braid outer diameter (D_{outer}). During the manufacturing of tubular braided composites variations to the aforementioned braid variables occur. In order to achieve reliable production of tubular braided composites and consistent mechanical properties the previously mentioned braiding parameters must be tightly controlled.

Braid mechanical properties can also be influenced by the matrix and fiber volume fractions within the braid structure. The matrix, fiber and void content of a tubular braid are examined in Chapter 3. The results in this chapter demonstrate that voids and imperfections are present throughout the structure of the examined tubular braid sample. Voids and imperfections like the ones shown in Chapter 3 will results in variations in braid mechanical properties and can also cause premature failure of braid samples. Tubular braided composites in this thesis were manufactured using a hand lay-up process in order to impregnate the braid preforms with resin. The hand lay-up process is highly user dependent and therefore automation of the braid impregnation process would be beneficial to the braid manufacturing process to allow for more consistent braid impregnation.

7.3   Future Work

In this thesis, the elastic properties of tubular braided composites were examined. Understanding the elastic properties of braided is an essential when designing structures using tubular braided composites; however, prediction of failure and

the ultimate strength of tubular braided composites are also necessary. Currently, little research has been performed on the prediction of failure of tubular braided composites. The tensile test results shown in Chapters 4 and 5 demonstrate that tubular braids undergo progressive failure. Tubular braids demonstrate a linear stress-strain region until matrix failure occurs. After matrix failure occurs, braid samples demonstrate a necking behaviour since braid yarns are no longer restricted by the matrix. The braid samples will continue to undergo necking until fiber failure occurs. Prediction of the ultimate strength of braided composites is essential to allow for tubular braided composites to be utilized in functional designs.

Tubular braided composites manufactured for this thesis utilized Kevlar yarns in order to form the braid structure. Many other yarns are available in order to produce tubular braided composites including: Carbon, Fiber glass or Dyneema yarns. Additionally, natural fiber yarns could also be used with the braiding process. Natural fiber yarns are a recent development that is gaining traction in industrial and research circles. One of the main advantages of natural fibers is that they can be produced from organic sources and have a lower carbon foot-print than conventional fibers which are produced from petroleum based products.

Appendix A.   Braid Model Code

The MATLAB script for determining the elastic properties of tubular braided composites is provided in this section. The main script for determining braid elastic properties is shown in Figure A-1. In this script the user will input tubular braid dimensions, yarn mechanical properties and the type of braid with is to be modeled.

The main script calls several functions to in order to predict the elastic properties of braided composites. The function shown in Figure A-2 allows for the undulations of braid yarns to be taken into account. Also included in this function are equations that are used to describe the different braiding patterns i.e Diamond, Regular and Hercules. The function *YarnStiffness.m* calls two other functions *CS123Stiffness.m* and *CS123Compliance.m* these functions are shown in Figure A-3 and Figure A-4. These two functions transform the yarn mechanical properties form the local *1-2-3* coordinate system to the undulation coordinate system *x'-y'-z'*. The functions shown in Figure A-3 and Figure A-4 also determine the average stiffness and compliance of the braid yarns over the length of one yarn undulation.

The braid angle of the tubular braided composites is taken into account using the function *transformXYZ.m* shown in Figure A-5. This function transforms the mechanical properties of the braid yarns from their local coordinate system (*x'-y'-z'*) to the global braid coordinate system (*X-Y-Z*).

```
%*********************************************************************
**********
%% Tubular braided composite analytical model
%Author: Garrett Melenka
%Email: gmelenka@ualberta.ca
%date: August 12, 2016
%Description:
%This program calculates the elastic constants for tubular
braided
%composites.  The model allows the user to input geometric
parameters of
%the composite braid as well as the material properties of the
matrix and
%fiber used.  Using these input values the elastic constants are
computed
%while accounting for the braiding angle and undulations that
occur during
%the braiding process.

%The following braid patterns can be analyzed using this method:
%1) diamond braid pattern (1/1)
%2) regular braid pattern (2/2)
%3) Hercules braid pattern (3/3)
%4) Diamond braid pattern with triaxial fibers (1/1) + axial
fibers
%5) Regular braid pattern with triaxial fibers (2/2) + axial
fibers
%6) Braid with no undulations- CLPT based cross-ply laminate with
two plies
%*********************************************************************
**********

%% Initial parameters for braid geometry
%*********************************************************************
*********
a = 0.38; %yarn thickness
b = 3.1; %yarn width
D = 11.1; %mandrel diameter
t = 2*a;
braidType = 3; %type of braid see above

R = D/2; % mandrel size mm
r0 = R+a; % nomial braid radius mm

%Define the braid angle between 30 and 60 degrees
angle = linspace(30,60,100);

%%Define braiding machine parameters
n = 18; %number of carriers
Nc = 2*n; % total number of carriers
beta = 2*pi / n; % braid shift angle (rad)


%*********************************************************************
**********
```

```matlab
%% Material Properties
%Matrix material properties
Em = 3.5;
Gm = 1.3;
num = 0.3;


Vf = 0.6;
% Vv = 4.35 / 100;
% %Vv = 0;
% Vm = 1 - Vf - Vv
%*******************************************************************
*********
% %Fiber, Matrix and Fiber+Matrix Material Properties from
Carey/Ayranci
% %Thesis
Ef1 = 130;
Ef2 = 7.3;
Ef3 = Ef2;
Gf12 = 2.86;
Gf13 = Gf12;
nuf12 = 0.35;
nuf13 = nuf12;
nuf21 = nuf12*(Ef2/Ef1);
nuf31 = nuf12*(Ef3/Ef1);
nuf23 = 0.1;
nuf32 = nuf23*(Ef3/Ef2);
%*******************************************************************
**********
% %Source: Cagri model
E1 = 79.7;
E2 = 5.9;
E3 = E2;
G12 = 1.5;
G13 = G12;
eta23 = (3 - 4*num + (Gm / Gf12)) / (4*(1-num));
G23 = (Gm*(Vf + eta23*(1-Vf))) / (eta23*(1-Vf) + Vf*(Gm/Gf12));
nu12 = 0.3;
nu13 = nu12;
nu23 = (E2/(2*G23)) - 1;
nu21 = nu12*(E2/E1);
nu31 = nu13*(E3/E1);
nu32 = nu23*(E3/E2);

%initial transversely isotropic compliance matrix for yarns+epoxy
S = [1/E1 -nu21/E2 -nu31/E3 0 0 0;...
    -nu12/E1 1/E2 -nu32/E3 0 0 0;...
    -nu13/E1 -nu23/E2 1/E3 0 0 0;...
    0 0 0 1/G23 0 0;...
    0 0 0 0 1/G13 0;...
    0 0 0 0 0 1/G12];



%initial compliance matrix for epoxy
Sm = [1/Em -num/Em -num/Em 0 0 0;...
     -num/Em 1/Em -num/Em 0 0 0;...
     -num/Em -num/Em 1/Em 0 0 0;...
```

215

```matlab
        0 0 0 1/Gm 0 0;...
        0 0 0 0 1/Gm 0;...
        0 0 0 0 0 1/Gm];


C = inv(S); Cm = inv(Sm);




%% Calculate effective stiffness for undulating fibers
for int = 1:length(angle)

    %Diamond Braid Pattern = 1
    %Regular Braid Pattern = 2
    %Hercules Braid Pattern = 3
    %Diamond / Triaxial = 4
    %Regular / Triaxial = 5
    %No undulations (CLPT) = 6


    %calls yarn stiffness function to account for yarn unduation
of braid
    %patterns
    [Sout(:,:,int), Cout(:,:,int), braidName] =
YarnStiffness(angle(int), r0, a, beta, braidType, S, C, int);


end

%% Transform stiffness matrix to global coordinate system XYZ
tb = a;
for i = 1:length(angle)


      %determine fiber volume within braid unit cell
      Vfuc = b * n ./ (8 * r0 * cosd(angle));

      %once unit cell has become jammed fiber volume is constant
        for k = 1:length(Vfuc)

            if Vfuc(k) >=1
                Vfuc(k) =1;
            end
        end
    VucF = Vfuc(i);

    theta = (angle(i)) * (pi/180);

    %transforms braid geometry to account for braid angle
    [SxyzPos, CxyzPos] = transformXYZ(theta, Sout(:,:,i),
Cout(:,:,i));
    [SxyzNeg, CxyzNeg] = transformXYZ(-theta, Sout(:,:,i),
```

```matlab
Cout(:,:,i));

    Cm = inv(Sm);
    Caxial = inv(S);

    VucM = 1 - VucF;

    %Stiffness averaging as per Quek
    Ctotal = VucF*0.5*CxyzPos + VucF*0.5*CxyzNeg + VucM*Cm;

    %Compliance averaging
    CtotalCompliance = VucF*0.5*inv(SxyzPos) +
VucF*0.5*inv(SxyzNeg) + VucM*Cm;



    Vf_overall(i) = VucF*Vf;

    if braidType == 4 || braidType == 5

        Ab = pi * 0.5 * b * 0.5 * tb; %braid yarn area

        ta = 0.38; % axial yarn thickness
        Wa = 3.1; %axial yarn width
        Aa = pi * 0.5 * Wa* 0.5 * ta; %axial yarn area

        t = 2 * tb + ta; %total yarn thickness



        VucFb = 8 * n * Ab / (8 * pi * r0 * cosd(angle(i)) * t);
% braid yarns volume fractions
        VucFa = 4 * Aa * n / (8 * pi * r0 * t); %axial yarn
volume fraction



         Ctotal = VucFb*0.5*CxyzPos + VucFb*0.5*CxyzNeg + VucM*Cm
+ VucFa *Caxial;
    end

    Stotal(:,:,i) = inv(Ctotal);

    StotalByun(:,:,i) = inv(CtotalCompliance);



end

%% Determine Elastic Constants in the global coordinate system
Ex = squeeze(1./Stotal(1,1,:));
Ey = squeeze(1./Stotal(2,2,:));
Ez = squeeze(1./Stotal(3,3,:));
Gxy = squeeze(1./Stotal(6,6,:));
```

```
Gyz = squeeze(1./Stotal(5,5,:));
Gzx = squeeze(1./Stotal(4,4,:));
vxy = squeeze(-Stotal(1,2,:)./Stotal(1,1,:));


ExCompliance = squeeze(1./StotalByun(1,1,:));
EyCompliance = squeeze(1./StotalByun(2,2,:));
EzCompliance = squeeze(1./StotalByun(3,3,:));
GxyCompliance = squeeze(1./StotalByun(6,6,:));
GyzCompliance = squeeze(1./StotalByun(5,5,:));
GzxCompliance = squeeze(1./StotalByun(4,4,:));
vxyCompliance = squeeze(-StotalByun(1,2,:)./StotalByun(1,1,:));


GxyCombined = (Gxy + GxyCompliance)*0.5;
GyzCombined = (Gxy + GyzCompliance)*0.5;
GzxCombined = (Gxy + GzxCompliance)*0.5;


close all;
%% Display Results
figure;
plot(angle, Ex, '-k', angle, Ey, '--k',angle, Ez,
':k','linewidth', 2)
xlabel('Braid Angle (degrees)')
ylabel('Elastic Modulus (GPa)')
title(braidName)
legend('\it{E_{xx}}', '\it{E_{yy}}', '\it{E_{zz}}', 'location',
'best')


figure;
plot(angle, GxyCombined, angle, GyzCombined, angle, GzxCombined,
'-k', 'linewidth', 2)
xlabel('Braid Angle (degrees)')
ylabel('Shear Modulus (GPa)')
%axis([15 60 0 20])
title(braidName)
legend('G_{xy}', 'G_{yz}', 'G_{zx}')



%% Save Results
if braidType == 1
    save melenkaModelPredictionDiamond.mat Ex Ey Ez GxyCombined
GyzCombined GzxCombined vxy angle a b D n
end

if braidType == 2
   save melenkaModelPredictionRegular.mat Ex Ey Ez GxyCombined
GyzCombined GzxCombined vxy angle a b D n
end

if braidType == 3
    save melenkaModelPredictionHercules.mat Ex Ey Ez GxyCombined
GyzCombined GzxCombined vxy angle a b D n
end
```

Figure A-1: Main script for proposed braid model. Mechanical properties and braid dimensions are the model inputs. Output figures display results and results can be saved for later use.

```matlab
function [Syarn, Cyarn, braidName] = YarnStiffness(angle, r0, a,
beta, braidType, S, C, int)

braidAngle = (angle)*(pi/180);
alpha = braidAngle;
Lund = r0 * beta / sin(braidAngle);


%%
*******************************************************************
*********
%Create a sinusoidal equation for each braid type using input
from braid
%geometry.  The sinusoidal equation will be used to determine the
%undulations that occur to the braid.  Undulations will affect
the in-plane
%and out of plane mechanical properties of the braid.
%*****************************************************************
**********
%% Diamond Braid Pattern
    if braidType == 1


        Lund = r0 * beta / sin(braidAngle); % GM confirmed May
15, 2015
        braidName = 'Diamond';
        npts = 1000;
        x = linspace(0,Lund,npts);
        xSpacing = (Lund - 0 ) / (npts - 1);
        k = 2*pi / (Lund);
        z = a*0.5*sin(k*x);
        zprime = a*0.5*k*cos(k*x);

    end

%% Regular Braid Pattern
%GM- changed undulation angle from cos to sin- braid angle
measured from
%longitudinal axis- Feb 3, 2014
    if braidType == 2
        braidName = 'Regular';

        Lund = r0 * beta / sin(braidAngle); % GM confirmed May
15, 2015
        %1) Create a piecewise function for the regular braid
        npts = 1000;
        %regular braid total length = 4p == 2*Lund
        x = linspace(0, 2 * Lund, npts);
        xSpacing = (2 * Lund - 0 ) / (npts - 1);
```

```matlab
        j=1;
        i = 1;
        k1 = 1.0;
        z = zeros(npts,1);
        while(x(i) < 2 * Lund)
        %while(x(i) < j*(k1+1)*beta*(r0/sin(alpha)))
            if abs(x(i)) >= (0 + ((j-
1)*(k1+1)*beta)*(r0/sin(alpha))) && abs(x(i)) < (k1*beta*0.5 +
((j-1)*(k1+1)*beta))*(r0/sin(alpha))
                z(i) = 0.5*a;
                zprime(i) = 0;
            elseif abs(x(i)) >= (k1*beta*0.5 + ((j-
1)*(k1+1)*beta))*(r0/sin(alpha)) && abs(x(i)) <= ((k1+1)*beta*0.5
+ (j-1)*(k1+1)*beta)*(r0/sin(alpha))
                z(i) = -0.5*a*sin((2*pi*sin(alpha)*x(i)) / (r0 *
beta) + pi*0.5);
                zprime(i) = -(0.5*a*2*pi*sin(alpha)/ (r0*beta)) *
cos((2*pi*sin(alpha)*x(i)) / (r0 * beta) + pi*0.5);
            elseif abs(x(i)) >= ((k1+1)*beta*0.5 + ((j-
1)*(k1+1)*beta))*(r0/sin(alpha)) && abs(x(i)) <= ((2*k1 +
1)*beta*0.5 + ((j-1)*(k1+1)*beta))*(r0/sin(alpha))
                z(i) = -0.5*a;
                zprime(i) = 0;
            %elseif abs(x(i)) >= ((2*k1 + 1)*beta*0.5 + ((j-
1)*(k1+1)*beta))*(r0/sind(alpha))  && abs(x(i)) <= ((k1+1)*beta +
((j-1)*(k1+1)*beta))*(r0/sin(alpha))
            else %gm added May 19- ensures that x and z are the
size length/same number of elements
                z(i) = 0.5*a*sin((2*pi*sin(alpha)*x(i)) / (r0 *
beta) + pi*0.5);
                zprime(i) = (0.5*a*2*pi*sin(alpha)/ (r0*beta)) *
cos((2*pi*sin(alpha)*x(i)) / (r0 * beta) + pi*0.5);

            end
            i = i+1;
        end
    end
%% Hercules Braid Pattern
if braidType == 3
    braidName = 'Hercules';
    %1) Create a piecewise function for the regular braid
    npts = 1000;
    %hercules braid total length = 6p == 3*Lund
    x = linspace(0, 3 * Lund, npts);
    xSpacing = (3 * Lund - 0 ) / (npts - 1);
    i = 1;
    z = zeros(npts,1);
    while(x(i) < 3 * Lund)
        if abs(x(i)) >= 0 && abs(x(i)) <
(beta*0.5)*(r0/sin(alpha))
            z(i) = 0.5*a;
            zprime(i) = 0;
        elseif abs(x(i)) >= (beta*0.5)*(r0/sin(alpha)) &&
abs(x(i)) < (2*beta*0.5)*(r0/sin(alpha))
            z(i) = 0.5*a;
            zprime(i) = 0;
```

```matlab
        elseif abs(x(i)) >= (2*beta*0.5)*(r0/sin(alpha)) &&
abs(x(i)) < (3*0.5*beta)*(r0/sin(alpha))
            z(i) = 0.5*a*sin((2*pi*sin(alpha)*x(i)) / (r0 * beta)
+ pi*0.5);
            zprime(i) = (0.5*a*2*pi*sin(alpha)/ (r0*beta)) *
cos((2*pi*sin(alpha)*x(i)) / (r0 * beta) + pi*0.5);
        elseif abs(x(i)) >= (3*0.5*beta)*(r0/sin(alpha)) &&
abs(x(i)) < (4*beta*0.5)*(r0/sin(alpha))
            z(i) = -0.5*a;
            zprime(i) = 0;
        elseif abs(x(i)) >= (4*beta*0.5)*(r0/sin(alpha)) &&
abs(x(i)) < (5*0.5*beta)*(r0/sin(alpha))
            z(i) = -0.5*a;
            zprime(i) = 0;
        %elseif abs(x(i)) >= (5*0.5*beta)*(r0/sin(alpha)) &&
abs(x(i)) < (6*beta*0.5)*(r0/sin(alpha))
        else %gm added May 19- ensures that x and z are the size
length/same number of elements
            z(i) = 0.5*a*sin((2*pi*sin(alpha)*x(i)) / (r0 *
beta) + pi*0.5);
            zprime(i) = (0.5*a*2*pi*sin(alpha)/ (r0*beta)) *
cos((2*pi*sin(alpha)*x(i)) / (r0 * beta) + pi*0.5);
        end
        i = i+1;

    end
end
%% Diamond / Triaxial = 4
if braidType == 4
    braidName = 'Diamond / Triaxial';


    %a - braid yarn thickness
    %aA - axial yarn thickness
    aA = a; % assume axial yarns are same size as braid yarns for
now...
    x = linspace(0,Lund,1000);
    k = 2*pi / (Lund);
    z = (a*0.5*aA*0.5)*sin(k*x);
    zprime = a*k*cos(k*x);



end
%% Regular / Triaxial = 5
if braidType == 5
    braidName = 'Regular / Triaxial';




end
%% No Undulation
if braidType == 6
    braidName = 'CLPT';
end
```

```matlab
% figure; plot(x,z)
% xlabel('Position x (mm)');
% ylabel('Position z (mm)')
%%
%*****************************************************************
*********
%Determine crimp angle along fiber strand path for each braiding
type
%braid crimp angle is used to determine the effect of undulations
on the
%braid effective stiffness
%*****************************************************************
**********
%% Diamond Braid
if braidType == 1
tanB = a*k*0.5*cos(k*x);
cosB = 1 ./ sqrt(1 + tanB.^2);
sinB = tanB ./ sqrt(1 + tanB.^2);
end

%% Regular Braid
if braidType ==2
    tanB = zprime;
    cosB = 1 ./ sqrt(1 + tanB.^2);
    sinB = tanB ./ sqrt(1 + tanB.^2);


    x = x(2:end);


end
%% Hercules Braid
if braidType == 3
    tanB = zprime;
    cosB = 1 ./ sqrt(1 + tanB.^2);
    sinB = tanB ./ sqrt(1 + tanB.^2);
    x = x(2:end);
end

%% Diamond Triaxial Braid
if braidType == 4
    tanB = zprime;
    cosB = 1 ./ sqrt(1 + tanB.^2);
    sinB = tanB ./ sqrt(1 + tanB.^2);


end

%% Regular Triaxial Braid
if braidType == 5
end


%% No Undulations
if braidType == 6
end


%% Evaluate the effective stiffness due to undulations in the 123
coordinate system
```

```
%performs coordinate system transformation along yarn undulation
and
%determines the average stiffness and compliance for one yarn
undulation
Syarn = CS123Stiffness(cosB, sinB, tanB, x, xSpacing, S,int);
Cyarn = CS123Compliance(cosB, sinB, tanB, x, xSpacing, C,int);
```

Figure A-1: Yarn Stiffness function. This function takes into account the yarn undulations of different braiding patterns.

```
function Sout = CS123Stiffness(cosB, sinB, tanB, x, xSpacing,
S,int)


for i = 1:length(cosB)
m=cosB(i);
n=sinB(i);


T = [m^2 0 n^2 0 2*m*n 0;
     0 1 0 0 0 0;
     n^2 0 m^2 0 -2*m*n 0;
     0 0 0 m 0 -n;
     -m*n 0 m*n 0 m^2-n^2 0;
     0 0 0 n 0 m];

 R = [1 0 0 0 0 0;
     0 1 0 0 0 0;
     0 0 1 0 0 0;
     0 0 0 2 0 0;
     0 0 0 0 2 0;
     0 0 0 0 0 2];

Sprime(:,:,i) = transpose(T) * S * T;


end


Sint11 = xSpacing * trapz(squeeze(Sprime(1,1,:)));
Sint12 = xSpacing * trapz(squeeze(Sprime(1,2,:)));
Sint13 = xSpacing * trapz(squeeze(Sprime(1,3,:)));
Sint14 = xSpacing * trapz(squeeze(Sprime(1,4,:)));
Sint15 = xSpacing * trapz(squeeze(Sprime(1,5,:)));
Sint16 = xSpacing * trapz(squeeze(Sprime(1,6,:)));

Sint21 = xSpacing * trapz(squeeze(Sprime(2,1,:)));
Sint22 = xSpacing * trapz(squeeze(Sprime(2,2,:)));
Sint23 = xSpacing * trapz(squeeze(Sprime(2,3,:)));
Sint24 = xSpacing * trapz(squeeze(Sprime(2,4,:)));
Sint25 = xSpacing * trapz(squeeze(Sprime(2,5,:)));
Sint26 = xSpacing * trapz(squeeze(Sprime(2,6,:)));

Sint31 = xSpacing * trapz(squeeze(Sprime(3,1,:)));
Sint32 = xSpacing * trapz(squeeze(Sprime(3,2,:)));
```

```
Sint33 = xSpacing * trapz(squeeze(Sprime(3,3,:)));
Sint34 = xSpacing * trapz(squeeze(Sprime(3,4,:)));
Sint35 = xSpacing * trapz(squeeze(Sprime(3,5,:)));
Sint36 = xSpacing * trapz(squeeze(Sprime(3,6,:)));


Sint41 = xSpacing * trapz(squeeze(Sprime(4,1,:)));
Sint42 = xSpacing * trapz(squeeze(Sprime(4,2,:)));
Sint43 = xSpacing * trapz(squeeze(Sprime(4,3,:)));
Sint44 = xSpacing * trapz(squeeze(Sprime(4,4,:)));
Sint45 = xSpacing * trapz(squeeze(Sprime(4,5,:)));
Sint46 = xSpacing * trapz(squeeze(Sprime(4,6,:)));


Sint51 = xSpacing * trapz(squeeze(Sprime(5,1,:)));
Sint52 = xSpacing * trapz(squeeze(Sprime(5,2,:)));
Sint53 = xSpacing * trapz(squeeze(Sprime(5,3,:)));
Sint54 = xSpacing * trapz(squeeze(Sprime(5,4,:)));
Sint55 = xSpacing * trapz(squeeze(Sprime(5,5,:)));
Sint56 = xSpacing * trapz(squeeze(Sprime(5,6,:)));


Sint61 = xSpacing * trapz(squeeze(Sprime(6,1,:)));
Sint62 = xSpacing * trapz(squeeze(Sprime(6,2,:)));
Sint63 = xSpacing * trapz(squeeze(Sprime(6,3,:)));
Sint64 = xSpacing * trapz(squeeze(Sprime(6,4,:)));
Sint65 = xSpacing * trapz(squeeze(Sprime(6,5,:)));
Sint66 = xSpacing * trapz(squeeze(Sprime(6,6,:)));



Sout = (1/(x(end))) * [Sint11 Sint12 Sint13 Sint14 Sint15 Sint16;
                       Sint21 Sint22 Sint23 Sint24 Sint25 Sint26;
                       Sint31 Sint32 Sint33 Sint34 Sint35 Sint36;
                       Sint41 Sint42 Sint43 Sint44 Sint45 Sint46;
                       Sint51 Sint52 Sint53 Sint54 Sint55 Sint56;
                       Sint61 Sint62 Sint63 Sint64 Sint65 Sint66];
```

Figure A-2: The function determines the average compliance of the undulating braid yarns.

```
function Cout = CS123Compliance(cosB, sinB, tanB, x, xSpacing,
C,int)

for i = 1:length(cosB)
m=cosB(i);
n=sinB(i);

T = [m^2 0 n^2 0 2*m*n 0;
     0 1 0 0 0 0;
     n^2 0 m^2 0 -2*m*n 0;
     0 0 0 m 0 -n;
     -m*n 0 m*n 0 m^2-n^2 0;
     0 0 0 n 0 m];
```

```
 R = [1 0 0 0 0 0;
     0 1 0 0 0 0;
     0 0 1 0 0 0;
     0 0 0 2 0 0;
     0 0 0 0 2 0;
     0 0 0 0 0 2];




Cprime(:,:,i) = inv(T) * C * R * T * inv(R);


end




Cint11 = xSpacing * trapz(Cprime(1,1,:));
Cint12 = xSpacing * trapz(Cprime(1,2,:));
Cint13 = xSpacing * trapz(Cprime(1,3,:));
Cint14 = xSpacing * trapz(Cprime(1,4,:));
Cint15 = xSpacing * trapz(Cprime(1,5,:));
Cint16 = xSpacing * trapz(Cprime(1,6,:));

Cint21 = xSpacing * trapz(Cprime(2,1,:));
Cint22 = xSpacing * trapz(Cprime(2,2,:));
Cint23 = xSpacing * trapz(Cprime(2,3,:));
Cint24 = xSpacing * trapz(Cprime(2,4,:));
Cint25 = xSpacing * trapz(Cprime(2,5,:));
Cint26 = xSpacing * trapz(Cprime(2,6,:));

Cint31 = xSpacing * trapz(Cprime(3,1,:));
Cint32 = xSpacing * trapz(Cprime(3,2,:));
Cint33 = xSpacing * trapz(Cprime(3,3,:));
Cint34 = xSpacing * trapz(Cprime(3,4,:));
Cint35 = xSpacing * trapz(Cprime(3,5,:));
Cint36 = xSpacing * trapz(Cprime(3,6,:));

Cint41 = xSpacing * trapz(Cprime(4,1,:));
Cint42 = xSpacing * trapz(Cprime(4,2,:));
Cint43 = xSpacing * trapz(Cprime(4,3,:));
Cint44 = xSpacing * trapz(Cprime(4,4,:));
Cint45 = xSpacing * trapz(Cprime(4,5,:));
Cint46 = xSpacing * trapz(Cprime(4,6,:));

Cint51 = xSpacing * trapz(Cprime(5,1,:));
Cint52 = xSpacing * trapz(Cprime(5,2,:));
Cint53 = xSpacing * trapz(Cprime(5,3,:));
Cint54 = xSpacing * trapz(Cprime(5,4,:));
Cint55 = xSpacing * trapz(Cprime(5,5,:));
Cint56 = xSpacing * trapz(Cprime(5,6,:));

Cint61 = xSpacing * trapz(Cprime(6,1,:));
Cint62 = xSpacing * trapz(Cprime(6,2,:));
```

```
Cint63 = xSpacing * trapz(Cprime(6,3,:));
Cint64 = xSpacing * trapz(Cprime(6,4,:));
Cint65 = xSpacing * trapz(Cprime(6,5,:));
Cint66 = xSpacing * trapz(Cprime(6,6,:));


 Cout = (1/(x(end))) * [Cint11 Cint12 Cint13 Cint14 Cint15
Cint16;
                       Cint21 Cint22 Cint23 Cint24 Cint25 Cint26;
                       Cint31 Cint32 Cint33 Cint34 Cint35 Cint36;
                       Cint41 Cint42 Cint43 Cint44 Cint45 Cint46;
                       Cint51 Cint52 Cint53 Cint54 Cint55 Cint56;
                       Cint61 Cint62 Cint63 Cint64 Cint65 Cint66];
```

Figure A-3: This function determines the average stiffness of the undulating braid yarns.

```
function [Sout, Cout] = transformXYZ(alpha, S, C)

c = cos(alpha);
s = sin(alpha);
%Rotation matrix- transformation about the z axis
T = [c^2 s^2 0 0 0 2*c*s;...
     s^2 c^2 0 0 0 -2*c*s;...
      0   0   1 0 0  0;...
      0   0   0 c -s 0;...
      0   0   0 s  c 0;...
     -c*s c*s 0 0 0 (c^2-s^2)];


 R = [1 0 0 0 0 0;
      0 1 0 0 0 0;
      0 0 1 0 0 0;
      0 0 0 2 0 0;
      0 0 0 0 2 0;
      0 0 0 0 0 2];

 %Byun transformation
 Sout = transpose(T) * S * T;


 %transform eqn and reuters matrix Jones pg 77
 Cout = inv(T) * C * R * T * inv(R);


end
```

Figure A-4: Braid angle coordinate system transformation

Appendix B.   Fiber Reinforced 3D Printer Model Code

B.1   MarkOne 3D Printer Mechanical Model

Inclosed in this appendix is an annotated version of the MATLAB script which was used to determine the mechanical properties of fiber reinforced 3D printed samples using a Volume Averaging method.

Author: Garrett Melenka

Email: gmelenka@ualberta.ca

Date: November 26, 2015

Description:

This file determines the effective mechanical properties of a Kevlar fiber reinforced 3D printed part using nylon as a the thermoplastic. Sources: Nylon Mechanical Properties:

Nylon 6, Extruded Matweb

http://www.matweb.com/search/DataSheet.aspx?MatGUID=726845c457b94b7cafe31d2e65739e1d&ckck=1

Kevlar Mechanical Properties: Table A.2 Engineering Mechanics of Composite Materials by Isaac Daniel

```
%   Kevlar 29 Mechanical Properties
%   Kawabata 1990
%% Volume Averaging Technique:
%% Melenka, G.W., Carey, J.P., Development of an Analytical Model for
% Tubular Braided Composites, ICCM20, Copenhagen, Denmark
```

```
% Kregers, AF; Teters GA; Use of averaging methods to determine
% viscoelastic properties of spacially reinforced composites. Mec Compos
% Mat 1979
```

B.1.1 Load and Display Image of 3D Printed Layer Geometry

```
figure;
img=imread('MarkOneLayerGeometry.jpg');
img2 = imresize(img,0.5);
imshow(img2);
title('3D Printed Layer Geometry');
```
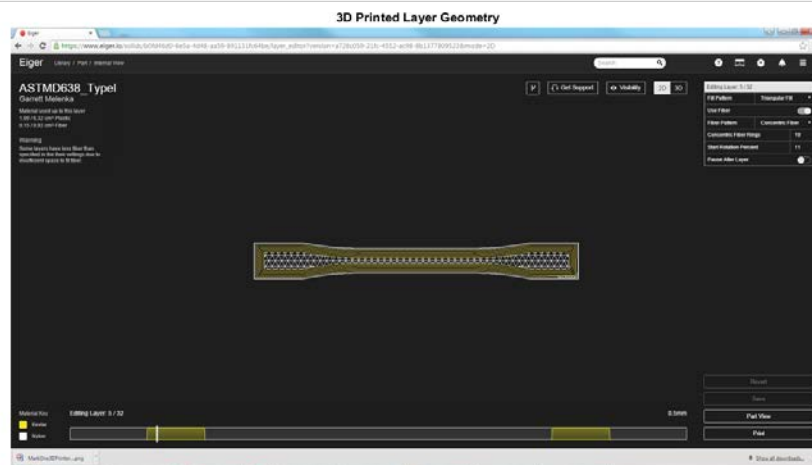

B.1.2 Nylon Mechanical Properties

```
E = 0.75; %GPa
nu = 0.35;
G = E / (2*(1+nu)); %GPa
```

B.1.3 Kevlar 29 Mechanical Properties see Kawabata 1990

```
Ef1 = 79.8; %GPa
Ef2 = 2.59; %GPa
Ef3 = Ef2; %GPa
Gf12 = 2.1; %GPa
Gf13 = Gf12; %GPa
Gf23 = 1.5; %GPa
nuf12 = 0.33;
nuf13 = nuf12;
nuf21 = nuf12*(Ef2/Ef1);
nuf31 = nuf12*(Ef3/Ef1);
nuf23 = 0.1;
nuf32 = nuf23*(Ef3/Ef2);
```

B.1.4 Micromechanical model from Rodriquez et al 2003

Rodríguez, J. F., Thomas, J. P., & Renaud, J. E. (2003). Mechanical behavior of
acrylonitrile butadiene styrene fused deposition materials modeling. Rapid Prototyping
Journal, 9(4), 219–230. doi:10.1108/13552540310489604

```
rho = 0.9; % infill
E1 = (1-rho)*E; %GPa
E2 = (1-rho^0.5)*E; %GPa
E3 = E2; %GPa
G12 = G*(1-rho)*(1-rho^0.5) / ((1-rho) + (1-rho^0.5)); %GPa
G13 = G12; %GPa
G23 = (1 - rho^0.5) * G; %GPa
nu12 = (1 - rho)*nu;
nu13 = nu12;
nu23 = (1 - rho^0.5)*nu;
nu21 = (1 - rho^0.5)*nu;
nu31 = nu21;
nu32 = nu21;
```

B.1.5 Compliance Matrix

```matlab
%Exterior nylon shell Compliance matrix
Sshell = [1/E -nu/E -nu/E 0 0 0;...
    -nu/E 1/E -nu/E 0 0 0;...
    -nu/E -nu/E 1/E 0 0 0;...
    0 0 0 1/G 0 0;...
    0 0 0 0 1/G 0;...
    0 0 0 0 0 1/G];

% %Assume shells have voids
%
% Sshell = [1/E1floor -nu21floor/E2floor -nu31floor/E3floor 0 0 0;...
%     -nu12floor/E1floor 1/E2floor -nu32floor/E3floor 0 0 0;...
%     -nu13floor/E1floor -nu23floor/E2floor 1/E3floor 0 0 0;...
%     0 0 0 1/G23floor 0 0;...
%     0 0 0 0 1/G13floor 0;...
%     0 0 0 0 0 1/G12floor];

%Compliance Matrix of floor and ceilings
Sfloor = [1/E1floor -nu21floor/E2floor -nu31floor/E3floor 0 0 0;...
    -nu12floor/E1floor 1/E2floor -nu32floor/E3floor 0 0 0;...
    -nu13floor/E1floor -nu23floor/E2floor 1/E3floor 0 0 0;...
    0 0 0 1/G23floor 0 0;...
    0 0 0 0 1/G13floor 0;...
    0 0 0 0 0 1/G12floor];




% Compliance matrix for infill layers
Sinfill = [1/E1 -nu21/E2 -nu31/E3 0 0 0;...
    -nu12/E1 1/E2 -nu32/E3 0 0 0;...
    -nu13/E1 -nu23/E2 1/E3 0 0 0;...
    0 0 0 1/G23 0 0;...
    0 0 0 0 1/G13 0;...
    0 0 0 0 0 1/G12];

% Compliance matrix for kevlar fibers
Skevlar = [1/Ef1 -nuf21/Ef2 -nuf31/Ef3 0 0 0;...
    -nuf12/Ef1 1/Ef2 -nuf32/Ef3 0 0 0;...
    -nuf13/Ef1 -nuf23/Ef2 1/Ef3 0 0 0;...
    0 0 0 1/Gf23 0 0;...
    0 0 0 0 1/Gf13 0;...
    0 0 0 0 0 1/Gf12];
```

B.1.6 Coordinate System Transformation for infill and solid layers

```
alpha = 45 * (pi / 180);

SinfillPos= transformXYZ(alpha, Sinfill);
SinfillNeg= transformXYZ(-alpha, Sinfill);

% SsolidPos = transformXYZ(alpha, Sshell);
% SsolidNeg = transformXYZ(-alpha, Sshell);

%use solid layers and assume layers have 10% voids
SsolidPos = transformXYZ(alpha, Sfloor);
SsolidNeg = transformXYZ(-alpha, Sfloor);
```

B.1.7 Invert compliance matricies to get stiffness matricies

```
CinfillPos = inv(SinfillPos);
CinfillNeg = inv(SinfillNeg);
CsolidPos = inv(SsolidPos);
CsolidNeg = inv(SsolidNeg);
Cshell = inv(Sshell);
Cfibers = inv(Skevlar);
```

B.1.8 Determine Dogbone Sample Area and Volume

```
%Determine tensile volume of Sample

H = 57; %height of tensile area (mm)
W = 13; %width of sample (mm)
T = 3.2; %overall sample thickness (mm)

TLayer = 0.1; %layer thickness (mm)
numFloor = 4; %number of floor layers
numCeiling = 4; %number of ceiling layers
numSolid = 8; %number of solid infill layers
numInfill = 10; %number of infill layers
```

```matlab
%Need to confirm width for fibers
%WFiber = 0.7; %assume fiber width of 1.0mm
WFiber = 0.7;
numFiber = 6; %number of fiber layers
numFiberConcentric = 5; %number of concentric fiber rings


VTensile = H * W * T;

%Need to confirm width of shells
WShellInd = 0.39;
%WShellInd = 0.5; %Assume Shell Width of 1.0mm
numShells = 2; %each side of dogbone

WShell = WShellInd * numShells; %Shell width will vary based on number of shells
used during printing

VShell = WShell * H * T * 2;

%Volumes of floor and ceiling layers
VFloor = (W - (WShell * 2)) * H * TLayer * numFloor;
VCeiling = (W - (WShell * 2)) * H * TLayer * numCeiling;

%Volumes of solid layers (needed to support fibers)
VSolid = (W - (WShell * 2)) * H * TLayer * numSolid;

VInfill = (W - (WShell * 2)) * H * TLayer * numInfill;


VFiber = WFiber * TLayer * H * numFiberConcentric * 2 * numFiber;

%Volume of infill in fiber layers

VInfillFiber = (W - (2 * WShell) - (WFiber * numFiberConcentric * 2)) * TLayer *
H * numFiber;
```

B.1.9 Determine Volume Fraction of RP Components

```matlab
vfShell = VShell/ (VTensile);%shell volume fraction
vfInfill = VInfill / (VTensile);%infill volume fraction
vfFibers = VFiber /  (VTensile); %fiber volume fraction

%VfFibers = 0.76;
vfSolid = VSolid /(VTensile); %volume fraction of solid infill layers
vfFloor = VFloor / VTensile;
vfCeiling = VFloor / VTensile;
vfInfillFiber = VInfillFiber / VTensile;
```

```
totVol = VfShell + VfInfill + VfFibers + VfSolid + VfFloor + VfCeiling +
VfInfillFiber;
```

B.1.10   Determine Effective Stiffness from Constituent

Stiffness and Volume Fractions

```
Ctotal = VfShell*Cshell + VfInfill*CinfillNeg*0.5 + VfInfill*CinfillPos*0.5 +
VfInfillFiber*CinfillNeg*0.5 + VfInfillFiber*CinfillPos*0.5  +
VfSolid*CsolidPos*0.5 + VfSolid*CsolidNeg*0.5 + VfFibers*Cfibers;

% Savg = VfShell*Sshell + VfInfill*SinfillNeg*0.5 + VfInfill*SinfillPos*0.5 +
VfSolid*SsolidPos*0.5 + VfSolid*SsolidNeg*0.5 + VfFibers*Skevlar;
%
%
% Cavg = inv(Savg);
```

B.1.11   Determine Effective Compliance

```
Stotal = inv(Ctotal);
```

B.1.12   Determine Effective Mechanical Properties

```
Ex = 1/Stotal(1,1)
Ey = 1/Stotal(2,2)
Ez = 1/Stotal(3,3)
Gxy = 1/Stotal(6,6)
Gyz = 1/Stotal(5,5)
Gzx = 1/Stotal(4,4)
vxy = -Stotal(1,2)/Stotal(1,1)

VF = VfFibers;

Headings = ['Ex' 'Ey' 'Ez' 'Gxy' 'Gyz' 'Gzx' 'vxy', 'VF'];
Results = [Ex Ey Ez Gxy Gyz Gzx vxy VF];
```

B.1.13   Output Results for Different Fiber Reinforcement

Options

```
Appendix C. if numFiberConcentric == 0
        xlswrite('NyModelResults', Results)
    end

    if numFiberConcentric == 5
        xlswrite('5RModelResults', Results)
    end

    if numFiberConcentric == 4
        xlswrite('4RModelResults', Results)
    end

    if numFiberConcentric == 2
        xlswrite('2RModelResults', Results)
    end

    E1 = VF*Ef1 + (1-VF)*E
```

Bibliography

[1] (2016). *AIAC Guide to Canada's Aerospace Industry*. Available: http://aiac.ca/guide/.

[2] (2016). *Boeing 787 Dreamliner*. Available: http://www.boeing.com/commercial/787/.

[3] J. Carey, G. Melenka, A. Hunt, B. Cheung, M. Ivey and C. Ayranci, "Braided composites in aerospace engineering," *Advanced Composite Materials for Aerospace Engineering: Processing, Properties and Applications,* pp. 175, 2016.

[4] G. W. Melenka, A. J. Hunt, C. M. Pastore, F. K. Ko, M. Munro and J. P. Carey, "Manufacturing processes for braided composite materials," in *Handbook of Advances in Braided Composite Materials: Theory, Production, Testing and Applications*, J. P. Carey, Ed. Woodhead Publishing, 2016, .

[5] C. Ayranci and J. P. Carey, "Predicting the longitudinal elastic modulus of braided tubular composites using a curved unit-cell geometry," *Composites Part B: Engineering,* vol. 41, pp. 229-235, 2010.

[6] J. Carey, A. Fahim and M. Munro, "Predicting elastic constants of 2D-braided fiber rigid and elastomeric-polymeric matrix composites," *J Reinf Plast Compos,* vol. 23, pp. 1845-1857, 2004.

[7] G. W. Melenka, C. M. Pastore, F. K. Ko and J. P. Carey, "Advances in 2D and 3D braided composite materials modeling," in *Handbook of Advances in Braided Composite Materials: Theory, Production, Testing and Applications*, J. P. Carey, Ed. Woodhead Publishing, 2016, .

[8] S. C. Quek, A. M. Waas, K. W. Shahwan and V. Agaram, "Analysis of 2D triaxial flat braided textile composites," *Int. J. Mech. Sci.,* vol. 45, pp. 1077-1096, 2003.

[9] J. H. Byun, "The analytical characterization of 2-D braided textile composites," *Composites Sci. Technol.,* vol. 60, pp. 705-716, 2000.

[10] L. Xu, S. J. Kim, C. -. Ong and S. K. Ha, "Prediction of material properties of biaxial and triaxial braided textile composites," *J. Composite Mater.,* vol. 46, pp. 2255-2270, 2012.

[11] X. Ji, A. M. Khatri, E. S. Chia, R. K. Cha, B. T. Yeo, S. C. Joshi and Z. Chen, "Multi-scale simulation and finite-element-assisted computation of elastic

properties of braided textile reinforced composites," *J. Composite Mater.,* vol. 48, pp. 931-949, 2014.

[12] G. Melenka, D. Nobes and J. Carey, "3D DIC measurement of tubular braided composites," in *ICCM 19,* Montreal, 2013, .

[13] C. Ayranci and J. Carey, "2D braided composites: A review for stiffness critical applications," *Composite Structures,* vol. 85, pp. 43-58, 2008.

[14] J. H. Byun, "The analytical characterization of 2-D braided textile composites," *Composites Sci. Technol.,* vol. 60, pp. 705-716, 2000.

[15] P. Qu, X. Guan, Y. Jia, S. Lou and J. Nie, "Effective elastic properties and stress distribution of 2D biaxial nonorthogonally braided composites," *J. Composite Mater.,* vol. 46, pp. 997-1008, 2012.

[16] P. Tan, L. Tong and G. P. Steven, "Modelling for predicting the mechanical properties of textile composites - A review," *Composites Part A: Applied Science and Manufacturing,* vol. 28, pp. 903-922, 1997.

[17] G. Fang and J. Liang, "A review of numerical modeling of three-dimensional braided textile composites," *J. Composite Mater.,* vol. 45, pp. 2415-2436, 2011.

[18] J. P. Carey, G. W. Melenka, A. J. Hunt and C. Ayranci, "Introduction to braided composite material behavior," in *Handbook of Advances in Braided Composite Materials: Theory, Production, Testing and Applications*, J. P. Carey, Ed. Woodhead Publishing, 2016, .

[19] P. Tan, L. Tong and G. P. Steven, "A three-dimensional modelling technique for predicting the linear elastic property of opened-packing woven fabric unit cells," *Composite Structures,* vol. 38, pp. 261-271, 1997.

[20] G. Fang and J. Liang, "A review of numerical modeling of three-dimensional braided textile composites," *J. Composite Mater.,* vol. 45, pp. 2415-2436, 2011.

[21] B. N. Cox and G. Flanagan, *Handbook of Analytical Methods for Textile Composites [Microform] : Under Contract NAS1-19243 / Brian N. Cox, Gerry Flanagan.* Hampton, Va. : National Aeronautics and Space Administration, Langley Research Center ; Springfield, Va. : National Technical Information Service, distributor, 1997], 1997.

[22] T. Chou and F. K. Ko, *Textile Structural Composites.* Amsterdam ; New York : Elsevier ; New York, NY, U.S.A. : Distributors for the U.S. and Canada, Elsevier Science Pub. Co., 1989, 1989.

[23] J. Carey, M. Munro and A. Fahim, "Longitudinal elastic modulus prediction of a 2-D braided fiber composite," *J Reinf Plast Compos,* vol. 22, pp. 813-831, 2003.

[24] C. Ayranci, "Predicting the elastic properties of two dimensionally braided tubular composite structures towards the design of braid-reinforced polymer medical catheters," *ProQuest Dissertations and Theses,* 2010.

[25] R. F. El-Hajjar, S. S. Shams and D. J. Kehrl, "Closed form solutions for predicting the elastic behavior of quasi-isotropic triaxially braided composites," *Composite Structures,* vol. 101, pp. 1-8, 2013.

[26] Z. Tang and R. Postle, "Deformation analysis of 3D braided structural composites," *Text. Res. J.,* vol. 73, pp. 563-569, 2003.

[27] L. Carvalho, R. A. S. Moreira and J. A. Simões, "Application of a vibration measuring technique to evaluate the dynamic stiffness of porcine periodontal ligament," *Technology and Health Care,* vol. 14, pp. 457-465, 2006.

[28] R. M. Jones, *Mechanics of Composite Materials.* Washington, Scripta Book Co. 1975], 1975.

[29] B. K. O. Cheung and J. P. Carey, "Macromechanics of composite materials," in *Handbook of Advances in Braided Composite Materials: Theory, Production, Testing and Applications*, J. P. Carey, Ed. Woodhead, 2016, .

[30] C. Ayranci and J. Carey, "2D braided composites: A review for stiffness critical applications," *Composite Structures,* vol. 85, pp. 43-58, 2008.

[31] I. S. Raju and J. T. Wang, "Classical Laminate Theory Models for Woven Fabric Composites," *J. Compos. Technol. Res.,* vol. 16, pp. 289-303, 1994.

[32] N. K. Naik and V. K. Ganesh, "An analytical method for plain weave fabric composites," *Composites,* vol. 26, pp. 281-289, 1995.

[33] T. Ishikawa and T. -. Chou, "Stiffness and strength behaviour of woven fabric composites," *J. Mater. Sci.,* vol. 17, pp. 3211-3220, 1982.

[34] T. Ishikawa and T. W. Chou, "Stiffness and strength properties of woven composites," in 1982, pp. 489-449.

[35] N. K. Naik and P. S. Shembekar, "Elastic behavior of woven fabric composites: I-lamina analysis," *J. Composite Mater.,* vol. 26, pp. 2196-2225, 1992.

[36] P. S. Shembekar and N. K. Naik, "Elastic behavior of woven fabric composites: II-laminate analysis," *J. Composite Mater.,* vol. 26, pp. 2226-2246, 1992.

[37] N. K. Naik and P. S. Shembekar, "Elastic behavior of woven fabric composites: III-Laminate design," *J. Composite Mater.,* vol. 26, pp. 2522-2541, 1992.

[38] J. Yang, C. Ma and T. Chou, "Fiber Inclination Model of Three-Dimensional Textile Structural Composites," *J. Composite Mater.,* vol. 20, pp. 472-484, 1986.

[39] A. Aggarwal, S. Ramakrishna and V. K. Ganesh, "Predicting the in-plane elastic constants of diamond braided composites," *J. Composite Mater.,* vol. 35, pp. 665-688, 2001.

[40] A. Aggarwal, S. Ramakrishna and V. Ganesh, "Predicting the strength of diamond braided composites," *J. Composite Mater.,* vol. 36, pp. 625-643, 2002.

[41] J. Carey, M. Munro and A. Fahim, "Longitudinal elastic modulus prediction of a 2-D braided fiber composite," *J Reinf Plast Compos,* vol. 22, pp. 813-831, 2003.

[42] C. Ayranci and J. P. Carey, "Predicting the longitudinal elastic modulus of braided tubular composites using a curved unit-cell geometry," *Composites Part B: Engineering,* vol. 41, pp. 229-235, 2010.

[43] C. Ayranci, D. Romanyk and J. P. Carey, "Elastic properties of large-open-mesh 2D braided composites: Model predictions and initial experimental findings," *Polymer Composites,* vol. 31, pp. 2017-2024, 2010.

[44] C. Ayranci and J. P. Carey, "Experimental validation of a regression-based predictive model for elastic constants of open mesh tubular diamond-braid composites," *Polymer Composites,* vol. 32, pp. 243-251, 2011.

[45] J. Carey, M. Munro and A. Fahim, "Regression-based model for elastic constants of 2D braided/woven open mesh angle-ply composites," *Polym Compos,* vol. 26, pp. 152-164, 2005.

[46] C. Pastore and F. K. KO, "A processing science model for three dimensional braiding," *How to Apply Advanced Composites Technology,* pp. 371-376, 1988.

[47] D. W. Whyte, *Structure and Properties of 3-D Braid Reinforced Composites,* 1986.

[48] H. B. Soebroto, T. Hager, C. M. Pastore and F. K. Ko, "Engineering design of braided structural fiberglas composites," in *National SAMPE Symposium and Exhibition (Proceedings),* 1990, pp. 687-696.

[49] C. M. Pastore and Y. A. Gowayed, "Self-consistent fabric geometry model: modification and application of a fabric geometry model to predict the elastic properties of textile composites," *J. Composites Technol. Res.,* vol. 16, pp. 32-36, 1994.

[50] C. Ayranci and J. Carey, "2D braided composites: a review for stiffness critical applications," *Composite Structures,* vol. 85, pp. 43-58, 2008.

[51] I. M. Daniel and O. Ishai, *Engineering Mechanics of Composite Materials.* New York: Oxford University Press, 2006.

[52] M. M. Shokrieh and M. S. Mazloomi, "An analytical method for calculating stiffness of two-dimensional tri-axial braided composites," *Composite Structures,* vol. 92, pp. 2901-2905, 2010.

[53] S. C. Quek, A. M. Waas, K. W. Shahwan and V. Agaram, "Analysis of 2D triaxial flat braided textile composites," *Int. J. Mech. Sci.,* vol. 45, pp. 1077-1096, 2003.

[54] Z. T. Kier, A. Salvi, G. Theis, A. M. Waas and K. Shahwan, "Estimating mechanical properties of 2D triaxially braided textile composites based on microstructure properties," *Composites Part B: Engineering,* vol. 68, pp. 288-299, 2014.

[55] M. Pankow, A. M. Waas, C. -. Yen and S. Ghiorse, "A new lamination theory for layered textile composites that account for manufacturing induced effects," *Composites Part A: Applied Science and Manufacturing,* vol. 40, pp. 1991-2003, 2009.

[56] A. F. Kreger and G. A. Teters, "Use of averaging methods to determine the viscoelastic properties of spatially reinforced composites," *Mechanics of Composite Materials,* vol. 15, pp. 377-383, 1980.

[57] A. K. Kaw, *Mechanics of Composite Materials.* CRC press, 2005.

[58] J. Carey, A. Fahim and M. Munro, "Predicting elastic constants of 2D-braided fiber rigid and elastomeric–polymeric matrix composites," *J Reinf Plast Compos,* vol. 23, pp. 1845-1857, 2004.

[59] J. H. Byun, "The analytical characterization of 2-D braided textile composites," *Composites Sci. Technol.,* vol. 60, pp. 705-716, 2000.

[60] J. H. Byun, "The analytical characterization of 2-D braided textile composites," *Composites Sci. Technol.,* vol. 60, pp. 705-716, 2000.

[61] M. Pankow, A. M. Waas, C. -. Yen and S. Ghiorse, "A new lamination theory for layered textile composites that account for manufacturing induced effects," *Composites Part A: Applied Science and Manufacturing,* vol. 40, pp. 1991-2003, 2009.

[62] H. Bale, M. Blacklock, M. R. Begley, D. B. Marshall, B. N. Cox and R. O. Ritchie, "Characterizing three-dimensional textile ceramic composites using synchrotron x-ray micro-computed-tomography," *J Am Ceram Soc,* vol. 95, pp. 392-402, 2012.

[63] P. Badel, E. V. Sallé, E. Maire and P. Boisse, "Simulation and tomography analysis of textile composite reinforcement deformation at the mesoscopic scale," *International Journal of Material Forming,* vol. 2, pp. 189-192, 2009.

[64] L. P. Djukic, I. Herszberg, W. R. Walsh, G. A. Schoeppner and B. Gangadhara Prusty, "Contrast enhancement in visualisation of woven composite architecture using a MicroCT Scanner. Part 2: Tow and preform coatings," *Composites Part A: Applied Science and Manufacturing,* vol. 40, pp. 1870-1879, 2009.

[65] L. P. Djukic, I. Herszberg, W. R. Walsh, G. A. Schoeppner, B. Gangadhara Prusty and D. W. Kelly, "Contrast enhancement in visualisation of woven composite tow architecture using a MicroCT Scanner. Part 1: Fabric coating and resin additives," *Composites Part A: Applied Science and Manufacturing,* vol. 40, pp. 553-565, 2009.

[66] F. Pierron and M. Grédiac, *The Virtual Fields Method. [Electronic Resource] : Extracting Constitutive Mechanical Parameters from Full-Field Deformation Measurements.* New York : Springer, c2012, 2012.

[67] S. V. Lomov, D. S. Ivanov, I. Verpoest, M. Zako, T. Kurashiki, H. Nakai and S. Hirosawa, "Meso-FE modelling of textile composites: Road map, data flow and algorithms," *Composites Sci. Technol.,* vol. 67, pp. 1870-1891, 2007.

[68] D. Goyal, X. Tang, J. D. Whitcomb and A. D. Kelkar, "Effect of various parameters on effective engineering properties of 2 × 2 braided composites," *Mechanics of Advanced Materials and Structures,* vol. 12, pp. 113-128, 2005.

[69] D. Goyal and J. D. Whitcomb, "Analysis of stress concentrations in 2 × 2 braided composites," *J. Composite Mater.,* vol. 40, pp. 533-546, 2006.

[70] P. Qu, X. Guan, Y. Jia, S. Lou and J. Nie, "Effective elastic properties and stress distribution of 2D biaxial nonorthogonally braided composites," *J. Composite Mater.,* vol. 46, pp. 997-1008, 2012.

[71] A. K. Pickett, J. Sirtautas and A. Erber, "Braiding simulation and prediction of mechanical properties," *Appl Compos Mater,* vol. 16, pp. 345-364, 2009.

[72] T. Alpyildiz, "3D geometrical modelling of tubular braids," *Text. Res. J.,* vol. 82, pp. 443-453, 2012.

[73] F. K. Ko, C. M. Pastore and A. A. Head, *Handbook of Industrial Braiding.* Covington, Kentucky: Atkins and Pearce, 1989.

[74] D. Branscomb, D. Beale and R. Broughton, "New directions in braiding," *Journal of Engineered Fibers and Fabrics,* vol. 8, pp. 11-24, 2013.

[75] F. K. Ko, "Braiding," in *ASM International, Engineered Materials Handbook*Anonymous American Society of Metals, 1987, pp. 519-528.

[76] C. Ayranci and J. P. Carey, "Predicting the longitudinal elastic modulus of braided tubular composites using a curved unit-cell geometry," *Composites Part B: Engineering,* vol. 41, pp. 229-235, 2010.

[77] T. Ishikawa and T. -. Chou, "Stiffness and strength behaviour of woven fabric composites," *J. Mater. Sci.,* vol. 17, pp. 3211-3220, 1982.

[78] N. K. Naik and P. S. Shembekar, "Elastic behavior of woven fabric composites: I-lamina analysis," *J. Composite Mater.,* vol. 26, pp. 2196-2225, 1992.

[79] P. Potluri, A. Rawal, M. Rivaldi and I. Porat, "Geometrical modelling and control of a triaxial braiding machine for producing 3D preforms," *Composites Part A: Applied Science and Manufacturing,* vol. 34, pp. 481-492, 2003.

[80] Y. Nishikawa, S. Baba and M. Takahashi, "Optimization of x-ray computerized tomography for polymer materials," *International Journal of Polymeric Materials and Polymeric Biomaterials,* vol. 62, pp. 295-300, 2013.

[81] A. E. Scott, I. Sinclair, S. M. Spearing, M. N. Mavrogordato and W. Hepples, "Influence of voids on damage mechanisms in carbon/epoxy composites determined via high resolution computed tomography," *Composites Sci. Technol.,* vol. 90, pp. 147-153, 2014.

[82] Anonymous "ASTM D2734-09 standard test methods for void content of reinforced plastics," ASTM International, West Conshohocken, PA, 2009.

[83] Y. A. Gowayed, "The Effect of Voids on the Elastic Properties of Textile Reinforced Composites," *J. Composites Technol. Res.,* vol. 19, pp. 168-173, 1997.

[84] F. J. Guild and J. Summerscales, "Microstructural image analysis applied to fibre composite materials: a review," *Composites,* vol. 24, pp. 383-393, 1993.

[85] M. H. Hassan, A. R. Othman and S. Kamaruddin, "Void content determination of fiber reinforced polymers by acid digestion method," *Advanced Materials Research,* vol. 795, pp. 64-68, 2013.

[86] Anonymous "ASTM E1441-11 standard guide for computed tomography (CT) imaging," ASTM International, West Conshohocken, PA, 2011.

[87] F. Desplentere, S. V. Lomov, D. L. Woerdeman, I. Verpoest, M. Wevers and A. Bogdanovich, "Micro-CT characterization of variability in 3D textile architecture," *Composites Sci. Technol.,* vol. 65, pp. 1920-1930, 2005.

[88] M. Kosek and P. Sejak, "Visualization of voids in actual C/C woven composite structure," in *Special Issue on the 12th European Conference on Composite Materials, ECCM 2006,* 2008, pp. 1465-1469.

[89] J. S. U. Schell, M. Renggli, G. H. van Lenthe, R. Müller and P. Ermanni, "Micro-computed tomography determination of glass fibre reinforced polymer meso-structure," *Composites Sci. Technol.,* vol. 66, pp. 2016-2022, 2006.

[90] J. E. Little, X. Yuan and M. I. Jones, "Characterisation of voids in fibre reinforced composite materials," *NDT and E International,* vol. 46, pp. 122-127, 2012.

[91] P. J. Schilling, B. P. R. Karedla, A. K. Tatiparthi, M. A. Verges and P. D. Herrington, "X-ray computed microtomography of internal damage in fiber reinforced polymer matrix composites," *Composites Sci. Technol.,* vol. 65, pp. 2071-2078, 2005.

[92] A. H. Kruesi and G. H. Hasko, "Computer controlled resin impregnation for fiber composite braiding," in *Int SAMPE Symp Exhib,* 1987, pp. 309-317.

[93] S. D. Senibi, "Application of thermal experimental study to the development of expandable mandrel RTM technique for fabrication of seamless composite tubes," in *International SAMPE Symposium and Exhibition (Proceedings),* 1998, pp. 1310-1321.

[94] Y. Nikishkov, L. Airoldi and A. Makeev, "Measurement of voids in composites by X-ray Computed Tomography," *Composites Sci. Technol.,* vol. 89, pp. 89-97, 2013.

[95] I. Kasa, "A circle fitting procedure and its error analysis," *Instrumentation and Measurement, IEEE Transactions On,* vol. 1001, pp. 8-14, 1976.

[96] W. Park and G. S. Chirikjian, "Interconversion between truncated Cartesian and polar expansions of images," *IEEE Trans. Image Process.,* vol. 16, pp. 1946-1955, Aug, 2007.

[97] H. Zhu, B. Wu, D. Li, D. Zhang and Y. Chen, "Influence of Voids on the Tensile Performance of Carbon/epoxy Fabric Laminates," *Journal of Materials Science and Technology,* vol. 27, pp. 69-73, 2011.

[98] P. Potluri, A. Manan, M. Francke and R. J. Day, "Flexural and torsional behaviour of biaxial and triaxial braided composite structures," *Composite Structures,* vol. 75, pp. 377-386, 2006.

[99] P. G. Young, T. B. H. Beresford-West, S. R. L. Coward, B. Notarberardino, B. Walker and A. Abdul-Aziz, "An efficient approach to converting three-dimensional image data into highly accurate computational models," *Philosophical Transactions of the Royal Society A: Mathematical, Physical and Engineering Sciences,* vol. 366, pp. 3155-3173, 2008.

[100] C. Ayranci, D. Romanyk and J. P. Carey, "Elastic properties of large-open-mesh 2D braided composites: Model predictions and initial experimental findings," *Polymer Composites,* vol. 31, pp. 2017-2024, 2010.

[101] C. Ayranci and J. P. Carey, "Effect of diameter in predicting the elastic properties of 2D braided tubular composites," *J. Composite Mater.,* vol. 44, pp. 2031-2044, 2010.

[102] J. Carey, A. Fahim and M. Munro, "Predicting elastic constants of 2D-braided fiber rigid and elastomeric–polymeric matrix composites," *J Reinf Plast Compos,* vol. 23, pp. 1845-1857, 2004.

[103] C. K. Leung, G. W. Melenka, D. S. Nobes and J. P. Carey, "The effect on elastic modulus of rigid-matrix tubular composite braid radius and braid angle change under tensile loading," *Composite Structures,* vol. 100, pp. 135-143, 2013.

[104] G. W. Melenka, S. Hoxha, D. S. Nobes and J. P. Carey, "Analytical and experimental analysis of tubular braided composites," in *CANCOM 2015-Canadian International Conference on Composite Materials,* Edmonton, Alberta, Canada, 2015, .

[105] M. A. Sutton, J. J. Orteu and H. W. Schreier, *Image Correlation for Shape, Motion and Deformation Measurements : Basic Concepts, Theory and Applications.* New York, N.Y: Springer, 2009.

[106] ASTM D3039 / D3039M-14, "Standard Test Method for Tensile Properties of Polymer Matrix Composite Materials," 2014.

[107] LaVision GmbH, "Product-Manual for DaVis 8.2.0 StrainMaster Item-Number(s): 1003017," 2014.

[108] D. Fleet and Y. Weiss, "Optical flow estimation," in *Handbook of Mathematical Models in Computer Vision*Anonymous Springer, 2006, pp. 237-257.

[109] F. Moisy. PIVMat A PIV post-processing and data analysis toolbox for matlab. 2015. Available: http://www.fast.u-psud.fr/pivmat/.

[110] S. M. Thomas and Y. T. Chan, "A simple approach for the estimation of circular arc center and its radius," *Computer Vision, Graphics, and Image Processing,* vol. 45, pp. 362-370, 1989.

[111] R. A. Naik, P. G. Ifju and J. E. Masters, "Effect of fiber architecture parameters on deformation fields and elastic moduli of 2-D braided composites," *J. Composite Mater.,* vol. 28, pp. 656-681, 1994.

[112] G. W. Melenka and J. P. Carey, "Development of an Analytical Model for Tubular Braided Composites," *ICCM20,* 2015.

[113] R. C. Hibbler, "Mechanical properties of materials," in *Mechanics of Materials*, 6th ed., R. C. Hibbler, Ed. New York: Prentice Hall, 2004, pp. 83.

[114] R. C. Hibbler, "Torsion," in *Mechanics of Materials*, 6th ed., R. C. Hibbler, Ed. New York: Prentice Hall, 2004, .

[115] D. Brunnschweiler, "Braids and Braiding," *Journal of the Textile Institute Proceedings,* vol. 44, pp. P666-P686, 09/01; 2015/02, 1953.

[116] D. Brunnschweiler, "The Structure and Tensile Properties of Braids," *Journal of the Textile Institute Transactions,* vol. 45, pp. T55-T77, 01/01; 2015/02, 1954.

[117] C. Ayranci and J. P. Carey, "Predicting the longitudinal elastic modulus of braided tubular composites using a curved unit-cell geometry," *Composites Part B: Engineering,* vol. 41, pp. 229-235, 2010.

[118] J. Carey, M. Munro and A. Fahim, "Longitudinal elastic modulus prediction of a 2-D braided fiber composite," *J Reinf Plast Compos,* vol. 22, pp. 813-831, 2003.

[119] P. Potluri, A. Rawal, M. Rivaldi and I. Porat, "Geometrical modelling and control of a triaxial braiding machine for producing 3D preforms," *Composites Part A: Applied Science and Manufacturing,* vol. 34, pp. 481-492, 2003.

[120] G. W. Melenka, E. Lepp, B. K. O. Cheung and J. P. Carey, "Micro-computed tomography analysis of tubular braided composites," *Composite Structures,* vol. 131, pp. 384-396, 11/1, 2015.

[121] A. Kregers and Y. G. Melbardis, "Determination of the deformability of three-dimensionally reinforced composites by the stiffness averaging method," *Mechanics of Composite Materials,* vol. 14, pp. 1-5, 1978.

[122] A. Kregers and G. Teters, "Determination of the elastoplastic properties of spatially reinforced composites by the averaging method," *Mechanics of Composite Materials,* vol. 17, pp. 25-31, 1981.

[123] A. Kregers and A. Zilauts, "Limiting values of reinforcement factors for fibrous composites with a three-dimensional structure," *Mechanics of Composite Materials,* vol. 20, pp. 530-536, 1985.

[124] A. Hallal, R. Younes and F. Fardoun, "Review and comparative study of analytical modeling for the elastic properties of textile composites," *Composites Part B: Engineering,* vol. 50, pp. 22-31, 2013.

[125] I. Gibson, D. Rosen and B. Stucker, *Additive Manufacturing Technologies : 3D Printing, Rapid Prototyping, and Direct Digital Manufacturing.* New York, NY : Springer, 2015; Second edition, 2015.

[126] G. W. Melenka, J. S. Schofield, M. R. Dawson and J. P. Carey, "Evaluation of dimensional accuracy and material properties of the MakerBot 3D desktop printer," *Rapid Prototyping Journal,* vol. 21, pp. 618-627, 2015.

[127] J. F. Rodriguez, J. P. Thomas and J. E. Renaud, "Characterization of the mesostructure of fused-deposition acrylonitrile-butadiene-styrene materials," *Rapid Prototyping Journal,* vol. 6, pp. 175-186, 2000.

[128] S. Ahn, M. Montero, D. Odell, S. Roundy and P. K. Wright, "Anisotropic material properties of fused deposition modeling ABS," *Rapid Prototyping Journal,* vol. 8, pp. 248-257, 2002.

[129] J. F. Rodríguez, J. P. Thomas and J. E. Renaud, "Mechanical behavior of acrylonitrile butadiene styrene fused deposition materials modeling," *Rapid Prototyping Journal,* vol. 9, pp. 219-230, 2003.

[130] (2016). *ColorFab BrassFill 3D Printing Filament*. Available: http://colorfabb.com/brassfill.

[131] 3DXTech, "Carbon Fiber Reinforced PLA Filament," 2014.

[132] K. Mori, T. Maeno and Y. Nakagawa, "Dieless Forming of Carbon Fibre Reinforced Plastic Parts Using 3D Printer," *Procedia Engineering,* vol. 81, pp. 1595-1600, 2014.

[133] A. Kreger and G. Teters, "Use of averaging methods to determine the viscoelastic properties of spatially reinforced composites," *Mechanics of Composite Materials,* vol. 15, pp. 377-383, 1980.

[134] A. Kregers and Y. G. Melbardis, "Determination of the deformability of three-dimensionally reinforced composites by the stiffness averaging method," *Mechanics of Composite Materials,* vol. 14, pp. 1-5, 1978.

[135] A. Kregers and A. Zilauts, "Limiting values of reinforcement factors for fibrous composites with a three-dimensional structure," *Mechanics of Composite Materials,* vol. 20, pp. 530-536, 1985.

[136] ASTM D638-14, "Standard Test Method for Tensile Properties of Plastics," 2014.

[137] S. Kawabata, "Measurement of the transverse mechanical properties of high-performance fibres," *Journal of the Textile Institute,* vol. 81, pp. 432-447, 1990.

[138] (2015). *Overview of materials for Nylon 6, Extruded*. Available: http://www.matweb.com.

[139] H. Hsiao and I. Daniel, "Effect of fiber waviness on stiffness and strength reduction of unidirectional composites under compressive loading," *Composites Sci. Technol.,* vol. 56, pp. 581-593, 1996.